DOCTOR OF SCIENCES

Advanced chemical characterization of organic electronic materials and devices

langer, eric

Award date:
2019

Awarding institution:
University of Namur

UNIVERSITÉ DE NAMUR

FACULTÉ DES SCIENCES

Advanced chemical characterization of organic electronic materials and devices

Dissertation présentée en vue de l'obtention du grade de Docteur en Sciences

Eric LANGER

Mars 2019

Pour être présentée et soutenue devant un jury composé de :

Laurent HOUSSIAU, Professeur, Université de Namur, promoteur de thèse

Jean-Paul BARNES, Ingénieur de recherche, CEA-LETI, Grenoble, co-encadrant

Olivier RENAULT, Ingénieur de recherche, CEA-LETI, Grenoble, co-encadrant

Jean-Jacques PIREAUX, Professeur, Université de Namur

Robert SPORKEN, Professeur, Université de Namur

Cécile COURREGES, Ingénieur de recherche CNRS, IPREM, Université de Pau et des Pays de l'Adour

Abstract

This thesis is directed towards the development of novel characterization protocols to probe the chemical composition at the nano scale of devices that are used in organic electronics. This enables the investigation of chemical processes like the degradation of molecules or dopant migration that occur during device operation as well as the detection of contaminants. This information is much needed to improve the lifetime and the efficiency of the device. Time of Flight Secondary Ion Mass Spectrometry (ToF-SIMS) and X-ray Photoelectron Spectroscopy (XPS) are two commonly used techniques to study the chemistry of inorganic and organic materials. Combined with a sputter gun, depth profiling can be performed to gain 3 dimensional chemical reconstructions of the sample. However, modern organic electronic devices like OLEDs represent a real challenge for chemical depth profiling because of film thicknesses of only a few nanometers, molecules with very similar structure that can be damaged during analysis, and inorganic-organic interfaces that are problematic to sputter through because of substantial differences in sputter rates.

To overcome these obsacles, single layers and bilayers are studied as simplified systems to develop reliable and precise characterization protocols with minimal analysis induced damage to the organic materials. The combination of ToF-SIMS and XPS is key in this part.

Then,these protocols are adapted to study complete OLED devices. Electrically aged devices are compared to non-aged devices to study the degradation of the molecules.

Finally a new sample preparation technique with the creation of extremely shallow beveled craters is explored for an even gentler analysis. This technique is very promessing and could lead to an improvement of the characterization protocol in the future.

Résumé

Cette thèse est orientée vers le développement de nouveaux protocoles de caractérisation pour sonder la composition chimique à l'échelle nanométrique des dispositifs qui sont utilisés dans l'électronique organique. Cela permet d'étudier des processus chimiques tels que la dégradation des molécules ou la migration de dopants qui se produisent pendant le fonctionnement du dispositif, ainsi que la détection des contaminants. Cette information est nécessaire pour améliorer la durée de vie et l'efficacité de ces systèmes organiques. La spectrométrie de masse des ions secondaires à temps de vol (ToF-SIMS) et la spectroscopie photoélectronique à rayons X (XPS) sont deux techniques couramment utilisées pour étudier la chimie des matériaux inorganiques et organiques. Combiné avec un canon d'abrasion, un profilage en profondeur peut être effectué pour obtenir des reconstructions chimiques en 3 dimensions de l'échantillon. Cependant, les appareils électroniques organiques modernes comme les OLED représentent un véritable défi pour le profilage chimique en raison des épaisseurs de couches de seulement quelques nanomètres, des molécules de structures très similaires qui peuvent être endommagées pendant l'analyse, et des interfaces inorganiques-organiques qui posent problème à la pulvérisation à cause de différences substantielles dans les taux de pulvérisation.

Pour surmonter ces obsacles, des couches simples et des bicouches sont étudies comme des systèmes simplifiés pour développer des protocoles de caractérisation fiables et précis avec une analyse qui induit un minimum d'endommagement aux matériaux organiques. La combinaison de ToF-SIMS et XPS est la clé du succès de ces mesures.

Ensuite, ces protocoles sont adaptés à des empilements complets d'OLED. Des dispositifs vieillis électriquement sont comparés aux appareils non vieillis pour étudier la dégradation des molécules.

Enfin, une nouvelle technique de préparation d'échantillon est explorée pour une analyse encore plus douce avec la création de cratères biseautés extrêmement peu escarpés. Cette technique est très prometeuse et pourrait conduire à une amélioration du protocole de caractérisation à l'avenir.

Acknowledgement

Firstly, I would like to express my sincere gratitude to my advisers at the CEA-LETI, Jean-Paul Barnes and Olivier Renault, and the director of my thesis, Laurent Houssiau, for giving me the opportunity of doing this thesis and for the continuous support and guidance.

Thanks to Tony Maindron for sharing your knowledge about OLEDs during our fruitful discussions. Also, thank you for establishing the contact to Yolande Murat who I want to thank as well for the solution-processed OLEDs and the work on the publication. I want to thank Sylvia Meunier-Della-Gatta as well for providing the numerous samples.

I would like to acknowledge the NanoCharacterisation PlatForm (PFNC) of CEA Grenoble and all of the members that helped me and supported me during this thesis work.

I would also like to acknowledge, Jean-Jacques Pireaux, Robert Sporken and Cécile Courreges who have kindly accepted to evaluate this thesis work as a part of the jury.

I would like to thank my colleagues from the PFNC group that I had the opportunity to meet during this experience and that I worked with on a daily basis. I am not going to name everyone because I will surely forget someone. Thank you all for making these three years so joyful and an experience that I won't forget.

Finally, there are some people from outside of the work that I need to thank. Of course my parents, thank you for supporting me always, not only during this thesis but in everything I do. Thanks as well to Monika, Patrick and Thierry for always being there to talk. Thanks to my friends who supported me. And the biggest thank goes to Maiglid for your patience and for keeping me motivated especially during these past months.

Thank you all!

Table of Contents

Abbreviations

LCD	Liquid-crystal display
LED	Light emitting diode
OPV	Organic photovoltaic
OLED	Organic light emitting diode
SIMS	Secondary ion mass spectrometry
ToF-SIMS	Time of flight secondary ion mass spectrometry
XPS	X-ray photoelectron spectroscopy
HIM	Helium ion microscopy
AFM	Atomic force microscopy
RSF	Relative sensitivity factor
HOMO	Highest occupied molecular orbital
LUMO	Lowest unoccupied molecular orbital
UHV	Ultra-high Vacuum
EML	Emissive Layer
HIL	Hole Injection Layer
EIL	Electron Injection Layer
HTL	Hole Transport Layer
ETL	Electron Transport Layer
HBL	Hole Blocking Layer
TADF	Thermally activated delayed fluorescence
NR	Neutron reflectivity
PL	Photoluminescence spectroscopy
EL	Electroluminescence spectroscopy
AES	Auger electron spectroscopy
HCLP	High Performance Liquid Chromatography
LDI-MS	Laser Desorption/Ionization Mass Spectrometry
MALDI-ToF-MS	Matrix Assisted Laser Desorption/Ionization Time-of-Flight Mass Spectrometry
FWHM	Full width at half maximum
GCIB	Gas cluster ion beam

LMIG	Liquid metal ion gun
BA	Burst alignment
HCBU	High current bunched
PMMA	poly(methyl methacrylate)
ITO	Indium tin oxide
MS/MS	Tandem mass spectrometry
PVD	Physical vapor deposition
RSF	Relative sensitivity factor
PIN	p-doped transport layer, intrinsic emitting layer, n-doped transport layer

Chapter I:

Context and Background

1. Organic Electronics: An emerging alternative to existing semiconductor devices

Electronic devices of all kinds are found everywhere in our everyday life. Smartphones have become the most important gadget in our lives. The world is becoming more and more connected. Intelligent devices have found their way into our homes. Those devices are powered by photovoltaic cells and newly developed batteries. Our cars are equipped with dozens of sensors to guarantee our safety. Devices like this produce immense amounts of data that are stored on efficient memory devices. All of those applications need to be improved constantly to keep up with increasing consumer demands. Innovative technologies are needed to make these devices better, faster, smaller and more efficient.

The biggest part of the electronics market is represented by the consumer electronics like smartphones, TVs or laptops. These devices have undergone a fundamental change since the early 2000's. The introduction of liquid-crystal display (LCD) and light emitting diode (LED) technology as well as the shrinking of transistor dimensions have been crucial milestones in the progression of consumer electronics. Silicon-based devices have dominated the market from the beginning, but devices with organic materials have found increasing success in recent years.

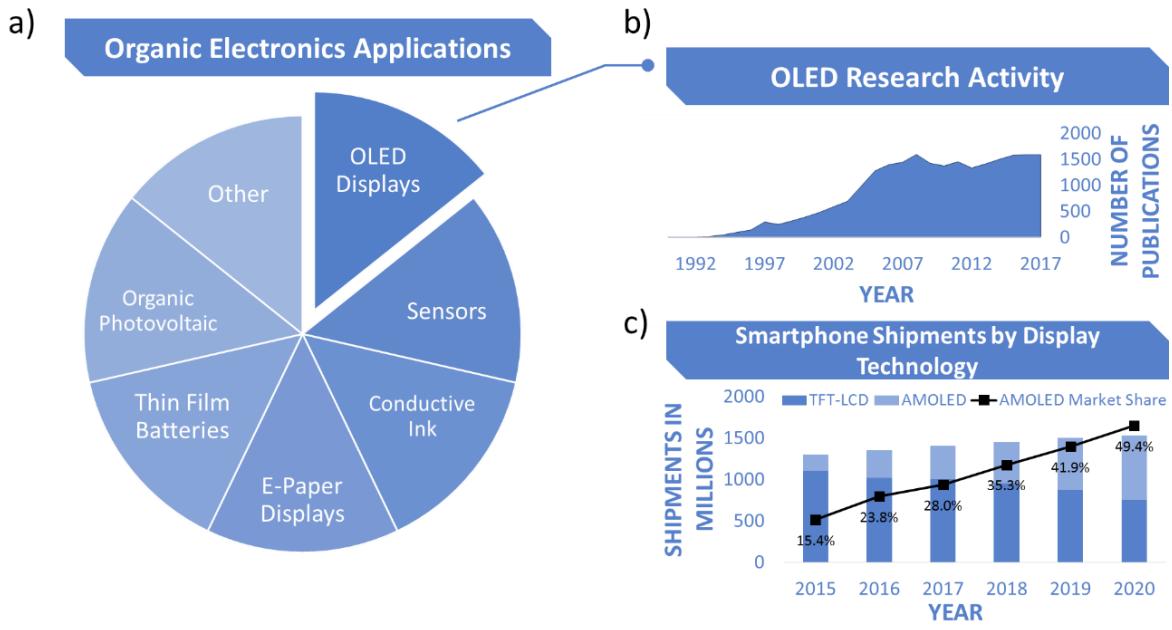

Figure 1 *a) Main applications for organic electronic materials, b) the number of publications on OLEDs since their invention (Source: Scopus search engine) and c) forecast for the development of display technologies that will be used in smartphones in the following years (Source: Wits View, July 2017)*

Flexibility, transparency and the possibility of solution processing are some of the characteristics of organic electronics that have attracted a lot of attention. The field of possible applications for organic electronics is very wide (Figure 1 a)). The focus of this work will lie on lighting and display applications.

Organic light emitting diodes (OLED) are a mature technology and already commercially available in contrast to organic photovoltaics (OPVs), organic sensors or other applications.

LEDs have proven to be efficient and bright devices that can emit light of all colors. The phenomenon of electroluminescent diodes is known since 1907 when H. J. Round discovered it by applying a voltage between two points on a crystal of silicon carbide [1]. But it was only in 1927 when Oleg Losev invented the first working LED using silicon carbide as emitter [2]. For a long time, there was no follow up on Losev's work. But in 1955, the interest in LEDs began to grow after R. Braunstein observed infrared emission from semiconductor alloys [3] which paved the way for the development of the first modern LED in the visible spectrum in 1962 by N. Holonyak [4]. Inspired by Braunstein's work as well as the discovery of organic electroluminescence in the 1950s by A. Bernanose [5], M. Pope produced the first operating organic light emitting diode (OLED) in 1960 using anthracene crystals [6]. At this time, most devices emitted light in the infrared to red spectrum. That is why there was put a lot of effort in developing new semiconductor materials with larger band gaps to produce yellow, green and blue light emitting devices. The main focus was on inorganic materials since their efficiency and operating voltage was much lower than that of their organic counterparts.

It was only when Kodak presented their OLED operating at significantly lower voltages in 1987 [7], that there was a renewed interest in OLEDs. They used a two-layer system where the hole and the electron injection were separated. This structure allows the charge carriers to recombine only in the organic emissive layer. This results in an increased efficiency and a decrease of operating voltage of the devices. Already in 1977, Heeger, MacDiarmid and Shirakawa discovered π-conjugated conductive polymers [8] for which they were rewarded the Nobel Prize in Chemistry in 2000. In 1990, Burroughes and his coworkers presented a green OLED based on such polymers [9]. These publications suggested that organic semiconductors constitute a viable alternative to inorganic materials.

Based on these historical cornerstones, the research interest in OLEDs started to grow very fast at the end of the 20th century and the number of publications related to OLEDs continues to be very high until today (Figure 1 b)). As a result, OLEDs are the first mature technology from the field of organic electronics. Displays are commercially available and Apple, Samsung and LG are using OLEDs in their smartphones and TVs. Forecasts predict an increasing importance of OLED displays for the market (Figure 1 c)).

1.1. OLED devices: State of the Art

Since the introduction of the very first modern OLED in 1987 by Kodak [7], the structure of the devices has changed significantly. They used two organic materials with a thickness of 60 – 75 nm between the electrodes. Modern devices use several additional organic layers to facilitate the charge carrier injection which has helped to drastically increase the efficiency.

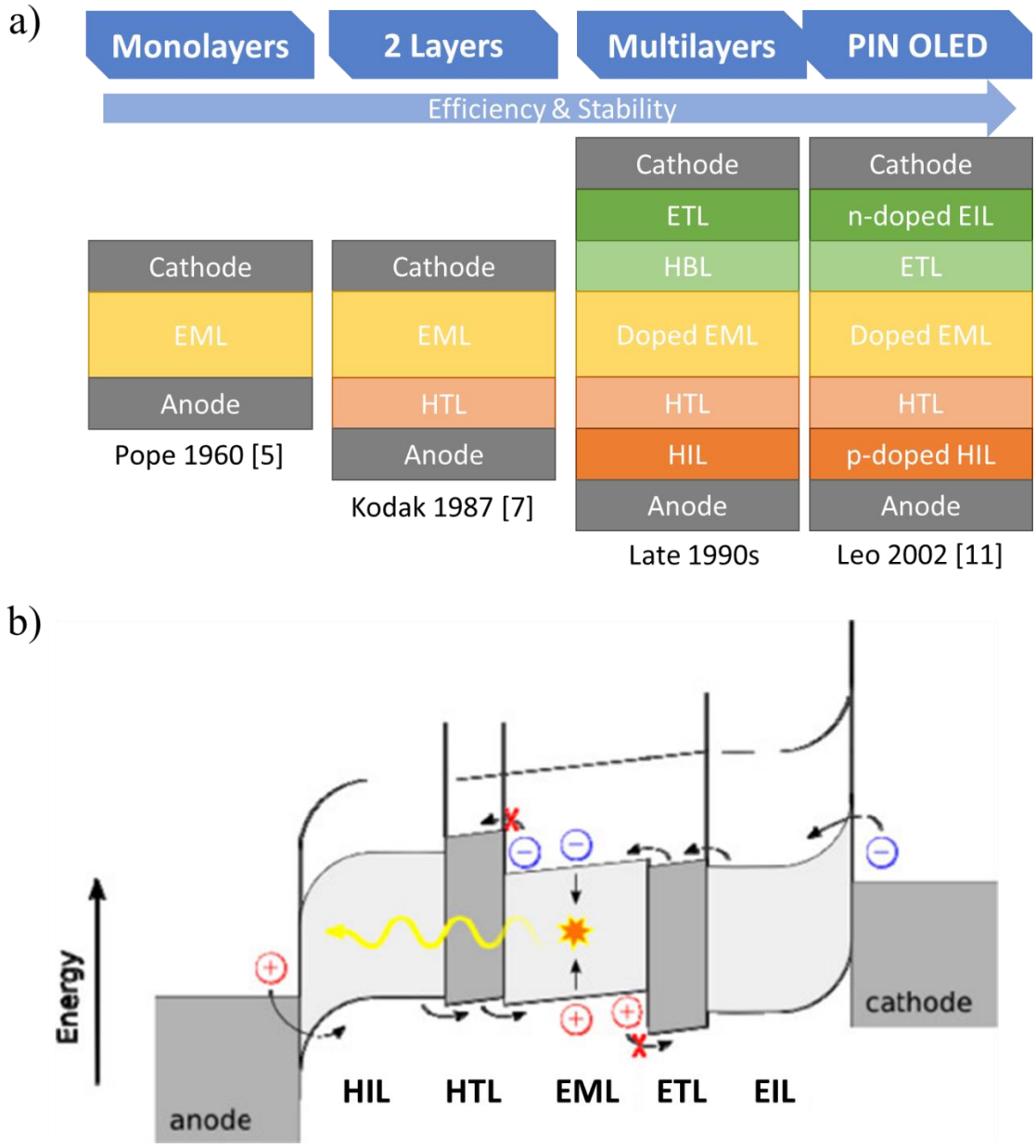

Figure 2 *a) Evolution of OLED devices from a single organic emissive layer to PIN OLEDs. b) Schematic representation of the band diagram of a modern OLED device [10].*

Figure 2 a) shows the evolution of OLEDs from devices with only a single organic emissive layer (EML) to a two-layer device to complex multilayer devices. The PIN structure that has been introduced by Karl Leo and his coworkers in 2002 [11] is still used in today's devices. A p-doped hole injection layer (HIL) and a n-doped electron injection layer (EIL) have been added at the cathode and anode, respectively. This is to facilitate the charge carrier injection from the electrodes into the organic layers. The term PIN results from the device structure with an intrinsic emitting layer between the doped layers (p-doped, intrinsic, n-doped). Figure 2 b) shows a schematic representation of the band diagram for such a PIN OLED device. HIL and EIL form a low energy barrier at the interface with the inorganic electrodes. Charge carriers will flow towards the hole transport layer (HTL) and the electron transport layer (ETL). The HTL and ETL handle two tasks. They provide a smooth band transition from the injection layers

towards the EML and at the same time they act as blocking layers for opposite charge carriers. Electrons coming from the cathode into the device will face a high energy barrier at the HTL-EML interface. Holes coming from the anode will be blocked at the EML-ETL interface. As a result, there will always be several excited electrons available in the conduction band of the emissive material that will recombine with holes in the valence band.

This radiative recombination is very efficient if all layers of the device work as intended and there is a balanced charge carrier injection of electrons and holes. A measure for the efficiency is the external quantum efficiency (EQE). It represents the ratio between the number of charge carriers put into the device and the number of photons that leave it. Ideally, every injected electron could recombine in the EML and emit a photon that can leave the device. A high EQE means that the device can be operated at low voltages with low power consumption. The EQE is dependent on various parameters like the interfacial energy alignment between the different layers [12], the electrode work function [13], the absorption of light in the device itself [14] or even the layer thickness of transport layers [15]. The efficiency can also be measured as current efficiency in cd/A or power efficiency in lm/W.

Another important index for OLEDs is the luminance in cd/m^2. The combination of a high EQE at high luminance is the key to good OLED devices. The emitted wavelength is a third parameter that defines the characteristics of OLEDs. Generally, red, green and blue OLEDs are needed in display applications. OLEDs are very popular because of their vivid color reproduction.

By incorporating the above described supporting layers, the EQE of OLEDs could be increased drastically in the past decades. But the change to the use of phosphorescent emitters or thermally activated delayed fluorescent (TADF) emitters instead of regular fluorescent emitters had the biggest impact on the improvement. Fluorescent emitters can only use 25% of the electron-hole pairs for light generation whereas phosphorescent emitters use all of them (see section 2.1).

These novel materials in combination with adapted device structures can result in very high EQE values. Numbers over 25% could be reached for red [16], green [17] and blue [18] devices. But those record devices often exhibit a rather low luminance. Devices for an industrial application need to have values in the range of several thousands of cd/m^2. Typical EQE values are in the range of 15 - 20% at a luminance of 1000 cd/m^2 with a maximum luminance around 10 000 – 30 000 cd/m^2 [19].

1.2. Perspectives and challenges

With the immense increase in efficiency of OLED devices, people have started looking into other interesting properties of organic materials. Recently, efficient transparent and flexible devices have been demonstrated [20] (Figure 3). Flexible devices have already found their way into the stores and it is believed that the market share of OLED displays will further grow in the following years (Figure 1 c)). Several applications like foldable or rollable displays are in the works.

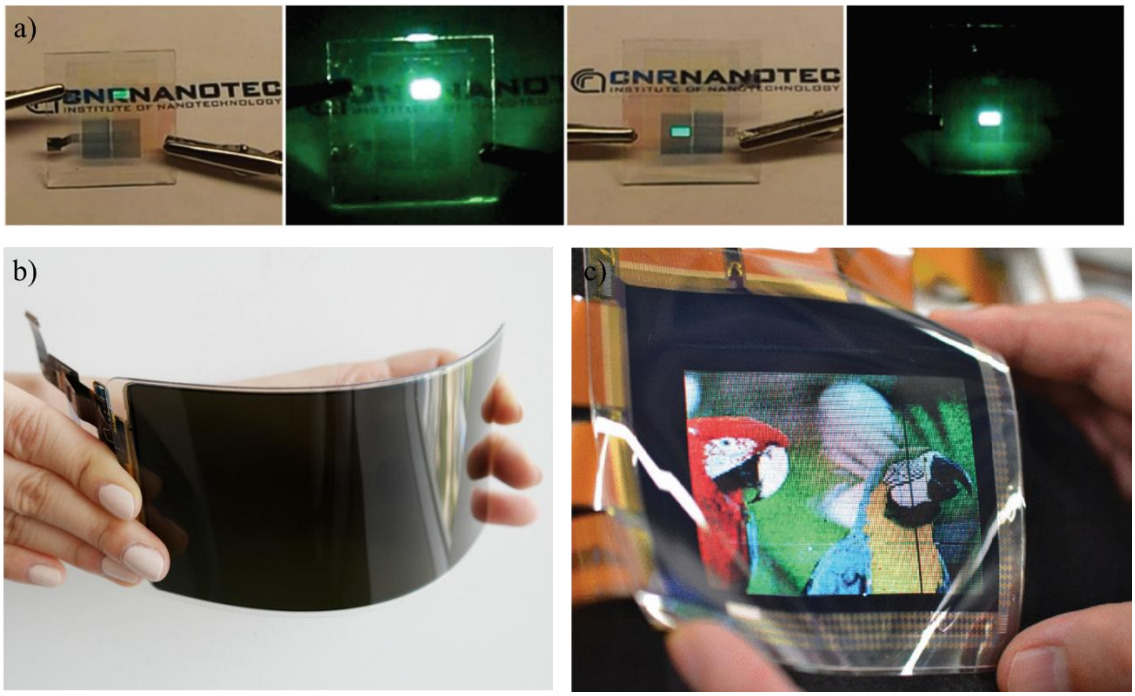

Figure 3 *a) Transparent OLED devices with high luminance and high efficiency [20] b) Samsung Display's "Unbreakable Flexible OLED Panel" (source: Samsung Newsroom, July 25, 2018) c) Flexible OLED display driven by ink-jet printed organic thin film transistors (OTFT) [21]*

Flexible substrates not only open up new possibilities for innovative applications, but they also allow the use of new, high throughput processing methods. Roll-to-Roll processing has become increasingly popular [22]. This technique can be used to produce large lighting panels as well as display applications. Conventional manufacturing systems use multi-chamber evaporation systems with robots that transfer substrates from one chamber to the next. It takes a relative long time to transfer the substrate between the chambers. The material consumption is also quite elevated in these systems. In roll-to-roll systems, the substrate will pass different evaporation steps without the need of being transferred from chamber to chamber. The materials can be deposited with less material loss and the overall manufacturing time is reduced which brings a cost reduction with it. The OLEDs can be deposited directly onto plastic barrier substrates. This is not possible in conventional systems. It makes the production of flexible devices much easier.

Another advantage of OLEDs is that organic materials are generally solution processable. This can reduce the production costs even more because no vacuum is needed during the deposition process. The efficiency and the lifetime of completely solution processed devices are rather low however [23]. This is mainly due to the fact that solution processed layers have a higher roughness than evaporated layers. Also, solvents of upper layers can attack and damage underlying layers. This results in more possible pathways for electrical shortcuts and more electrochemical stress in the device which shortens the lifetime [24]. Yet, some devices that exhibit excellent electro-optic properties contain solution processed

layers [25]. A consequence of the developments in solution processed materials is the emergence of printable electronics[21], [26] (Figure 3 c)).

The potential of OLED applications seems enormous but some of the high brightness devices still have lifetime problems. Commercially available LED lamps have a typical nominal lifetime in the range of 25k – 100k h [27].

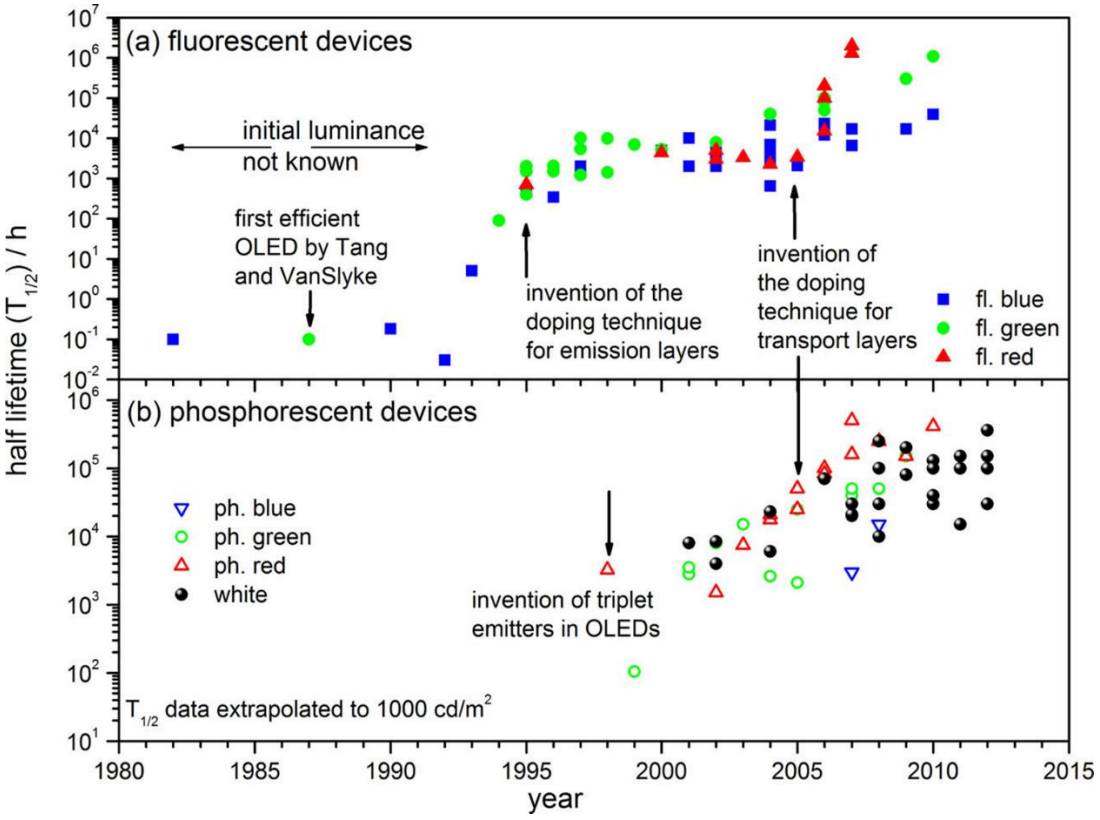

Figure 4 Lifetime evolution of fluorescent (a) and phosphorescent (b) blue, green, red and white OLEDs [28].

OLED devices have typical lifetimes of 20k h [29] and only red and green devices can sometimes reach values up to 100k h as it can be seen in Figure 4. The difference is due to the degradation of organic molecules that is discussed in the following section. In order to make OLEDs competitive, it is necessary to improve the lifetime especially for the high brightness devices.

It is also important to reduce the fabrication costs of OLED panels and displays since their production costs are high in comparison to other lighting solutions. Moreover, the power efficiency is not quite yet on the same level as LCD displays.

2.Degradation in organic materials and devices

OLEDs have shown significant overall improvement in recent years thanks to enormous research efforts. But in terms of cost-efficiency, lifetime, and power efficiency, they are not yet competitive compared to other lighting or display options.

Degradation of the organic materials is one of the main drawbacks of organic electronic devices that needs to be addressed. Especially for OLEDs, researchers have been successful in creating highly efficient and economically profitable devices. But the durability of high brightness devices seems to limit commercial applications. An overview of organic semiconductors that are used in these devices will be given in this section. Different forms of degradation will be discussed, and the corresponding degradation mechanisms explained with a special focus on OLED materials.

2.1. Organic semiconductors

The discovery of organic semiconductors dates back to the late 1940s [30] and in the 1970s, MacDiarmid, Heeger and Shirakawa showed the conductivity of doped polymers for which they were awarded the Nobel Prize in Chemistry in 2000 [31]. These findings made clear that organic materials are a valid alternative to inorganic semiconductors. The conductivity, the color and other properties of the materials are tunable thanks to a wide range of different molecules and the possibility of doping. Industry has also been taking advantage of other interesting properties of organic materials like flexibility, high transparency or low-cost manufacturing.

These interesting properties are a result of the molecular structure of organic materials. In inorganic semiconductors, the atoms are strongly linked with one another in a crystalline structure through covalent bonds. This results in continuous energy bands. In organic materials, the molecular orbitals form discrete energy levels. A highest occupied molecular orbital (HOMO) and a lowest unoccupied molecular orbital (LUMO) can be defined rather than a valence band or conductive band like in their inorganic counterparts.

The key to conductivity in organic semiconductors are conjugated systems. Connected carbon atoms develop overlapping π-orbitals due to sp^2-hybridization. The overlap causes the π-electrons to be delocalized. For molecules and polymers, the π-bonds become connected and form π-conjugated systems with delocalized π-bonds in which the charge carriers can move with high mobility. The energy gap between occupied bonding orbitals and unoccupied anti-bonding orbitals is sufficiently small in π-systems to exhibit semiconducting properties [32].

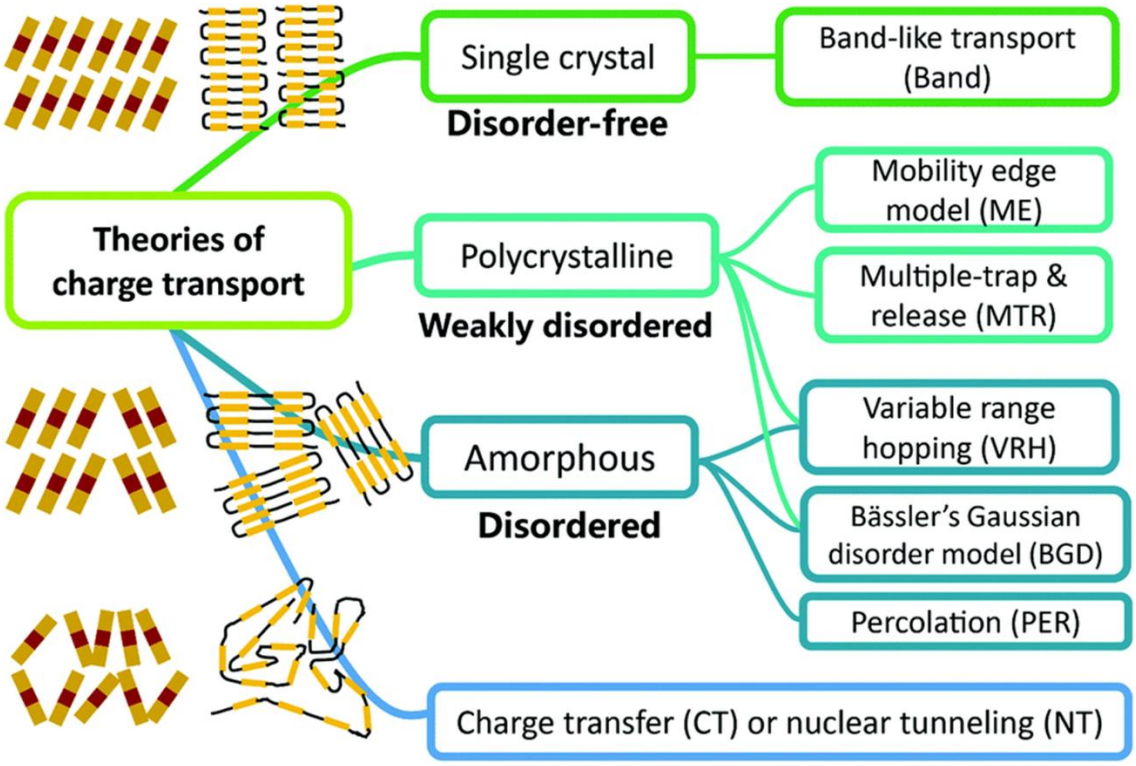

Figure 5 *A brief summary of charge transport theories in organic semiconductors (Small molecules and polymers). According to the degree of order or crystal structure, these theories can be divided into several categories* [33].

The charge transport is strongly determined by the packing of the molecules. Figure 5 gives an overview of different charge transport theories for organic semiconductors depending on their degree of order [33]. The crystalline structure is very important for small molecules because they do not possess long range intramolecular delocalization like polymers. The molecular arrangement and the intermolecular interactions determine the conductive properties of small molecule materials [34]. For single crystal systems at low temperatures, the charge transport can be described as band-like. It is however very difficult to create disorder-free layers. Most layers are weakly disordered. The charge transport in these systems can't be explained with traditional models due to the non-covalent bonds between neighboring molecules. There are multiple theories that try to explain the charge carrier transport between molecules in organic materials. If the temperature increases or the film becomes more disordered, the single molecular orbitals dissociate more and more, and the transport is most often described as thermally assisted polaron hopping (or variable range hopping) where charge carriers jump between adjacent chains [35]. Polycrystalline films are often found in OPVs. The mobility edge model or the multiple trap and release model can be applied to describe the charge transfer in such samples. In these models, charge transfer occurs band-like inside the crystalline part. When a charge reaches an impurity, like a grain boundary, it can be trapped. The trapping energy is gate-voltage dependent and can be overcome thermally [36]. In completely disordered systems, charge carriers can tunnel from one molecule to another.

A dense and highly ordered molecular packing is therefore needed to reach high charge carrier mobility in organic semiconductors. This is desired for the supporting layers in the OLED stack. The emissive layer needs to exhibit additionally other properties like efficient charge carrier recombination or defined band gaps. Emissive layers typically consist of a host material in which the light emitting material is incorporated. Fluorescent, phosphorescent and TADF emitters for the use of light emitting materials have been mentioned briefly in section 1.1.

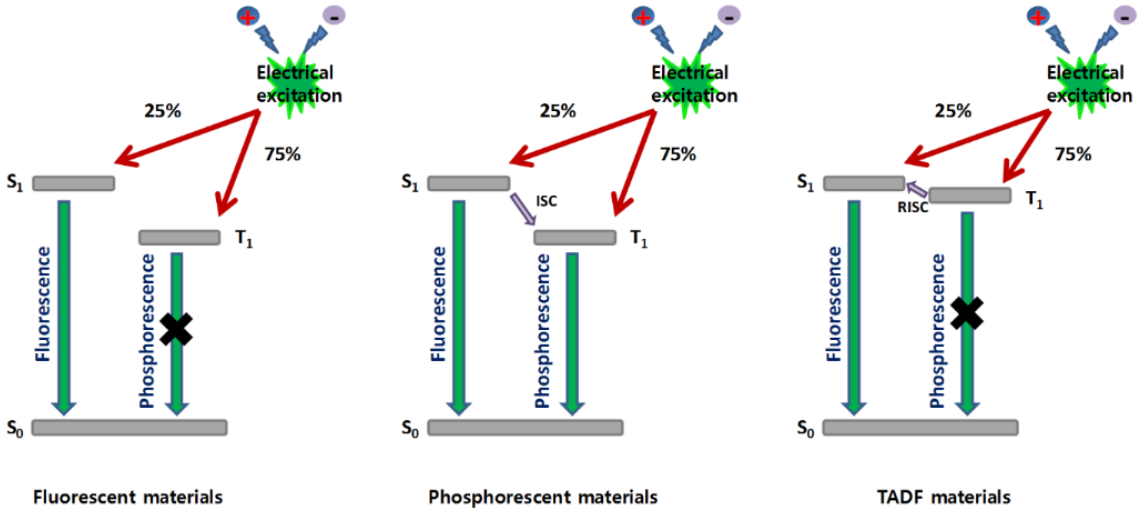

Figure 6 *Radiative pathways existing in fluorescent, phosphorescent and TADF emitters [37].*

Figure 6 shows the radiative pathways that exist in the different types of emitters. Fluorescent emitters are those which only emit light after the recombination of singlet excitons. Excitons are electron-hole pairs that are bound trough Coulomb interaction. It is considered a quasiparticle which can transport energy without transporting net charge because of its electrical neutrality. The bound exciton has slightly less energy than an unbound electron-hole pair. Singlet and triplet states for excitons are a result of quantum mechanics. Two electrons in the ground state in the same orbital must be paired. They possess opposite spins. If one electron is excited, they occupy different orbitals and can have either opposite or parallel spins. Electrons generate magnetic angular momentums as a result of their spin. For electron pairs, in the case of opposite spins, the magnetic angular momentum is always 0 (as a result of one spin “up” and one spin “down”). Those electrons are in a singlet state. For parallel spins however, there are three different possibilities for this angular momentum (both spins “up”, both spins “down” and one “up”, one “down” but in phase). Electron pairs with parallel spins are therefore in a triplet state. Two electrons with parallel spin will avoid one another more effectively because of the Pauli Exclusion Principle. The electron-electron repulsion is minimized and the triplet states are energetically advantageous compared to singlet states. Following this principle for the formation of excitons in the emissive layer of organic light emitting diodes, it is three times more probable for an electro-hole pair to be in a triplet state than a singlet state [38].

Coming back to fluorescent materials, 75% of the excitons formed are triplet excitons that lose their energy in the form of non-radiative recombination and can therefore not contribute to the generation of light. Only 25% of the excitons are singlet excitons that will be transformed into photons. Phosphorescent emitters on the other hand incorporate transition metal ions that induce spin orbit coupling to open up radiative paths from the excited triplet to the singlet ground state. Moreover, the transition energy that is needed by the 25% singlet excitons to reach the emitting triplet states is very low [39]. This makes phosphorescent emitters four times as effective as fluorescent emitters. However, blue phosphorescent emitters are very unstable due to their relative high bandgap. The emitted photons have higher energies than in red or green OLEDs. Often, the photon energy is sufficient to dissociate weak bonds between transition metals and the organic part [40]. That is also the reason why the lifetime generally increases when comparing blue to green to red OLEDs (Figure 4). The charge injection into high bandgap materials is generally a problem of blue OLEDs because it requires higher operation voltages [37]. TADF emitters have been identified as possible solution for this lifetime problem. In TADF materials triplet excitons, that would normally be lost in regular fluorescent materials, can be upconverted to radiative singlet states. If the energy barrier between triplet and singlet state is small enough, it can be overcome thermally at room temperature [37].

2.2. Forms of degradation in OLEDs

Every single layer in the OLED is important for the efficient functioning of the device. Small changes in the band structure (Figure 2 b)) can lead to decreased efficiency of the device. Obviously, the destruction of the emissive material will cause the luminance to decrease. But also degradation of molecules in the HBL or the EBL will lower the device efficiency. Charge carriers won't be blocked efficiently by the EML interface anymore and will instead migrate towards the opposite electrode. Finally, degradation in HIL and EIL will make the charge carrier injection more difficult.

Since their introduction, OLEDs have been struggling with lifetime issues. Organic layers are much more vulnerable to environmental impacts and are more sensitive to an applied voltage compared to inorganic materials. This results in a significantly shortened lifetime of organic electronic devices. Stable luminance and emission spectra as well as a constant operational voltage are the major concerns for device engineers.

As discussed in the previous section, a highly ordered crystalline structure is very important to achieve high charge carrier mobility in organic materials. During degradation of organic layers, it comes to chemical conversion of molecules during device operation. The products of this conversion can then act as deep charge traps, non-radiative recombination centers or electroluminescent quenchers [41]. Deep charge traps are localized electronic states in molecules where charge carries are trapped. The trap energy cannot be overcome by the thermal energy of the charge carrier. The accumulation of these

immobilized charges can cause an increase of the operation voltage because they are filled before other charges can continue to travel through the device. Non-radiative recombination centers will lead to a decrease in both, luminance and efficiency of the device. Electroluminescent quenchers are molecules that can absorb energy from the emissive layer and will therefore reduce the luminance of the device as well.

The observable effects of device degradation can be split into four groups [28]:

- **'Dark-Spot' Degradation**

  Dark spots can be described as inhomogeneous loss of performance through local, non-emissive regions in the device [42]. These initially small regions are mainly created during device production and can grow during device ageing [7,8]. A common source of dark spots has been identified to be delamination of cathode material [45]. Humidity is another cause of this kind of degradation.

- **'Catastrophic Failure'**

  The device breaks down completely. This sort of breakdown is caused by the formation of undesired electrical pathways in the device which result in electrical short circuits. The origin of such pathways are most commonly particles and other impurities on the substrate surface [46], rough surfaces and local heating effects [11,12].

- **Short- and long-term decay of luminescence**

  When there is no observable abrupt failure of the OLED device, there may still be degradation in the form of a slow decrease of device luminance. This can be caused by reactions between different layers or migration of small molecules and dopants into other layers. In some cases, an initial increase in device efficiency may even be observed before the decay of luminescence [28].

- **Color shift**

  The emission color of OLED devices may change over time due to quenching of emissive species or accumulation of new emissive species [28].

Dark-spot degradation and catastrophic failure occur very rarely in modern OLED devices. This is thanks to effective encapsulation techniques, improved device fabrication techniques and the regulation of heat-flow [49]. However, the latter two degradation effects are directly linked to the before mentioned chemical conversion during device operation. The detection of the chemical products of this conversion is essential to gain a good understanding of the degradation process itself. The next section will give an overview of the mechanisms that can lead to such degradation products.

2.3. Degradation mechanisms

Generally, all of the above forms of observable degradation can be caused by either intrinsic or extrinsic factors as indicated in Figure 7. Extrinsic factors can often be adjusted and are rather well controlled. Intrinsic mechanisms are less known and not as easily controllable, since they often depend on material specific parameters that cannot be adjusted. Degradation during device operation cannot completely be avoided. The working principle of OLEDs requires molecules to be in an excited state. Generally, not all of the energy that is put into the device can be transferred into light that can leave the device. Some devices show internal quantum efficiencies very close to 100 %, which means that almost every injected electron emits a photon during recombination [50]. But the light cannot be coupled out effectively. On their way out, photons can be absorbed by impurities and charge carriers. This will again create molecules with electrons in excited states which can lead to more degradation.

Schmidbauer and Hohenleutner identified two main intrinsic degradation mechanisms [41]:

- **Charge carrier induced degradation**

  Charge carrier induced degradation is caused by electrons and holes moving through the molecules. This can cause bond rupture and subsequent radical reactions with surrounding molecules. This type of degradation occurs mainly in the bulk of the supporting layers. The results are deep charge traps that will lead to an increased operation voltage. Charge carriers in the vicinity of the recombination zone can also absorb emitted light and can have significant influence on the efficiency of the device. The number of electrons and holes must be in good balance throughout the device to ensure minimal degradation effects. Uneven charge carrier balance can result in strong local electric fields that can lead to device degradation through electomigration. Molecules with permanent dipoles can be reoriented [51] or diffusion and drift processes can be enhanced [52].

- **Exciton induced degradation**

  Excitons can lead to degradation in the emissive layer and at its interfaces with the surrounding supporting layers. Exciton induced degradation has a big impact on the device because it attacks the emissive molecule directly. Since the molecules are in an excited state, high lying dissociative states of molecules can be reached. The exciton induced degradation is a result of exciton-exciton or exciton-polaron interaction [53]. When an exciton recombines non-radiatively to its ground state, it can transfer energy to another exciton or a polaron. This causes the new exciton or polaron to reach an excited state which can be dissociative. These mechanisms are called exciton-exciton annihilation and exciton-polaron annihilation, respectively. The results are charged

fragments or radicals that can further react with other molecules and therefore ultimately lead to deterioration of the emissive material.

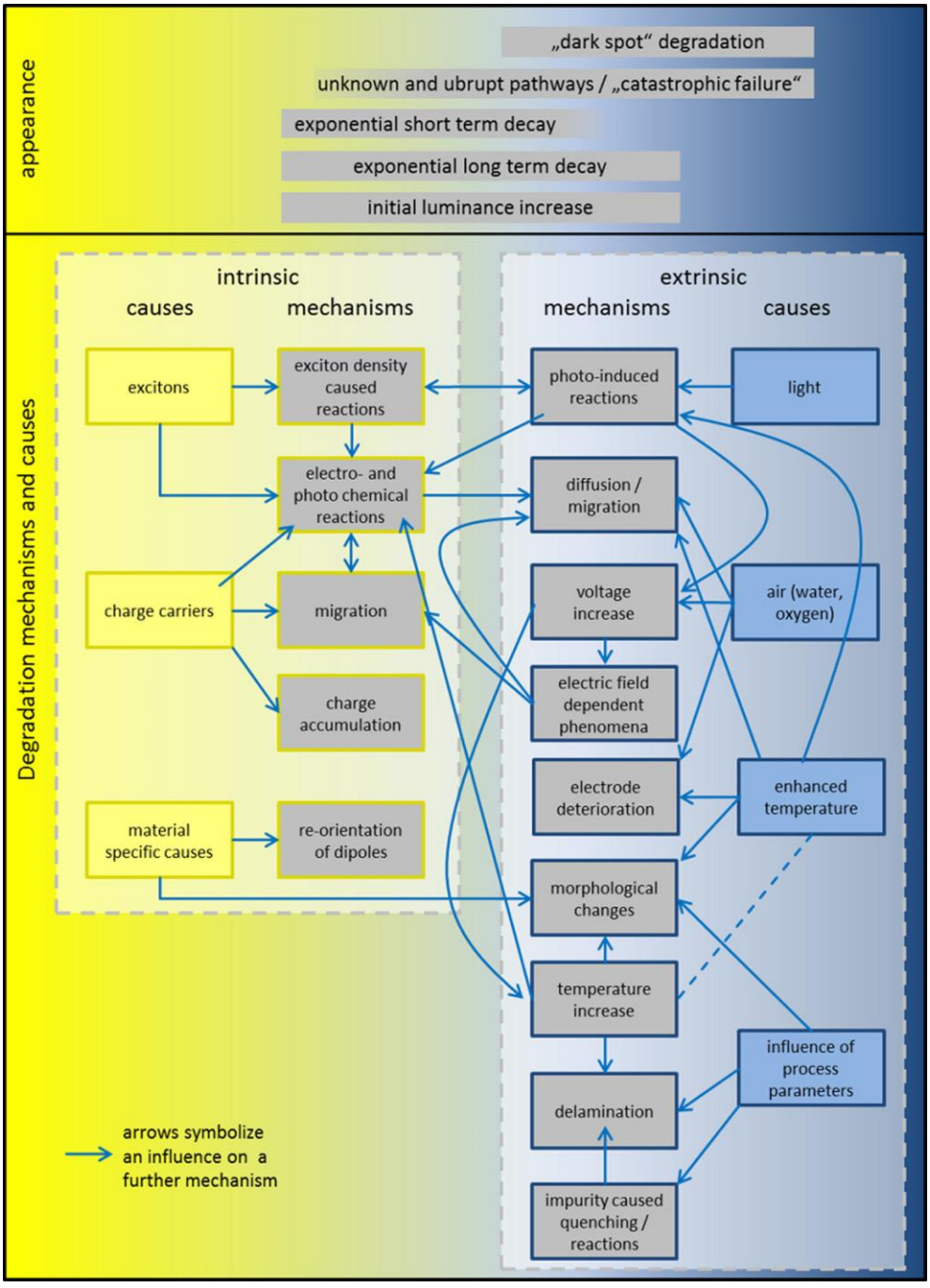

Figure 7 Degradation mechanisms in OLEDs according to Scholz et al. [28].

As for the extrinsic mechanisms, water diffusion is the one with the biggest impact on device performance. It is known, that OLEDs degrade fast under ambient conditions if they are not encapsulated properly. It has been shown that diffusion of water and oxygen with subsequent oxidation of organic molecules and electrodes or hydrolysis of chelate molecules are the reason for this degradation [53, 54, 55].

Furthermore, the choice of the right process parameters is important. It has already been mentioned, that impurities can act as deep charge traps or non-radiative recombination centers. Other parameters like substrate heating during deposition or the deposition rate may influence the morphology of the device which can have an impact on the device performance as well [57].

3. State-of-the-art for chemical characterization techniques of organic electronics

There are numerous electrical analysis techniques that show the direct effects of device degradation. Measurement of current-voltage characteristics as well as electroluminescence over time will illustrate the loss in luminance. But there is a need for chemical characterization techniques to get an insight on the causes of this decreased luminance.

Organic electronics impose some special requirements to these techniques. The method needs to be sensitive to inorganic as well as organic materials. Ideally, they will provide molecular information instead of only elemental. In addition, the method should provide high depth resolution since the different layers in working devices are only a few nanometers thick. At the same time, a high detection limit is required to ensure the detection of the smallest possible amount of diffusion. Most importantly, the method should be able to analyze the device chemistry in depth. This is imperative for the analysis of working devices. This way, aged devices can be compared to virgin devices to gain the required information about changes in chemistry during device operation. Finally, the technique should not alter the device chemistry during the analysis. This means, no damage should be induced by the technique during the measurements.

In the following, a brief introduction of state-of-the-art chemical characterization methods for organic electronics is given and advantages as well as disadvantages will be highlighted in order to evaluate their suitability to characterize the degradation in organic electronics.

- **Auger Electron Spectroscopy (AES)**

  Early on, there have been investigations of degradation products by AES. Depth profiles through working OLED devices could reveal degradation in OLED electrodes [58]. Depth profiles through dark spots could provide useful insights on their creation mechanisms. Even depth profiles of organic multilayer structures have been carried out and led to the conclusion of molecular diffusion through different layers [59]. However, AES cannot provide any direct molecular information. The method is restricted to following certain elements throughout a depth profile. The ability to investigate complex OLED devices is very limited, because most of the materials used in a multilayer stack contain the same elements (carbon, oxygen and nitrogen).

- **High Performance Liquid Chromatography (HPLC)**

  Over time, more suitable chemical characterization methods were developed for organic electronics. HPLC is one of them. It has successfully been used to identify specific degradation products in OLEDs and OSCs [15]. This approach uses solvents to dissolve

fully processed organic electronic devices. The obtained solutions are analyzed by mass spectrometry. That way, it is possible to detect degradation products of the various materials that are present in the device. Assumptions on the degradation paths in these devices can be made by comparing aged devices with virgin ones. The method can detect concentrations as low as several parts per billion which is a very important feature that helps to detect even the smallest amounts of degradation products. The technique struggled in the beginning with dissolving certain materials. Some molecules could not be separated from the injection solvent and thus could not be analyzed. The technique has since been developed and is adaptable to a wider range of materials [61]. But it is still not applicable to all molecules which makes it a very case specific method to use. Some molecules possess a small hydrolytic stability in the used solvents. They are decomposed in the presence of the solvent [60]. Additionally, the top electrode layers that consist of inorganic materials need to be removed to get access to the organic part to dissolve them. Furthermore, only information about dissociation and recombination of molecules is gained. Diffusion cannot be investigated since a localization of the different detected species is not given by the method.

- **Laser Desorption/Ionization Mass Spectrometry (LDI-MS)**

  In parallel to HPCL, there is another technique that has been developed and adapted for the characterization of organic electronics: LDI-MS. This method seems most powerful for characterization of organic electronics. Derived from Matrix Assisted Laser Desorption/Ionization Time-of-Flight Mass Spectrometry (MALDI-ToF-MS), it has been shown that this technique can provide useful information on degradation products in working devices. MALDI is commonly used and a well-established technique in tissue characterization. However, a matrix material needs to be applied to the sample to ensure efficient ionization of surface species. In organic electronics, this matrix is not necessary because of the nature of the molecules in the devices. Electron and hole injection layers are usually p- or n-doped layers that are easily ionized. Because of these supporting layers, there exist intrinsically enough protons and electrons in the device to provide a sufficiently effective ionization. In contrary to HPLC, all molecules can be detected even though sometimes two measurements are necessary, one with detection of positive ions and one with detection of the negative ones. Some materials are very difficult to ionize positively and are therefore only detectable in negative mode [62]. The laser that is used to sputter the surface is powerful enough to remove even the inorganic materials that are used in electrode layers. Therefore, there is no need to remove the top electrode before the measurement which is an important advantage to other chemical characterization techniques. While high spatial resolution has recently been shown for LDI-MS measurements [63], depth resolution remains an important

problem. Depth profiles can be created as a function of laser pulses, but the desorption of the material is not very consistent and depth profiles of multilayer thin film devices like OLEDs are not very sharp [62].

- **Combined neutron reflectivity and photoluminescence spectroscopy (NR/PL)**

  Burn and his coworkers showed in 2004 a possibility to relate the physical structure and the optical properties of polymers by using a combined methodology of neutron reflectivity and photoluminescence spectroscopy [64]. In NR measurements, the sample surface is bombarded with neutrons. The intensity of the reflected neutrons is detected as a function of the incident angle or neutron wavelength. In that way, the technique is similar to other reflectivity techniques like ellipsometry or x-ray reflectometry. But its higher sensitivity for lighter elements like carbon or nitrogen makes NR very appealing to use for characterization of organic electronics. The shape of the reflectivity profile provides information about thickness, roughness or density for any films layered on the surface up to a depth of about 150 nm. This is sufficient to probe complete OLED stacks. By comparing fresh and artificially aged samples, it is possible to detect layer intermixing and diffusion of small molecules with this technique. The addition of PL measurements can complement the findings of the NR and further reveal the composition of diffused layers [65, 66]. One of the drawbacks of this technique is that it is impossible to detect degradation products such as molecular fragments or radicals.

Conclusion

Organic electronics are a viable alternative to inorganic devices. OLEDs are the first mature technology that uses organic materials and that finds a wide range of applications in consumer electronics. Forecasts predict an increasing importance of OLEDs for the market. That is why it is important to constantly work on improving OLED devices. The main driving force in OLED research is the increase in brightness and improvement of efficiency. Numerous new emitter molecules and materials for supporting layers are produced every year. But often it is the lifetime that prevents new developments to reach the market.

At the source of these lifetime problems lies the degradation of organic molecules. Extrinsic degradation due to external influences on the devices like humidity or oxygen is well controlled thanks to effective encapsulation techniques. There are however still intrinsic degradation mechanisms that cause severe performance losses during device operation.

Intrinsic degradation mechanisms are poorly understood. They include charge carrier and exciton induced degradation mechanisms. In order to improve OLED devices, it is necessary to understand what happens during device operation and which molecules break down or diffuse. There is a need for a characterization technique that can provide chemical information of degraded OLEDs.

Currently used methods are not completely adapted for the characterization of organic electronics. Many of them can only analyze certain parts of the device, but not the whole stack. That prevents the analysis of aged devices. It is therefore not possible to investigate the device degradation during operation with these techniques. Other methods will analyze the whole stack at once. They can detect degradation products, but they can’t localize them. It is possible to see humidity in the device for example, but it is not possible to predict where it is accumulated. Diffusion or accumulation of certain dopants cannot be seen either.

ToF-SIMS and XPS depth profiling can possibly provide both, detection of degradation products and their localization. The goal of this work is therefore to study organic light emitting diodes with these two techniques by optimizing analysis parameters for organic electronics.

Chapter II:

ToF-SIMS and XPS for chemical characterization in organic electronics

1. Characterization techniques

As concluded in Chapter 1, Time-of-Flight Secondary Ion Mass Spectrometry (ToF-SIMS) in combination with X-ray Photoelectron Spectroscopy (XPS) could potentially be used to localize degradation products in organic electronics by their advanced depth profiling capabilities. SIMS and XPS are two methods that have been used for a long time to study the chemical composition of all kinds of samples. But it is only recently with the introduction of cluster primary ion sources that organic materials could be reliably analyzed with ToF-SIMS and XPS depth profiling. These cluster sources have proven to only induce small amounts of damage to organic molecules, in stark contrast to the monoatomic sputter sources used previously.

In this section, a closer look will be taken at both techniques in order to understand the fundamental processes that occur during analysis and to emphasize their outstanding utility for chemical characterization of organic electronics.

1.1. Time-of-Flight Secondary Ion Mass Spectrometry

Firstly, the basic principle of ToF-SIMS analysis will be explained before the different possible acquisition modes are shown. Secondly, with this basic understanding, the theory behind the fundamental processes during ion bombardment is given. Finally, this theory is applied to organic materials to make the connection to organic electronics. The instrumentation that was used in this work is described in the appendix.

1.1.1. History and basic principle

The discovery of the basic Principle of ToF-SIMS analysis goes back to J. J. Thomson who observed the first ion-induced emission of secondary ions in 1910. His results were published three years later, when he showed the detection of secondary rays containing positive charged particles after hitting a metal target with cathode rays [67]. His apparatus for the detection of these positive ions constitutes basically the first mass spectrograph. Following this work, many physicists used Thomson's approach to determine the mass of elements and their isotopes. Primarily A. J. Dempster in 1916 and H. D. Smyth in 1922 made great progress in developing simpler detection instruments than the one used by Thomson [19, 20].

Finally, F. L. Arnot and M. A. Milligan presented the first secondary ion mass spectrometer [70]. They studied the energy distribution of negatively charged secondary ions that were created by an impact of positive primary ions on a flat surface. In the late 1940's, R. F. K. Herzog and F. P. Viehböck developed

an instrument that can be seen as an early prototype for modern SIMS instruments [71]. It was the first instrument to use an electron impact primary ion source.

Following this work, the interest in secondary ion mass spectrometers grew steadily and multiple research groups worked on improving the technique. Two decades later, the NASA financed a project to develop an instrument that would be able to examine the chemical composition of extraterrestrial samples that were brought back from space missions. As a result, GCA Corporation released the first commercial available SIMS instrument [72]. After Beske and Werner showed the possibility to use SIMS for characterization of thin film semiconductors in the microelectronic industry [73], the interest in the technique grew even faster.

Up to this point, SIMS instruments mainly worked in the so called "dynamic mode", which means that the ion source was continuously operated in dc mode and the detection of secondary ions was performed by magnetic detectors. But in 1969, A. Benninghoven introduced the concept of "static" SIMS in which the primary ion beam is pulsed [74]. That way, only a small fraction of surface atoms is released as secondary ions after the pulsed impact. This creates an extremely surface sensitive characterization method. Another advantage of the static mode is the easy integration of time of flight detectors. This development marks therefore an important step towards ToF-SIMS as we know it today.

R. D. Macfarlane and D. F. Torgerson first used a Time of Flight detector in 1976 in their mass spectrometer to detect secondary ions. At that time, they used nuclear fission fragments of a Cf-plasma as the primary ion source in dynamic mode [75]. The first to take advantage of pulsed primary ions in static SIMS were B. T. Chait and K. G. Standing in 1981 [76]. Building upon these early instruments, Benninghoven started working on the commercialization of ToF-SIMS instruments during the 1980's in Münster (Germany), which led to today's modern ToF-SIMS instruments.

ToF-SIMS has become a standard technique for chemical characterization of all kind of samples. This is thanks to the many advantages that this technique offers. All elements and even complex molecules can be detected with high sensitivity: The detection limit is of the order of some parts per million or even parts per billion for favorable elements. By using an electron flood gun, the surface potential can be kept constant and even insulating materials can be analyzed. The mass resolution can reach up to $m/\Delta m \approx 20000$, which allows isotopes and molecules with very similar masses to be distinguished. This high mass resolution is not always achievable or sometimes not high enough to resolve certain mass overlaps, especially for complex organic samples with large molecules. Recent advances in instrument technologies can help deal with this problem such as the combination of ToF-SIMS instruments with tandem mass spectrometry (MS/MS) [11, 12] or orbitraps [79]. Furthermore, modern instruments provide a lateral resolution of about 50 – 100 nm. Recently, it has been shown that the lateral resolution can be improved by coupling SIMS with other techniques like Helium Ion Microscopy (HIM) [80]. More importantly, ToF-SIMS gives chemical information in depth which allows for a 3-dimensional chemical reconstruction of the sample volume. The depth resolution is of the order of a couple of

nanometers. However, there are some drawbacks to the technique as well. First of all, it is a destructive technique that prevents further investigation of the same sample spot. Another disadvantage is the variation of secondary ion yields for different elements and a matrix effect which can make quantification difficult or sometimes even impossible (see section 1.1.2.2). However, quantification is in some cases possible with the help of standards and Relative Sensitivity Factors (RSFs). Finally, compromises between certain instrument parameters have to be made. High mass resolution often comes with a reduction of the lateral resolution and vice versa. This subject will be treated later on in this chapter. Despite these drawbacks, ToF-SIMS is a very versatile technique to determine the chemical composition of any sample with high lateral and depth resolution. Figure 8 a) shows a schematic representation of a ToF-SIMS dual-beam setup. A short primary ion pulse is generated in the analysis source. The primary ions are focused and typically accelerated in a 45° angle towards the sample surface where they will collide with surface atoms. Nowadays, bismuth is often used as the analyzing element. Either in the form of monoatomic ions or in form of small charged clusters with up to 5 atoms per cluster. Clusters have been introduced to reduce the energy per atom with which the sample is bombarded. This results in gentler sputtering that is beneficial for the analysis of organic materials because it increases the yield of molecular ions (section 2). Even bigger cluster like C_{60} molecules or argon cluster with up to 10000 atoms per cluster might be used.The impact of the primary ion will initiate a collision cascade at the sample surface causing a number of surface atoms to be released. A small fraction of these sputtered surface atoms or molecules are charged and can be accelerated as secondary ions towards the time of flight detector that is mounted surface normal over the sample. The whole measurement is performed under ultra-high vacuum (UHV) at about 10^{-8} mbar to avoid any additional collision between particles after they have been released from the sample surface (however, recombination and reactions between secondary ions cannot be completely excluded). With the initial primary ion pulse as starting point, it is possible to measure the time that every ion took to reach the detector at the end of the time-of-flight column and it is possible to calculate the respective mass of these secondary ions. In this way, a mass spectrum is created after each analysis pulse.

To create depth profiles, a second gun can be used to sputter more of the sample away. Each analysis cycle is followed by a sputter cycle. During the sputter cycle, ions are accelerated towards the sample surface, at a 45° angle. The sputter cycle is significantly longer (80 µs compared to 1 ns) than the short analysis pulses which causes much more surface material to be released. Typically, cesium, argon, oxygen or xenon ions are used as sputter species. For organic samples there is the possibility to use cluster sources to preserve molecular information. By alternating between analysis and sputter cycle, it is possible to obtain depth profiles of the sample chemistry. The cycle diagram in Figure 8 b) clarifies this principle.

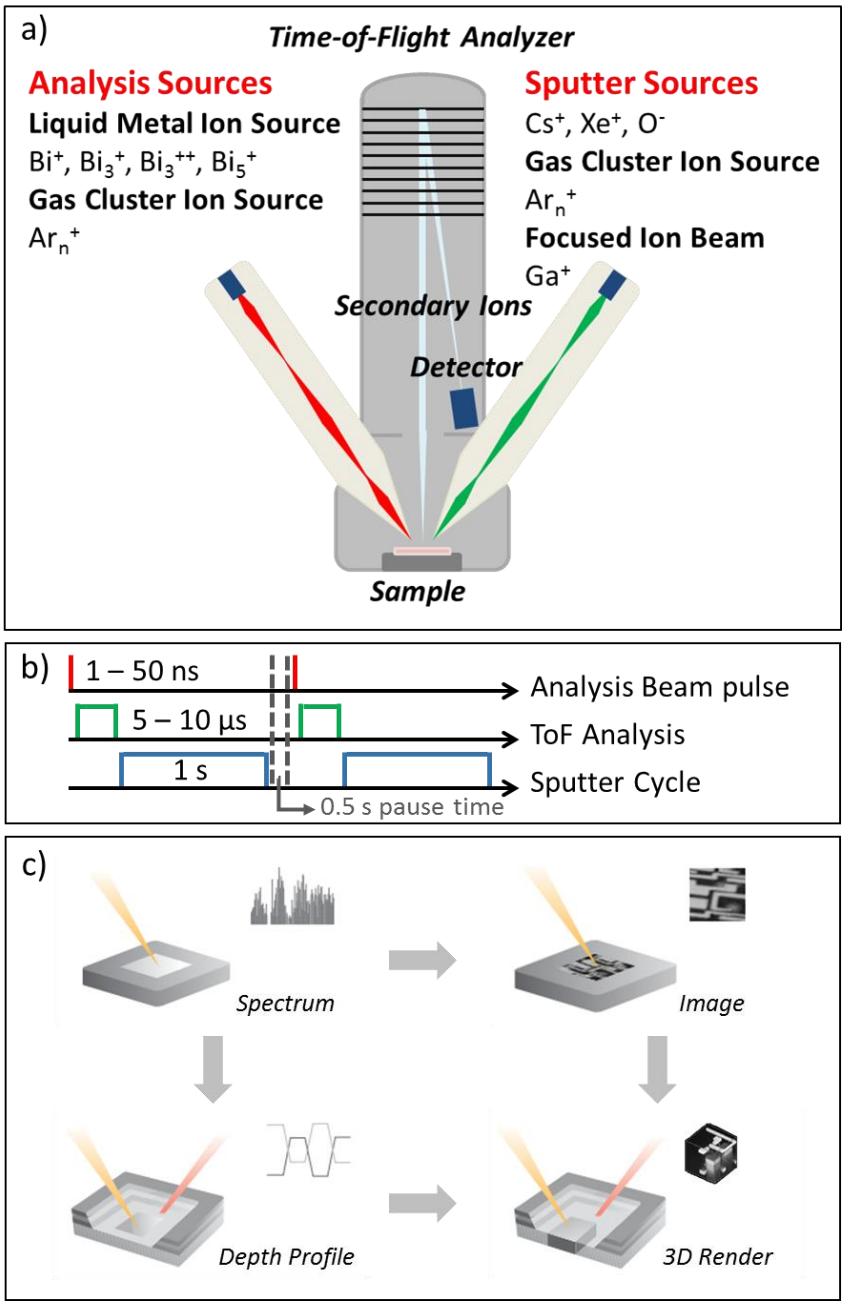

Figure 8 *a) Schematic of a typical ToF-SIMS dual-beam setup, b) cycle diagram during a dual-beam acquisition and c) basic acquisition modes* [81].

The different time values of every sub-cycle can be adapted to satisfy certain needs for every individual analysis. A shorter analysis pulse or a lower current will for example induce less damage to the sample surface but at the same time it will also cause less collisions and therefore result in a lower secondary ion intensity. The time for the time-of-flight analysis can be extended to permit heavier atoms or molecules to be detected. But prolonging the ToF analysis times means prolonging the overall analysis time and also increasing the data file size of the measurement. ToF-SIMS data files can become very quickly several gigabytes in size. Even though the storage capacity is not a major concern for modern PCs, the time-of-flight analysis time should be minimized in a way that the heaviest secondary ion of interest still can be detected. The sputter cycle determines the depth resolution for a big part. The depth resolution can be improved when the sputter time is shortened. However, the sputter cycle is also used

to remove the zone at the surface that has been damaged by the high energy analysis beam. A compromise between high depth resolution and accumulation of sample damage needs to be made. Additionally, a short break between this sputter cycle and the next analysis pulse can help to regain a thermodynamic and electric equilibrium before the next cycle starts. An electron gun can help to achieve this equilibrium faster.

Before the fundamental theory behind the analysis and sputter processes will be explained, a short overview of the basic acquisition modes will be given (Figure 8 c)). A complete **mass spectrum** will be recorded after each analysis pulse as mentioned earlier. The instrument can generally extract either positive or negative secondary ions at a time. The choice of polarity is made with respect to the species to be observed in the mass spectra. The analysis beam is scanned over the surface. Depending on the beam parameters, different modes can be distinguished.

During the "**imaging mode**", the instrument works with the highest possible lateral resolution of 50 – 100 nm. The analysis source will shoot several pulses on the same sample spot and the mass spectra will be summed to gain high secondary ion intensities.

In the "**depth profiling mode**" the lateral resolution is often less important. The focus lies on depth resolution. The analysis beam is again scanned over the surface but this time, the sputter gun is used in between individual analysis cycles. The sputter beam is typically scanned over a bigger area than the analysis beam with a ratio of about $A_{analysis}/A_{sputter} \approx 0.4$ to avoid analysis of the sputter crater walls. To reduce the damage induced by the high energy primary ions, the ratio between the sputter beam and the analysis beam should be minimized (ideally this should be kept below 600) or the pulse width can be reduced. This reduction comes with a lower intensity, but it is a necessary trade-off if the depth resolution needs to be kept high.

The third acquisition mode is a combination of ToF-SIMS imaging and depth profiling. During a "**3D rendering**" acquisition, the lateral resolution and the depth resolution both need to be high while maintaining an acceptable secondary ion intensity. Several chemical images are stacked on top of each other in these kinds of measurements to obtain a 3-dimensional chemical reconstruction of the sample. However, the 3D reconstructions are not always precise. There are some restrictions like the need of a flat sample surface, and preferential sputtering that can create distorted reconstructions. Recent advances in methodology suggest a combination of ToF-SIMS and Atomic Force Microscopy (AFM) to account for initial sample topography [14 – 16].

1.1.2. Theory of fundamental processes

Data treatment of ToF-SIMS measurements can become very complex because of the destructive nature of this technique. Surface recombination or oxidation, layer intermixing, molecular fragmentation, matrix effects and other processes make the data processing very challenging. To gain a deeper

understanding of what actually happens during a measurement at the atomic scale, a closer look at the fundamental processes at a surface during ion beam bombardment and the creation of secondary ions will be taken.

1.1.2.1. Sputtering and secondary ion generation

Primary ion beam bombardment provokes two phenomena at the sample surface. First of all, the sputtering of surface atoms and molecules as an immediate result of the ion impact at the surface and the resulting collision cascade (Figure 9 a), b)). Secondly, the ionization of sputtered species which makes the acceleration and detection by the time of flight detector possible. The sputtering and the ionization take place quasi-simultaneously but are often analyzed separately in order to construct simpler empirical models that can predict the secondary ion generation [85].

Modelling of the sputtering process starts with simplified models. Elastic potential models can be used as a basic approach to describe Ion-Surface interaction. These models are based on the ion interaction potentials that can be described by shielding functions. The shielding function describes the repulsive force between two atoms that approach each other and is proportional to the Coulomb interaction between these two atoms.

The energy transfer from the moving incident ion to static surface atoms is the crucial event for sputtering the surface. Scattering cross sections are used to describe the average energy loss of a particle that travels a certain path. The corresponding equations have been known for quite some time [86].

Such elastic models are however rather basic. For a precise model it is necessary to take also inelastic losses into account. These losses are of electronic nature. A part of the projectile energy can be dissipated to electrons. This phenomenon is inversely proportional to the atomic number *Z*. The inelastic energy transfer can therefore be important for low-*Z* projectiles but the effect in SIMS experiments is rather small due to the high-*Z* materials used as primary ions [87].

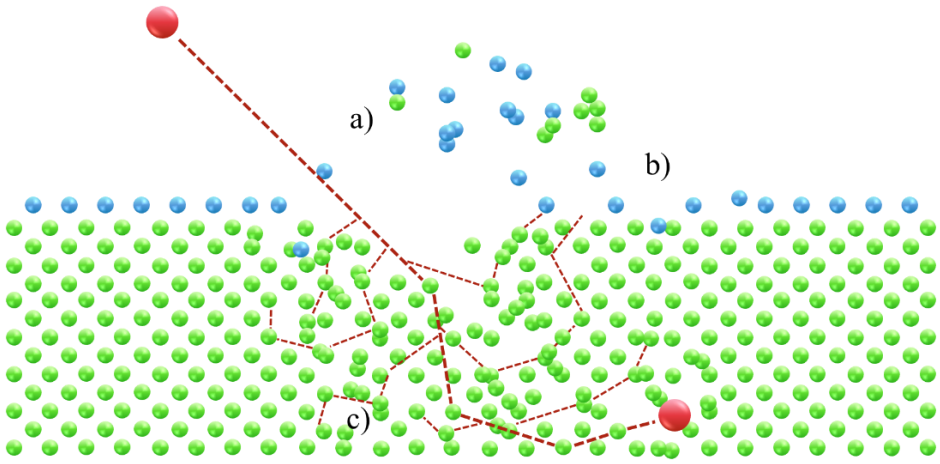

Figure 9 Schematic of collision cascade after a single atom impact at the surface. a) Sputtered surface species that are released upon direct primary ion impact, b) sputtered species that are released as a result of the energy transfer during the collision cascade and c) the zone that is impacted by the collision cascade [88].

Starting with the basic equations for elastic and inelastic energy losses with their respective cross sections, it is possible to generate models to extract ToF-SIMS relevant information like projectile penetration depth, escape depth, sputter rate, and finally the secondary ion yield.

These models are generated by molecular dynamics simulations. They can provide an estimation of the mean path that a projectile penetrates below the surface taking into account a linear collision cascade. The model of linear collision cascades only considers collisions of recoil atoms with resting target atoms. The number of recoils can be simulated. The number of defects that are created in the initial atomic structure can then be estimated if the displacement energy threshold is known. The displacement energy is the minimal amount of energy that is needed for the formation of a stable Frenkel pair which is a defect where an atom is displaced from its initial lattice position to an interstitial place, leaving behind a vacancy. In this way, it is possible to gain knowledge of energy implantation and damage distribution at the surface. This permits then finally to describe the sputtering process for SIMS measurements.

The sputter yield is the value that is most relevant in this context. It is defined as the number of released surface atoms per incident projectile. The sputter yield *Y* depends on the mass and atomic number as well as the incident energy and angle of the primary ion but also on the mass and atomic number of the target material and its material properties. It can be quantified with the following formula [89]:

$$\mathrm{Y} = \frac{1}{\pi^2} \frac{\mathrm{F}(\mathrm{x}, \mathrm{E}, \eta)}{\mathrm{U}_0} \Delta\mathrm{x} \qquad (1)$$

where the sputter yield *Y* depends on the energy *F* that is deposited in the system, the depth of origin of sputtered atoms Δx and the surface binding energy U_0.

The deposited energy *F* is a parameter that can be defined by molecular dynamic simulations as described before. To summarize, it depends on the primary ion energy *E*, and a material specific energy loss coefficient η that takes into account elastic and inelastic energy losses, the incident angle and on the scattering cross section, and therefore on the mass and atomic number of both incident and target atoms. Moreover, it is a function of depth *x* into the target surface. *F* takes into account all of these parameters and can be modelled quite well. A surface atom will be released from the surface if this energy is high enough to overcome a surface potential barrier of height U_0. This potential barrier can be set equal to the cohesive surface energy or sublimation energy of the solid.

The depth of origin Δx however is a far more interesting parameter for SIMS measurements. The depth from which sputtered atoms originate defines the depth resolution of the experiment. It can be expressed by the following equation [87]:

$$\Delta\mathrm{x} = \frac{1}{1 - 2\mathrm{m}} \frac{\mathrm{E}^{2\mathrm{m}}}{\mathrm{NC}_\mathrm{m}} \qquad (2)$$

where the *m* exponent is a measure for the interaction potential for low-energy recoils, *E* is the energy of the sputtered atom, *N* is the number of sputtered atoms with that energy and C_m the cross-section constant taking into account masses and atomic numbers of bombarding and target atoms. The depth of origin can be simulated as well via molecular dynamics. Simulations are in good agreement with equation (2) [46, 47].

The sputter yield and the depth of origin are two important parameters that can be calculated and simulated by molecular dynamics. But the most relevant parameter in SIMS measurements is the secondary ion yield Y_S. The basic SIMS equation gives the secondary ion current I_m for a surface species *m*:

$$I_m = I_p Y_m \alpha \theta_m \eta \qquad (3)$$

where I_p is the primary ion flux, Y_m is the sputter yield of species m, α is the ionization probability, θ_m is the fractional concentration of the species m in the surface layer and η is the transmission of the analysis system.

After simulating Y_m with the help of equation (1) and with η being in the range of 90 – 95 % for modern instruments this leaves α as the only unknown value. α depends on many parameters and cannot easily be determined. It not only depends on the electronic properties of the analyzed surface species, but also on the bombarding primary ions and on the electronic environment (see section 1.1.2.2). The secondary ion current is very sensitive to the electronic state of the analyzed material and can change during analysis as a result of the primary ion bombardment and ensuing sample damage or surface modification.

Typical values for the ionization probability are in the range of 10^{-7} – 10^{-3} [92]. That means that only a very small fraction of all sputtered atoms or molecules are actually ionized and can be detected. The ionization probability depends strongly on the chemical environment of the sputtered species. Surrounding elements or molecules that can act as donor or acceptor of charge carriers will facilitate the ionization. A technique that has been studied to enhance the secondary ion yield during ToF-SIMS measurements is laser post ionization [93]. The idea is to use short laser pulses that are fired just above the sample surface for photoionization of atoms or molecules after they have been sputtered from the sample surface.

Independently from the ionization potential and sputter yields, there are two other important parameters in ToF-SIMS that depend heavily on the primary beam: Mass resolution and lateral resolution. Both parameters vary with different operation modes of the primary ion gun. The nature of the primary ions already puts some restraints to these parameters. Over the past decades, liquid metal ion guns (LMIG) have become the standard primary ion source in ToF-SIMS analysis. Mainly bismuth sources are used

in modern instruments. LMIGs offer high current densities and good stability [94]. With bismuth being a high-*Z* element, these sources offer excellent sputtering characteristics (equation (1)). They can attain spot sizes in the range of 100 nm that can be easily scanned. LMIGs produce small clusters alongside the monoatomic Bi^+ ion. A mass filter is used to select the required species. For bismuth sources, it is possible to choose between monoatomic Bi_1, and small clusters like Bi_3 or Bi_5 which can be singly or doubly charged. The pulse width can be reduced down to about 1 ns but is typically in the range of a few tens of nanoseconds [94]. The pulse width is an important parameter, since it determines for a large part the primary ion flux to the sample surface. This has a direct impact on the secondary ion current and therefore on the intensity of the detected signal, as seen in equation (3). The pulse width has also an impact on the mass resolution. Longer exposure of the sample surface by the primary ion beam results in a longer time during which secondary ions can leave the surface. Secondary ions with the same mass are emitted with a delay that becomes longer with the primary ion pulse width. They will be detected with a small delay which will cause peak broadening and therefore a deterioration of the mass resolution. Shortening the pulse width for a good mass resolution is usually only practical when working with large spots and high currents due to instrumental constraints. Small spots with short pulse widths are associated with low currents that do not produce enough secondary ions to be useful. Generally, a compromise has to be made between good mass resolution and good lateral resolution.

Several operation modes for the LMIG primary ion beam have been developed [95]. In the so-called burst alignment mode (BA), the beam diameter is held in the range of a few hundred nanometers by an electrostatic lens system. The pulse width is at the same time rather elevated in the range of several tens of nanoseconds. This results in a relatively bad mass resolution. On the other hand, there is the possibility of using the high current bunched mode (HCBU). In this mode, the pulses are shortened by a buncher system that compresses the pulse width. This ensures a very good mass resolution that comes at the price of reduced lateral resolution. The compressing of the pulse in one direction leads to higher ion densities and therefore to repulsive forces in another direction that lead to chromatic abbreviations in the lens system. The result is an increased beam diameter. A good compromise between high mass resolution and high lateral resolution can be achieved by using BA in burst mode. The relatively long BA pulses with high lateral resolution can be cut into shorter, successive ion pulses with high mass resolution. The problem is, that each of the short pulses creates identical sub spectra that are separated by about 25 ns in the final mass spectrum. For simple samples with only a few different species, this is no problem, but spectra will become very complex with increasing sample complexity for example in organic materials. Moreover, the resulting secondary ion intensity is rather low since the initial primary ion pulse has been chopped up into shorter pulses. The choice of the operation mode depends on the purpose of the analysis. For spectrometric purposes or depth profiles, a high mass resolution and high secondary ion intensities may be needed. Whereas for surface imaging a better lateral resolution is needed.

A problem of LMIGs is the fact, that they only produce monoatomic ions or very small clusters. These species will penetrate relatively deep into the sample and damage underlying layers. The created damage

is especially problematic for organic samples because atomic bonds inside of the molecules can be broken and the chemical structure can be destroyed. That is why gas cluster ion beam (GCIB) sources have become more and more popular as primary ion sources for organic samples. GCIBs can create huge clusters with several thousands of atoms per cluster. The energy per projectile is heavily decreased which results in a gentler sputtering process and lesser penetration depth. This topic will be discussed in more depth in section 2.1.

For depth profiles, it is in any case important to remove the layers that were damaged by the primary ion beam with the sputter beam after each analysis step. Commonly used sputter species include cesium, oxygen, xenon, argon clusters or C_{60} molecules. More on sputter sources will be found in section 2.1.

1.1.2.2. Matrix Effect

The low ionization probability is one of the main problems that holds the progression of ToF-SIMS back. On top of that, the ionization probability can vary several orders of magnitude for different materials. It can even change significantly for the same material as a function of its chemical environment. This is called the matrix effect. It is possible that the ionization probability of a species is enhanced or reduced at the interface of two materials. The matrix effect makes quantification in ToF-SIMS extremely difficult. Many references are needed to determine the concentration of a certain element in different chemical environments. Recent studies on the matrix effect suggest a charge transfer model to explain the effect for elemental systems [96].

But the matrix effect can be used as an advantage as well. Clever surface modification during measurements can enhance the secondary ion yield substantially. That is why oxygen and cesium are commonly used sputter sources. Oxygen deposition at the sample surface during the sputter cycle can result in an increase of the work function and a higher ionization probability for electropositive elements like metals and semimetals [97]. Oxygen atoms will form covalent bonds at the sample surface. During the analysis cycle, these bonds will be broken. The oxygen will take up an additional electron due to its high electronegativity, leaving behind a positively charged ion. It is even possible to flood the main chamber with oxygen during analysis to achieve the same effect and enhance the secondary ion yield [98]. Implantation of cesium on the other hand will have the opposite effect. It will decrease the work function and increase the negative secondary ion yield [99].

The same idea of surface modification to improve the secondary ion yield lies behind more recent studies that use more exotic clusters as a sputter source. Water clusters [100] or argon clusters doped with reactive species have been studied [89, 90]. These techniques have been proven effective in enhancing secondary ion yields especially in organic materials where protonation is often the involved ionization mechanism [102]. The presence of water during analysis is however undesirable with respect to the study of degradation in organic materials since it enhances the degradation effects that were discussed in chapter 1 of this thesis.

1.1.2.3. Time of Flight analysis

Once the secondary ions have been formed and left the sample surface, they are accelerated towards the detector using an extraction field. The extraction field is created by a fixed potential difference between the sample and the entrance of the time of flight analyzer. It serves to direct the secondary ions towards the analyzer and to accelerate them to a constant value. A time of flight analyzer can detect all secondary ions in parallel. This is a major advantage over other detectors like quadrupole mass spectrometers that are used in dynamic SIMS and that work sequentially. The parallel acquisition of mass spectra is very fast and especially for organic samples it is advantageous since they often exhibit several fragmental peaks.

The extraction field is normally already activated before the primary ion pulse even hits the surface to make sure that all produced secondary ions will be extracted. However, another extraction technique has been used to increase secondary ion intensities. The idea is to delay the activation of the extraction field for several hundred nanoseconds after the primary ion pulse has been applied to the surface. This delayed extraction was already introduced in 1955 by Wiley et al. [103]. It has regained some attention after the introduction of GCIBs as primary ion gun. GCIBs have worse mass resolution than LMIGs when used as analysis beam due to an increased pulse length. However, LMIGs can struggle as well with mass resolution when used in imaging mode with high lateral resolution. Delayed extraction is a method that can be used after secondary ion formation to improve the mass resolution significantly. The starting point for the time of flight measurement is the ion pulse of the primary ion gun for conventional extraction. During long pulses, several secondary ions with the same mass will reach the analyzer delayed in time. This will cause broadening of detected peaks and therefore bad mass resolution. Delayed extraction will improve the mass resolution by shifting the starting point of the ToF measurement to a precise moment after the broad primary ion pulse has generated all secondary ions. That way, all secondary ions with the same mass will arrive at the same time at the analyzer. However, fast secondary ions can leave the extraction zone during the field free time. Secondary ion intensities will be lower and light elements might not be detected [104]. This can make mass calibration very difficult since elements like hydrogen or carbon, that are often used to calibrate spectra, will not be detected.

After extraction and acceleration of the secondary ions, they will reach the UHV chamber of the analyzer. Thanks to the ultra-high vacuum, they can pass the chamber without collisions between atoms and ions. The time of flight t_{ToF} is directly dependent on the mass m of the ion and can be calculated as follows with the assumption of a negligible impact of gravity during the flight [105]:

$$t_{ToF} = L\sqrt{\frac{m}{2z\,U}} \qquad (4)$$

Where L is the length of the drift tube, z the charge of the ion, and U the potential difference creating the extraction field. L and U are known parameters and t_{ToF} is measured during analysis.

At the end of the analysis chamber, the secondary ions will hit a microchannel plate which will amplify the signal of the incoming ion and at the same time determine the end of the time of flight measurement for that particle. The time of flight can then be used to assign a certain mass to charge ratio to that particle:

$$\frac{m}{z} = 2U \frac{t_{ToF}^2}{L^2} \qquad (5)$$

At the furthest point of the time-of-flight chamber, the secondary ions will be slowed down to near zero velocity and then be accelerated in the opposite direction in a so called reflectron. This is to correct small differences in velocity of particles with the same mass. These differences can for example stem from different initial energies after the ions have been released from the sample surface and before they have been accelerated by the extraction field. The reflectron consists of a series of electrodes that create an electric field to reflect the incoming ions. If two ions with the same mass but different velocity enter the reflectron, the one with higher velocity will take longer to be slowed down and it will travel further into the reflectron before its trajectory is inverted. Both particles will reach the detector at the same time, because of the increased path of the faster ion.

It should be mentioned, that either positive or negative secondary ions can be detected at a time. Certain elements or molecules have very low ionization potentials for a certain polarization. It is therefore advisable to perform measurements in positive and negative secondary ion mode to ensure the detection of all species that are present at the sample surface.

Moreover, it is important to keep the secondary ion intensity as high as possible to detect even the least abundant species. Species with intensities that saturate the detector should not be considered during data treatment.

1.2. X-ray Photoelectron Spectroscopy

Similar to the previous section about ToF-SIMS, the basic principle of XPS measurements will be explained first. The fundamental processes will then be used to elucidate the use of this technique for chemical characterization of materials. Once again, the information about the instrumentation that was used for XPS measurements can be found in the appendix.

1.2.1. History and basic principle

XPS measurements make use of the photoelectric effect in atoms. This effect was first observed by Hertz in 1887 [106] and has first been explained by Einstein in 1905 [107]. In 1921 he was awarded the Nobel Prize in Physics for this work. It describes the interaction of photons with electrons in an atom shell. If

the energy of the photon is higher than the work function of the electron that it hits, the electron can leave the atom and it becomes a free photoelectron.

It took more than 50 years before Kai Siegbahn constructed with his coworkers an analytic instrument that made use of the photoelectric effect. He was awarded the Nobel Prize in Physics for this work in 1981 [108]. Novel vacuum techniques helped to achieve sufficiently high energy resolution and detection intensities. Siegbahn's work revealed the full power of XPS analysis. The interest in the technique rose quickly. Many studies have been carried out and the instrumentation has further been improved.

Figure 10 shows a schematic representation of an XPS setup. One of the key elements of the instrument is the X-ray source.

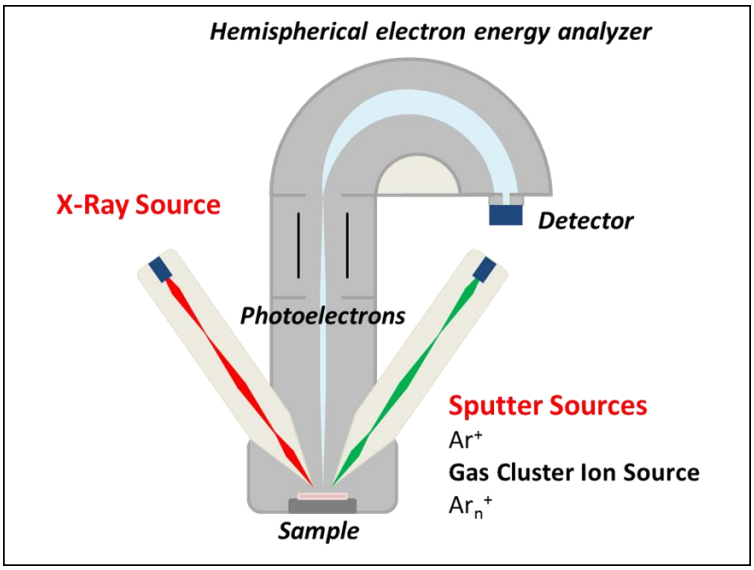

Figure 10 Schematic of a typical XPS setup.

Several X-ray sources are commercially available. Generally, the x-rays are produced by bombarding a metallic anode with an electron beam. As a result of electron-metalatom interaction, X-rays are emitted. Aluminum has become the most used anode material thanks to its high energy and high intensity Kα X-rays and the possibility of easy monochromatization. Synchrotron radiation can also be used as excitation source. Synchrotron sources provide a beam that can be focused to an extremely small area (< µm compared to about 10 - 100 µm for standard X-ray sources) with higher electron flux in a wide energy spectrum which opens the possibility of tunable energy with a very narrow spread.

The produced X-rays are focused and monochromated by a quartz crystal and led into the analysis chamber onto the sample. The interaction of these X-rays with surface atoms will result in the release of photoelectrons with element specific energies. The X-ray incident angle by default is 45° but can be adjusted to get a more or less glancing incident angle. UHV is needed for a precise analysis. This will prevent surface contamination during the analysis and is needed for a clean extraction of photoelectrons without additional elastic impacts with gas atoms and consequently energy losses. This is important

because the kinetic energy of the photoelectrons carries the elemental information of interest. The photoelectrons must therefore reach the detector unaltered.

The detection system is usually a combination of a hemispherical electron energy analyzer and an electron multiplier. The hemispherical electron energy analyzer will split the incoming photoelectrons according to their kinetic energy. This way, only photoelectrons with a certain energy will reach the electron multiplier.

Typically, at first, a **survey spectrum** is recorded to gain a good overview of the atomic species that are present at the sample surface. During survey spectra, the energy of the photoelectrons over a wide range is recorded.

Once an overview of the surface is established, **high energy resolution** valence band or core level spectra can provide more specific information about chemical binding states for every element present at the surface.

Moreover, it is possible to couple the X-ray analysis with a sputter gun. By alternating between analysis and sputter cycles, it is possible to acquire **depth profiles** by following the evolution of intensity for certain elements or even specific binding states with depth.

Angle resolved XPS measurements can provide depth information in a non-destructive way, but the technique is limited to a depth of less than 10 nm from the sample surface. XPS spectra are measured with varying collection angle of the photoelectrons, thereby modulating the maximum escape depth of the electrons. At glancing collection angle, most photoelectrons originate from near surface atoms. By teating the spectra, it is possible to gain information on elements or binding states that exist directly at the surface or more in the bulk material of the sample.

Line scans or imaging can be helpful on a patterned surface. The analysis area is in the range of the X-ray spot size, i.e. > 10 µm for lab instruments. As mentioned earlier, the lateral resolution can be improved by using synchrotron radiation as the X-ray source.

Most instruments are equipped with the possibility to scan over the surface area and detecting the secondary electron intensity for each pixel. This provides a good way to locate specific sample areas in a quick way.

1.2.2. Theory of fundamental processes

In this part, a closer look towards the fundamental processes during XPS analysis will be given. The characteristic binding energy of the extracted photoelectrons E_{bin} is the information that will be obtained by XPS analysis. The measured energy is the kinetic energy E_{kin} of the photoelectrons. Both, E_{bin} and E_{kin}, are connected over the incident photon energy of the X-rays hv in the basic XPS equation [109]:

$$E_{bin} = h\nu - E'_{kin} - \phi_a \qquad (6)$$

where Φ_a is the spectrometer work function and E'_{kin} the measured kinetic energy. Figure 11 b) shows a schematic representation of a band diagram to illustrate this relation. The knowledge of the sample work function is not necessary as soon as it is electrically connected to the spectrometer and properly grounded so that the sample and spectrometer Fermi levels align. The spectrometer WF can be determined by measuring the core-level binding energy of a clean, noble metal surface (e.g. Au $4f_{7/2}$ at 83.96 eV). The sample work function can be accessible by measuring the low-energy cut-off energy of the photoelectron spectra.

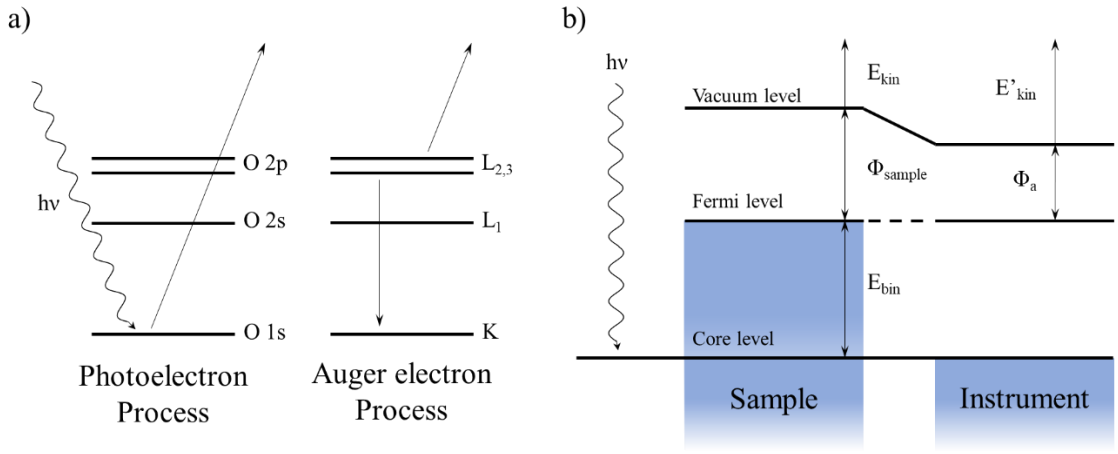

Figure 11 a) Schematic example of the photoelectric process (left) and subsequent Auger electron emission (right). b) Schematic band diagram for the photoionization process for a conductive sample.

Before equation (6) can be used to transform the detected kinetic energy into a binding energy that is characteristic for the chemistry at the sample surface, photoelectrons need to be generated and detected. Berglund and Spicer proposed a three-step model to describe the photoemission as a function of the optical excitation (photoionization), the transport of the electron to the surface and its escape to the vacuum [110].

1.2.2.1. Photoionization

The impact of a photon on an electron that is bound to an atom can cause the ejection of the electron. After the emission of the photoelectron, another electron from the outer shell will recombine to take the lower energetic state of the ejected electron. During the recombination it can lose its excess energy by emitting a photon or it can transfer it to another electron that can use the energy to escape from the atom. The later process is called the Auger process. Auger electrons will be detected as well during XPS analysis. The kinetic energy of the Auger electrons is independent from the x-Ray energy since the electrons are the result of an auto-ionization process. Both, the photo effect and the Auger process are schematically shown in Figure 11 a).

Differences in core level binding energies for different elements arise from the interaction of the electrons with the nucleus. There is a difference in binding energies for electrons in atoms with different

atomic number Z. Furthermore, the binding energy depends on the local environment of the atom. Electrons in different bonding states can be distinguished by their slightly different binding energy. An electron in a carbon atom that is in a bond with another carbon atom has a different energy than an electron in a carbon atom that is in a bond with an oxygen atom for example.

Finally, the binding energy for electrons in the same orbital of the same atom differ because of the so-called spin orbit splitting. This effect describes energetic splitting of electrons in non-symmetric orbitals. It stems from the coupling of the magnetic field that is created by the electronic spin with the magnetic field that is created by its motion around the atom's nucleus [109]. The spin S of an electron around its own axis is defined by the quantum number m_s and can be either 1/2 or -1/2. The shape of the orbitals is given by the quantum number l (l = 0 for s orbitals, l = 1 for p orbitals, l = 2 for d orbitals …). The sum of m_s and l is the total angular momentum quantum number j. It is defined as $j = l + m_s$. Electrons with larger j have a slightly lower binding energy, giving rise to two different peaks very close to each other in the XPS spectrum. Because the angular momentum around the nucleus goes into the equation, the splitting of the energy levels increases with the size of the nucleus, the Z value of the atom. For heavier elements the effect becomes increasingly significant.

Since detected photoelectrons are named after the orbital that they originate from (1s, 2s, 2p …), the quantum number j is added to the notation for electrons originating from orbitals with l > 0 ($2p_{1/2}$, $2p_{3/2}$…) to differentiate the different peaks in the XPS spectrum. The relative intensity of these doublet peaks is given by the ratio of their degeneracies with which they occur. The number of degeneracies is defined as 2j + 1. This results in a peak intensity ratio of 1:2 for the $p_{1/2}$ / $p_{3/2}$ doublet (2:3 for the $d_{3/2}$ / $d_{5/2}$ doublet …) [111].

Similar to spin orbit splitting, there is a second effect that occurs during photoelectron generation: multiplet splitting. It stems also from the interaction of magnetic fields created by the electrons. When a core electron is ejected as a photoelectron, it leaves an unbound electron behind. The magnetic field created by the spin of this electron interacts with unbound electrons in the valence band. There is a splitting in energy levels depending on weather the spins of unbound electrons in the core and in the valence band are aligned or not. Multiplet splitting can occur in any orbital, including s orbitals [109].

Another effect that can be observed in XPS spectra are satellite peaks. These peaks with relative low intensity have their origin in different electron energy losses that occur during the photoelectron generation process. An ejected photoelectron can transfer some of its energy to valence electrons in the atom during the ejection process. The photoelectron leaves with reduced kinetic energy, which, in turn, results in an apparent higher binding energy. The valence electron can in return transit to discrete or non-discrete energy levels near the Fermi level ("shake-up satellites"). Some valence electrons can even use the energy to leave the atom into unbound continuum states ("shake-off satellites"). They will contribute to the background at higher binding energies [109].

1.2.2.2. Photoelectron transport to the surface and escape to the vacuum

Other energy loss processes can take place while the electron is traveling to the sample surface. X-Rays will pass through the whole sample. Electrons can be excited and photoelectrons can be produced deep in the sample. But only electrons that undergo zero energy loss on their way out of the sample can be assigned to a certain element. An inelastic mean free path λ for the electrons can be defined. It is the mean path that an electron can travel in a solid without undergoing inelastic scattering. Two parameters mainly define the mean free path. The initial kinetic energy of the electron and the solid it travels in. Figure 12 shows the dependence of the inelastic mean free path λ on the kinetic energy of the released electrons, with a theoretical line adjusted through experimental data points. The result is a universal curve which indicates that electrons can only travel a few nanometers in most materials (1 – 3 nm or 5 – 10 monolayers for aluminum Kα radiation). This illustrates the high surface sensitivity of this technique. Statistically, 67 % of all photoelectrons are scattered elastically within 1λ on their way to the surface after their creation. 95% of all detected electrons escaped within a depth of 3λ into the sample. This gives rise to the equation for the maximum sampling depth d_{max}:

$$\mathrm{d_{max}} = 3\lambda \, sin(\theta) \qquad (7)$$

For most materials, d_{max} takes values of about 10 nm at a collection angle θ of 45°.

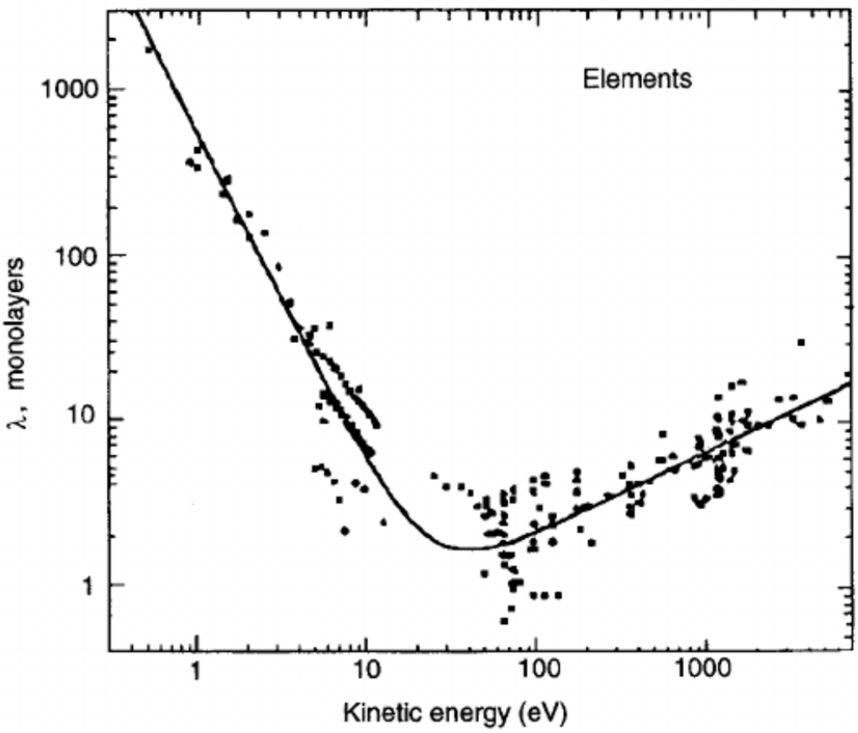

Figure 12 *Inelastic mean free path for photoelectrons in various elements. Theoretical line is derived from experimental data points* [112].

Electrons that have been scattered on their way out will contribute to the broad spectral background. Some spectra can exhibit periodic loss peaks (see shake-up satellites in the previous section). This is

indicative of plasmon losses. These losses are found in conductive samples. They are the result of the interaction of photoelectrons with other electrons in the sample. The production of photoelectrons causes movement of electrons to account for the local change in charge density. This can result in collective oscillations in the conduction band. This happens at specific frequencies. When a photoelectron passes these oscillations, it loses a specific amount of energy. This can happen several times which results in periodic appearance of loss peaks in XPS spectra [109]. Plasmon energies at the surface and in the bulk material are slightly different. Two different plasmon losses can be observed. The plasmon loss peaks can overlap with other elemental peaks which can make spectrum interpretation even more difficult.

1.2.2.3. Data treatment and quantification

Overlapping peaks, broadening of the photoelectron peaks and background noise make peak analysis of the detected signal necessary. The sensitivity of XPS lies in the range of 0.1 - 1 %. Elements with lower abundance than a few atoms per 1000 surface atoms cannot be detected due to a signal to noise ratio that is too low. Overlapping peaks need to be analyzed to separate contributions from different elements or contributions from the same electrons in different chemical environments.

The first step in data treatment should be energy calibration of the spectra. Due to charging effects as described before, it is possible that the energy scale is slightly shifted. In the case of uniform charging over the analyzed area, a known reference peak might be used to recalibrate the spectra. As carbon is often present at the sample surface as a form of contamination, it is possible to use the C 1s peak at 285 eV as a reference point [113].This method is effective in the case of bulk materials, but needs to be carefully used when multilayer, ultra-thin samples and semi-conductors are considered, as the C 1s binding energy carries the information of the potential variations in depth across the structure. The C 1s peak was also used throughout this thesis to calibrate the spectra.

The next step should be the subtraction of the background noise. As discussed before, there will always be a background signal in XPS spectra due to inelastic losses of the photoelectrons on their way to the detector. For quantitative analysis it is important to subtract this background from the spectrum because the calculated concentration for each element depends directly on the area under the corresponding peak. The most common background type that is easy to use and yields good results in most cases, is the so-called Shirley background. It is at each binding energy proportional to the number of electrons over the background and in lower binding energies. This results in a curved background that is sensitive to the selection of the endpoints, but not as strongly as a simple linear background [114].

Once the background is subtracted from the spectrum, a line fit of the resulting peak can be done. XPS peaks exhibit generally a Gaussian-Lorentzian line shape. An understanding of the chemical structure at the sample surface is key to a good peak fit. Figure 13 shows exemplarily the C1s core level spectrum of a nylon sample (the figure has been taken from the Casa XPS software manual). The chemical structure of the molecule is shown inside the graph. Three slightly different CH_2 binding states can be distinguished in the molecular structure (labeled with 1, 2 and 3). Without this information about the

chemical structure, the small contributions of the second and third CH_2 binding states (blue and red curves) could potentially be overseen during the peak fitting. They could be overshadowed by the main CH_2 peak (pink curve). Only the double bond to the oxygen atom provides a large enough shift in binding energy to detect it at first glance.

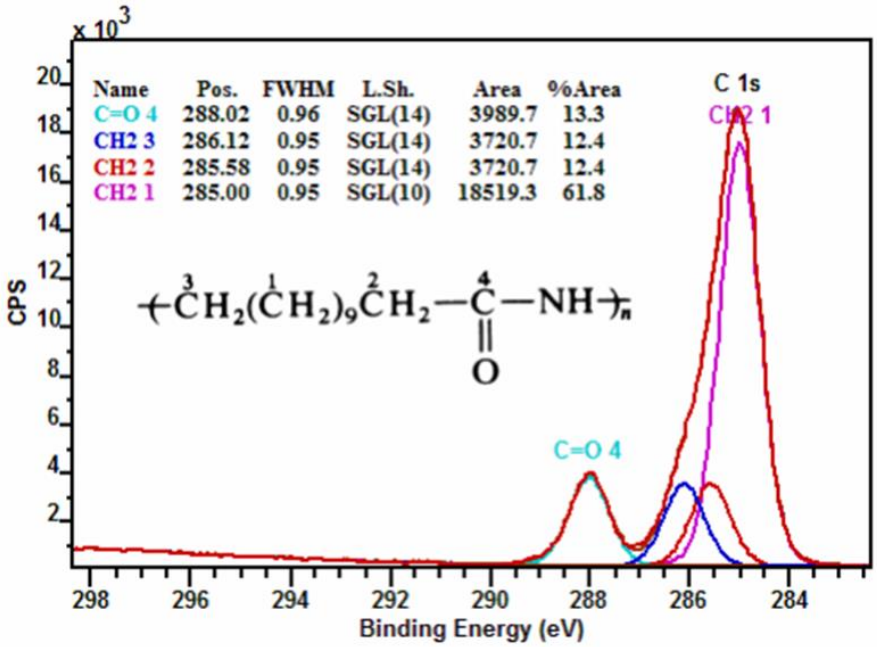

Figure 13 C 1s XPS core level spectrum of a nylon sample with the molecular structure shown inside the graph (taken from the Casa XPS Software manual).

To finally quantify the XPS spectrum it is necessary to apply relative sensitivity factors (RSF) to the data for peak areas. The intensity I_A for an element A in a homogeneous sample is primarily proportional to the number of emitting atoms N_A and can be written as follows [114]:

$$I_A = N_A \, f(\sigma(h\nu) \, L_A(\gamma) \, J_0 \; \lambda(E_A) \, D(E_A) \, G(E_A) \; cos\,\theta) \qquad (8)$$

With the instrument parameters $cos\ \theta$ for the photoelectron emission angle (relative to the surface normal), the detection efficiency $D(E_A)$ for electrons with energy E_A and $G(E_A)$ as the so-called analyzer étendue which gives the transmission of the instrument for electrons of energy E_A. The more interesting material parameters are the inelastic free mean path λ that has been mentioned before, the atom density N_A, the X-ray characteristic line flux J_0, the angular asymmetry of the intensity of the photoemission $L_A(\gamma)$ and the cross-section $\sigma(h\nu)$ for emission of a photoelectron from the relevant core level by a photon of energy $h\nu$ [114].

From this equation it can be seen that the detected intensity not only depends on the transmission and the detection efficiency of the instrument but also on various material parameters. Moreover, it depends over the cross-section on the core level peak that is analyzed. It is therefore important to include RSFs in the calculations during quantification of XPS data. Many calculations and reference measurements have been performed in the past to provide libraries with RSFs for all elements.

With respect to organic samples which are the focus in this thesis, some particularities can be noted. Aromatic groups that are important for the charge transport in organic semiconductors exhibit a distinct shake-up structure in C 1s core level spectra. Photoelectrons can lose about 6 to 7 eV of their kinetic energy by exciting a π-electron to the π* state. This results in a shake-up peak at higher binding energies in the XPS spectrum. The evolution of this shake-up peak can be used as an indicator of analysis induced damage during depth profiling [113].

Moreover, it is evident from the example in Figure 13 that it might be difficult to differentiate certain polymers or small molecules that only consist of hydrogen and carbon since the energy shifts are marginal. It has been shown however that the valence bands provide distinct fingerprints for all materials [115]. XPS is an excellent tool to record the density of states in the valence band region of organic materials. Often, ultraviolet photoelectron spectroscopy (UPS) is used to record the valence band region of materials. With lower excitation energies (21.2 or 40.8 eV), only photoelectrons that origin from near the valence band can be produced. With this method, the work function of metals and semi-conductors can be determined by localizing the fermi-edge and the energy cut-off in the UPS spectrum. However, here we want to study the density of states of the materials to gain precise information of changes in the electronic structure of different molecules. XPS is better suited for this task than UPS. The small photon energies in UPS lead to final state effects, where electrons are excited to the vacuum level, but they remain in quasi-bound states. They cannot leave the solid and they will not be detected by the measurement. In XPS, these electrons have enough kinetic energy to leave the material completely. The actual density of states in the valence band region is therefore better depicted in XPS measurements than in UPS measurements.

2. State of the art for chemical depth profiling of organic electronic devices

Organic materials and organic electronic devices in particular present some distinct problems for chemical depth profiling techniques.

First of all, the organic molecules are more vulnerable to ion bombardment and high energetic X-rays than inorganic materials. As discussed in section 2 of the first chapter, X-ray irradiation can lead to degradation of organic molecules. This X-ray induced degradation and the heavy fragmentation of molecules after ion bombardment will be further discussed in this section.

Secondly, devices can be fairly complex with an array of several ultrathin organic layers. XPS and ToF-SIMS are both highly surface sensitive techniques, but the analysis parameters need to be chosen wisely when analyzing layers with a thickness of only a few nanometers. Moreover, there are also inorganic materials used in organic electronics. That poses problems during depth profiling because of big differences in sputter rates between organic and inorganic materials.

Recently, there has been significant improvements in depth profiling of organic materials especially by using cluster ion sputter sources. The state of the art for cluster depth profiling with focus on ToF-SIMS and XPS analysis will be summarized in this part of the work. The before mentioned analysis induced damage and the complexity of devices will be discussed later on. Finally, the advantages of combining ToF-SIMS and XPS will be examined.

2.1. Cluster depth profiling

Under ion beam bombardment, molecules behave considerably differently than inorganic crystalline samples. The low secondary ion yields as well as the low sputter rate for polymer materials due to interlinking of polymer chains limited the possibilities of monoatomic sputter sources for organic depth profiling. The introduction of cluster ion sources has been a crucial turning point in the history of chemical depth profiling. Early on, Briggs and Hearn showed that higher mass ions improve the secondary ion yields of polymer materials in ToF-SIMS measurements [116]. Following this work, several groups increased the mass of the sputter source further by using small ion clusters. SF_6 molecules showed promising results on polymer samples and pharmaceutical compounds [52, 53].

Figure 14 illustrates quite well the improvement by using clusters for ToF-SIMS depth profiling. It shows the comparison of two depth profiles of a glutamate film that was deposited on a silicon substrate. The profile on the left was created by using a monoatomic Ar^+ sputter source. It can be seen that the molecular ion signal of the glutamate ($M+H^+$, the molecule + a proton) decreases rapidly at the beginning

of the measurement. The molecular structure is destroyed by the monoatomic ion bombardment. Moreover, the silicon substrate could not be reached within 900 s of sputtering. This indicates a low sputter rate, especially in direct comparison with the cluster profile on the right. This profile that was created using SF_5^+ molecules as a sputter source, reaches the substrate within this 900 s timeframe. But more importantly, the molecular ion signal of glutamate stays constant throughout the organic layer [119].

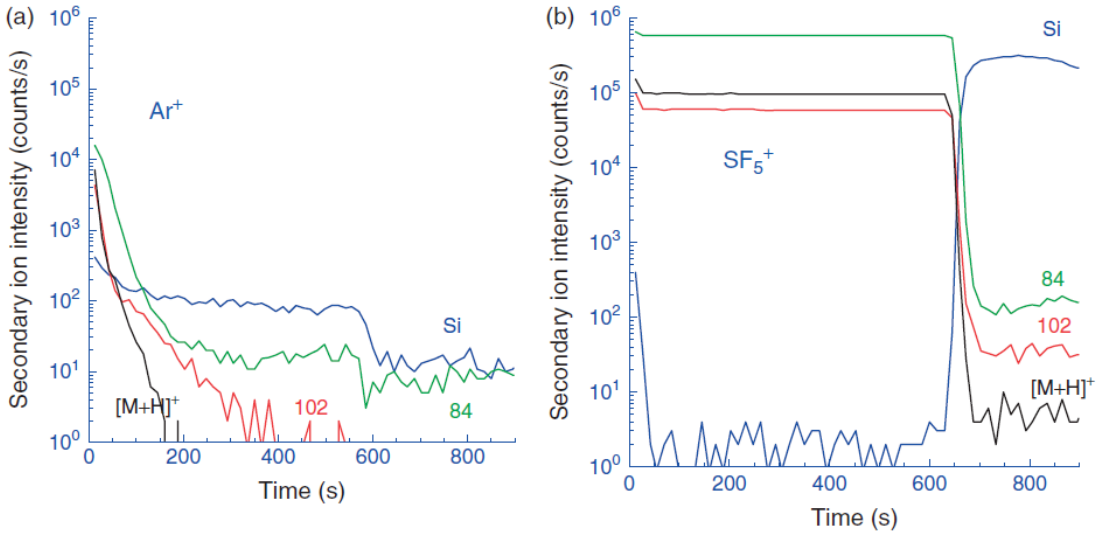

Figure 14 *Comparison of depth profiles of a glutamate film that was deposited on a silicon substrate produced by a) Ar^+ and b) SF_5^+ sputtering (profiles were recreated by* [119] *from* [120]*). The molecular glutamate ion signal (M+H) as well as characteristic molecular fragments (84. 102) are shown together with the Si substrate signal.*

After SF_6 and SF_5 molecules, several other cluster sources were developed. Most notably heavy metal clusters like Au_3^+ and later Bi_3^+, C_{60}^+ molecules and large argon clusters $Ar_{x>500}^n$ [119]. The introduction of these sputter sources made the depth profiling of organic materials possible. The molecular information can at least be partially preserved, and the fragmentation can be minimized. Much effort has been put into developing sources with high mass selectivity that can be focused to spot sizes below 1 µm that can be scanned over the sample surface.

Cluster sputtering can offer two main advantages to the two techniques that are used in this work for depth profiling, ToF-SIMS and XPS. The low induced damage is extremely important to get reliable elemental and molecular information as well as information about bonding states in XPS. The enhancement of the secondary ion yield is another plus for clusters as a sputter source. However, the sputtering is not the only source of damage during ToF-SIMS and XPS analysis. The analysis beams are another one. Even though the dose of primary ions is very small during the ToF-SIMS analysis step, it will still inflict sample damage similar to the sputter induced damage. It has also been shown that the X-ray beam during the XPS analysis step can lead to degradation of organic materials. A closer look to the analysis beams and the important parameters during depth profiling will be taken later in this section in the respective subsections.

First, the characteristics of the sputter beam which both techniques have in common will be discussed. As mentioned before, one of the advantages of using cluster sputtering for organic materials is the enhancement of the sputter yield. The sputter yield is a nonlinear function of cluster size meaning that a cluster consisting of *n* atoms has a higher sputter yield than *n* impacts of a single atom with the same energy per atom [121]. Molecular dynamics simulations suggest that cluster impacts only interact with the topmost layers of organic materials [122].

Single atoms will penetrate much deeper into the sample. The trajectory of monoatomic projectiles remains undeflected for some nanometers into the layer. The interaction with target atoms and molecules is not strong enough to deviate the projectile. Due to this penetration, collision cascades will be formed deep in the sample, which results in damage to the underlying molecules.

For cluster impacts, most of the cluster atoms are stopped in the uppermost layers of the sample. The energy is deposited at the very surface of the sample. A cluster impact creates radial motions around the impact center which will lead to high emission yields for surface molecules without significantly damaging them [121].

A secondary effect of the size of the cluster is a more uniform sputtering. For monoatomic projectiles, the sputter yield depends strongly on the exact location of the impact. The difference in the sputter yield can be quite big for an impact with head-on collisions or an impact where the atom channels deeper into the sample. Cluster cover however a bigger area of the sample surface upon impact. The resulting sputter yield is therefore often more uniform than with monoatomic sputter sources [121].

Both effects, the high sputter rate of clusters for organic materials and the homogeneity of the sputtering process are demonstrated in Figure 15. The upper part shows a comparison of the sputter depth of poly(methyl methacrylate) (PMMA) over the sputter dose for argon clusters and monoatomic argon [123]. The slope of the curves is proportional to the sputter rate of the material. The curve for cluster sputtering is much steeper which indicates that the sputter rate is about one order of magnitude higher than for monoatomic sputtering. On the lower part with adjusted axes, the linearity of the sputter rate for the cluster sputtering can be seen. Compared to the decreasing sputter rate of the monoatomic sputtering in the upper graph, it is an indication of the homogeneity of the cluster sputtering.

A possible explanation for the decrease in sputter rate for the monoatomic sputtering was assumed to be the chemical transformation of PMMA to a carbon richer material due to the damage that monoatomic projectiles cause to organic materials. As it can be seen by the dotted-dashed line, the sputter rate of pure carbon materials like Graphite is extremely low for monoatomic argon. By becoming a carbon richer material due to accumulated damage, the sputter rate of PMMA could approach the sputter rate of Graphite more and more.

Even with cluster sputtering, sputter induced damage cannot be completely avoided. Chemical depth profiling by sputtering is by definition a destructive technique. But it is important to minimize the

damage during the sputtering process. A lot of studies have been focused on this topic since the introduction of cluster sources for depth profiling to demonstrate the low damaging character of cluster sputtering of organic materials [111, 112]. These studies suggest that large argon gas clusters cause only little to no damage at the surface of organic materials. The estimated thickness of the damaged area was less than 1 nm.

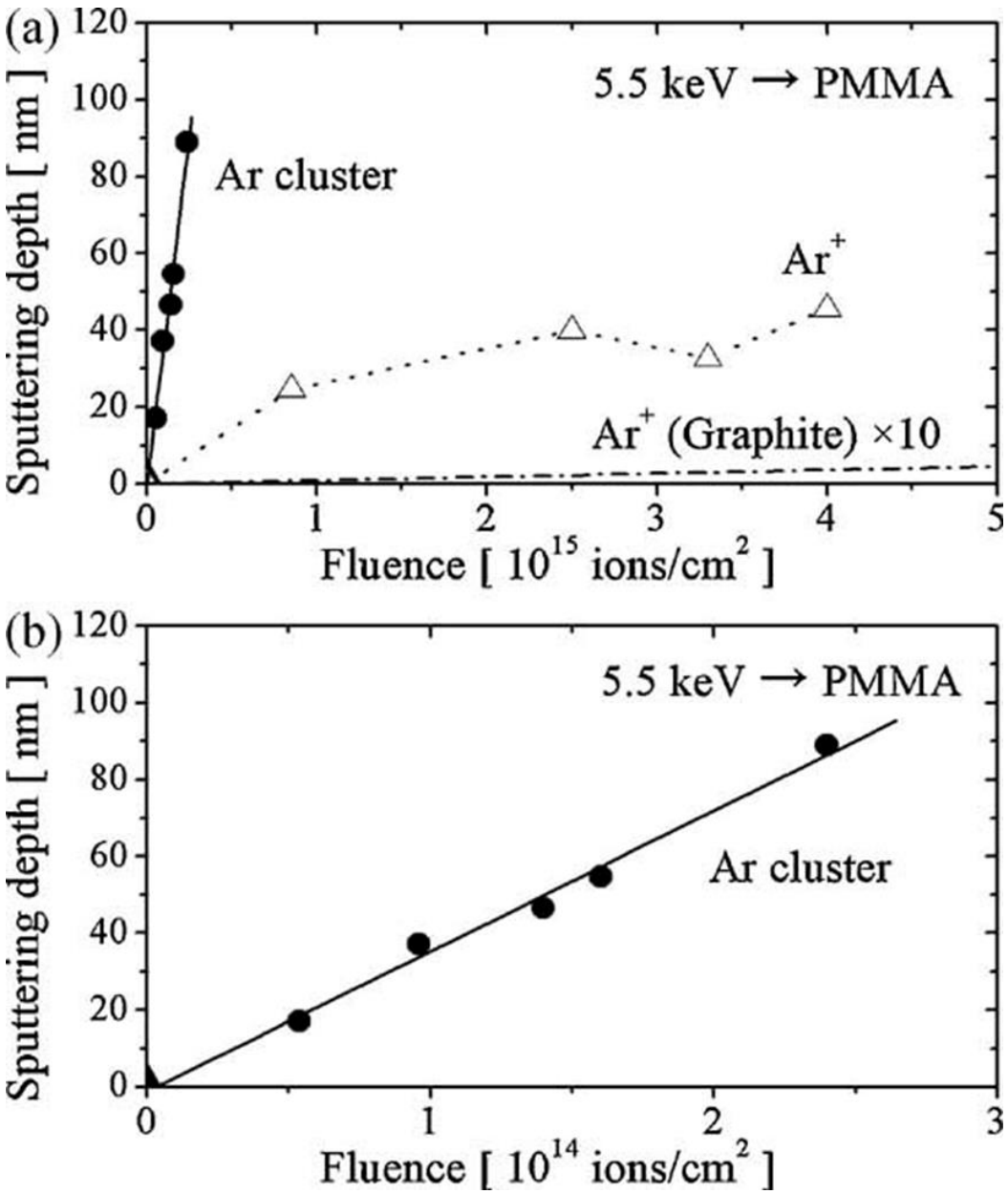

Figure 15 *a) Comparison of the sputter depth over the sputter ion fluence during argon cluster sputtering (filled circles) and monoatomic argon sputtering (empty triangles) of PMMA. The dashed-dotted line shows the same parameters for sputtering of Graphite by monoatomic argon. b) Magnification of the curve for argon cluster sputtering in a)* [123].

The overall reduction of the sputter induced damage is however not only a function of the cluster size, but also of the energy of the projectile. It has been shown, that the sputter yield and the fragmentation of organic molecules during cluster sputtering is dependent on the energy of the incident cluster and more specifically on the energy per atom in the cluster [126]. Typical ion energies for monoatomic

sputtering are 0.5 to 2 keV. For argon cluster sputtering it is in the range of 5 to 20 keV. But if the number of atoms per cluster is considered (about 500 to 10000), the energy per atom in the cluster lies in the range of only a few eV. This is almost three orders of magnitude smaller than for monoatomic projectiles.

Molecular dynamics simulations as well as experimental data show the dependence of the sputter rate and the damaging of the sample surface on both, the cluster size and the energy per atom [115, 116]. Generally, low energy per atom ratios show minimal induced damage for all cluster sizes, but the cluster should not be too small because the sputter rate will decrease heavily.

With regard to organic electronic devices, there are some specific obstacles to overcome for depth profiling. Until now, the sputtering of single organic layers has been considered. These single layers are basic samples. In reality, devices in organic electronics are much more complex. Figure 16 shows the OLED structure of a modern display. Layer thicknesses can be as thin as only a few nanometers. The whole organic stack consisting of up to 6 layers has a thickness of only 100 to 200 nm. There are a red, a green and a blue OLED in each pixel of the display. The emissive layers for each of the colors are of different thickness. This results in height differences of the whole stack for each color.

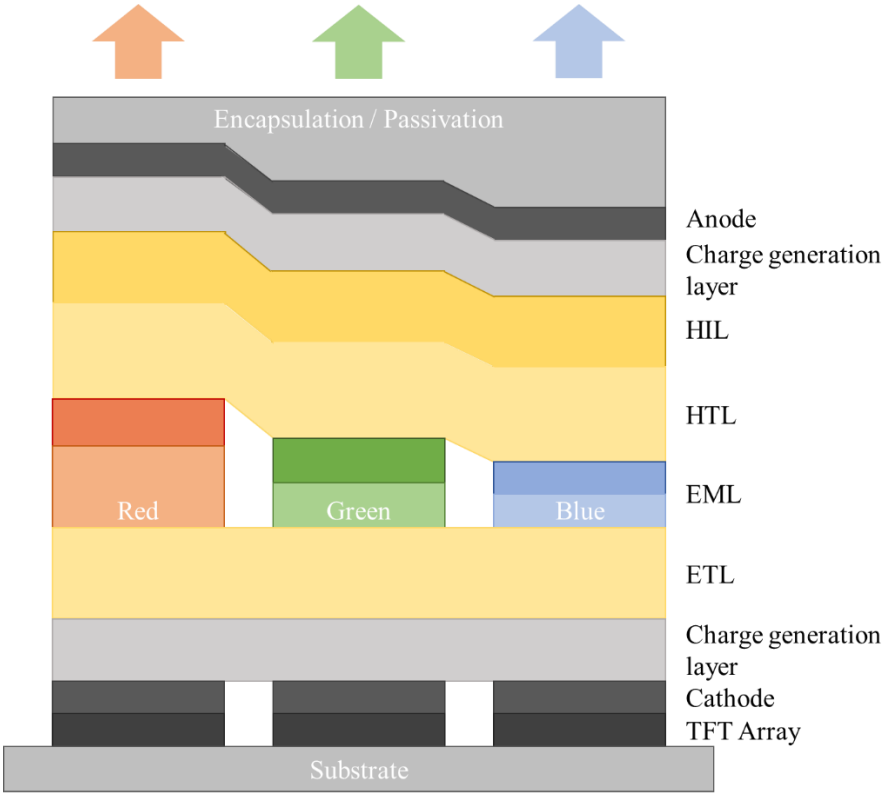

Figure 16 Schematic representation of the different layers of an OLED pixel in the newest technology displays.

The organic stack is wrapped in inorganic layers. The electrodes are inorganic materials like silver, aluminum, calcium or indium tin oxide (ITO). At least one of them should be transparent so that the light can be coupled out through that side of the device. The encapsulation layers consist also of inorganic materials. This presents a problem for depth profiling analysis. While argon clusters can

sputter organic materials without inducing damage, they often cannot break the strong covalent bonds in inorganic crystals. Analyzing the whole device with only one sputter source is very difficult. There are some options to circumvent this problem. The energy per atom in the cluster can be increased. This can potentially increase the sputter rate of the inorganic materials. However, once the organic stack is reached, the clusters can damage the molecules because of the too high damage.

Another possibility is to use a monoatomic source for the inorganic part at the top and switch to a cluster source at the inorganic-organic interface. This method can cause problems because of deep penetration of monoatomic projectiles that damage the organic materials before the interface can be reached.

There have also been attempts to use co-sputtering of monoatomic sources and clusters. The idea is to sputter quickly through inorganic materials with the monoatomic projectiles and to smoothen the surface and to take away some of the damaged region at the surface.

All of those methods have their drawbacks. In the literature, this obstacle is often circumvented by analyzing the device only partially. Monoatomic sputter sources are used to gain information about the inorganic part of the device. The destruction of the molecular information in the organic part is accepted. Cluster sputter sources are used on devices without the inorganic top layers. Only the organic stack is analyzed. The problem here is that the devices cannot be tested and aged electrically without a top electrode. To analyze the organic stack of complete devices there is the possibility to remove the top inorganic layers by applying scotch tape to the sample surface. When the scotch tape is torn off, it will take some layers with it. The breaking point will be at the interface with the weakest adhesion between the layers. This might be at the inorganic-organic interface at the top electrode. In that case it would be possible to analyze the organic stack by cluster sputtering. This technique is however not 100 % reliable.

Another difficulty during the analysis of devices in organic electronics stems from the ultrathin nature of the layers. Even though cluster sputtering does not damage the molecules, there might occur ion bombardment induced intermixing of different materials at their interface.

Figure 17 illustrates this effect. It shows molecular dynamics simulations of cluster impacts of 10 keV C60 (a) and c)) and nanodrops consisting of four polystyrene molecules in a trimethylbenzene matrix (b) and)) on a polyethylene sample [127]. The different colors show regions of 3 nm thickness 20 ps after the cluster impact. The origin of the material can be traced back until before the impact. The intermixing effect is stronger for the bigger nanodrop cluster. Molecules that originate from the very surface will end up in the deepest layers that are impacted by the bombardment (blue and red molecules). Furthermore, there is a redeposition and accumulation of material at the sample surface at the outer crater ring. All white molecules are after the impact located on top of the initial surface.

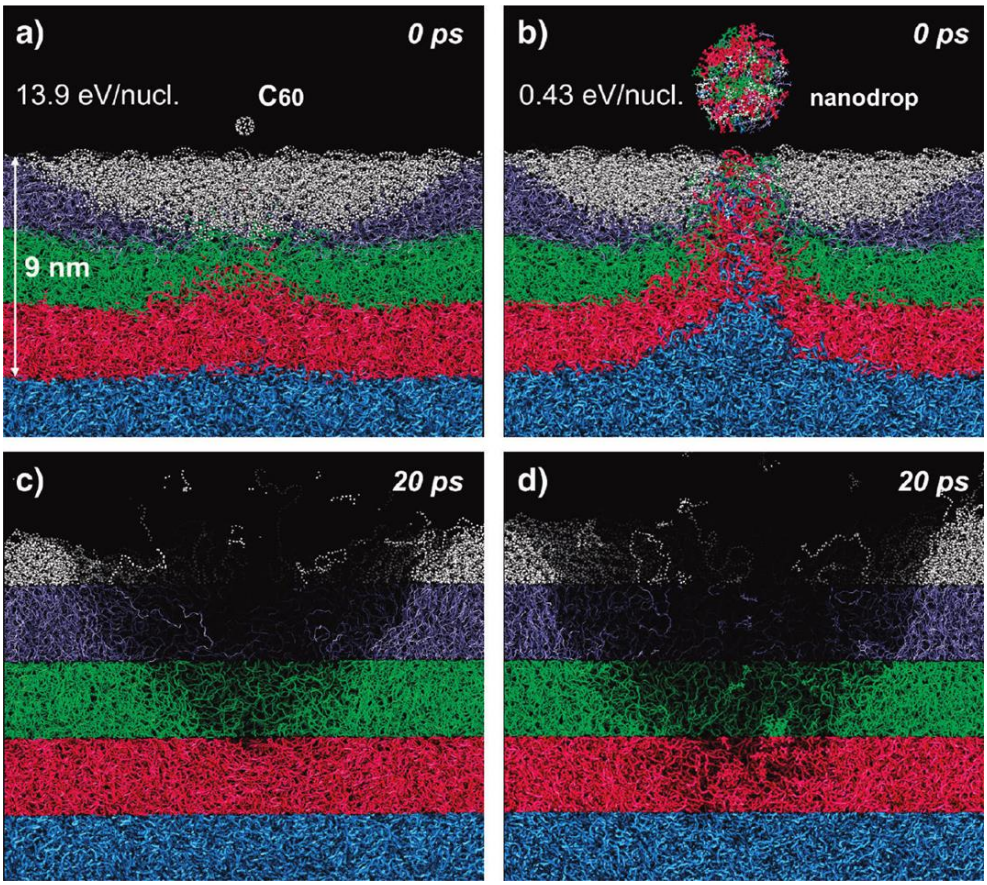

Figure 17 *Illustration of the material flow during impacts of 10 keV C_{60} (a) and c)) and organic nanodrops (b) and d)) on a polyethylene sample with "reverse" color coding. The different colors show 3 nm thick sections 20 ps after the impact (c) and d)). In the pictures before the impact, the origin of this material can be seen, indicating intermixing (a) and b))* [127].

2.1.1. ToF-SIMS for characterization of organic electronics

The first molecular depth profiles with SIMS measurements were done in the dynamic SIMS mode with a continuous primary ion beam of clusters as it can be seen in Figure 14. With the development of dual beam instruments and ToF-SIMS technology however, the way of depth profiling organic materials changed considerably.

During ToF-SIMS depth profiles, there are now two different ion beams in use. The primary ion gun is used in short pulses with relatively small fluences. The sputter gun is used to remove more material in between each analysis step to get the depth profiling effect. As discussed earlier, the most common sputter beam for organic materials is an argon cluster beam with numbers of atoms per cluster ranging from 500 to 10.000. Earlier in this section it was shown, that these huge clusters induce only minimal damage to the surface of organic materials.

Even though the sputter rates for argon clusters are very high on organic materials, they are rarely used in ToF-SIMS measurements as the analysis beam. Short pulsing of GCIBs is very difficult. This has a negative impact on the mass resolution as discussed earlier in section 1.1.2. However, this problem can

be circumvented by using the GCIB in continuous mode and pulsing the secondary ion beam [129]. Another drawback is the fact that the cluster beam cannot be focused to a small enough spot size. Latest generation GCIBs exhibit a spot size of about 2 µm which is considerably larger than LMIGs with spot sizes in the range of 100 nm. That is why LMIGs with small bismuth clusters have become the state of the art for organic depth profiling.

However, bismuth clusters are considerably smaller than argon clusters (n = 1 to 5). So the energy per atom is much higher. That means that the sample surface will be damaged by the primary ion beam. It is therefore important that all of the damaged area during an analysis step is removed during the sputter step. Otherwise, damage will start to accumulate, and the molecular signals will decay over time. That is why the ratio of sputter beam dose to analysis beam dose is very important during depth profiling measurements.

A good mass resolution is essential for the analysis of organic materials. As mentioned before, the fragmentation and damaging of molecules cannot be suppressed completely. The acquired mass spectra will always consist of hundreds of peaks for different fragments. Sometimes, fragments of different molecules can have very similar masses and their peaks will overlap. The existence of isotopes for certain elements makes these mass spectra even more complex. But isotopes can also be used to an advantage. The actual origin of a fragment that could belong to two different mother molecules can be confirmed by cross checking certain isotopes for that fragment.

There have been studies on the penetration depth and the escape depth of secondary ions for small bismuth clusters on organic materials [117, 118]. In these studies, it was found that the escape depth and the penetration depth depend on the cluster size and its energy. The best results were shown for big, low energetic clusters. They combine low penetration with low escape depth with results in high depth resolution. However, they also show the lowest secondary ion yield. That means, that a compromise between signal intensity and depth resolution has to be found.

Signal intensity is another issue in organic materials. The ionization of organic molecules follows often different mechanisms than ionization of inorganic atoms. Possible ionization mechanisms for molecules during SIMS measurements were described by Detter et al. [132]. Generally, organic materials can eject or take on electrons like inorganic materials (M^+ or M^-). But there are other ionization mechanisms. Polarized molecules can undergo Bronsted acid-base reactions. This results in adding or subtracting a proton to the molecule (M+H or M-H). In the presence of other positive (Cs^+, K^+, Na^+ …) or negative (F^-, O^-, Cl^- …) ions there may be Lewis acid-base reactions. Damaging of the organic material can cause fragmentation of molecules and therefore produce other organic radicals that may recombine with each other. In conclusion, the secondary ion yield can be greater when the primary ion bombardment is more violent so that more of these ionization processes can be triggered. Big clusters with low energy often result in low signal intensities when used as an analysis source.

Organic electronic devices have been studied with ToF-SIMS using varying approaches. Most of the time, only certain parts of the device are analyzed. This is due to the fact that complete devices consist not only of organic materials but also of inorganic encapsulation layers and electrodes (Figure 16). The encapsulation layers are necessary to protect the organic materials from environmental impacts like oxygen and moisture that can lead to degradation of organic materials. The problem of sputtering through inorganic-organic interfaces was discussed earlier in this section. That is why most studies have focused either on the general chemical structure of the device without the necessity of molecular information [120, 121] or on the organic part of the device without the top inorganic layers[122 – 124].

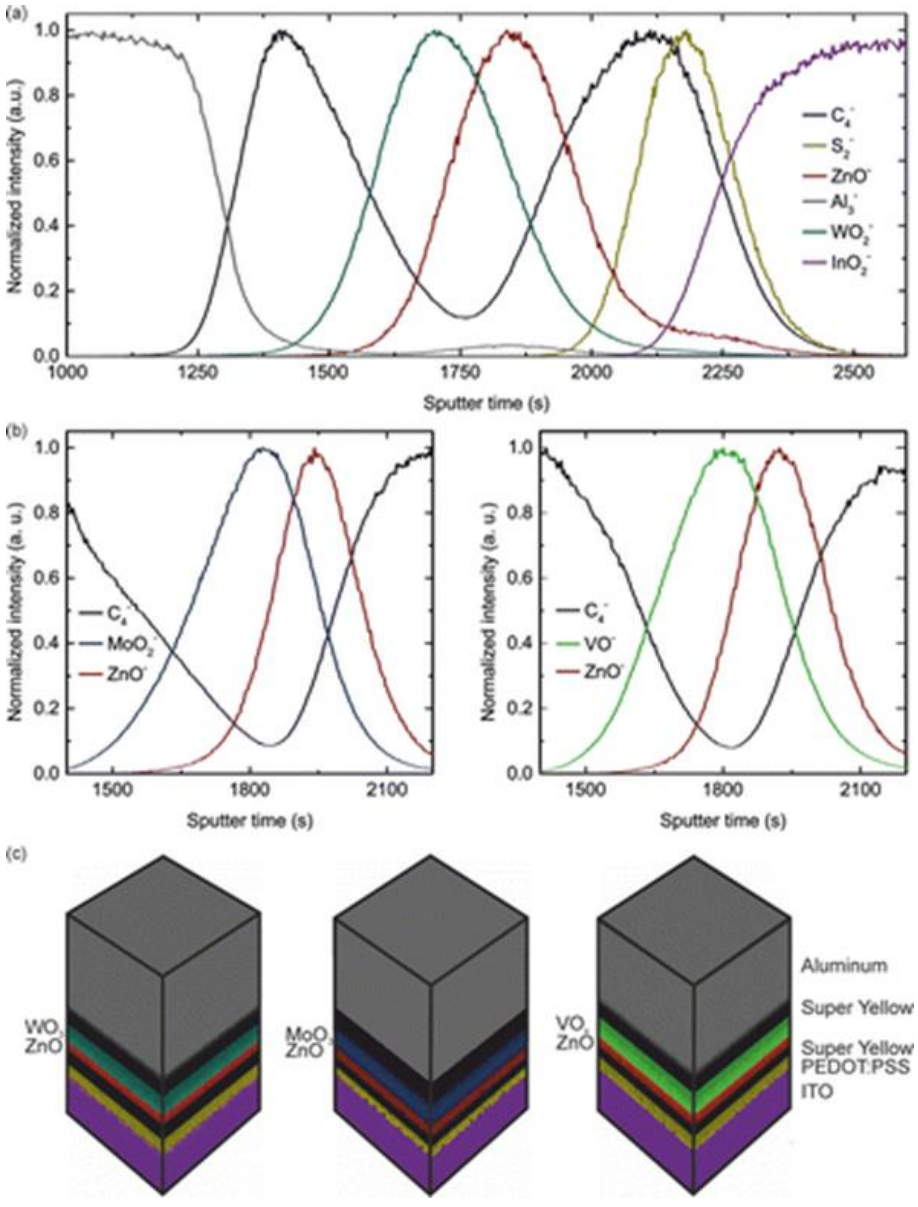

Figure 18 *a) Normalized depth profile of the characteristic ions of each layer in a complete tandem OLED stack. b) Magnification of the profile around the charge generation zone for different samples. c) 3D chemical reconstruction of three samples with different charge generation layers* [133].

Figure 18 shows an example of complete ToF-SIMS depth profiles and 3D chemical reconstructions for all solution processed tandem OLEDs. The analysis has been carried out using a 25 keV Bi_1^+ primary ion beam and a 1 keV Cs^+ sputter beam [133]. The purpose of this measurement was to show the feasibility of producing solution processed tandem OLEDs. The area of interest was the charge generation zone in between two Super Yellow based OLEDs. They used three different transition metal oxides in that zone. Figure 18 a) shows the depth profile for the tandem OLED using WO_3 in the charge generation zone. In Figure 18 b), a magnification of the depth profile around the charge generation layers of the two other devices using MoO_3 (left) and Vo_x (right) can be seen. All profiles show clear separation of all different solution processed layers which is visualized by the 3D reconstructions in Figure 18 c). Since Bi_1^+ and Cs^+ were used as analysis beam and sputter beam, respectively, the molecular information was lost completely. The Super Yellow layers and the PEDOT:PSS layers were identified by the C_4^- and the S^- characteristic ions, respectively.

An example of profiles of only the organic stack without the top inorganic layers is shown in Figure 19 [138]. In this case, a relatively simple two-layer OLED stack is analyzed with argon clusters. 5 keV Ar_{700} clusters were used as analysis beam and as sputter beam. The result is a clean depth profile through the organic stack.

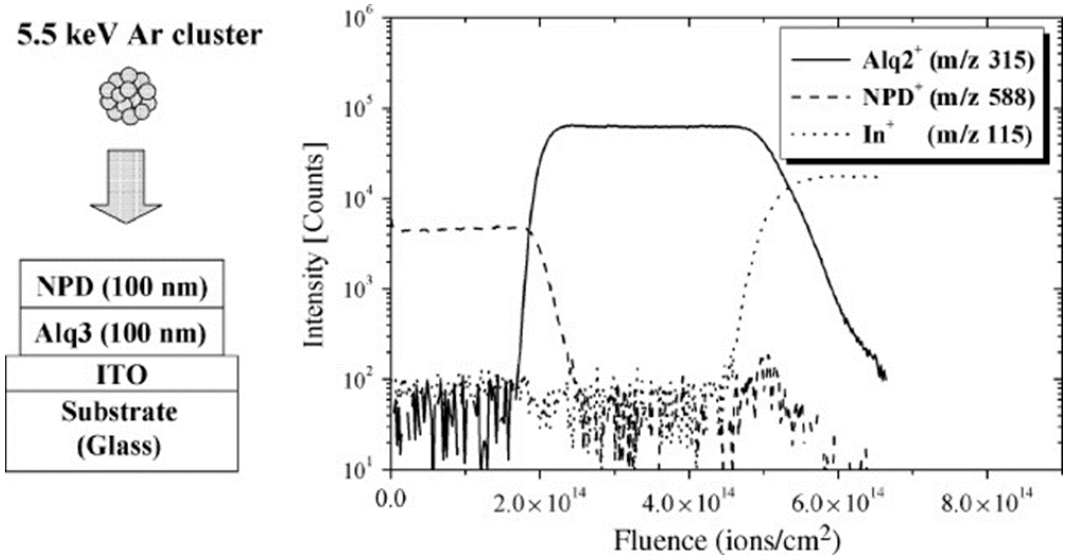

Figure 19 ToF-SIMS depth profile of the organic multilayer stack that is presented on the left. 5 keV Ar_{700} clusters were used as analysis beam and sputter beam [138].

There have been several similar studies on organic stacks. The purpose of those studies is often to verify the correct stacking of organic materials without intermixing or diffusing of different molecules.

In terms of ageing of organic electronic devices, there have been some publications on environmental ageing of OLEDs due to humidity, heat or irradiation. These studies compare artificially aged with freshly produced devices [126 - 128]. Artificial environmental ageing can be achieved by storing the devices under unfavorable conditions without encapsulation, annealing them or exposing them to UV-irradiation for some time.

However, to my best knowledge there is only one study on electrically aged devices by ToF-SIMS [137]. The structure of the OLED device that has been analyzed in that study is presented in the inset of Figure 20 a). ITO is used as the bottom electrode. On top of this electrode, a thin layer of PEDOT:PSS is used as hole injection layer. The emissive layer consists of a blend of PVK as a hole transport material, OXD-7 as an electron transport material and FIrpic as a commonly used emitter material. All of these molecules are shown in Figure 20 b). The depth profile in Figure 20 a) shows the fresh device in solid lines and the aged device in dashed lines. As analysis source, a 15 keV Bi_3^+ beam was used. Sputtering was done by 5 keV Ar_{1500} clusters. There are some small changes for the characteristic fragments of the molecules, but the main difference is the change in intensity for different fragments of the FIrpic emitter. The authors of the paper attribute the loss in luminance during device operation to the degradation of this emitter molecule which is indicated by the loss in intensity of the characteristic fragment with mass 632.02 u at the interface with PEDOT:PSS. Although this study shows the possibilities of ToF-SIMS for characterizing electrically aged OLEDs, it is not quite clear how they acquired the depth profiles without the top electrode.

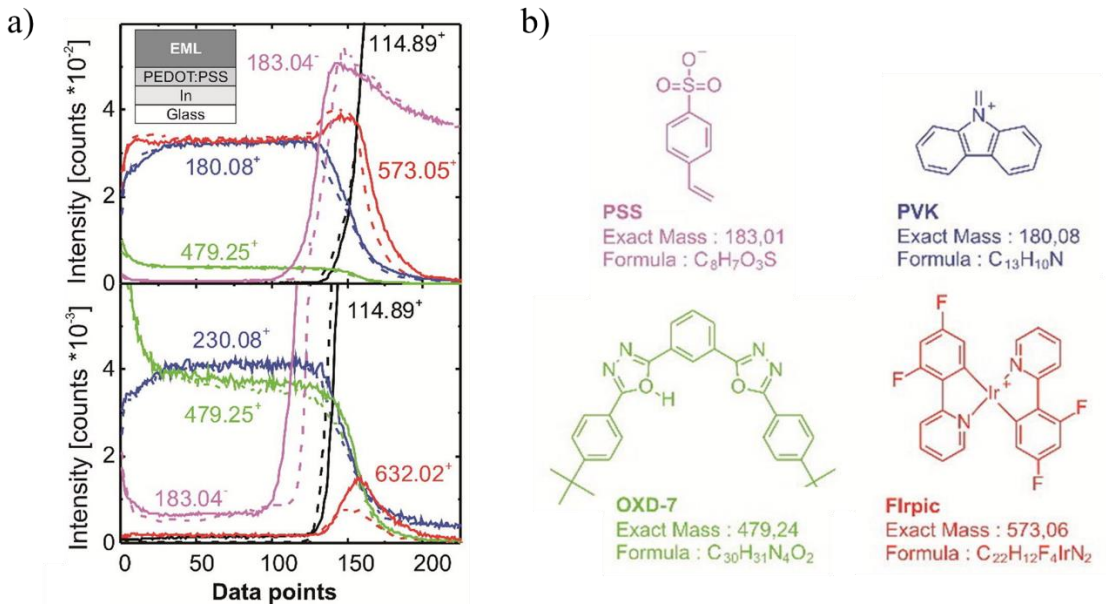

Figure 20 *a) Depth profile of the organic part of an OLED. The inset on the top left corner shows the structure of the device. The emissive layer consists of a blend of PVK, OXD-7 and FIrpic. Solid lines show the depth profile before electric ageing and dashed lines after. b) Molecular structure of the materials that were used in this device* [137].

2.1.2. XPS depth profiling for characterization of organic electronics

XPS depth profiling has also widely been used to study organic materials. Sputtering has already been discussed extensively and as shown before, it is possible to sputter away organic samples without

inducing damage to the surface. However, the X-ray beam that is used during analysis can lead to photoinduced fragmentation of small molecules or polymers.

X-rays will constantly interact with all the layers in organic electronic devices with thicknesses up to only a few hundred nanometers. Underlying layers may be damaged if the irradiation is too high. Contrary to ToF-SIMS, the damage that is induced by the analysis beam cannot always be taken away by the cluster sputtering in between each analysis step. The only way to reduce the damage is to reduce the X-ray dose during the measurement.

Nevertheless, XPS can be used effectively to analyze the chemistry in OLEDs [122, 129]. Figure 21 shows an example of XPS depth profiling [143]. In this particular case, co-puttering of 10 keV C_{60} clusters and 0.2 keV monoatomic argon was used to pass through the whole organic stack and the ITO bottom electrode until the glass substrate was reached.

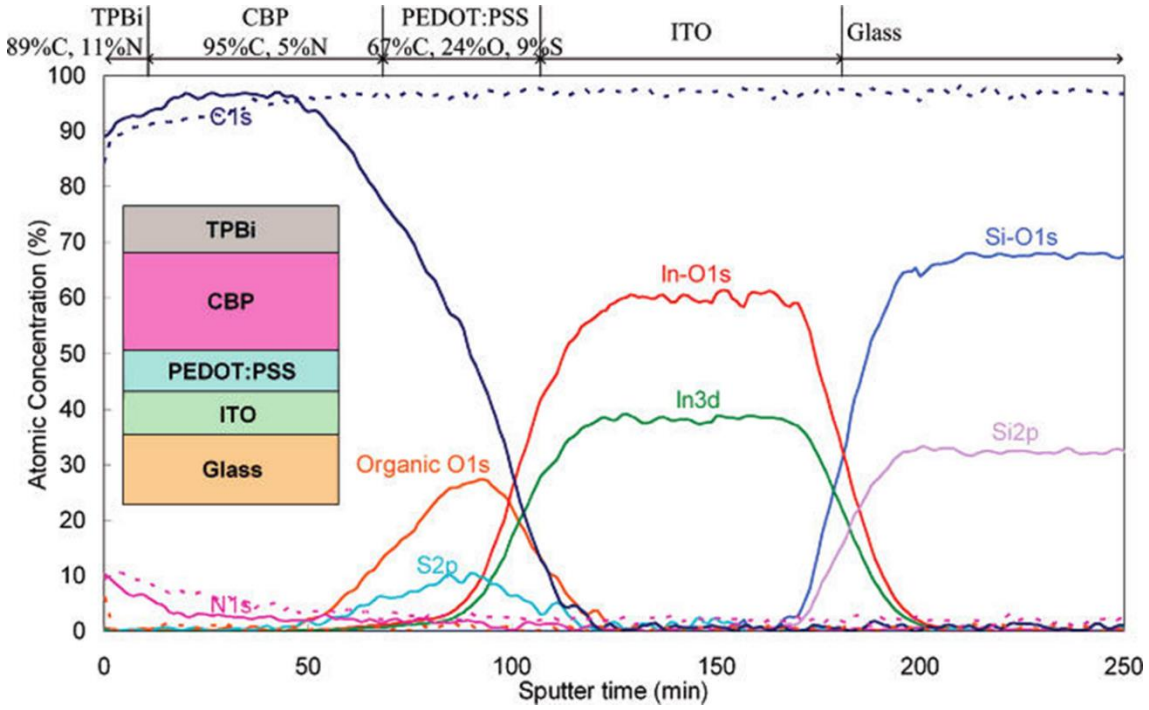

Figure 21 *XPS depth profile of the OLED structure that can be seen in the inset. Sputtering was done by a mixed beam of 10 keV C_{60} clusters and 0.2 keV monoatomic argon. The XPS spectra were recorded with an Al Kα source at 25 W and 100 µm beam diameter* [143].

The XPS spectra were recorded using an Al Kα source at 25 W. No further information about the X-ray dose is given. The mixed cluster and monoatomic sputter beam works well for sputtering through the inorganic bottom electrode but in the organic part, it is difficult to distinguish the three different layers. The PEDOT:PSS layer can be identified quite well thanks to the sulfur and oxygen in the molecule. The TPBi and the CBP layer are distinguished by a slightly different nitrogen content in the different molecules. This illustrates a problem of depth profiling of organic electronic devices with XPS: the chemical resemblance of the molecules. The molecules consist often only of carbon, nitrogen and hydrogen and the bonding states of these elements are often the same. Benzene rings for example were

already depicted in chapter 1 to be one of the main building blocks for organic semiconductors. This makes the distinction of certain layers very difficult. A high energy resolution in the core level spectra is needed together with high intensity. The problem is, that the analysis will take longer for a high energy resolution. That means, that a higher X-ray dose will be applied to the sample which in consequence may damage the molecules in the whole stack.

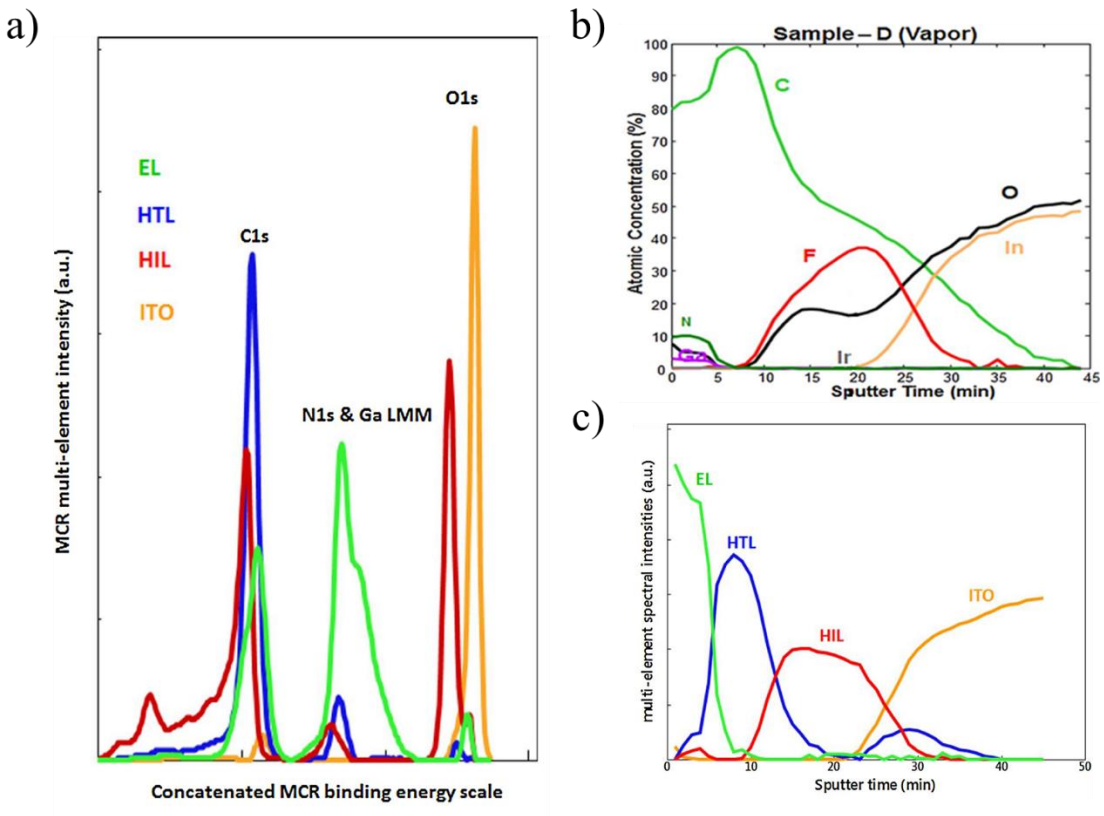

Figure 22 *a) Compressed data of XPS core level peaks of C 1s, O 1s and N 1s + Ga LMM for each of the analyzed layers. b) XPS depth profile acquired by 10 keV C_{60} sputtering through EL, HTL, HIL and the bottom ITO electrode of an OLED. c) Reconstructed depth profile by correlation of each point of the depth profile with the reference spectra in a)* [144].

For organic electronic devices, there is also the problem of information depth. Typically, the upper 10 nm of the sample are probed. At interfaces, there will always be contributions of both layers in the acquired spectra. This is commonly known in XPS measurements, but some layers in modern state-of-the-art devices are only a few nanometers thick. That means that there might even be contributions of three different layers in the same spectra. This effect reduces the depth resolution in XPS depth profiling in combination with the before mentioned material intermixing during sputtering. Recently, an attempt in using multivariate analysis to improve depth profiles of OLEDs and to facilitate the distinction of different layers has been published [144]. The authors used C_{60} sputtering at 10 keV to analyze the emissive layer, the hole injection layer and the hole transport layer of an OLED. The X-rays came from an Al Kα source at 1486.6 eV. They used a high pass energy of 177.4 eV to record all relevant elemental core levels. Afterwards, the data was fitted by using a mathematical deconvolution process. This method

ensures the acquisition of data with high counts and high sensitivity while keeping the acquisition time low to minimize the X-ray induced damage on the sample.

The acquired depth profile is presented in Figure 22 b). In Figure 22 a) the core level spectra of C 1s, O 1s and N 1s together with the auger peak Ga LMM are combined in one graph for each of the different layers. The data in between these characteristic peaks has been deleted to compress the data and backgrounds have been subtracted. This data treatment has been done for each point in the depth profile. The correlation between each point and the reference spectra from Figure 22 a) can then be expressed as a depth profile as shown in Figure 22 c). Compared to the initial data in Figure 22 b) it gives a clearer image of the chemical structure in the sample. Even diffusion of the HTL through the HIL towards the ITO interface that was not visible in the untreated data can now be suspected.

2.2. Combining ToF-SIMS and XPS depth profiling

ToF-SIMS and XPS are very powerful techniques on their own when it comes to chemical depth profiling. However, combining both techniques can be advantageous in some cases.

The importance of reducing the analysis-induced damage has been discussed thoroughly in the previous sections. The structural and chemical changes caused by the characterization techniques can be very subtle. The detection of this damage needs therefore to be done with great precision and sensitivity. Recording core level spectra or the valence band region in XPS can fulfil this task. Small changes in the chemical environment at the sample surface can be detected. That is why there have been several studies on the impact of sputtering on organic materials.

Figure 23 shows a study during which a thick leucine film has been sputtered with different sputter sources [125]. Afterwards, the C 1s (a)), N 1s (b)) and O 1s (c)) core level spectra have been recorded and compared with an unsputtered reference. It can clearly be seen that the peak shape changes significantly for the bombardment with argon monomers.

For low energy Ar_{5000} clusters at 10 keV or 20 keV the intensities of the peaks change. Since XPS is a quantitative technique, it is possible to calculate the elemental composition at the surface. This is shown in Figure 23 d), where the percentage abundance of each element for the different measurements is indicated. No significant change in the chemical composition can be observed for cluster sputtering. However, there is a strong increase in carbon content at the sample surface after sputtering with argon monomers. The only observable change during cluster sputtering is at the O 1s core level. There is a small shift from binding energies of about 531 eV towards about 531.7 eV. These values were assigned to $O{=}C{-}O^-$ and O=COH bonding states, respectively.

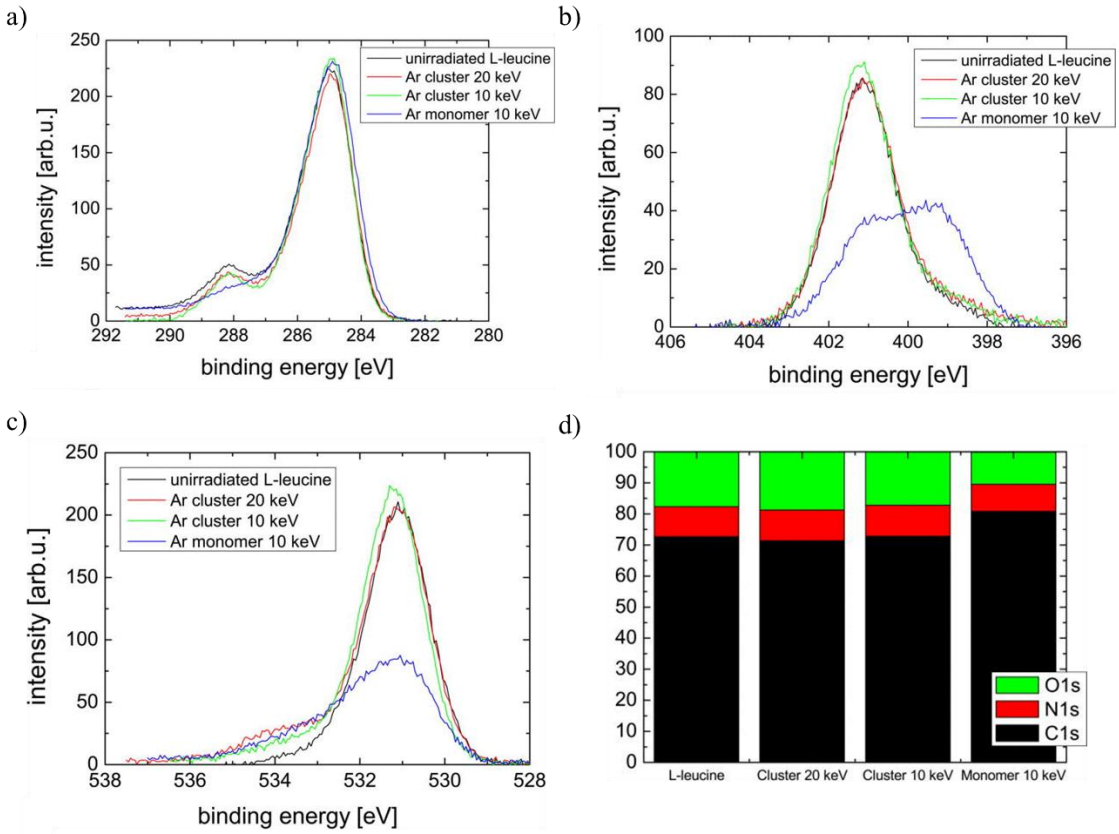

Figure 23 *a) XPS C 1s, b) N 1s and c) O 1s core level spectra before and after sputtering with 10 keV argon monomers or 10 keV and 20 keV Ar_{5000} clusters. d) Percentage elemental composition for the different measurements* [125].

These studies provide important information on the degradation of organic materials during analysis. Similar studies have been done on materials that have been exposed to excessive X-ray irradiation. However, no general behavior of organic molecules under irradiation of X-rays or ion beams can be derived from these studies. Every molecule behaves differently and studies like these should be repeated for every material that is used and characterized in an OLED stack.

Besides the advantage of detecting analysis induced damage by combining XPS and ToF-SIMS, both techniques can be used to gain complementary information. Analyzing core levels in XPS does not provide direct molecular information. ToF-SIMS however can directly detect molecular fragments. On the other hand, ToF-SIMS is not a quantitative technique due to the strong dependence of the secondary ion yield on the chemical environment. XPS however is quantitative. Each technique can complement the other with important information. An interlaboratory study showed the possibility to correlate the quantification that XPS provides with the secondary ion intensities in ToF-SIMS depth profiles on organic multilayer samples [145].

Studies on organic electronic devices have also used both techniques in combination. Hermenau *et al.* combined both techniques to analyze organic solar cells for example [141]. The analyzed structure is presented in Figure 24 a). The aluminum top electrode was removed by using scotch tape, leaving the BPhen layer exposed. The goal of the study was to examine the water and oxygen induced degradation

of the solar cell. The device has therefore been operated under air conditions. During the operation, XPS and ToF-SIMS measurements have been performed on the BPhen surface. Figure 24 b) shows the evolution of the elemental concentration at the surface. The oxygen content rises with ongoing device operation. This quantitative data can then be correlated to a corresponding ToF-SIMS intensity as can be seen in Figure 24 c). This calibration makes further ToF-SIMS measurements quantitative and the superior depth resolution of ToF-SIMS can be used to acquire precise depth profiles of the oxygen diffusion into the organic layers.

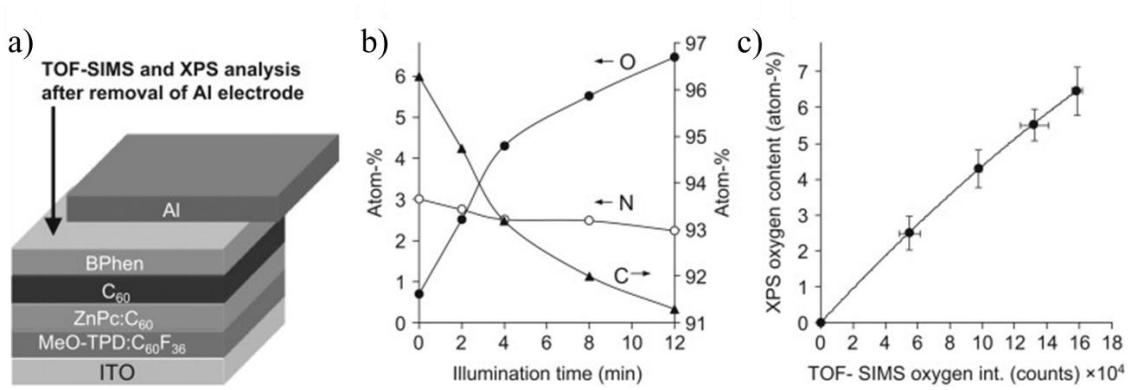

Figure 24 *a) Schematic representation of the analyzed device. b) Elemental composition of the BPhen surface measured by XPS. c) Calibration curve that make ToF-SIMS measurements quantitative by correlating its intensities with XPS quantification* [141].

There are also examples in the literature where both techniques have been used in a complementary fashion to get molecular information that the other technique cannot provide. Scholz et al. used for example ToF-SIMS to identify fragments of organic materials and XPS to identify oxidation of metallic electrodes [134]. The oxidation can be clearly identified in XPS because of the significant energy shift towards higher binding energies for the oxidation binding state compared to the metallic binding state. The relatively high information depth of XPS can be used as an advantage here. In ToF-SIMS measurements it is possible, that detected metal oxides are formed during sputtering if an oxygen source is available. In XPS this can happen as well, but the oxide can already be detected before the sputter beam has an impact on the interface.

Finally, there is another advantage in combining both techniques. It has been mentioned that the mass spectra of organic materials are full of peaks of molecules and their fragments. In multi-layer stacks, it is often not evident which peaks correspond to which molecule. There might be fragments, contaminants or dopants that are hidden in the densely packed mass spectra. Especially during the analysis of samples with unknown composition this might be a problem. In this case, XPS can identify elements and quantify them. This can facilitate the assignment of certain molecules to an unknown peak.

All of these examples show the improvement of data quality and information that can be gained by combining both techniques instead of using only one.

Conclusion

ToF-SIMS and XPS are two highly surface-sensitive characterization methods that can be used to analyze organic electronic devices. Combining both techniques opens up interesting opportunities to get even more information out of the measurements.

A first plus is the possibility to study the impact of the analysis beam or the sputter beam on organic materials. In that context it has been shown that the introduction of gas cluster ion sources (GCIB) has been a critical breakthrough. It is possible to sputter organic materials without damaging the molecules. However, the primary ion beam in ToF-SIMS and the X-ray beam in XPS are still damage sources that need to be considered.

Liquid metal ion guns (LMIG) present the best option for the primary ion beam in ToF-SIMS. The easy handling and focusing of the ion beam are big advantages together with the high mass resolution that can be provided in the high current bunched mode. Especially for depth profiles in organic materials it is important to have a sufficiently high mass resolution to identify the fragments of different molecules. The LMIG provides also a high primary ion current which is important for high secondary ion yields. Ionization probabilities of organic materials are often low and cannot easily be enhanced by artificially creating matrix effects as in cesium or oxygen sputtering.

In XPS measurements, the X-ray exposure should be minimized. This is often not easy because to gain sufficient energy resolutions, low pass energies are necessary. Low pass energies imply weaker XPS signals and therefore, longer analysis times.

Another advantage of combining both techniques is the complementary information that can be extracted from measurements. ToF-SIMS can provide useful molecular information with very high depth resolution and sensitivity, whereas XPS provides quantification and chemical information.

Chapter III:

Impact of ToF-SIMS and XPS analysis parameters on organic materials

1. Studied materials

1.1. Sample structure

It is important to characterize the damage that is induced during depth profiling of organic electronic devices in the perspective of characterizing ageing mechanisms. As mentioned in Chapter 2, combined ToF-SIMS and XPS measurements can be a very powerful solution for this task.

Since every molecule behaves differently under ion beam bombardment or X-ray irradiation, it is important to study every material separately. The simplest possible sample structure to study are single layer samples. Figure 25 shows the schematic representation of the studied samples. The organic material is easily accessible, and no other layer has to be removed in order to probe the material.

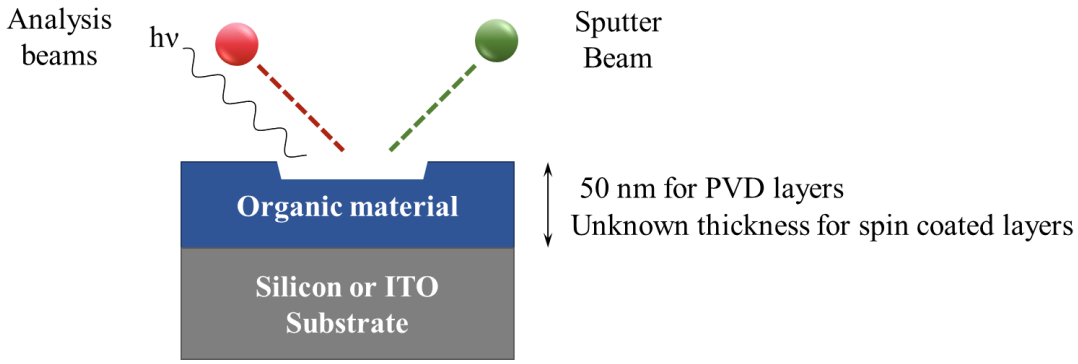

Figure 25 *Schematic representation of the studied sample structure. 50 nm thick organic layers were deposited on silicon substrates by physical vapor deposition (PVD). Solution processed polymer layers were spin coated with an unknown thickness onto ITO substrates.*

Most of the layers were deposited by physical vapor deposition (PVD) onto silicon substrates. PVD is the standard deposition method used in organic electronics. The deposition takes place in an UHV environment. It is important to reduce the water and oxygen content during the deposition to reduce degradation due to these contaminants [146]. Moreover, the layer thickness is very well controlled and samples can be patterned easily by using masks during the PVD process.

These PVD samples have been provided by Tony Maindron's group at the Optoelectronics Department of CEA-LETI in Grenoble. The thickness is 50 nm for all the vapor deposited materials. This ensures sufficiently thick layers for XPS measurements where only the organic layer is probed. At the same time, depth profiles through the layers are fast but with enough data points to precisely determine sputter rates.

With these samples it is possible to study the impact of each analysis parameter separately. The three main damage sources are the sputtering beam which ToF-SIMS and XPS depth profiling have in

common and the respective analysis beam. For ToF-SIMS it is the primary ion beam and for XPS the X-ray beam.

As mentioned before, organic materials are sensitive to oxygen exposure and humidity. To prevent degradation after the deposition process, all samples have been boxed and sealed under nitrogen environment in a glove box. They have then been transferred and stored in the glove box that is directly attached to the ToF-SIMS instrument.

The deposition was performed on 200 mm wafers. The wafers have then been cleaved to produce 1 x 1 cm^2 samples that fit onto ToF-SIMS and XPS sample holders.

For a cooperation with Yolande Murat at the IMS in Bordeaux, some spin coated materials were provided. The thickness of spin-coated cannot easily be determined. The roughness and homogeneity of the layers is often a problem for solution processed layers. Due to these problems, solution processed OLEDs don't reach the same efficiency as evaporated OLEDs yet. However, advantages of this technique are the easy and fast preparation of the layers. No vacuum is needed and the process can be adapted to very large scales. This reduces the fabrication costs emensly and therefore, a lot of research effort is put into solution processed OLEDs.

For the spin-coated samples, ITO substrates were used rather than silicon substrates to simulate the final OLED structure, where ITO functions as an electrode.

1.2. Organic molecules

All the studied materials are commonly used in organic electronic devices. Figure 26 gives an overview of the molecular structure for each material. Most of the materials are small molecules with masses between 270 and 1100 g/mol. These small molecule type materials can be evaporated.

However, solution processed OLEDs have also been studied during this thesis. The materials used in this type of OLED are polymers. They are spin coated onto an ITO substrate. The spin coating process requires the polymer to be in a stable solution. The PEDOT:PSS and the PEIE polymers are solved in water. The PEDOT:PSS is spin coated directly from this solution. The PEIE solution is mixed with 2-Methoxyethanol before it can be spin coated onto the substrate. The Super Yellow emitter polymer is diluted in toluene. The only small molecule that was used in the solution processed OLEDs is TPBi. It has been diluted in ethanol.

Some of the studied materials are industrial products that are designed especially for the use in certain layers of OLEDs. The molecular structure of those materials is unknown. Nevertheless, reference measurements can be performed on those materials to gain information about characteristic mass fragments in ToF-SIMS or peak shapes and elemental information in XPS. This concerns a hole transport material that will be labeled with HTM throughout this thesis, a dopant for the hole injection

layer (HID), an electron transport material (ETM) as well as an emitter combination that consists of a host (emitter host material EHM) and the emitter itself (EM).

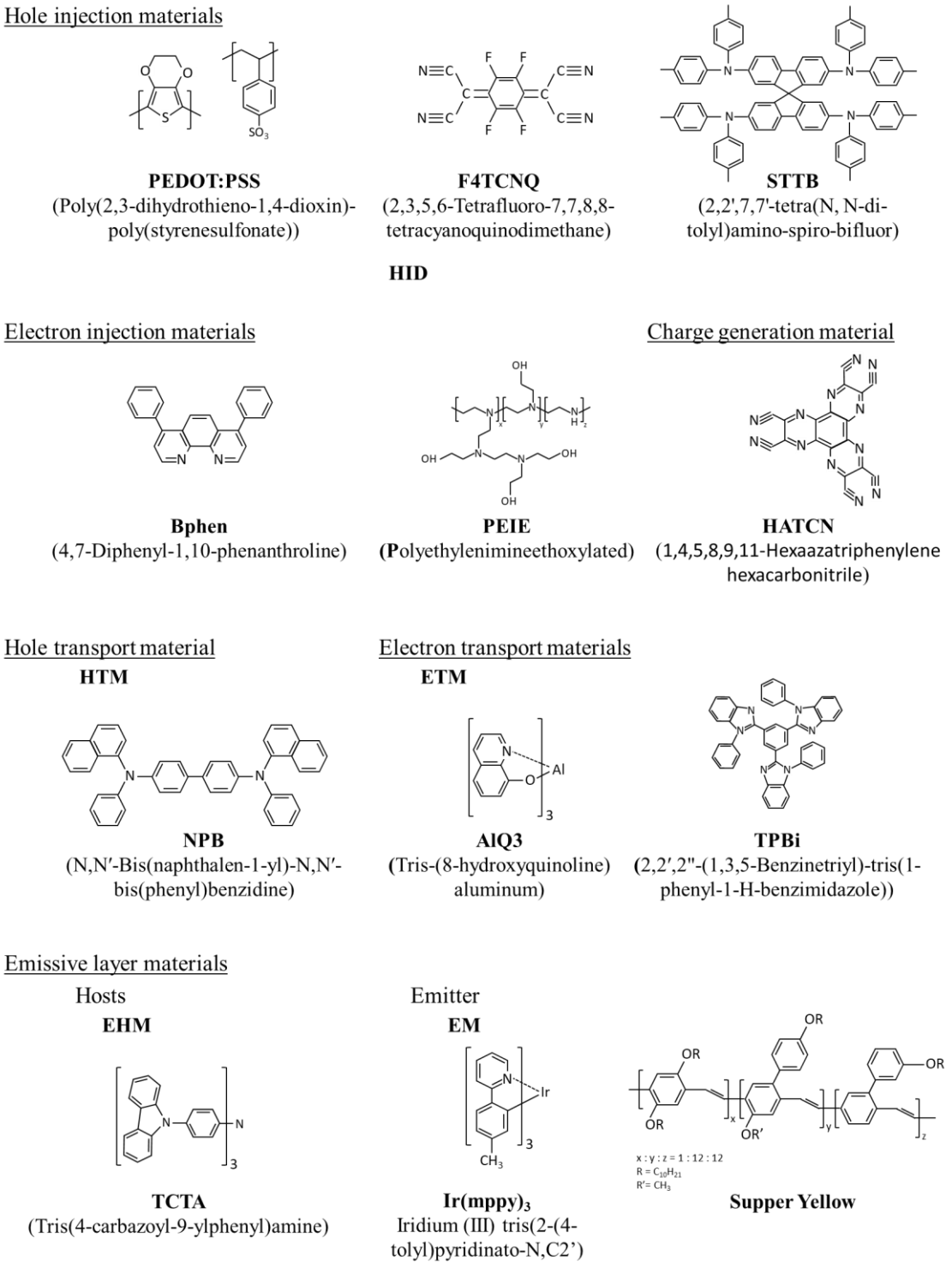

Figure 26 Chemical structures of the different molecules that were studied.

1.3. Reference measurements

To study the impact of different parameters during analysis, a starting point needs to be determined. Therefore, reference measurements have been acquired by ToF-SIMS and XPS to gain some basic information about each material.

1.3.1. ToF-SIMS

1.3.1.1. Experimental method

Starting with ToF-SIMS, the reference measurements have been performed using standard parameters for the depth profiling of organic materials.

The instrument was used in dual beam mode with Bi_3^{++} as the analysis beam. The beam was operated at 30 keV with a current of 0.4 to 0.45 pA. The beam was scanned over an area of 300 x 300 μm^2 at 128 by 128 pixels. As sputter beam, an argon cluster gun was used to produce clusters with a size of 5000 atoms per cluster. The energy of the beam was 5 keV which results in an energy of 1 eV/atom. The current was about 1 nA and the beam was scanned over an area of 500 x 500 μm^2.

The instrument was used in the non-interlaced mode where the analysis beam and the sputter beam are completely decoupled. After one analysis frame, the sputter gun is switched on for one frame. Before the next analysis step, there is a break of 0.5 seconds to allow the surface to reach an electrical and thermodynamic equilibrium.

The depth profiles have been run up to a point where the substrate signal has settled in a flat plateau and the organic signal has fallen to close to zero intensity. A mass calibration has then been performed on the measurement data by using the C signal, the substrate signal (Si or In), several hydrocarbon signals or even the molecular signal of the organic material as reference points.

1.3.1.2. Results

One information that can be gained from this type of measurement is the sputter rate of the material. Since the thickness of the organic layers is known for the evaporated molecules, it is possible to calculate the sputter rate for each material. However, the result is only valid for these exact analysis parameters. The sputter rate will change if the energy or the current of any of the beams changes or the cluster size of the sputter beam gets altered. The values of the sputter rate are therefore not of great interest, but the comparison of the relative sputter rates of different materials might show differences between the materials if they are all analyzed using the same conditions. This kind of information can be useful for depth calibration in multilayer stacks. For all the small molecule type materials that were analyzed, the sputter rate was in the range of 0.98 to 1.3 nm/s with most of the materials being around 1 nm/s. The difference in sputter rate for these materials is negligible. For polymers however, the sputter rates are

significantly lower. It is harder to eject the long polymer chains from the surface. The chains must be broken. This leaves many possibilities for cross-linking of broken polymer chains at the surface which can additionally hinder the sputtering process. Polymers can generally be split into two groups [147]. Type I polymers will cross link under irradiation. The polymers in this group have often very little branching or aromatic parts. Type II polymers will rather degrade by chain scission processes. These polymers exhibit increased branching and weak points on the main chain back bone [148]. The differences between the sputter rates of the analyzed polymers indicate different types of polymers. PEDOT:PSS and PEIE exhibit a sputter rate of about 0.1 nm/s at the given analysis parameters. Super Yellow on the other hand has a sputter rate of 0.25 nm/s. This big difference might be an indication that PEDOT:PSS and PEIE are type I polymers where cross linking occurs during sputtering which decreases the sputter rate. Super Yellow with its heavy branching seems to be a type II polymer.

Reference profiles can thus provide a comparison of sputter rates for different materials. But the main goal of these measurements was to identify the characteristic fragments for all molecules that were analyzed during this thesis. For that purpose, only the organic part of the acquired depth profile has been reconstructed via the data treatment software “Surface Lab 6” from IONTOF. The result is a mass spectrum that is integrated over the whole organic layer for the analyzed 300 x 300 µm area. The reference spectrum for the NPB layer is shown as an example in Figure 27.

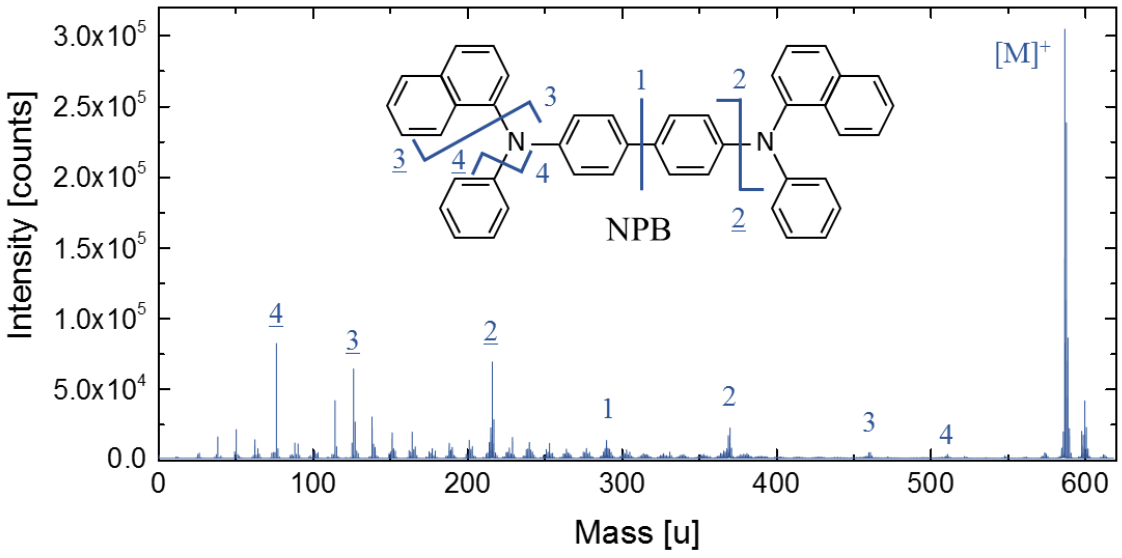

Figure 27 ToF-SIMS reference spectrum for NPB showing the molecular ion ([M]) characteristic fragments as well as characteristic fragments of the molecule (1-4).

The strong signal at a mass of 588.74 u corresponds to the positive molecular signal of NPB ($[M]^+$). But a heavy fragmentation of the molecule can also be observed. Certain peaks can be assigned to characteristic fragments of the molecule. The inset of the molecular structure shows different possible fragmentation patterns. These fragments are labeled with the numbers 1 to 4 in the mass spectrum.

However, it can also be seen that there are many unlabeled peaks. More than only the proposed fragments can be formed during the analysis. During depth profiling of multilayer devices or 3D

patterned devices, the possibilities of fragmentation increase even further, and it can become difficult to identify different parent molecules among hundreds of peaks. This illustrates clearly the necessity for reference spectra.

1.3.1.3. Summary

The same measurements have been done for all of the molecules. This way, a database for characteristic fragments can be created. This database can be found in Table 1. It gives an overview of the different materials that were used throughout this thesis. Besides the molecular signal at the nominal mass, there are several fragments for each molecule that can be observed. For the unknown molecules, the chemical formula cannot be defined with 100 % certainty, but characteristic fragments can be defined. Not all monomers can be detected during the analysis of the polymers. But thanks to the presence of sulfur in PEDOT:PSS and nitrogen in PEIE, there are some characteristic fragments for each material.

The hole injection material HATCN and the dopants in hole injection layers like F4TCNQ and PSS are p-type dopants with low lying energy bands. This means that they are strong electron acceptor materials and they will very likely take a negative charge during ionization. Therefore, it is very hard to identify positive characteristic ions for these materials. Mainly highly fragmented hydrocarbons are detected in the positive analysis mode. This makes the analysis in positive and negative ion mode necessary if these materials want to be detected.

Thanks to Table 1, each molecule will be clearly identified in depth profiles of multi-layer structures that will be studied in Chapters 4 and 5. The reference spectra that were used to create this overview can be found in the appendix. It should be noted at this point, that for the unknown molecules, only peaks at certain m/z values were identified as characteristic fragments, without the knowledge of the exact chemical formulas. For simplification, these peaks will be labeled by their respective mass with the unit “u” even though it is possible that doubly charged secondary ion with twice the mass contribute as well to those peaks.

Table 1 Overview of the different analyzed materials, their chemical formula as well as the nominal molecular mass and characteristic fragments that have been identified by ToF-SIMS reference measurements.

Material	Chemical formula	Nominal mass [u]	Characteristic fragments
Small molecules			
STTB	$C_{81}H_{68}N_4$	1097.43	$C_7H_7^+$, $C_{14}H_{14}N^+$, $C_{74}H_{61}N_4^+$, $C_{67}H_{54}N_3^+$
F4TCNQ	$C_{12}F_4N_4$	276.15	F^-, CN^-, C_3N_2, $C_9F_4N_2^-$, $C_{12}F_3N_4^-$
BPhen	$C_{24}H_{16}N_2$	332.40	$C_6H_5^+$, $C_{12}H_6N_2^+$, $C_{18}H_{11}N_2^+$
HATCN	$C_{18}N_{12}$	384.27	CN^-, $C_4N_3^-$, $C_{14}N_9^-$, $C_{17}N_{10}^-$, $C_{18}N_{11}^-$
NPB	$C_{44}H_{32}N_2$	588.74	$C_6H_5^+$, $C_{10}H_7^+$, $C_{16}H_{12}N^+$, $C_{22}H_{16}N^+$, $C_{28}H_{20}N^+$, $C_{34}H_{25}N_2^+$, $C_{38}H_{27}N_2^+$
Alq_3	$C_{27}H_{18}N_3O_3$	459.43	Al^+, $C_9H_6NOAl^+$, $C_{18}H_{12}N_2O_2Al^+$
TPBi	$C_{45}H_{30}N_6$	654.76	$C_6H_5^+$, $C_{39}H_{25}N_6^+$
TCTA	$C_{54}H_{36}N_4$	740.89	$C_{18}H_{12}N^+$, $C_{44}H_{28}N_3^+$
$Ir(mppy)_3$	$C_{36}H_{30}N_3Ir$	654.78	$C_{12}H_{10}N^+$, $C_{24}H_{20}N_2Ir^+$
Polymers			
PEDOT	see Figure 26	-	C_4S^-
PSS		-	SO_3^-
PEIE		-	$C_2H_5N^+$, $C_3H_7N^+$, $C_4H_9N^+$, $C_2H_5NO^+$
Super Yellow		-	$C_2H_5^+$, $C_3H_7^+$, $C_4H_9^+$
Unknown molecules			
ETM	-	-	228.1, 256.1, 340.1, 852.35, 864.35
HTM	-	-	1096
HID	-	-	213.02, 286.01, 461.03, 672.05 (neg. mode)
EHM	-	-	77.04, 104.06, 267.1, 368.1, 591.3, 603.3
EM	-	-	345, 499.1, 501.1, 655.15

1.3.2. XPS

1.3.2.1. Experimental Method

Not only ToF-SIMS but also XPS reference spectra have been acquired. From the molecular structures that were shown in Figure 26, it can be seen that almost all of the molecules exhibit the same kind of bonding states for the carbon and nitrogen atoms. It is therefore very difficult to distinguish the different molecules by comparing only the C 1s or N 1s signal. For some materials like Alq_3 or $Ir(mppy)_3$, there is an additional metal atom that is characteristic for the material. In the case of no additional atoms, the valence band region can be used as an additional reference. The reference spectra were recorded using a monochromated aluminum Kα X-ray source with a photon energy of 1486 eV at a power of 25 W and a beam diameter of 100 µm. The pass energy at the detector was 23.5 eV for the C 1s and N 1s core levels and 46.95 eV for the valence band region with a step size of 0.05 eV for both settings. The overall energy resolution ΔE for those settings can be calculated with equation (9), neglecting the natural width of the photoelectric line and the thermal broadening:

$$\Delta E = \sqrt{\Delta E_{spec}^2 + \Delta E_{X-ray}^2} \qquad (9)$$

where the spectrometer specific energy resolution E_{spec} is 0.62 and 0.80 eV for pass energies of 23.5 and 46.98 eV, respectively. The X-ray broadening $E_{X\text{-}ray}$ is 0.26 eV. This results in an overall energy resolution of about 0.67 and 0.84 eV for the 23.5 and 46.95 eV pass energies, respectively.

The higher pass energy for the valence band region was chosen to allow for higher counting statistics in these spectra. Since the overall intensity is very low for valence band spectra in XPS due to poor ionization cross-sections, it is indeed necessary to increase the pass energy to gain intensity. For the core level spectra, the signal of 25 analysis cycles has been averaged to get the final spectrum. For the valence band region, 50 cycles were used. However, the valence band spectra still exhibit an important amount of noise. The data has therefore been smoothened using the numerical convolution algorithms (linear Savitzky-Golay smoothing using 5 datapoints) of the CasaXPS software that has been used for data treatment.

1.3.2.2. Results

The XPS reference measurements for the NPB and STTB molecules are shown in Figure 28 to illustrate the utility of valence band measurements as fingerprints for organic materials.

The chemical structures of NPB and STTB that were shown in Figure 26 indicate that both materials only consist of carbon, nitrogen and hydrogen. The core level peaks of carbon and nitrogen are the only elemental peaks that are measured since hydrogen possesses no core levels and can therefore not be detected in XPS.

The relative elemental abundance of carbon and nitrogen are very similar within 1 % for both materials as can be seen in the chemical formulas in Table 1. NPB is built of 44 carbon atoms with 2 nitrogen

atoms while STTB possesses 81 carbon atoms with 4 nitrogen atoms. By peak fitting of the C 1s and N 1s core level spectra, it is possible to quantify the elemental abundance of carbon and nitrogen in each material. Figure 28 a) – d) shows these core level fits for NPB and STTB.

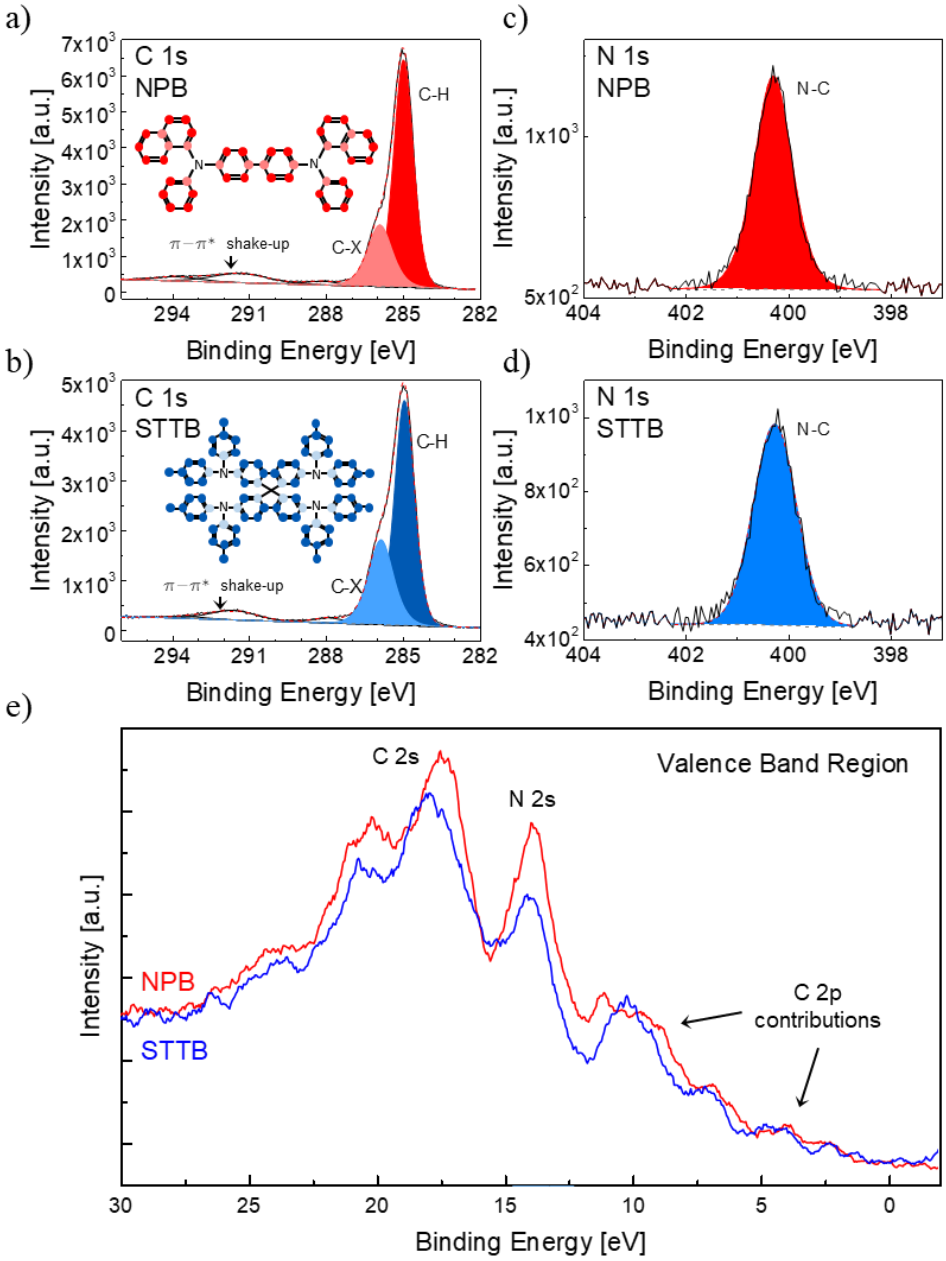

Figure 28 XPS reference spectra of the C 1s core level spectra for NPB (a)) and STTB (b)), N 1s core level spectra for NPB (c)) and STTB (d)) and an overlay of the valence band region for NPB and STTB(e)).

The N 1s peak in Figure 28 c) and d) consists of only one symmetrical contribution from the nitrogen atoms between three benzene groups in both materials. For the C 1s peak in Figure 28 a) and b), there is a main peak at a binding energy of 285 eV which can be attributed to the C-H bonds in the aromatic parts of the molecules. The π- π* shake-up at a binding energy of about 292 eV is an effect which has been discussed in Chapter 2. It is another indicator for the aromatic groups. An additional contribution to the C 1s signal can be identified. It forms a shoulder to the main peak at higher binding energies and

is labeled with C-X. In the NPB sample, this refers to the carbon atoms around the nitrogen atoms. In the STTB sample, these nitrogen surrounding atoms as well as the carbon atoms that form the spiro-link can be attributed to the C-X signal. The results of the experimental quantification for the elemental composition in both materials are summarized in Table 2. At this point, it should be stressed that additional contributions to the C 1s peak could be identified in accordance to some studies that were found in literature [149], [150]. However, the resolution of the recorded spectra is too poor here so that these contributions were excluded for consistency reasons.

Table 2 Overview for the XPS quantification of the NPB and STTB single layer samples.

Element	**Bonding State**	**Position**		**At%**	
		NPB	**STTB**	**NPB**	**STTB**
C		**285**	**285**	**96.49**	**95.89**
	C-H	285	285	62.67	58.71
	C-X	285.98	285.93	22.31	28.56
	C shake-up	-	-	11.42	8.62
N		**400.26**	**400.30**	**3.51**	**4.11**

All values are in good agreement with the numbers expected from the chemical formulas and lie well within the typical 15% uncertainty in XPS.

The materials can hardly be distinguished when only the ratio of carbon to nitrogen is considered. However, peak fitting of the high-resolution core level spectra can reveal the small differences between both materials. The contribution at higher binding energies (C-X) is more pronounced in the STTB sample. It accounts for about 30 % of the total C 1s signal whereas it is only 22 % in the NPB sample.

Additionally to the core level spectra, the valence band regions of both materials have been recorded and are shown in Figure 28 e). The valence band for all reference materials in this thesis is predominantly defined by carbon contributions. The nitrogen atoms add some intensity to certain peaks [151]. The valence band spectra of NPB and STTB exhibit very similar features. The peak around 14 eV, which can be attributed to the N 2s core level lies at the exact same energy for both spectra. This is expected as the nitrogen exhibits the same bonding state in both molecules. The main peak, that is an indicator for the C 2s orbital is slightly shifted by about 0.5 eV between both spectra. The peak at 10 eV which has contributions from the C 2p orbital shows a different shape as well. This might be because the carbon in the STTB molecule is not only present in aromatic rings but also in methyl groups.

1.3.2.3. Summary

Overall, these differences can only be detected in high resolution spectra. In depth profiles, which are the ultimate goal in this thesis, the energy resolution is often sacrificed to some extent in order to reduce the analysis time and X-ray exposure to reduce the damage that is induced during the analysis. That is why small differences like these can easily be overseen. The valence band spectrum can be used as a fingerprint, even for chemically very similar materials.

With valence band reference measurements as in Figure 28 e), it is possible to identify the materials without peak fitting as it is needed for the core level spectra. Especially for depth profiles with multiple different materials and ultrathin layers as they can be found in inorganic electronics, it is important to reduce the X-ray exposure time to a minimum. The example in Figure 28 shows the utility of the valence band spectrum as fingerprint. Instead of using up to 8 different atomic core levels that are recorded during a depth profile, it is worth considering to only focus on the valence band to drastically reduce the analysis time.

Similar XPS reference measurements have been performed for the other evaporated materials. These reference spectra can again be found in the appendix.

2. Impact of the sputter beam on organic materials

With the reference measurements, it is now possible to change the analysis parameters one by one to investigate their impact on the analysis results. The goal is to gain information about the damage to organic molecules that is induced by the characterization technique in order to reduce the damage to a minimum.

The first study shows the impact of the sputter beam on the organic materials. Both techniques, ToF-SIMS and XPS, have the sputter beam in common. The sputter beam is defined by three main parameters. The species that is used for sputtering, its primary energy and in the case of clusters, the cluster size, which, combined with the impact energy, provides the effective impact energy per atom. The incidence angle also plays a role, but it is fixed at 45° in both instruments.

2.1. Comparison of monoatomic sputtering and cluster sputtering

2.1.1. Experimental setup

The first parameter that is studied is the most basic one. Generally, it is possible to use either monoatomic sputter sources or cluster sputter sources. In Chapter 2 of this thesis it has already been mentioned that cluster sputtering is considered as essential for depth profiling of organic materials. The non-damaging character of C_{60} or more bulky argon clusters has been demonstrated on several occasions [132, 133].

To demonstrate the damage that is induced by different sputter species, craters with monoatomic argon and with argon clusters are made on organic materials. Afterwards, XPS measurements are performed inside these craters and compared with the above described reference measurements.

2.1.2. Results

Figure 29 shows the C 1s and N 1s core level spectra of the emitter host material TCTA.

The reference spectrum in black was taken before sputtering of the surface. Then, sputtering with monoatomic argon at 1 keV and with 5 keV Ar_{4200} clusters was performed at two different sample spots for 6 seconds. Finally, XPS spectra have been taken inside the sputter crater. The XPS core levels after monoatomic and cluster sputtering are shown in red and blue, respectively.

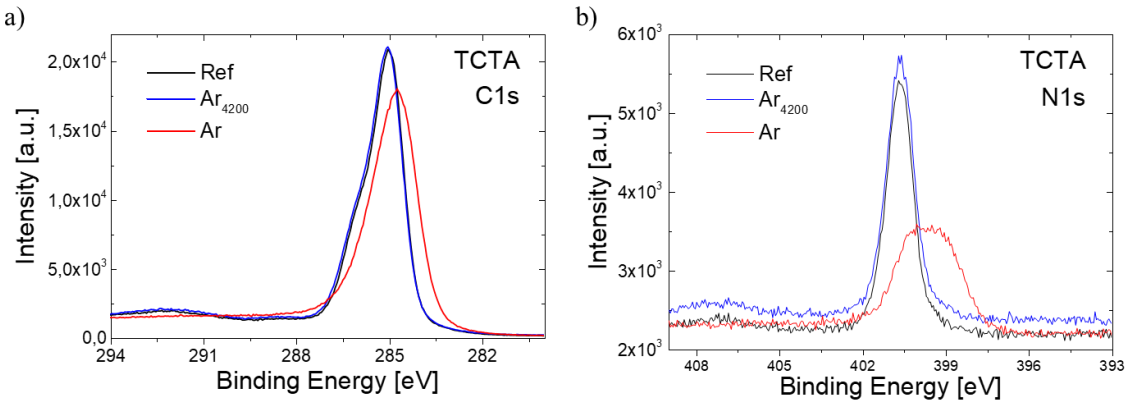

Figure 29 *XPS a) C 1s and b) N 1s core level spectra of TCTA. Reference spectra are shown in black. Spectra that were taken in the sputter crater after 5 keV Ar_{4200} sputtering and 2 k eV monoatomic argon sputtering are shown in blue and red, respectively.*

The red lines for the monoatomic sputtering show clear signs of damage to the organic molecule. The C 1s signal lost some intensity and underwent an energy shift towards lower binding energies alongside peak broadening. Most importantly, the peak appears now symmetrically. The reference measurement indicates a clear shoulder peak which can be attributed to C-N bonds in the molecule. The disappearance of this shoulder indicates the rupture of those bonds. Moreover, there is no π shake-up anymore around 292 eV in the red spectrum. This means that even the benzene rings have been damaged. The expected rupture of C-N bonds is confirmed by the decrease and the heavy peak broadening of the N 1s signal in Figure 29 b).

On the other hand, the blue lines for cluster sputtering indicate that the cluster sputtering induces only minimal amounts of damage. The reference line for the C 1s core level is almost perfectly reproduced by the spectrum after sputtering. The C-N shoulder and the π- π* shake-up structure are unchanged. The only difference between the reference and the cluster sputtering spectrum is the increased background signal in the N 1s signal after sputtering. This indicates generally that the photoelectrons undergo more loss processes while leaving the sample.

2.1.3. Summary

These results confirm the non-damaging character of argon clusters as sputter source, as discussed in Chapter 2. Argon clusters need to be used for sputtering of the organic materials if the molecular structure wants to be preserved.

2.2. Impact of the cluster size and the energy per atom on the analysis

2.2.1. Experimental setup

Next, the impact of the cluster size on the sputter induced damage will be analyzed. For that purpose, a series of sputter craters with different cluster sizes has been made.

In the XPS instrument there are three predefined cluster sizes available: Ar_{1000}, Ar_{2500} and Ar_{4200}. To cover a wider range of cluster sizes, the sputtering has been performed in the ToF-SIMS instrument. Ar_{1000}, Ar_{2500}, Ar_{5000} and Ar_{7500} clusters were used. All clusters had an energy of 5 keV. The craters have been created by sputtering 5 frames of 500 µm by 500 µm in size. No analysis beam was used in the ToF-SIMS instrument to ensure only argon cluster sputtering. Table 3 gives a summary of the sputter parameters.

Table 3 Summary of the different sputter parameters that were used for creation of sputter craters with different argon cluster size and energy per atom.

Cluster	Cluster energy	Energy per Atom	Raster size	Sputter time
Ar_{1000}	5 keV	5 eV	500 x 500 µm	5 frames (7.3 s)
Ar_{2500}	5 keV	2 eV	500 x 500 µm	5 frames (7.3 s)
Ar_{5000}	5 keV	1 eV	500 x 500 µm	5 frames (7.3 s)
Ar_{7500}	5 keV	0.66 eV	500 x 500 µm	5 frames (7.3 s)

The ToF-SIMS instrument is connected to a glove box under nitrogen environment. After the creation of the sputter craters, the samples have been taken out of the analysis chamber and transferred into a leak-proof transfer vessel under nitrogen environment to protect the organic material from humidity, oxygen and adventitious carbon contamination. The transfer vessel fits on the transfer chamber of the XPS instrument.

For this study, Alq_3 single layers have been examined.

2.2.2. Results

The C 1s, O 1s, N 1s and Al 2p core level spectra are shown in Figure 30.

The differences between the spectra in the different sputter craters are very small in terms of shape and intensity. In the C 1s spectrum, a slight increase in intensity can be observed for the spectrum that was

taken in the crater that was sputtered with Ar_{1000} clusters. The broad shape of the C 1s peak corresponds well to other spectra that can be found in literature [149]. A fit for the C 1s peak of the reference sample can be found in the appendix.

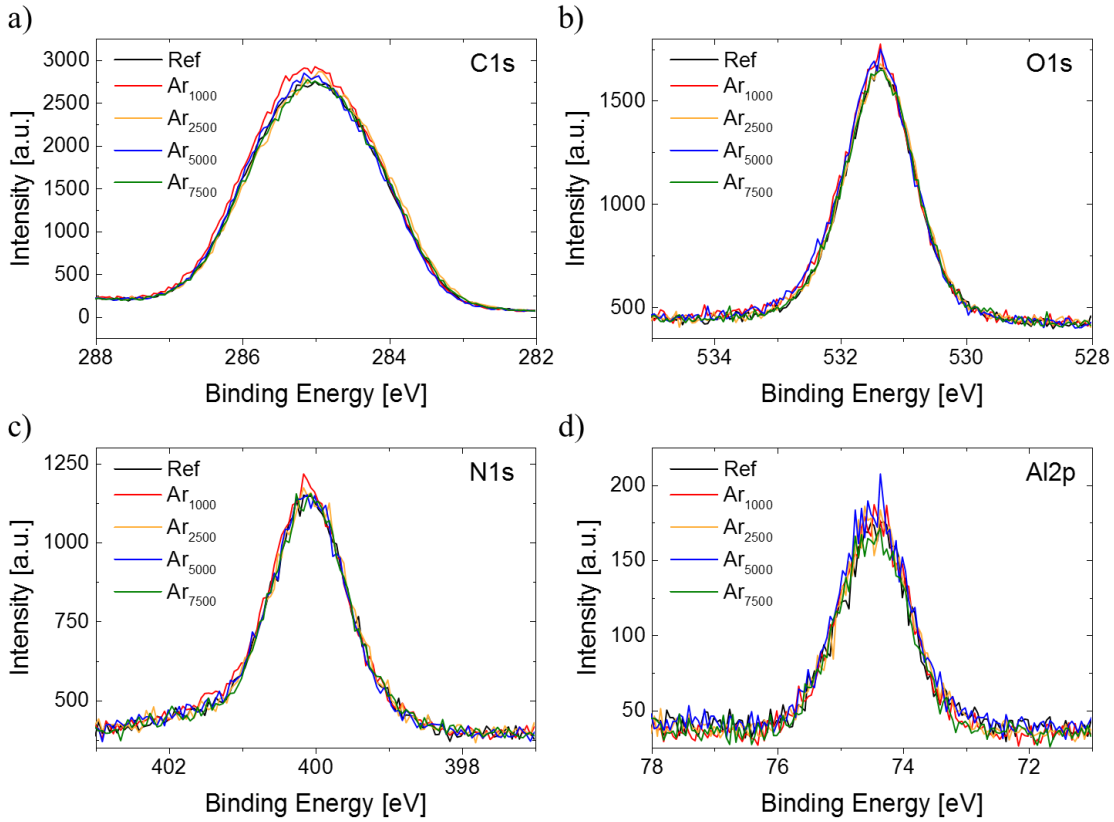

Figure 30 *XPS a) C 1s, b) O 1s, c) N 1s and d) Al 2p core level spectra of Alq_3. Reference spectra are shown in black. Spectra that were taken in the sputter crater after 5 keV Ar_{1000}, Ar_{2500}, Ar_{5000} and Ar_{7500} sputtering are shown in red, orange, blue and green, respectively.*

These results indicate very low induced damage overall. To get a better image of the damage by clusters, it is therefore useful to also check the valence band region for differences.

Figure 31 shows the valence band spectra from the craters that have been created by the clusters with different sizes. The differences in the spectra are again very small, but for the smallest sizes of 1000 and 2500 atoms per cluster, an increase of the peaks at binding energies of 3, 15, 20 and 25eV can be observed. Bigger clusters seem to preserve the electronic and molecular structure perfectly. This confirms the results that have been published by Seah et al. before [126]. Again, all features in the valence band exhibit a dominant contribution of carbon, but the feature at a binding energy of about 3 and 6 eV has also contributions from the chelated oxygen atom [149]. Also the peak at 25 eV has a contribution of the oxygen atom [151]. This might be an indication for changed electronic states of the oxygen atom. The peaks at 15 and 20 eV are completely dominated by carbon contributions. The aluminum atom makes no contributions to the valence band and can therefore not be used to describe the electronic changes that the molecule undergoes during cluster bombardment.

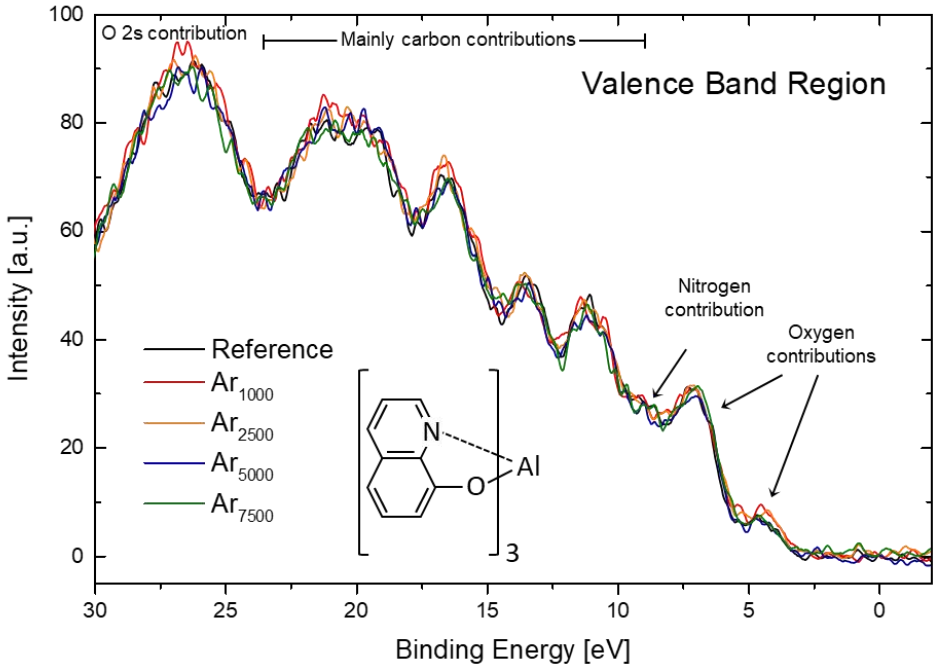

Figure 31 *XPS Valence band region of Alq_3. Reference spectrum is shown in black. Spectra that were taken in the sputter crater after 5 keV Ar_{1000}, Ar_{2500}, Ar_{5000} and Ar_{7500} sputtering are shown in red, orange, blue and green, respectively.*

As can be seen from Table 3, there is not only the cluster size, that differs, but also the energy per atom in the cluster. For the smallest cluster (Ar_{1000}) with an energy of 5 keV, the energy per atom *E/n* is 5 eV and for the biggest cluster (Ar_{7500}) it is only 0.66 eV. In the literature, it has been stated that this energy per atom and the cluster size need to be treated as two different parameters even though they are somewhat connected [126].

Unfortunately, the impact of clusters with the same size but with different primary energies could not be studied during this thesis. The instruments allow generally the use of energies of 5, 10, 15 and 20 keV for all different cluster sizes that were shown in section 2.2, but the sputter yield for any kind of cluster at 10 keV or above was really high. The only 50 nm thick single layers were sputtered within seconds. No series of sputter craters for different energies per atom with the same cluster size could be acquired.

The damaging of organic materials by clusters with different energy per atom *E/n* will therefore be discussed on an example from literature for reasons of completeness.

Fleischmann *et al.* studied different PCDTBT:PCBM blends by ToF-SIMS [128]. For their study, they varied both the cluster energy as well as the cluster size.

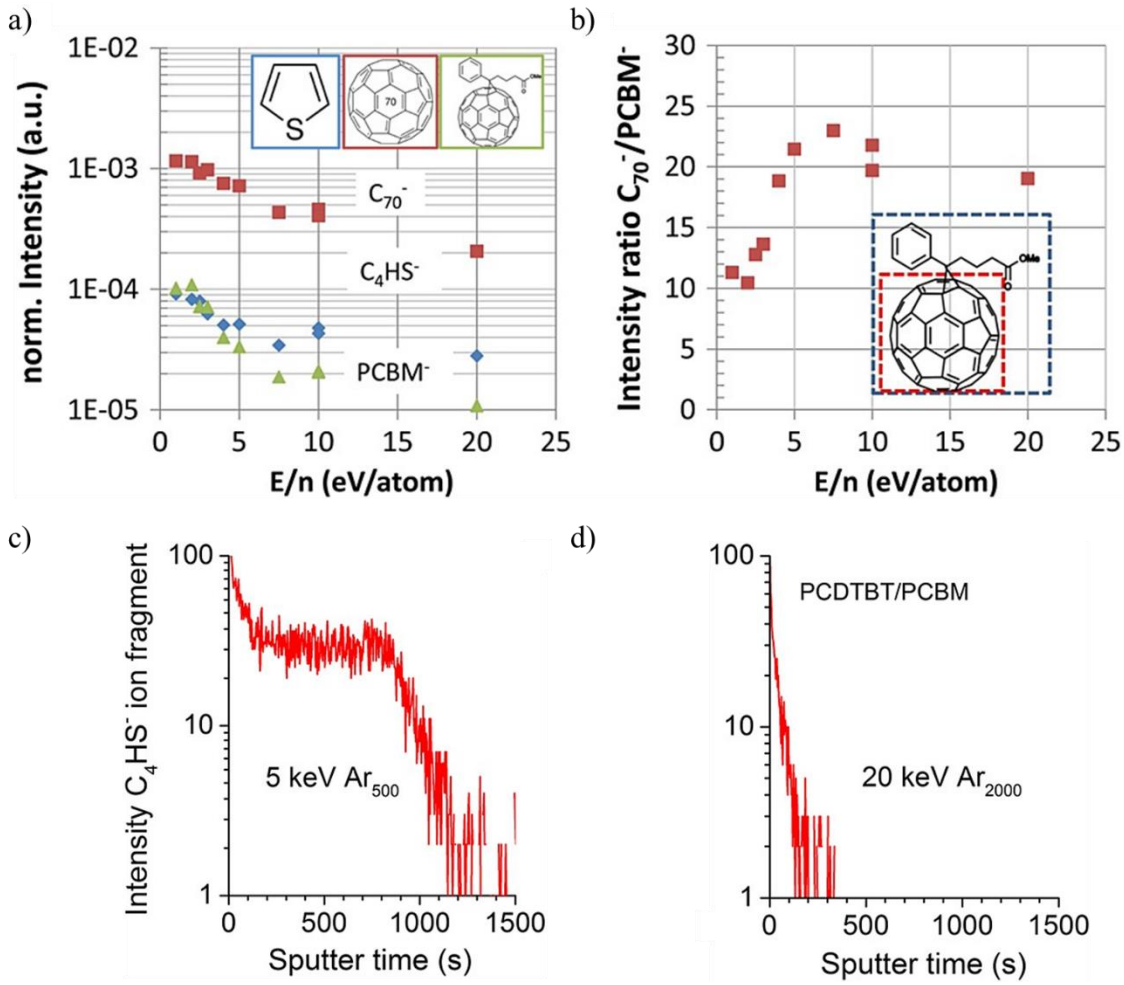

Figure 32 *a) Change of the C_4HS (blue), C_{70} (red) and PCBM (green) normalized secondary ion intensities as a function of the average Ar_n^+ energy/atom acquired on a PCDTBT:PCBM (1:4) blend. The variation of E/n was achieved by varying both the energy (E=5, 10, 15, and 20 keV) and the cluster size (n=500, 2000, 5000). b) Steady-state ion intensity ratio of the C_{70} to PCBM. c) Depth profiles recorded with 10 eV/atom on the PCDTBT:PCBM blend for Ar_{500} and d) Ar_{2000} clusters* [128].

Figure 32 a) shows the normalized secondary ion intensities for characteristic fragments of the polymer PCDTBT (C_4HS^-) and the molecule PCBM (C_{70}^- and $PC_{70}BM^-$ ($C_{82}H_{14}O_2$)) as a function of the energy per atom of the argon sputter clusters.

The variation in energy per cluster was achieved by varying the cluster size (n = 500, 2000, 5000) and the energy of the cluster (E = 5, 10, 15, 20 keV). The data points in the graph were acquired by sputtering with different combination of these parameters. A general trend of reduced fragmentation can be observed for low E/n values. The molecular signal of PCBM increases by one order of magnitude when the energy per atom is reduced from 20 to 1 eV. The reduced fragmentation is demonstrated clearly in Figure 32 b) where the ratio of the secondary ion intensities for C_{70}^- and $PCBM^-$ is shown as a function of the energy per atom of the sputter beam. For E/n values under 5 eV, the fragmentation ratio decreases heavily. These findings are consistent with the results from Figure 31.

These results show again the simultaneous variation of cluster size end energy per atom. But the consistent trend of reduced fragmentation for different combinations of energy and cluster size indicates, that only the E/n ratio is important for fragmentation. However, to clarify the impact of the cluster size on the measurement, they included depth profiles of the PCDTBT:PCBM blend with 5 keV Ar_{500} clusters and 20 keV Ar_{2000} cluster, which are shown in Figure 32 c) and d), respectively. For both depth profiles, the energy per atom is 10 eV. The larger clusters have a significantly higher sputter yield and the profile degrades instantly.

2.2.3. Summary

In conclusion, the values for the energy per atom should be kept under 5 eV to minimize fragmentation and surface damage. Preferably around 1 eV/atom, where the intensities in Figure 32 a) seem to reach a steady state. Also, the removal of the damage, that is induced by the analysis beam, is one of the main tasks for the sputter beam. It is therefore important that the sputter rate is high enough to sputter away all of the damaged zone.

3. Impact of the analysis beam on organic materials

Contrary to the sputter beam, ToF-SIMS and XPS use different analysis beams.

The ToF-SIMS primary ion beam can be compared to the sputter beam that has been examined in the previous section. However, the primary ion beams that were used in this thesis are monoatomic species or very small clusters (up to 5 atoms per cluster). The energy of these primary ions is significantly elevated compared to the rather low energy sputter clusters. Energies between 15 and 60 keV can be used.

The X-ray source that was used in this thesis provides no particular adjustment possibilities. The only possibility to reduce the induced damage by the beam is to reduce the exposure time or the power of the beam.

The impact of both beams on the damaging of organic materials during analysis will be discussed in this section.

3.1. ToF-SIMS Analysis Beam

3.1.1. Experimental setup

In this thesis, a bismuth liquid metal ion gun (LMIG) has been used as the primary ion gun. The gun can provide monoatomic Bi^+ ions or Bi_3^+ and Bi_5^+ clusters. Both clusters can also be doubly charged (Bi_3^{++} and Bi_5^{++}). The acceleration voltage can be chosen to be 15 or 30 keV. For the doubly charged primary ions, this results in a cluster energy of 30 or 60 keV.

The surface of a single layer sample of NPB has been analyzed to investigate the fragmentation by the different primary ion species. The instrument has been operated in the 2D imaging mode. Only the primary ion beam is scanned over the sample surface in this mode. This way, the influence of the sputter gun is removed from the measurement. The energy of all the primary ions was 30 keV.

3.1.2. Fragmentation analysis by ToF-SIMS

3.1.2.1. Results

The results of this analysis are shown in Figure 33. The molecular secondary ion signal of NPB was used as reference to normalize the intensity of the spectra (black squares). Two additional characteristic fragments have been chosen to illustrate the fragmentation of the molecule during analysis (C^+ and $C_{38}H_{27}N_2^+$).

The Bi_1^+ spectrum shows the highest fragmentation. The C^+ intensity is much higher than for any other primary ion in comparison to the molecular signal NPB^+. There is not much difference in the fragmentation of the other four species. The doubly charged ions Bi_3^{++} and Bi_5^{++} exhibit slightly lower fragmentation than their respective singly charged counterparts. However, there is another parameter that needs to be considered: the absolute intensity of the molecular signal. The uncorrected intensity of NPB^+ is depicted as empty blue squares in Figure 33. The intensity is rather low for Bi_1^+ because of the heavy fragmentation. The highest signal is observed for the Bi_3^+ and Bi_3^{++} species. For Bi_5^+ and Bi_5^{++}, the intensity is again more than one order of magnitude lower than for the Bi_3 species. This is mainly due to the fact that the primary ion current for the Bi_5 species is lower than the current of the other species. This is a known result of the cluster formation mechanism in LMIGs [154].

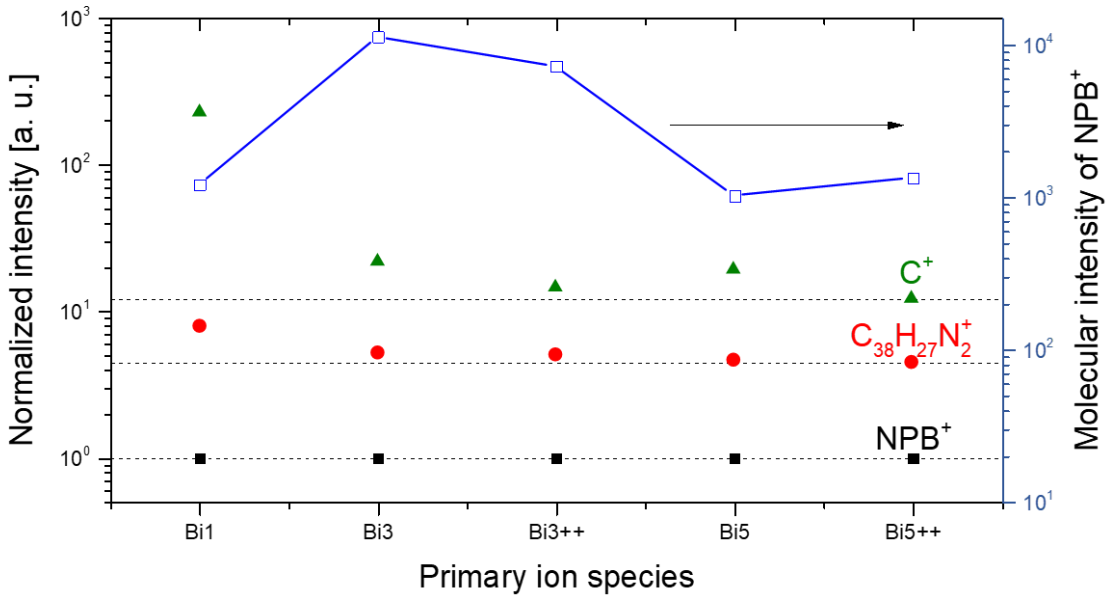

Figure 33 *Intensities of characteristic fragments of NPB that have been normalized to the molecular intensity of NPB^+ for ToF-SIMS mass spectra with different primary ion species at 30 keV. The overall intensity of the NPB^+ secondary ion is given by the empty blue squares.*

3.1.2.2. Summary

In consequence of these findings, Bi_3^{++} has been chosen to be used throughout this thesis as the primary ion species. It shows minimal fragmentation in combination with relatively high overall intensity. This is important to detect also small amounts of certain secondary ions throughout a depth profile.

3.1.3. Damage analysis by ToF-SIMS

3.1.3.1. Results

Next, depth profiles of Alq_3 single layer samples have been created to further investigate the damage induced by the primary ion beam. Three different sample areas have been exposed to different fluences of Bi_3^{++} bombardment. Afterwards, depth profiling in a dual beam setup with Ar_{5000}^{+} at 5 keV as the sputter beam has been performed on those areas and been compared to a reference depth profile.

The result can be found in Figure 34. The molecular signal of Alq_3 has been monitored until the silicon signal was reached which is indicated by the rise of the Si^+ signal. The reference profile and the profile for the smallest bismuth fluence show no significant differences. However, the initial signal decreases before it reaches a steady state. This is indicative for non-sufficient sputtering between each analysis step. The bismuth ions penetrate the sample too deep and damage underlying molecules. During the sputter step, not enough material is removed so that it comes to the accumulation of damage which finds a steady state after about 13 nm of the layer has been analyzed.

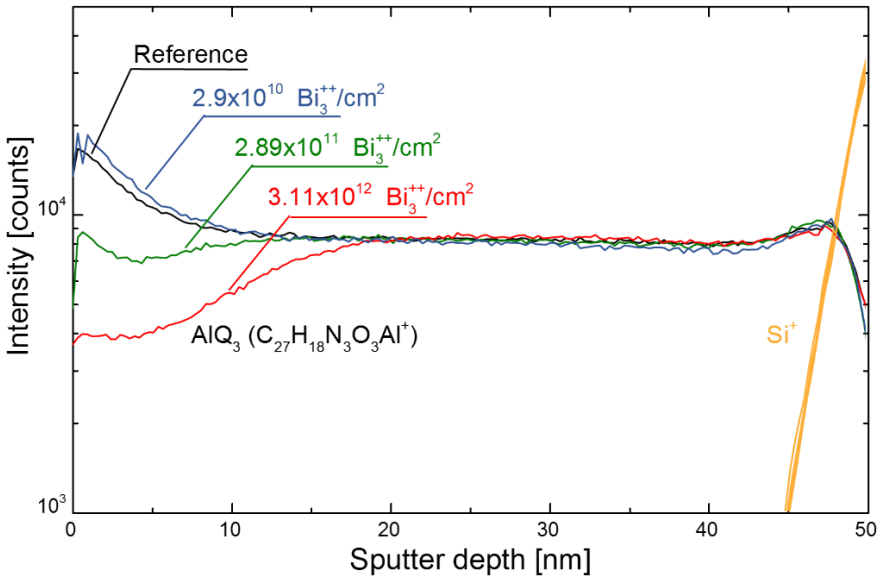

Figure 34 ToF-SIMS depth profiles of Alq_3 single layer samples that have been exposed to different Bi_3^{++} fluences prior to the analysis.

For higher initial bismuth exposure, it can be noticed that the surface has already been severely damaged. The initial intensity for the depth profiles is decreased.

The highest fluence of 3.11 x 10^{12} ions/cm^2 has caused the heaviest damage to the surface. The initial damage is higher than the accumulated damage that is represented by the steady state that is reached deeper into the profile. The non-damaging character of the argon cluster sputtering helps to regain some of the molecular signal.

3.1.3.2. Summary

Excessive bismuth bombardment leads to heavily damaged layers. Even at low fluences, the bismuth will penetrate far into the sample and damage the molecules. The argon cluster sputtering can help to remove this damage, but the ratio of the sputter dose to the analysis dose needs to be adjusted. Otherwise, damage will accumulate during depth profiling until it reaches a steady state.

3.1.4. Modifying of the analysis current with respect to the sputter current

3.1.4.1. Results

The depth profiles up to Figure 34 have all been acquired with standard parameters of 25 ns primary ion pulses which is a setting that is proposed by the instrument manufacturer. These parameters are used for high mass resolution which is necessary to analyze organic multilayer stacks. Figure 35 shows again ToF-SIMS depth profiles of Alq_3 single layers but this time with different bismuth pulse widths to decrease the primary ion current and therefore the fluence that is applied to the surface at each analysis step. The data is normalized to the maximum intensity. Table 4 summarizes the different parameters that were used for the analysis beam.

Table 4 Summary of the analysis parameters that were used for the creation of depth profiles with different bismuth doses for the analysis beam.

Species	Energy	Pulse width	Dose per analysis step	Current	Sputter dose / analysis dose
Bi_3^{++}	30 keV	1 ns	7,93 x 10^8 cm^{-2}	0.22 pA	2257.25
Bi_3^{++}	30 keV	5 ns	1,97 x 10^9 cm^{-2}	0.57 pA	918.78
Bi_3^{++}	30 keV	12 ns	3,55 x 10^9 cm^{-2}	1.02 pA	509.56
Bi_3^{++}	30 keV	25 ns	5,93 x 10^9 cm^{-2}	1.72 pA	306.30

The 5 keV Ar_{5000} sputter beam current has been kept constant at 0.5 nA during all measurements. For decreasing pulse width of the analysis beam, the ratio between the sputter dose and the analysis dose increases.

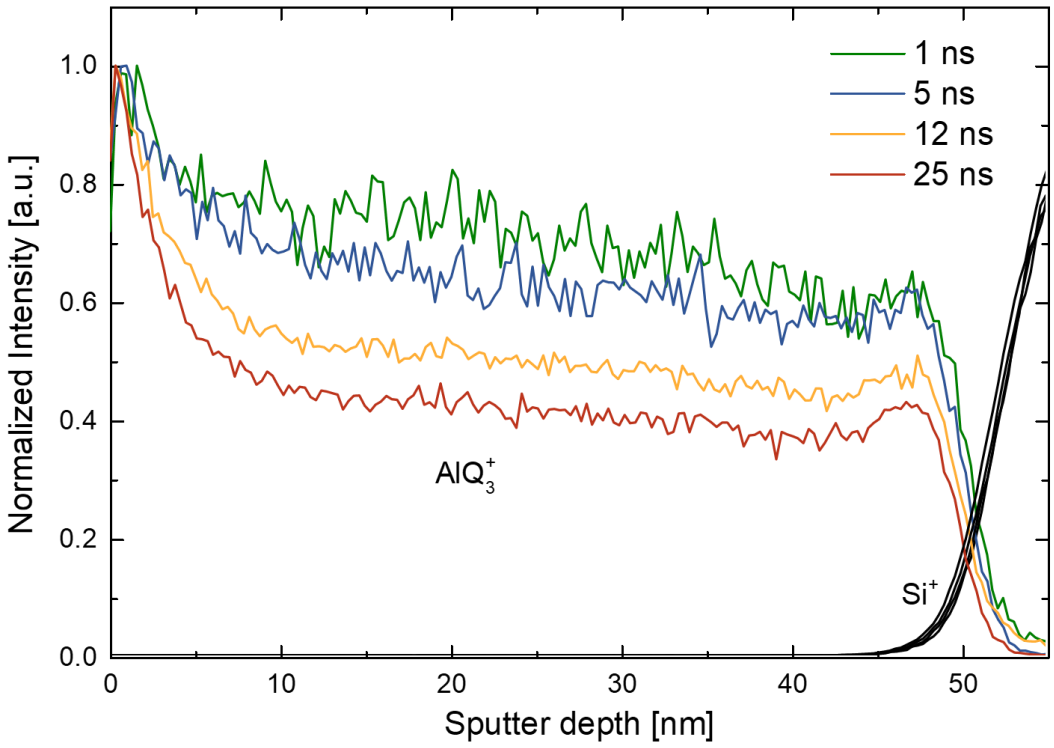

Figure 35 *Normalized ToF-SIMS depth profiles on Alq_3 single layers with different primary ion pulse widths between 1 and 25 ns.*

As explained earlier, there is a drop of initial intensity that indicates damage accumulation due to the bismuth bombardment. From the normalized spectrum for the standard parameters in red, it can be deducted that this drop of intensity is quite heavy. The intensity decreases to less than 50 % of its initial value before it reaches a steady state. But as the pulse width is decreased, the intensity loss decreases as well. The improvement from the 12 and 25 ns profiles to the 1 and 5 ns profiles is significant. From Table 4 it can be seen that the ratio of the sputter dose to the analysis dose increases to values over 900 for the 1 and 5 ns profiles.

However, it must be noted, that the variation of the signal becomes bigger for shorter pulses. This is due to the fact that the absolute intensity decreases because the primary ion current is lower. As for the choice of the primary ion species, a choice between the lowest fragmentation and sufficient secondary ion intensities has to be made. The signal of some secondary ions is more intense than others, but overall, pulses with a length of 5 ns seem to be a good compromise between both parameters.

Yet, even for these short pulses, a loss of about 20 to 30 % of the initial signal is observed in Figure 35. To prevent this accumulation of damage, it is necessary to further increase the ratio between sputter dose and analysis dose. Figure 36 shows two spectra that have been acquired using different sputter times. The intensity of the Alq_3^+ secondary ion is high enough to use a pulse width of 1 ns for the primary ion gun. For the red profile that was taken with only one frame of sputtering in between the analysis steps, a small accumulation of damage can be observed. The signal loses intensity towards the end of the profile.

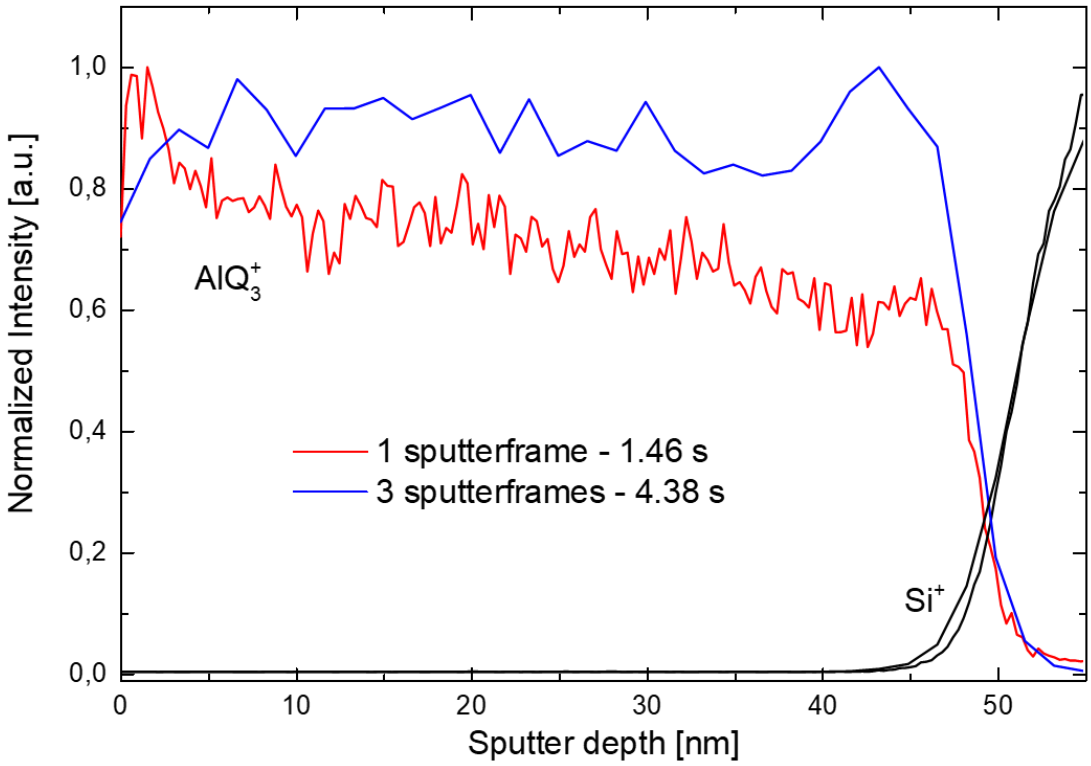

Figure 36 *ToF-SIMS depth profiles of an Alq_3 layer with a 1 ns primary ion pulse and different sputter times in between each analysis step.*

The blue curve on the other hand was acquired by sputtering three times longer during each cycle (3 sputter frames instead of 1), tripling the sputter dose – analysis dose – ratio to a value of about 6700. This results in a steady profile from the beginning to the end of the measurement. A drawback of the longer sputter time is a deterioration of the depth resolution. For three sputter frames, about 30 data points are collected throughout the whole organic layer. For a layer thickness of 50 nm, this results in about 1.66 nm of organic material that is sputtered away between each analysis step. This depth resolution should be small enough for most applications, even with regard to modern multilayer devices where film thicknesses of only 5 nm can be found.

3.1.4.2. Summary

To diminish the damage accumulation through bismuth bombardment during ToF-SIMS depth profiling, it is necessary to optimize the ratio between the sputter dose and the analysis dose. Values over 500 – 600 yield in acceptable profiles. However, only with an increase to over 6000, stable profiles are obtained. Keeping in mind that the secondary ion signal decreases with decreasing primary ion current and the depth resolution suffers under high sputter currents, compromises have to be made. An analysis pulse width of 5 ns with a sputter fluence of 3.6 x 10^{12} ions per sputter step results in a dose ratio of about 2500 – 3000 which should provide sufficiently high secondary ion yields and depth resolution.

3.1.5. Damage analysis by XPS

3.1.5.1. Results

The accumulation of damage during the ToF-SIMS depth profiles indicate clearly the damaging of the molecules by bismuth ion bombardment, even at low fluences. However, no significant differences between the reference measurement and the measurement with the smallest initial bismuth fluence were found (Figure 34).

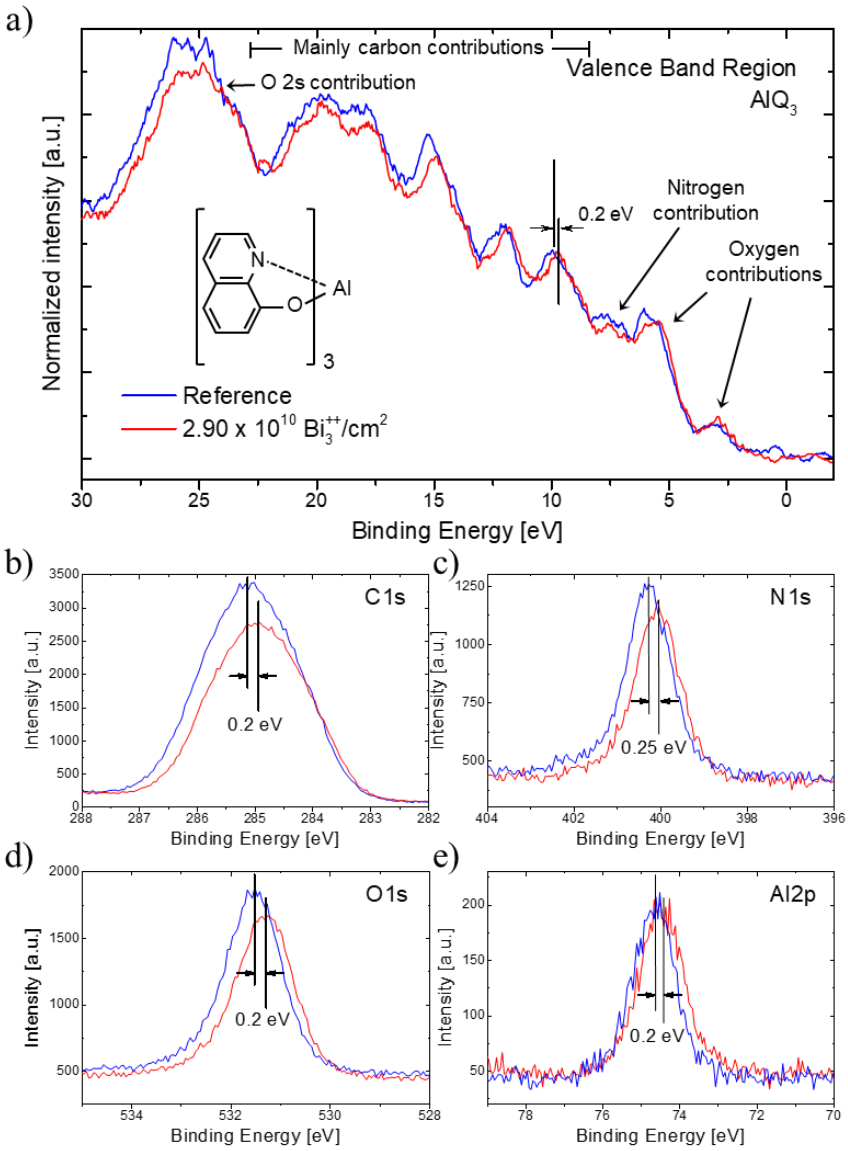

Figure 37 *XPS valence band spectra and C 1s, N 1s, O 1s and Al 2p core level spectra for an Alq_3 single layer reference sample (blue) and an Alq_3 sample that has been irradiated with a small fluence of bismuth of 2.9 x 10^{10} ions/cm^2 (red).*

To further investigate the damaging character of the bismuth bombarding, XPS measurements were performed on the Alq_3 single layer sample that has been bombarded with 2.9 x 10^{10} B_3^{++} ions per cm^2. A modification of the sample surface can be observed when the concerned area is analyzed by XPS. The XPS core level spectra and the valence band area are shown in Figure 37. Overall, a shift of the spectrum

by about 0.2 eV to lower binding energies can be observed. This shift is the same for all core and valence peaks, which may be indicative of an electronic change at the sample surface, possibly caused by negative charging of the surface. However, it could also indicate p-doping of the material. The shift of the valence band to lower binding energies means that the Fermi level moves closer to the valence band maximum within the band gap. This can be caused by doping of the material. The deposition of bismuth ions at the sample surface might be the source of this doping.

The shape of the valence band does slighty change with the bismuth bombardment. The chemistry seems to be altered at those low bismuth fluences, which is inconsistent with the ToF-SIMS data in Figure 34. In the oxygen contribution at about 6 eV as well as in the carbon contribution around 12 eV, a change can be observed. As far as the core level spectra are concerned, the intensities of the C 1s, N 1s and O 1s core levels are diminished while the Al 2p remains stable. This might indicate a relative accumulation of aluminum at the sample surface.

The quantification results in Table 5 show only a small increase of the aluminum content. The other concentrations remain within the margin of error. This confirms the assumption, that the small bismuth fluence does not affect the molecules significantly.

Table 5 Overview for the XPS quantification of the Alq_3 single layer reference sample and the sample that was bombarded with 2.9 x 10^{10} Bi_3^{++} ions/cm^2.

Element	**Bonding State**	**Position**		**At%**	
		Reference	**Bi exposed**	**Reference**	**Bi exposed**
C		**285**	**284.84**	**79.67**	**79.18**
	C-H	285	284.84	42.59	41.78
	C-X	285.77	285.66	25.28	24.85
	C-C	284.24	284.14	11.80	12.55
N		**400.02**	**399.89**	**7.76**	**8.05**
	N-Al	400.02	399.89	7.36	7.69
	N defect	401.91	401.83	0.40	0.35
O		**531.31**	**531.22**	**8.11**	**8.03**
	O-Al	531.31	531.22	7.86	7.72
	O defect	532.75	532.64	0.25	0.31
Al		**74.38**	**74.28**	**4.45**	**4.74**

3.1.5.2. Summary

The XPS measurements show that even though there is no evidence for damaged molecules in the ToF-SIMS depth profiles or the XPS spectra, there is an electronic modification of the surface by the bismuth bombardment. This illustrates perfectly the usefulness of combining ToF-SIMS and XPS for a combined analysis. Electrical modification at the sample surface can cause changing ionization potentials during ToF-SIMS analysis which would modify the results. A chemical change of the sample surface cannot be observed for bismuth bombardment.

3.2. X-Ray Beam

3.2.1. Experimental setup

To evaluate the damage that is induced by the X-ray beam during the XPS analysis, multiple XPS measurements at the same sample spot have been acquired.

3.2.2. Results

Figure 38 shows the comparison of the reference spectrum with a spectrum that has been taken after the sample has already been measured twice at the same spot. This simulates an excessive exposure of X-rays to the sample. The sample has been exposed for 220 min to the X-rays.

The X-rays have a different effect on sample degradation than the ion bombardment by clusters or primary ions. Only the core level peaks of C 1s, N 1s, O 1s and Al 2p are shifted by different values. However, there is no shift in the valence band region. The carbon peak and the oxygen peak shift quite heavily by about 0.6 eV and 0.5 eV towards higher binding energies while the nitrogen peak shifts by only 0.35 eV. The aluminum peak shifts about 0.1 eV towards higher binding energies, nearly at the sensitivity limit. These shifts indicate a change of oxidation states for the different elements. The large shift of the carbon peak compared to the other elements indicates a larger charge transfer from the carbon atoms towards the other elements.

The spectrum of the valence band region exhibits overall decreased intensity in the X-ray exposed spectrum. However, two distinct differences can be identified. The peak at 7.5 eV has almost completely disappeared. Previous studies have associated this peak mainly with the coordinated nitrogen atom in the molecule [149]. Also the shoulder peak at 23 eV on the right side of the broad peak at 25 eV has contributions from the nitrogen atom [151]. This might indicate some modification of the nitrogen bonds in the molecule. This could be the source of the shifted core levels.

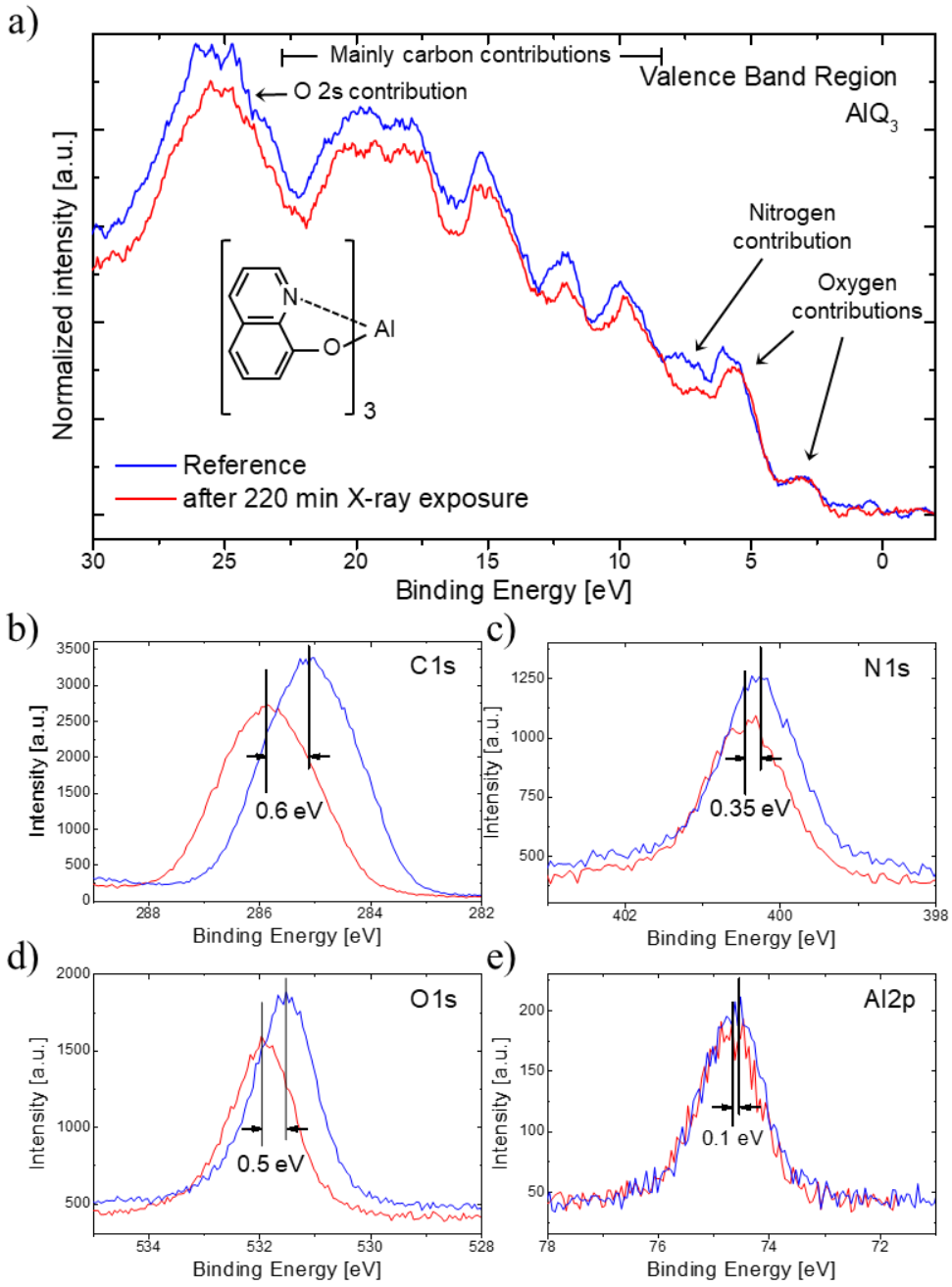

Figure 38 XPS valence band spectra and C 1s, N 1s, O 1s and Al 2p core level spectra for an Alq_3 single layer reference sample (blue) and an Alq_3 sample that has been measured three times at the same spot (red).

The quantification results that are summarized in Table 6 suggest again only small changes in the composition. The most prominent changes are the increase of the defect structures for nitrogen and oxygen that have previously been reported in literature [149] and the changes in the contributions to the C 1s peak. A slight increase of the C-C contribution to the C 1s peak might confirm the change of the chemistry in the molecule due to a charge transfer of the carbon electrons.

Table 6 Overview for the XPS quantification of the Alq_3 single layer reference sample and the sample that was exposed to X-rays for 220 min.

Element	Bonding State	Position		At%	
		Reference	**X-ray exposed**	**Reference**	**X-ray exposed**
C		**285**	**285.61**	**79.67**	**79.53**
	C-H	285	285.61	42.59	42.93
	C-X	285.77	286.38	25.28	24.21
	C-C	284.24	284.86	11.80	12.39
N		**400.02**	**400.37**	**7.76**	**7.59**
	N-Al	400.02	400.37	7.36	7.10
	N defect	401.91	402.19	0.40	0.49
O		**531.31**	**531.84**	**8.11**	**7.99**
	O-Al	531.31	531.84	7.86	7.45
	O defect	532.75	533.28	0.25	0.54
Al		**74.38**	**74.49**	**4.45**	**4.88**

Splitting of the q ligands from the molecule might be a source for the changes in the XPS spectra. This reaction has already been identified to be a possible degradation pathway for Alq_3 in combination with water from the environment or other impurities [56]. The X-rays could provide the necessary activation energy for the reaction to take place. However, in that case the aluminum oxidation states would change as well, but no significant shift or modification of the peak shape is observed for the Al 2p core level.

3.2.3. Summary

The X-ray beam modifies the chemistry of the Alq_3 molecule. This is confirmed by the valence band spectra as well as the core level spectra. Peak shifts and changes in concentrations might indicate ligand separation in the layer.

As already mentioned, there are not much modification possibilities for the analysis beam in XPS measurements. Mainly the time of X-ray exposure is important and should be minimized to prevent this kind of damage. It has been shown that the damage increases faster with increasing power of the X-rays [155]. However, no study on the change of X-ray power has been performed in the course of this thesis. The Al Kα source has always been used with a power of 25 W for a beam diameter of 100 µm unless stated otherwise. Lower power results in lower intensities which is undesired for the acquisition of valence band spectra.

Conclusion

Reference spectra are indispensable for the chemical characterization of the complex samples that are found in organic electronics. Single layer samples provide easy access to each material to acquire reference spectra in ToF-SIMS and XPS. The organic layers must however be handled carefully. Without encapsulation they are vulnerable to environmental impacts. To prevent degradation, they must be processed under nitrogen environment.

By depth profiling of single layer samples, it has been shown that the fragmentation of organic molecules during depth profiling poses challenges for ToF-SIMS analysis. Specific molecules can only be identified with the help of reference spectra. A database for all utilized materials has therefore been created.

For XPS measurements, a similar database has been created. Often, the different materials can be distinguished by the detection of different elemental core levels. However, the usefulness of valence band spectra as fingerprints for each molecule has been demonstrated. Throughout this thesis, it was found that in high-resolution depth profiles of organic multilayers, the molecules are damaged by the X-rays during the depth profiling, making it difficult to use high resolution core level spectra as markers for the different materials. A solution might be to only use the valence band as a marker. This would mean, that instead of about 8 high-resolution core levels, only one high resolution valence band would be taken, reducing the time of X-ray exposure immensely.

Based on these reference databases, the damaging by the sputter beam and the analysis beam during ToF-SIMS and XPS analysis has been investigated. The large argon clusters that are used for sputtering of organic materials have been shown to be very gentle. XPS measurements in sputter craters show no modification of the surface chemistry. The analysis beams however show damaging. The choice of the right analysis parameters is essential for the acquisition of precise molecular information. Generally, the fluence of the ToF-SIMS primary ions as well as the XPS X-rays should be minimized. Small fluences of the analysis beam come however with small intensities in the acquired spectra. Compromises have to be made for certain parameters.

The bismuth bombardment and the X-ray exposure show two different effects at the sample surface. XPS measurements revealed a doping of the sample whereas X-Rays seem to induce a modification of the chemistry by charge transfer.

With the analysis of the damage that is induced during the measurement, it was possible to define the acquisition parameters for both techniques that will be used throughout this thesis for the chemical depth profiling of OLEDs.

For sputtering, 5 keV Ar_{4500} clusters will be used at currents of 0.5 to 1 nA in the ToF-SIMS instrument. This cluster size was chosen to provide comparability with XPS depth profiles where the biggest cluster

that can be produced is Ar_{4200}. This cluster was used at 5 keV and 1 nA. These parameters ensure an energy per atom ratio of about 1.2 eV. This results in minimal damage.

Bi_3^{++} has been chosen as the analysis beam in ToF-SIMS. At 30 keV and with a pulse width of 5 ns, it provides a good compromise between low fragmentation and sufficient signal intensity.

The X-ray beam will be operated at a power of 25 W with a beam diameter of 100 µm.

Table 7 summarizes the ideal analysis parameters that have been determined in this chapter. These parameters will be used as standard parameters in the following chapters to analyze more complex samples.

Table 7 Summary of the ideal XPS and ToF-SIMS analysis parameters that have been determined by the characterization of the organic single layer samples.

ToF-SIMS	**Species**	**Energy**	**Current**	**Raster size**
Analysis	Bi_3^{++}	30 keV	0.2 pA	300 x 300 µm
Sputter	Ar_{5000}	5 keV	0.5 nA	500 x 500 µm

XPS	**Source**	**Energy**	**Power**	**Diameter**
X-Rays	Al Kα	1486.6 eV	25 W	100 µm
	Pass energy	**Energy step**	**Energy resolution**	**Elements**
Core-level analysis	23.5 eV	0.05 eV	0.67 eV	C 1s, N 1s, Al 2p, Ca 2p, F 1s, Ir 4f, Ti 2p
Valence band analysis	46.95 eV	0.05 eV	0.84 eV	-2 eV to 30 eV

Chapter IV:

Analysis of critical interfaces in organic and hybrid bilayer structures

1. Studied systems and materials

1.1. Sample Structure

Figure 39 shows the schematic representation of the bilayer structures that are analyzed in this chapter. Two different materials have been deposited onto a silicon or ITO substrate.

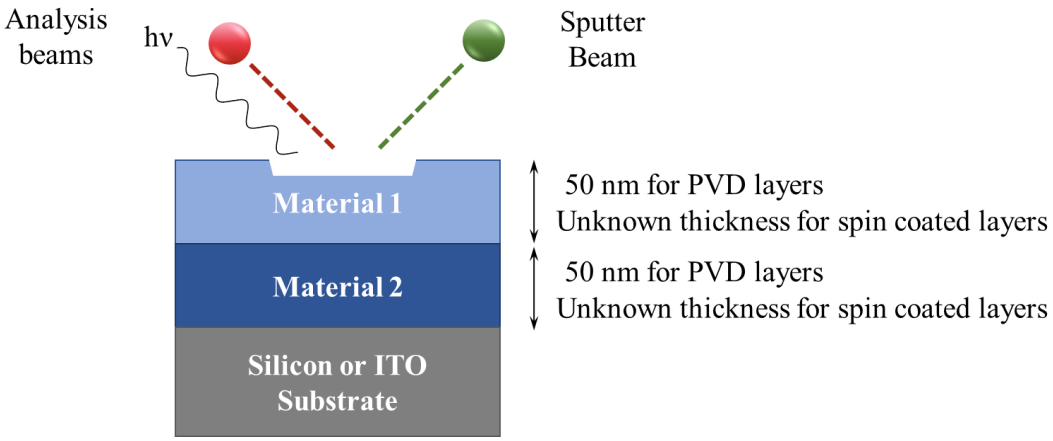

Figure 39 Schematic representation of the studied bilayer sample structure. Two 50 nm thick organic layers were deposited on silicon substrates by physical vapor deposition (PVD). Solution processed layers were spin coated with an unknown thickness onto ITO substrates.

These bilayer samples have been fabricated to get an easy access to certain interfaces of OLED devices. Again, in the case of purely organic bilayers, the organic materials have not been encapsulated. The samples have therefore to be handled in a protected environment to prevent degradation through humidity or oxygen.

The thickness of both layers is 50 nm. In the OLED stack, they will be much thinner (between 5 and 35 nm). With the increase of the layer thickness, it is easier to study the system. XPS spectra at the surface will only provide information on the top layer without contribution from the underlying layers. There will also be enough time during the sputtering to reach a steady state before reaching the interface. Finally, the second layer is sufficiently thick to prevent unwanted effects in the depth profile due to the underlying inorganic substrate like increased intensities at the interface.

Solution processed bilayers have been investigated in a collaboration with Yolande Murat at the IMS Bordeaux. Theses layers have been deposited by spin coating onto ITO or ZnO substrates. Reference samples have been produced by spin coating one material after the other. However, a solution containing both materials has also been produced. During spin coating, there should be a phase separation of both materials. This has been verified by ToF-SIMS measurements. These samples will be discussed in section 4.

1.2. Choice of Materials

The materials considered in this chapter are the same that were presented in chapter 3. Certain critical bilayer combinations are chosen to be studied in this chapter. Figure 40 a) shows the structure of the OLEDs with organic layers that are deposited by physical vapor deposition and the bilayer samples that have been produced for this device structure.

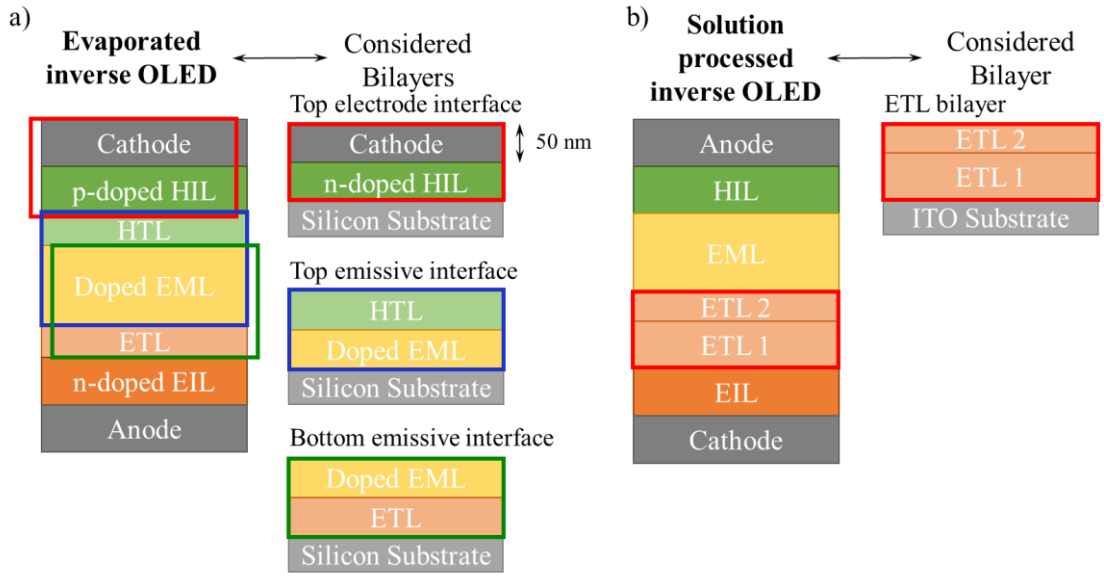

Figure 40 *a) Schematic representation of PVD processed OLEDs and bilayer structures of critical interfaces. b) Schematic representation of solution processed OLEDs and the bilayer structure with a two-part electron transport layer.*

Firstly, the inorganic-organic interface at the top of the device represents the most difficult part to depth profile. Generally, inorganic materials should be sputtered with monoatomic sources to avoid the slow sputter rates of cluster sputtering [156]. However, in chapter 3 it has been shown that cluster sputtering is necessary to preserve the molecular information in organic layers. A solution for a complete analysis of inorganic-organic interfaces without the loss of molecular information has not yet been found. Different approaches for the analysis of this bilayer sample have been investigated.

As far as purely organic bilayers in the evaporated OLED devices are concerned, the two interfaces around the emissive layer will be studied. The degradation of the emissive material results directly in a loss of luminance. The luminance will be the reference parameter during the electrical ageing of the complete devices in chapter 5. That is why the bilayers containing the emissive material are chosen for analysis. Degradation of other materials could result in poor performance through an increased driving voltage or higher current throughput sometimes without a loss in luminance. Degradation of those material would not necessarily be detected during the artificial ageing procedure that was used in this thesis.

In addition to these evaporated bilayer samples, one solution processed interface has been analyzed. In the solution processed OLED, there are two parts to the electron transport material (Figure 40 b)).

Between the emissive layer and the conventional PEIE transport layer, an ultrathin layer of TPBi is added. Usually, both materials are deposited separately. Here, the possibility of spin coating both materials at the same time from one solution has been investigated.

2.Organic-Organic bilayers

2.1. Top Interface around the Emissive Layer: NPB/TCTA:Ir(mppy)$_3$

2.1.1. Sample description

The first bilayer that was characterized was the interface between the NPB hole transport layer and the TCTA:Ir(mppy)$_3$ emissive layer. Figure 41 gives a schematic representation of the location of this interface in the OLED stack.

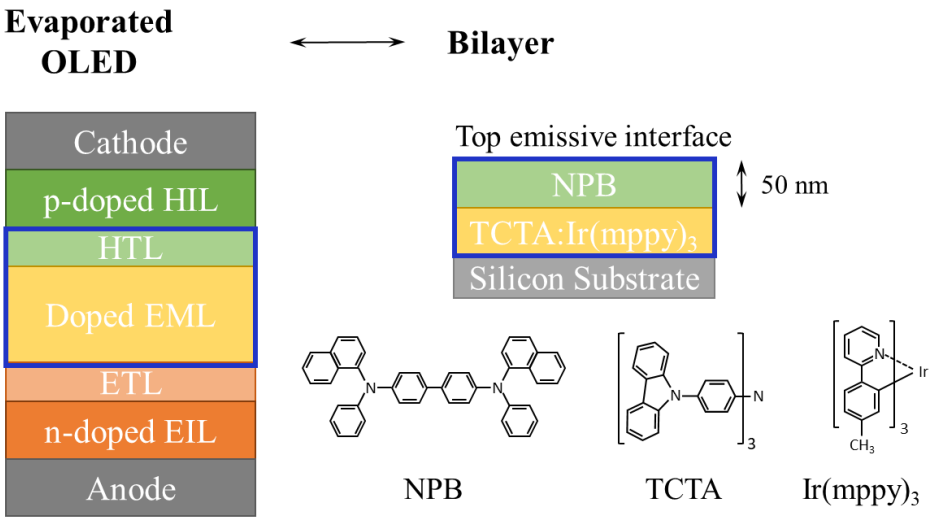

Figure 41 Schematic representation of the NPB/TCTA:Ir(mppy)$_3$ bilayer and the location of the interface inside the OLED stack.

Similar to the single layer samples, reference spectra of the bilayer samples have been acquired with the analysis parameters that have been determined in chapter 3.

2.1.2. ToF-SIMS depth profiling

Figure 42 a) shows the results of the ToF-SIMS depth profiling of this bilayer sample. It shows strong molecular signals and steady intensities for all three materials. Figure 42 b) – d), excerpts of the mass spectrum for the molecular masses of the three molecules are shown. In the depth profile, three regions of interest (ROI) have been created. The black one in the NPB layer, the green one in the TCTA:Ir(mppy)$_3$ layer and the red one at the interface. The black, green and red curves in the bottom graphs correspond to the mass spectra in those ROIs. Although a significant amount of the NPB molecular signal is visible in the TCTA:Ir(mppy)$_3$ layer in the logarithmic scale of the depth profile, the mass spectra show that the amount is negligible.

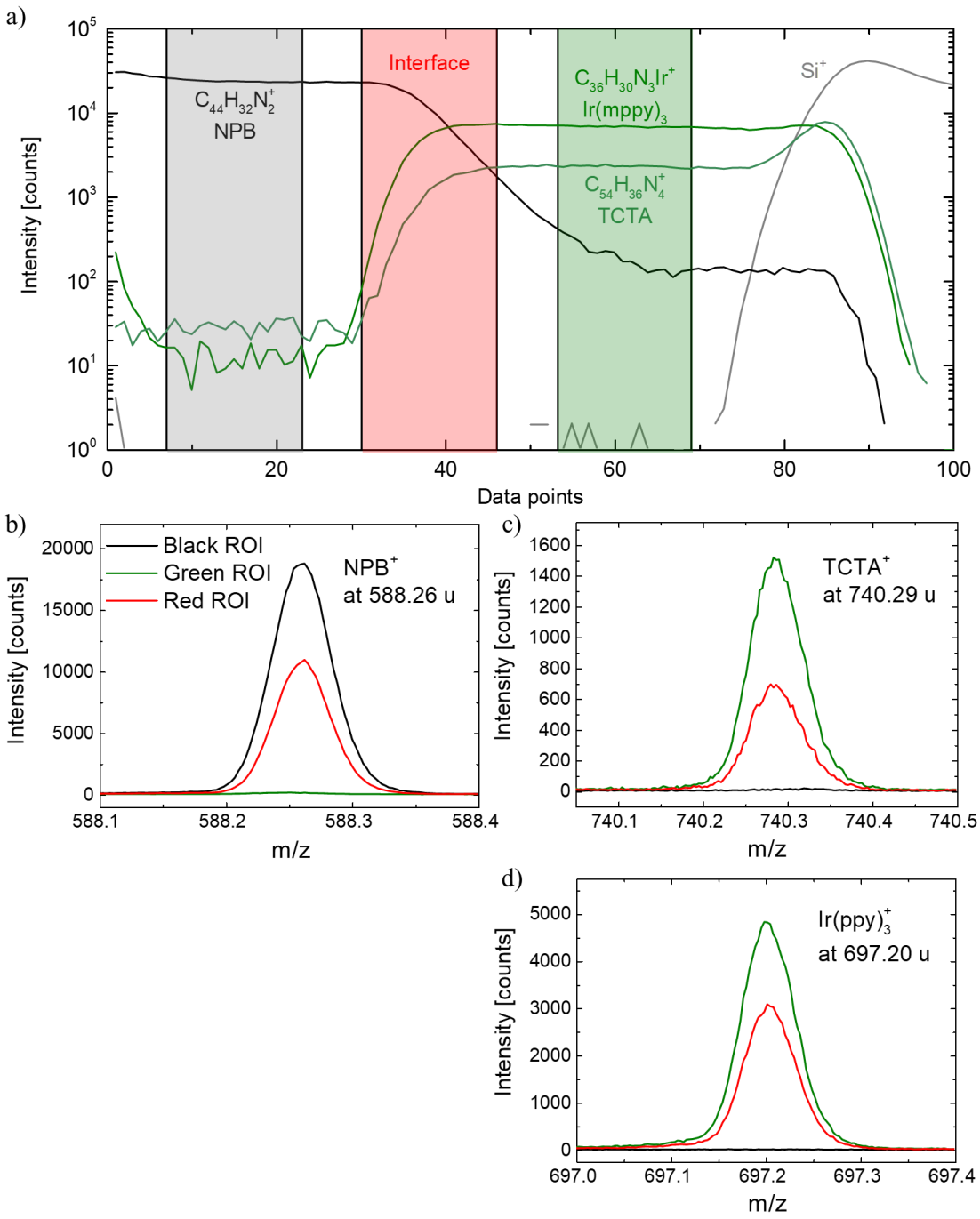

Figure 42 *a) ToF-SIMS depth profile of the NPB/TCTA:Ir(mppy)$_3$ bilayer sample. b)-d) Mass spectra at the molecular masses of the three different materials. The signals in three different regions of interest for the NPB layer (black), the interface (red) and the TCTA:Ir(mppy)$_3$ layer (green) are shown.*

By converting sputter time into relative depth, it is possible to estimate the interface width of the profile. Both layers are assumed to have a thickness of 50 nm. The middle of the interface can be defined at the point where the NPB$^+$ signal reaches 50 % of its intensity in the steady part of the NPB layer. This point will be set to a depth of 50 nm. With this depth calibration, the interface width can be calculated. The interface can be defined as the area between 84 % and 16 % of the steady state intensity [157]. For this profile, a width of about 11.4 nm can be calculated. The interface width is of the same order of magnitude (10.8 nm) when only one sputter frame in between each analysis step is used instead of two. These

values are large in comparison to the film thicknesses that the materials will have in the final device. The NPB layer will for example only have a thickness of 5 nm. This can pose problems in the depth profiling of complete devices. An interlaboratory study showed depth resolutions between 5 and 10 nm for argon cluster sputtering of organic materials [158]. The NPB/TCTA:$Ir(mppy)_3$ interface is with 11.4 nm within the range of those values.

The red curve in the mass spectra which represents the mass spectrum at the interface has half of the intensity of the black curve for the NPB^+ signal. However, the other two molecular signals show a small difference. The $Ir(mppy)_3^+$ signal seems to be relatively higher at the interface compared to the $TCTA^+$ signal. This might indicate that there is a slightly higher concentration of $Ir(mppy)_3$ at the interface than in the bulk of the layer. However, it could also be due to an increased ionization potential of $Ir(mppy)_3$ at the interface with NPB. Other characteristic fragments of both molecules that are not shown here exhibit the same trend.

Another trend that can be observed is the linear decrease of the $Ir(mppy)_3^+$ signal throughout the layer. On the logarithmic scale of the depth profile it is hard to see, but the signal decreases by about 10 % while the $TCTA^+$ signal stays steady.

2.1.3. XPS depth profiling

XPS depth profiles have also been acquired in addition to the ToF-SIMS profiles. The profile of the NPB/TCTA:$Ir(mppy)_3$ bilayer sample is shown in Figure 43 a). The depth profile has been generated using the area of high-resolution C 1s, N 1s and Ir 4f peaks. Moreover, valence band spectra have been recorded along the depth profile.

The atomic concentration of each element has been calculated for each data point. The rise of the nitrogen and iridium signals indicate the interface to the emissive layer. The calculated elemental composition corresponds well to the expected values. In the NPB layer, there is obviously no iridium expected nor detected. By using the chemical formula $C_{44}H_{32}N_2$ for NPB, a nitrogen concentration of 4.35 % is predicted which corresponds well to the measured value of 4.02 %. Both, the nitrogen and the iridium concentration increase throughout the interface until a sputter time of 36 s. The measured concentrations in the TCTA:$Ir(mppy)_3$ layer deviate more from the expected values but they lie within a reasonable range. For a dopant concentration of 12 % $Ir(mppy)_3$, an elemental composition of 92.8 % carbon, 6.9 % nitrogen and 0.2 % iridium should be observed. The measured concentrations are 94.1 % carbon, 5.6 % nitrogen and 0.3 % iridium. There is a slight depletion of nitrogen and an accumulation of iridium at this point. This could possibly be a confirmation of the enhanced dopant concentration of the $Ir(mppy)_3$ dopant at the interface as it was noticed in the ToF-SIMS measurements.

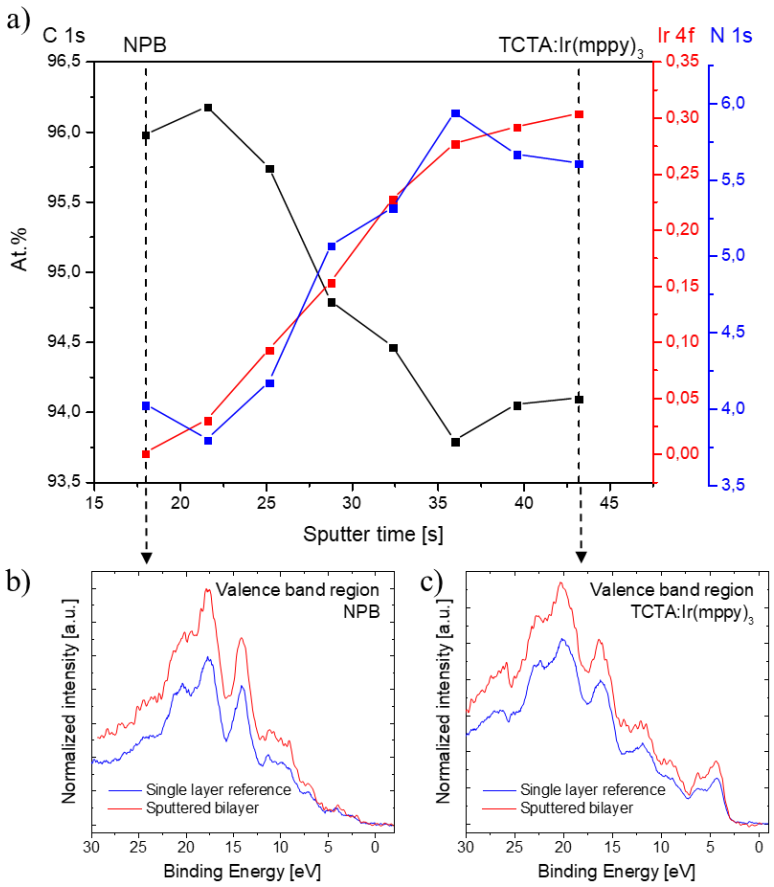

Figure 43 *a) XPS depth profile of the NPB/TCTA:Ir(mppy)$_3$ bilayer sample with the atomic concentrations of carbon, nitrogen and iridium. b) and c) Comparison of the valence band spectra of a reference sample and the bilayer sample after sputtering in the NPB and TCTA/Ir(mppy)$_3$ layers.*

Figure 43 b) and c) show the valence band region of the first data point and the last data point in the depth profile, respectively. The first data point lies in the NPB layer. The comparison of the valence band region from the depth profile in blue with the reference spectrum in red shows very good accordance. All features from the reference spectrum can also be identified in the sputtered bilayer sample. The intensity for some of the peaks changes, but the shape of the curve is preserved even after 18 s of sputtering.

The last data point lies in the TCTA:Ir(mppy)$_3$ layer. The comparison of the valence band region with the reference is shown in Figure 43 c). Again, all features of the reference spectrum are preserved, even after sputtering for 43 s and with the acquisition of several high resolution XPS spectra and therefore heavy X-ray exposure. This confirms once again the optimal analysis parameters. The depth profile was acquired with minimal induced damage by the analysis.

2.1.4. Summary

The ToF-SIMS as well as the XPS depth profiling show overall good results. The molecules do not seem to accumulate damage during the analysis. The valence band is preserved during the whole XPS analysis and the ToF-SIMS depth profiles show high and stable intensities for all molecular ions. However, the

interface width appears quite broad in the ToF-SIMS depth profile and the signal of the dopant in the emissive layer ($Ir(mppy)_3$) seems to appear earlier than the signal of the host material (TCTA). This might indicate slight diffusion of $Ir(mppy)_3$ towards the interface and even intermixing of this material with the hole transport layer. The increased iridium concentration that was measured with XPS at the interface strengthens this assumption.

2.2. Bottom Interface around the Emissive Layer: TCTA:$Ir(mppy)_3$/Alq_3

2.2.1. Experimental setup

The lower interface of the emissive layer was analyzed in the same way. This is the interface where the emissive TCTA:$Ir(mppy)_3$ layer meets the Alq_3 electron transport layer. Figure 44 shows the structure of the bilayer sample together with the location of the interface in the OLED stack.

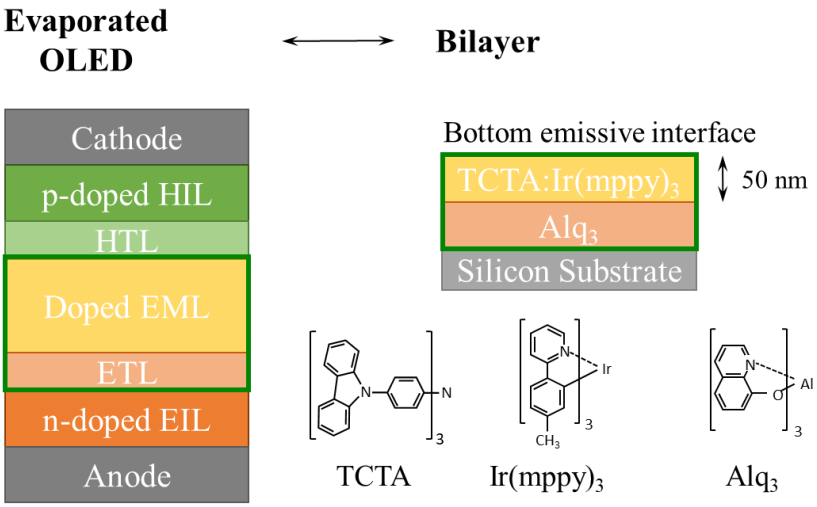

Figure 44 Schematic representation of the TCTA:$Ir(mppy)_3$/Alq_3 bilayer and the location of the interface inside the OLED stack.

2.2.2. ToF-SIMS depth profiling

Figure 45 shows the results of the ToF-SIMS depth profiling. The molecular signals are again very high. The intensities of $TCTA^+$ and $Ir(mppy)_3^+$ are steadier except for the initial intensity loss before the steady state is reached. The trend of decreasing $Ir(mppy)_3^+$ intensity that was observed in Figure 42 cannot be confirmed.

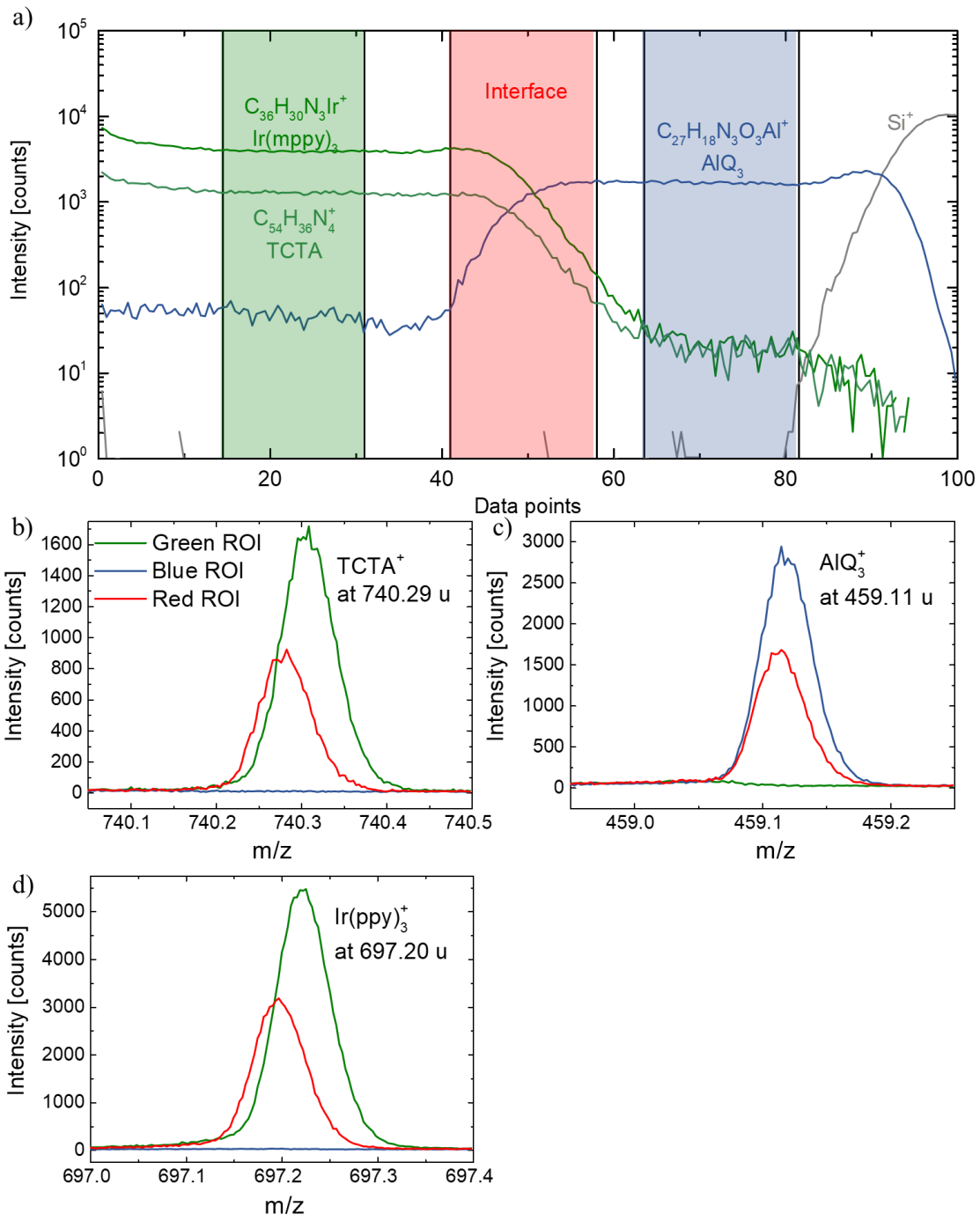

Figure 45 *ToF-SIMS depth profile of the TCTA:Ir(mppy)₃/Alq₃ bilayer sample (top). In the bottom graphs, the molecular signal of the three different materials is shown for regions of interest in the TCTA:Ir(mppy)₃ layer, at the interface and in the Alq₃ layer.*

The Alq_3^+ signal in the TCTA:$Ir(mppy)_3$ layer is again negligible as can be seen from the mass spectra for the different regions of interest at the bottom. The signal ratio between the interface ROI and the TCTA:$Ir(mppy)_3$ ROI for the $TCTA^+$ and $Ir(mppy)_3^+$ peaks is uniform. There is no diffusion of the $Ir(mppy)_3$ molecule towards the interface as it could be suspected at the NPB/TCTA:$Ir(mppy)_3$ interface in the previous section.

The calculated interface width is 8.2 nm which is smaller than the interface with NPB. However, the smaller interface width for this bilayer could be another confirmation of slight intermixing of the NPB and TCTA:Ir(mppy)$_3$ layers in the previous section, with a slightly higher concentration of Ir(mppy)$_3$ at that interface.

The depth profile shows overall steady signals with no particularities. However, at the interface there is one secondary ion signal that cannot be attributed to either material. It exists only in the interface ROI.

Figure 46 shows the mass spectra around a mass of 482 u for all three ROIs. A broad peak around 482 u can be seen for all three regions. However, at about 482.2 u, there is a relatively intense peak that only appears in the interface region. This peak does not appear in any of the reference spectra of either Alq$_3$ or TCTA:Ir(mppy)$_3$. It is only formed at the interface of both materials. It might be a combination of Alq$_3$ with mass 459.11 u and sodium with mass 22.99 u. The mass of this compound would be 482.1 u which corresponds well to the peak in Figure 46. Moreover, traces of sodium are found in the TCTA:Ir(mppy)$_3$ layer in the depth profiles of both bilayer samples as well as in the single layer reference spectrum of this material. The formation of complexes between Alq$_3$ and ions like sodium at the interface of the emissive layer could lead to the formation of deep charge traps which can deteriorate the device performance overall.

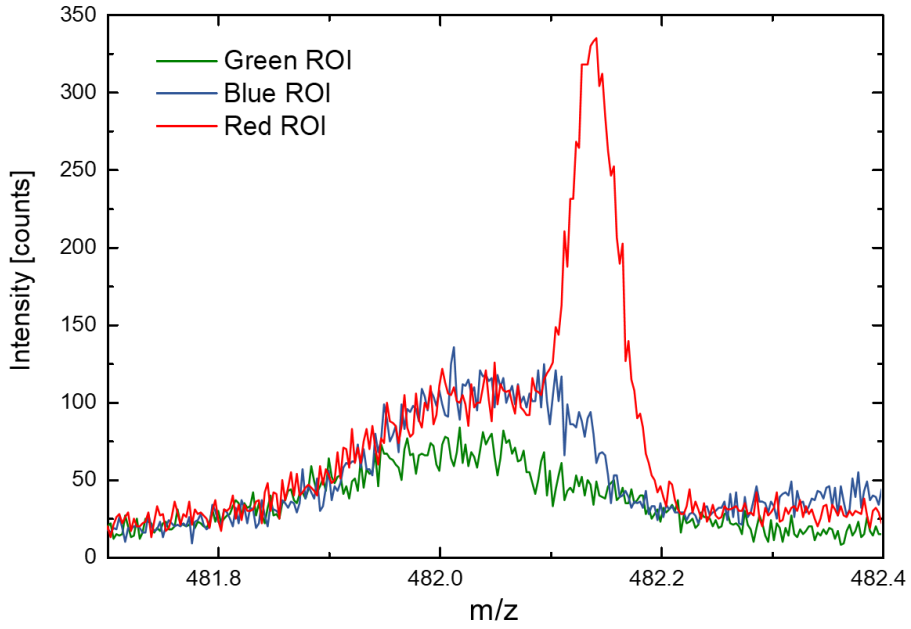

Figure 46 ToF-SIMS mass spectra around a mass of 482 u for the three regions of interest that are depicted in the depth profile of Figure 45.

2.2.3. XPS depth profiling

Figure 47 a) shows the XPS depth profile that has been acquired at the interface.

The sputtering could have been carried on a bit longer until steady concentrations of the components have been reached. However, the elemental concentrations are very close to the expected values. As mentioned before, the expected composition in the emissive layer is 92.84 % carbon, 6.95 % nitrogen

and 0.215 % iridium. Again, the iridium signal is calculated higher than the theoretical value (0.3 %), but within the margin of error. The same applies to carbon (91.4 %) and nitrogen (7.3 %). Overall, these values are much closer to the expected numbers than for the top emissive interface with NPB. Once again, this might be a confirmation for the $Ir(mppy)_3$ enrichment at that interface.

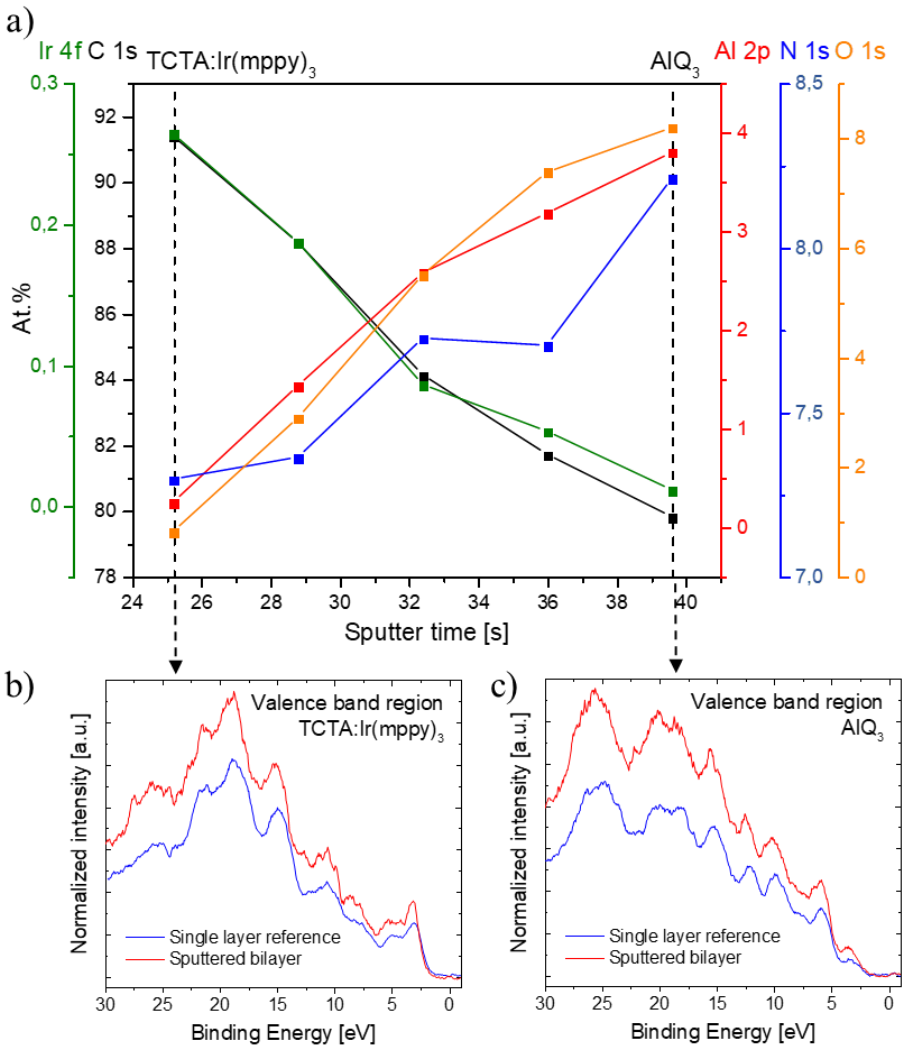

Figure 47 *a) XPS depth profile of the TCTA:Ir(mppy)$_3$/Alq$_3$ bilayer sample with the atomic concentrations of carbon, nitrogen, oxygen, aluminum and iridium. b) and c) Comparison of the valence band spectra of a reference sample and the bilayer sample after sputtering in the TCTA/Ir(mppy)$_3$ and Alq$_3$ layers.*

For the Alq_3 layer, the theoretical composition is 79.4 % carbon, 2.9 % aluminum and 8.8 % of both nitrogen and oxygen. The values of the last data point of the depth profile show good accordance to those values. The calculated values are 80.60 % carbon, 4.1 % aluminum, 8.4 % nitrogen and 6.9 % oxygen. The measured nitrogen and oxygen concentrations are lower than expected while the aluminum content is higher. The reason might be the X-ray exposure of the material. Indeed, in chapter 3, it was shown that the relative intensity of aluminum increased after continuous X-ray exposure.

The valence band spectra in the different layers after sputtering in Figure 47 b) and c) correspond again very well to the reference measurements that have been taken on the single layer references without

sputtering. The higher intensity for the spectra of the sputtered bilayers could again be a result of a contamination of the unsputtered single layer samples. Slight carbon contamination at the surface could suppress the signal to some extent.

Table 8 Overview for the XPS quantification of the Alq_3 single layer reference sample, the sputtered bilayer and the sample that was exposed to X-rays for 220 min.

Element	Bonding State	Position			At%		
		Single layer Reference	**Sputtered bilayer**	**X-ray exposed**	**Single layer Reference**	**Sputtered bilayer**	**X-ray exposed**
C		**285**	**285.75**	**285.61**	**78.67**	**80.68**	**79.53**
	C-H	285	285.75	285.61	42.59	40.52	42.93
	C-X	285.77	286.54	286.38	25.28	29.33	24.21
	C-C	284.24	285.03	284.86	10.80	10.83	12.39
N		**400.02**	**400.42**	**400.37**	**7.76**	**8.28**	**7.59**
	N-Al	400.02	400.42	400.37	7.36	7.81	7.10
	N defect	401.91	402.24	402.19	0.40	0.47	0.49
O		**531.31**	**531.73**	**531.84**	**8.11**	**6.89**	**7.99**
	O-Al	531.31	531.73	531.84	7.86	5.31	7.45
	O defect	532.75	533.17	533.28	0.25	0.34	0.54
	O-X	-	532.36	-	-	1.24	-
Al		**74.38**	**74.59**	**74.49**	**4.45**	**4.14**	**4.88**

Overall, the valence band in the Alq_3 region of the sputtered bilayer is very similar to the one that was recorded after extensive X-ray exposure of the Alq_3 single layer in chapter 3. The nitrogen contributions at binding energies of 7.5 and 24 eV appear weaker in the sputtered bilayer than in the unsputtered single layer sample. Moreover, the peak at 25 eV has two contributions in the reference spectrum and appears therefore very broad. In the spectrum of the sputtered bilayer, this peak appears rather sharp. The contribution at higher binding energies comes partially from the oxygen atom [151]. This contribution seems to diminish. Fitting of the elemental core level spectra can confirm the resemblance between the sputtered bilayer and the X-ray exposed single layer from chapter 3. Table 8 summarizes the results from the peak fitting of the C 1s, N 1s, O 1s and Al 2p core levels for the Alq_3 single layer reference sample, the sputtered bilayer sample and the single layer sample that was exposed to X-rays for 220 minutes.

The fits for all four core level spectra of the single layer reference and the sputtered bilayer sample are shown in Figure 48. The shifts in the core level spectra of the sputtered bilayer is comparable to those that were observed in the X-ray exposed single layer sample. The relative increase of the intensity of the N 1s peak and the appearance of a new contribution to the O 1s peak confirm the observations that were made on the valence band. The bonding states for these elements might have slightly changed. This could be the case when the molecule undergoes ligand separation as it is observed for Alq_3 during degradation [56]. However, it is not clear if this is the origin of the changes in the XPS spectra since a change of the aluminum atom would also be expected but is not observed. Moreover, the increase by about 15 % of the C-X contribution in the C 1s peak is another indicator for changes in chemistry in the sputtered bilayer sample.

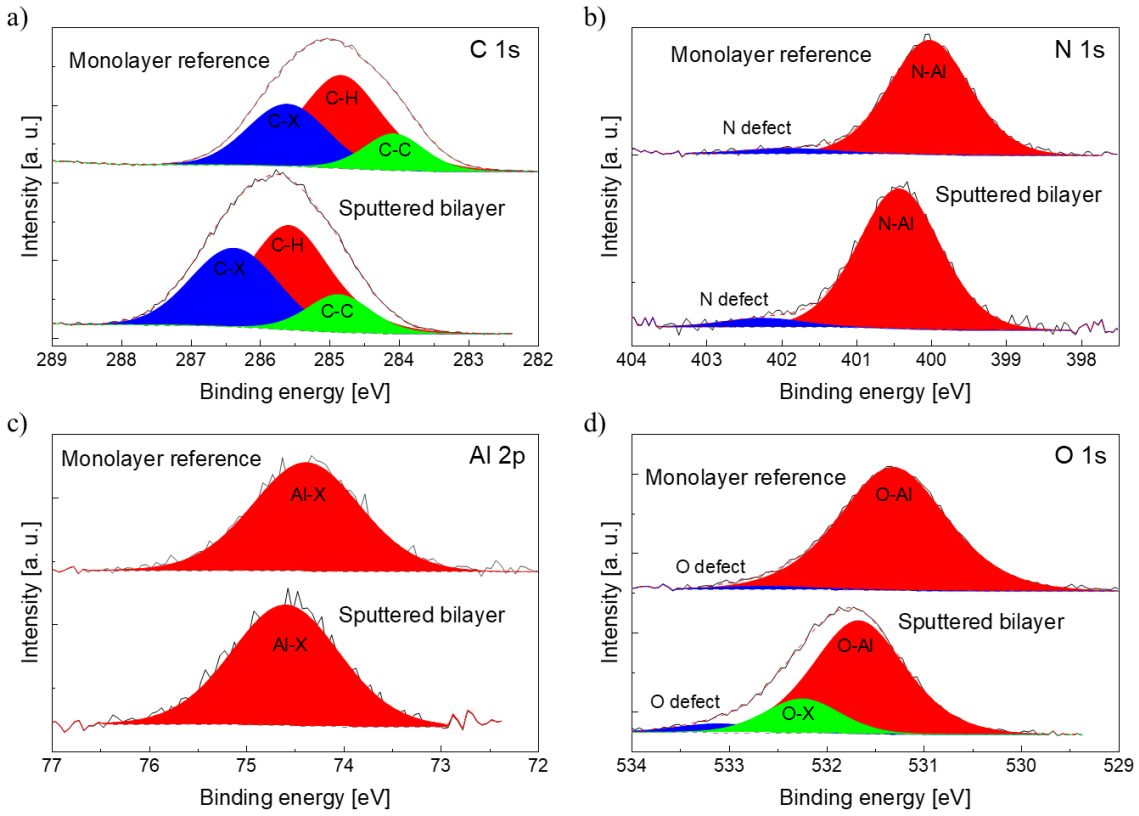

Figure 48 *a) – d) Fits of the C 1s, N 1s, Al 2p and O 1s core levels in the single layer reference (top) and in the sputtered bilayer (bottom) of Alq_3.*

2.2.4. Summary

The ToF-SIMS depth profiles for the lower emissive interface shows again good results overall. The ion intensities for the molecular secondary ions are high and stable throughout the profile which indicates low induced damage during the analysis. However, the XPS measurements reveal slightly modified molecules in the underlying Alq_3 layer. The damage is similar to the one that has been observed in chapter 3 on the X-ray exposed single layer surface. This leads to the assumption that the modification of the molecules stems from excessive X-ray exposure during the depth profile.

3.Hybrid inorganic-organic bilayers

3.1. Top electrode interface: Ag/STTB:F4TCNQ

As mentioned before, inorganic-organic interfaces pose big problems in depth profiling due to the different sputter rates for inorganic and organic materials. While removing the metal electrode, it is important to avoid damaging the underlying organic layer. Different possibilities for depth profiling these interfaces have been studied. The bilayer sample consists of a 50 nm silver layer deposited on 50 nm of STTB:F4TCNQ. It is depicted in Figure 49 together with the location of the interface in the OLED stack.

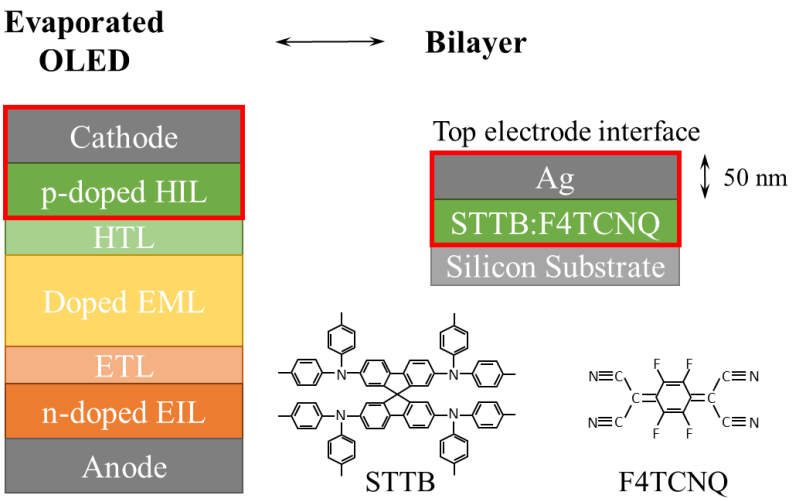

Figure 49 Schematic representation of the Ag/STTB:F4TCNQ bilayer and the location of the interface inside the OLED stack.

3.2. Different approaches to depth profiling of inorganic-organic interfaces

3.2.1. Low-energy monoatomic sputtering

3.2.1.1. Experimental setup

The first possibility for depth profiling inorganic-organic interfaces is to use a low energy monoatomic cesium source. It has been shown that cesium sputtering at energies below 500 eV can be used to analyze such systems and even preserve some molecular information in the organic part [159], [160].

3.2.1.2. Results

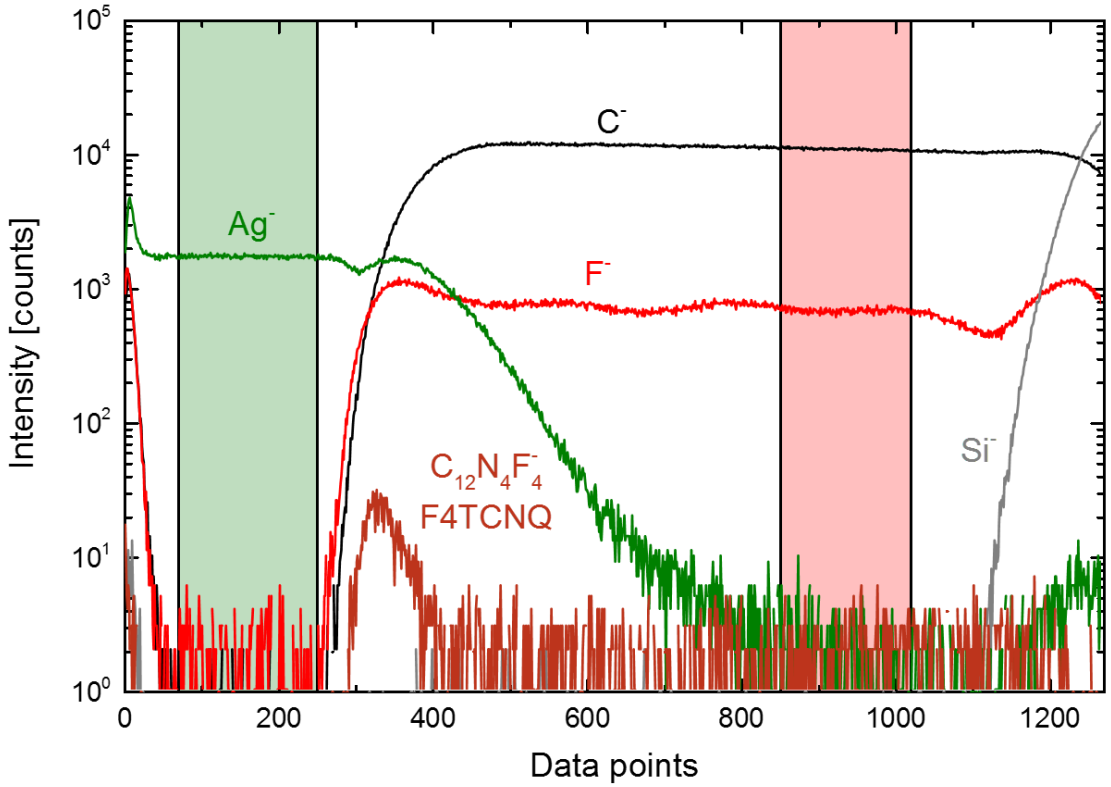

Figure 50 *ToF-SIMS depth profile of the Ag/STTB:F4TCNQ bilayer sample. The profile has been acquired using 250 eV Cs^+ for sputtering.*

Figure 50 shows the ToF-SIMS depth profile of the inorganic-organic bilayer sample. Both layers can clearly be distinguished by the Ag^- and C^- secondary ions. It can be seen that the sputter rate for the inorganic material is much higher than for the organic material as both layers have the same thickness.

However, no high mass characteristic fragment of the STTB molecule is detected. The $F4TCNQ^-$ signal is only present at the interface. In the bulk of the layer, the signal disappears. This means that there is a high fragmentation of these organic materials by monoatomic sputter sources, even for the low energy cesium ions. This fact is further illustrated by the mass spectra in Figure 51.

The mass spectrum in Figure 51 a) shows the spectrum that is integrated over the whole depth profile. Certain high intensity peaks at high masses can be identified. However, the mass spectra in Figure 51 b) and c) from the green and red ROIs in Figure 50 show clearly that all of those high intensity peaks stem from different silver combinations (some peaks that do not correspond to the green nor the red spectrum come from silicon aggregates that are detected once the substrate is reached). The graph in Figure 51 c) that corresponds to the ROI in the STTB:F4TCNQ layer shows a highly fragmented spectrum. The intensity of the F4TCNQ molecule is too low to even be seen on the magnified inset.

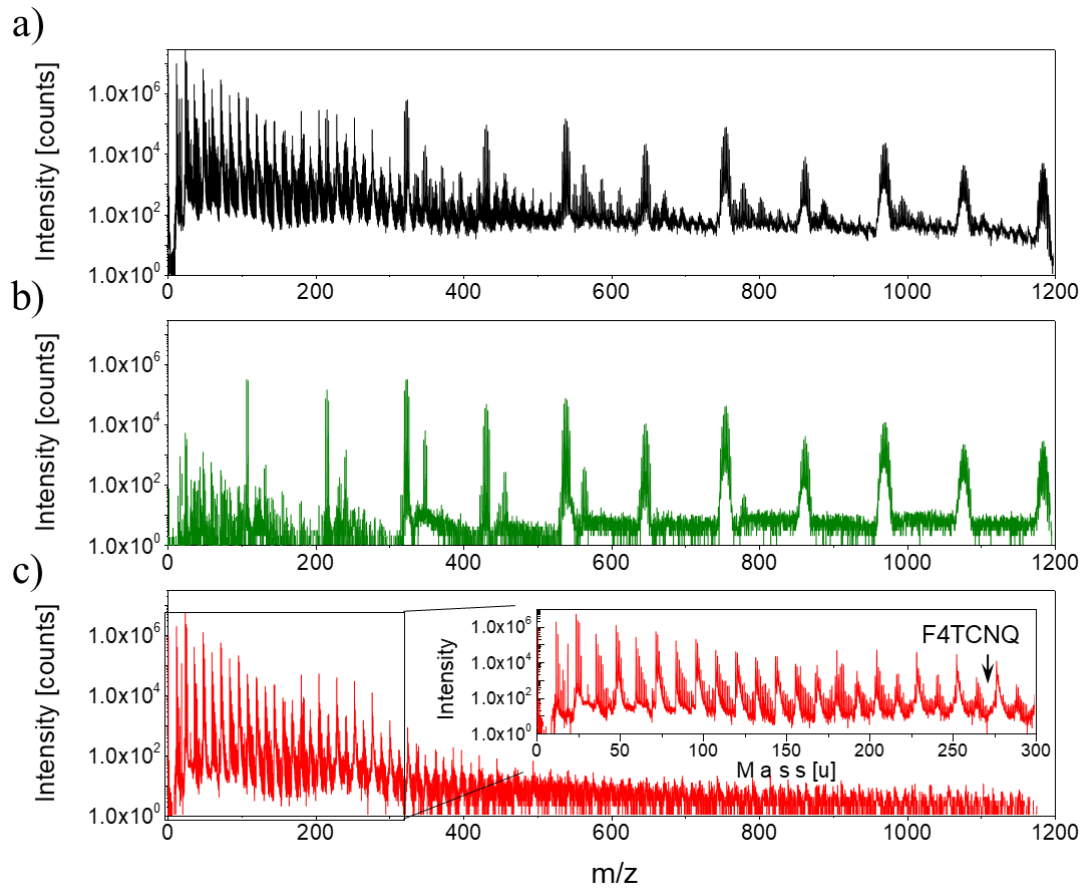

Figure 51 *a) ToF-SIMS mass spectrum of the Ag/STTB:F4TCNQ bilayer sample integrated over the whole depth profile. b) Mass spectrum from the green ROI in Figure 50 in the silver layer. c) Mass spectrum from the red ROI in Figure 50 in the STTB:F4TCNQ layer.*

3.2.1.3. Summary

Although low energy cesium sputtering might be a good solution for certain applications, it induces too much fragmentation to the organic part in this bilayer sample. It cannot be used for depth profiling of these kinds of materials.

3.2.2. High-energy cluster sputtering

3.2.2.1. Experimental setup

The next possibility is to take the opposite approach and to increase the energy of clusters rather than to decrease the energy of monoatomic sources.

In chapter 2 it was shown that the sputter rates for inorganic materials for clusters is very low. By increasing the energy per atom, it should be possible to get acceptable sputter rates.

However, a recent study showed that the energy per atom and the overall cluster energy should be kept low to achieve high quality depth profiles of inorganic materials [161]. The study confirmed at the same time, that the sputter rates are very low. Moreover, a significant increase of roughness can be observed for the low energy clusters compared to high energy clusters. In conclusion, a compromise between higher sputter rates with lower roughening of the surface and higher quality of the depth profiles must be made.

3.2.2.2. Results

Here, high energy cluster depth profiling was studied on the Ag/STTB:F4TCNQ sample. Figure 52 shows the results for the negative and positive mode on the top and bottom, respectively.

Both profiles have been acquired using 20 keV Ar_{1000} sputtering. This results in an energy of 20 eV/Atom. The spectrum that was taken in negative mode shows a clear signal of the electron acceptor dopant F4TCNQ. The organic layer is marked by the rise of the C^- signal. However, the Ag^- signal is also present in the organic part. At the end of the profile, the Si- signal has appeared as well, indicating that the substrate was reached. At this point, secondary ions from all three layers are detected at the same time. Only the molecular ion of F4TCNQ shows a defined layer.

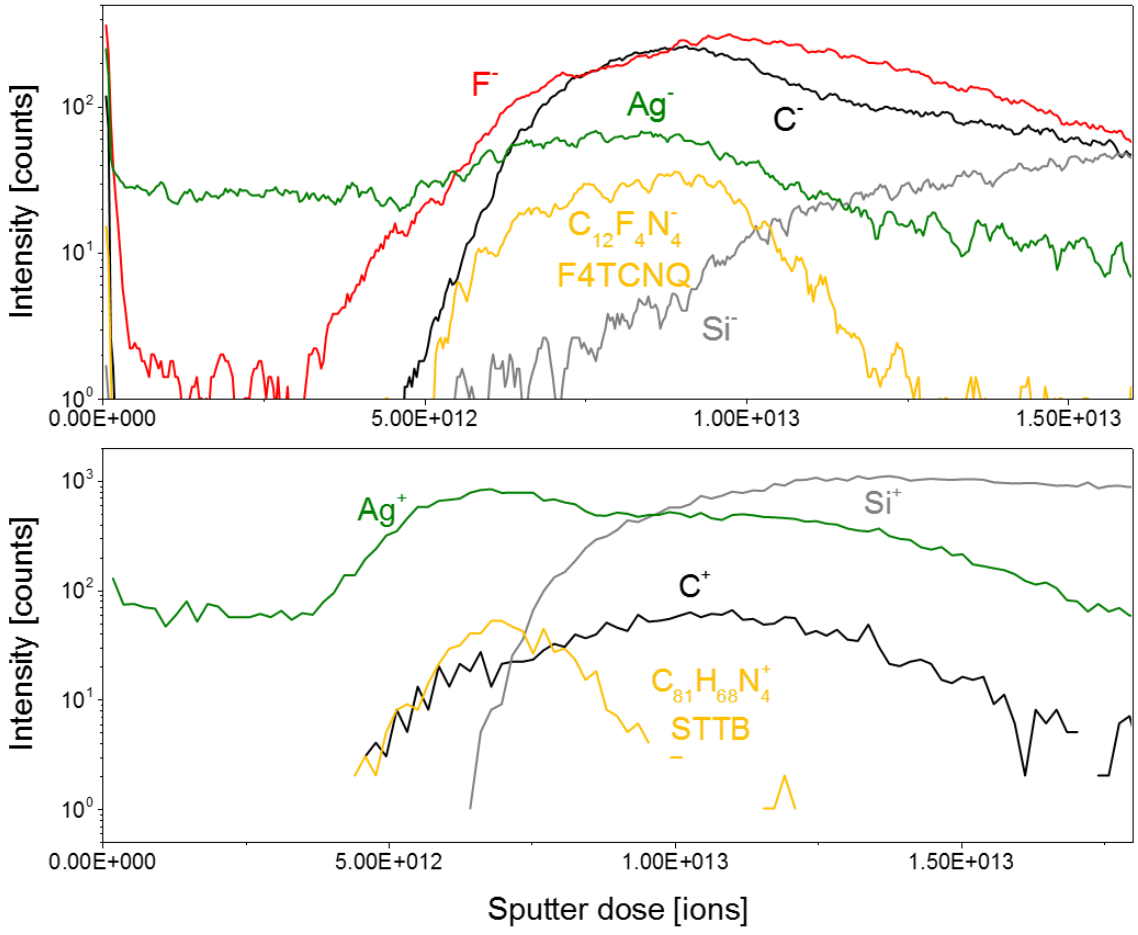

Figure 52 ToF-SIMS depth profiles in the negative (top) and positive (bottom) mode of the Ag/STTB:F4TCNQ bilayer sample for sputtering with 20 keV Ar_{1000}.

For the positive profile at the bottom, the same trend can be observed. The molecular signal of STTB, that is more likely to be positively ionized than F4TCNQ, appears at the interface of silver and silicon. However, the silver signal as well as the carbon signal decrease only slowly as sputtering of the silicon substrates continues.

3.2.2.3. Summary

From these profiles it is hard to define the layer interfaces. The organic part seems to be sputtered very fast and the silver atoms seem to be pushed through the organic material to the substrate surface. Keeping in mind that the layer thickness will shrink in the final OLED devices, this method is not suited for profiling inorganic-organic interfaces.

3.2.3. Combined Monoatomic-Cluster Sputtering

3.2.3.1. Experimental setup

By combining both, monoatomic and cluster sputtering, it is possible to use the advantages of both beams. Co-sputtering of monoatomic and cluster ions where the sample is bombarded with both species at the same time is possible. Mainly C_{60} clusters in combination with different monoatomic sources were used in literature. An XPS depth profile of a complete OPV device has been shown as well as the enhancement of secondary ion yields for certain organic materials when a reactive monoatomic sputter species like O_2^+ is used [143], [162] . However, co-sputtering was not examined during this thesis.

Another possibility to combine monoatomic and cluster sputtering is to take advantage of the strong assets of each beam. Monoatomic sources have proven to provide high quality depth profiles of inorganic materials and it was shown here, that argon clusters are indispensable for organic depth profiling. The approach that was studied here is therefore to change the sputter species at the interface. The inorganic silver layer is sputtered by a monoatomic cesium beam. Once the interface is reached, the profile is stopped, and the sputter beam is switched to argon clusters which are used to continue the profile through the organic layer. The stopping point was set at the end of the theoretic 84%/16% interface. This means, once the Ag^- signal drops down to only 16 % of the steady state intensity from the silver layer, the profile is stopped and the beam switched.

3.2.3.2. Results

The left part of Figure 53 shows the first part of the depth profile that has been taken by monoatomic cesium sputtering at different energies. The top graph shows the profile at 2 keV Cs^+ sputtering while for the bottom graph 500 eV Cs^+ was used.

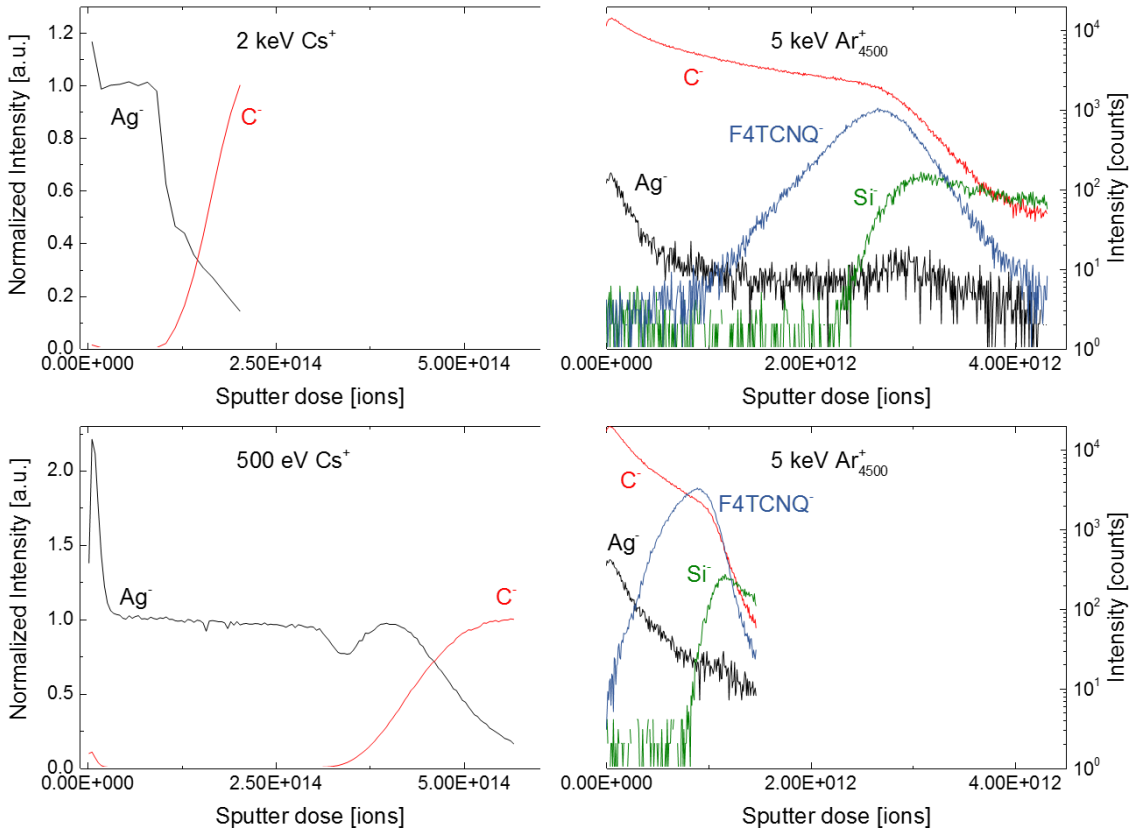

Figure 53 *ToF-SIMS depth profiles of the Ag/STTB:F4TCNQ bilayer sample where the sputter beam has been switched from monoatomic cesium sputtering to argon cluster sputtering at the interface of both layers. On the left, the monoatomic profile is shown for different cesium energies. In the top, 2 keV Cs^+ ions were used while at the bottom, 500 eV Cs^+ was used.*

The profiles have been normalized to the steady state intensity for the Ag^- signal in the silver layer. At the stopping point, the Ag- dropped to 16 % of this value in each of the profiles. It can be seen that for the 500 eV sputtering, the carbon signal almost reached a steady state at the end point while it keeps rising in the 2 keV profile.

The profiles of the organic part have both been acquired with the same parameters. 5 keV argon clusters with 4500 atoms per cluster were used at a current of about 0.8 nA. The sputter rate after the high energy cesium sputtering in the top graph is substantially slower than after low energy cesium sputtering. The scale on the x-axis is the same for the top and the bottom graph. However, the trend of both profiles is the same. Initially, none of the molecular signals can be detected. The organic layer at the interface was heavily damaged. The C^- signal is quite high, indicating strong fragmentation. During the profile, the damage can be removed constantly by the cluster sputtering. The C^- signal decreases and the molecular signal of F4TCNQ starts to appear.

After both, 2 keV and 500 eV cesium sputtering, the organic material is damaged. But it seems that the 2 keV sputtering induces heavier damage that reaches deeper lying molecules than the low energy ions. The slower sputter rate indicates strong intermixing and possible cross-linking of the molecules which makes sputtering with clusters harder. Moreover, the maximal intensity of the $F4TCNQ^-$ secondary ion

reaches higher values in the profile after 500 eV Cs^+ sputtering at the bottom. This is an indication of lower fragmentation and better damage recovery in this profile.

3.2.3.3. Summary

Similar tests with different switching point for the sputter beam are not shown here. Samples, where the switching point was chosen earlier to avoid damaging the organic layer by the cesium sputtering exhibited similar problems as they were shown in the previous section where silver atoms seem to be pushed all the way through the organic layer to the silicon substrate. Samples where the switching point was chosen later, after the silver signal had completely disappeared, showed similar recovering profiles.

These results suggest overall that this technique is not suited either for depth profiling of this kind of inorganic-organic interface.

3.2.4. Two-steps Analytical Approach: Monoatomic and Cluster Profiling

3.2.4.1. Experimental setup

Finally, there is another possibility of analyzing these inorganic-organic materials. A two-step analysis approach. The first analysis is carried out with monoatomic sputtering to gain information on the inorganic part. The loss of molecular information in the organic part is accepted. Then another analysis will be carried out where the inorganic part is removed before the analysis by applying scotch tape to the surface and ripping it off again. This will leave the organic layer exposed and ready for characterization by cluster sputtering. The analysis protocol will be explained in more detail for the complete OLED devices in chapter 5.

3.2.4.2. Results

Figure 54 shows the first analysis where 2 keV Cs^+ ions are used for sputtering. The profile shows a well-defined inorganic-organic interface. The molecular information is lost due to heavy fragmentation as it has been shown above. However, the characteristic secondary ion F^- can be traced to identify the F4TCNQ molecule.

The second part of the analysis is shown in Figure 55. A strong molecular signal of the STTB molecule is obtained. Characteristic fragments are detected as well. The signal is constant and has a well-defined interface to the silicon substrate. Almost no Ag^- ions are detected which indicates a complete removal of the silver layer by the scotch tape.

However, it is not clear at which point the rupture of the layers took place during the removal of the scotch tape because it could not be analyzed. Strong charging effects made the analysis impossible.

Moreover, the deposition of the tape onto the sample holder inside the glove box was extremely difficult. The prepared tape samples were very rough which hindered the analysis further.

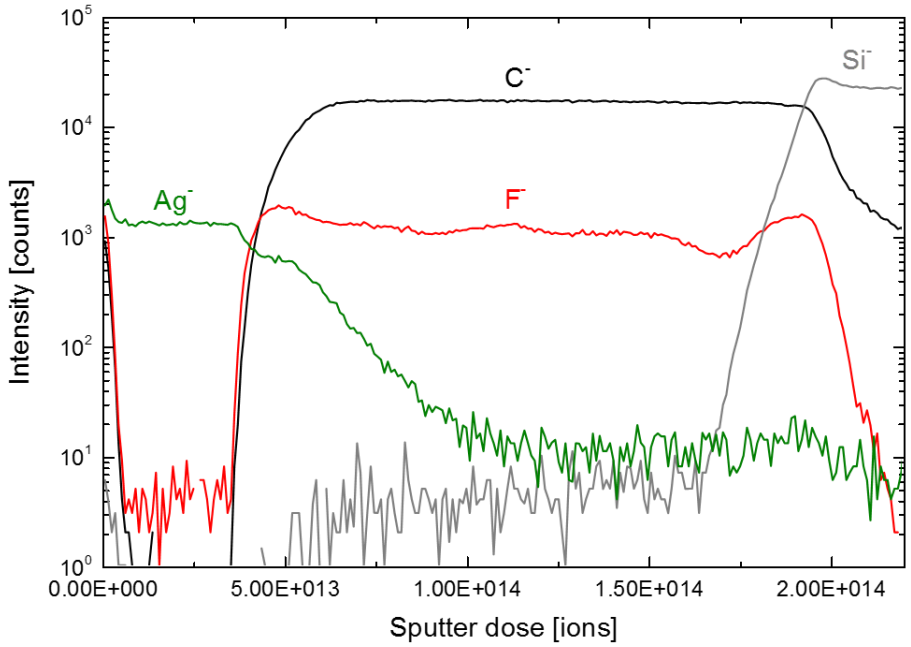

Figure 54 ToF-SIMS depth profile of the Ag/STTB:F4TCNQ bilayer sample. The profile has been acquired using 1 keV Cs^+ ions for sputtering.

Generally, 3M scotch tape was used because it showed consistency in removing the inorganic layers. However, double sided adhesive and conductive copper tape has also been used occasionally to try to reduce the charging effects during a possible analysis. The copper tape showed less consistency in removing the inorganic layers. It did not work on the studied inorganic-organic bilayer.

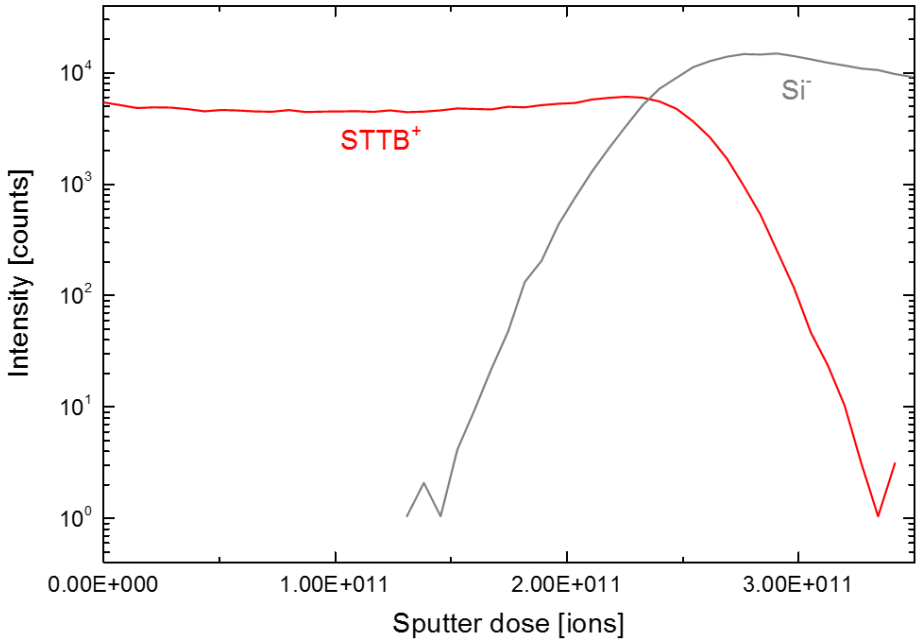

Figure 55 ToF-SIMS depth profile of the Ag/STTB:F4TCNQ bilayer sample after the removal of the silver layer by scotch tape. The profile has been acquired using 5 keV Ar_{4500}^+ clusters for sputtering.

That is why the investigation of the copper tape has been performed on different samples. In complete direct OLED devices, the inorganic-organic interface is an Ag/BPhen:Ca bilayer where the BPhen layer has a thickness of 26 nm. Figure 56 shows the XPS survey spectra of the copper foil in the upper part and the exposed organic layer on the lower part of such an OLED after the scotch tape removal process.

The spectrum that was taken on the copper tape shows strong silver peaks. However, carbon, calcium and nitrogen can also be clearly identified. This indicates that the rupture point during the removal process does not lie exactly at the inorganic-organic interface but somewhere in the organic layer. The thickness of the organic residual should be below 10 nm since the silver signal is clearly visible.

The survey spectrum shows no copper. The removal process is consistent and removes the whole silver layer without leaving any holes. This is confirmed by the lower survey spectrum which represents the surface of the exposed organic layer. No silver is left on the surface. Clear signals of carbon, calcium and nitrogen are detected which confirms the presence of BPhen at the surface. Considering that the underlying organic layer is Alq_3, the thickness of the BPhen layer that is left should be over 10 nm thick because there is no sign of aluminum at the surface. This is consistent with the assumption that less than 10 nm are ripped off by the tape, keeping in mind that the initial layer thickness was 26 nm.

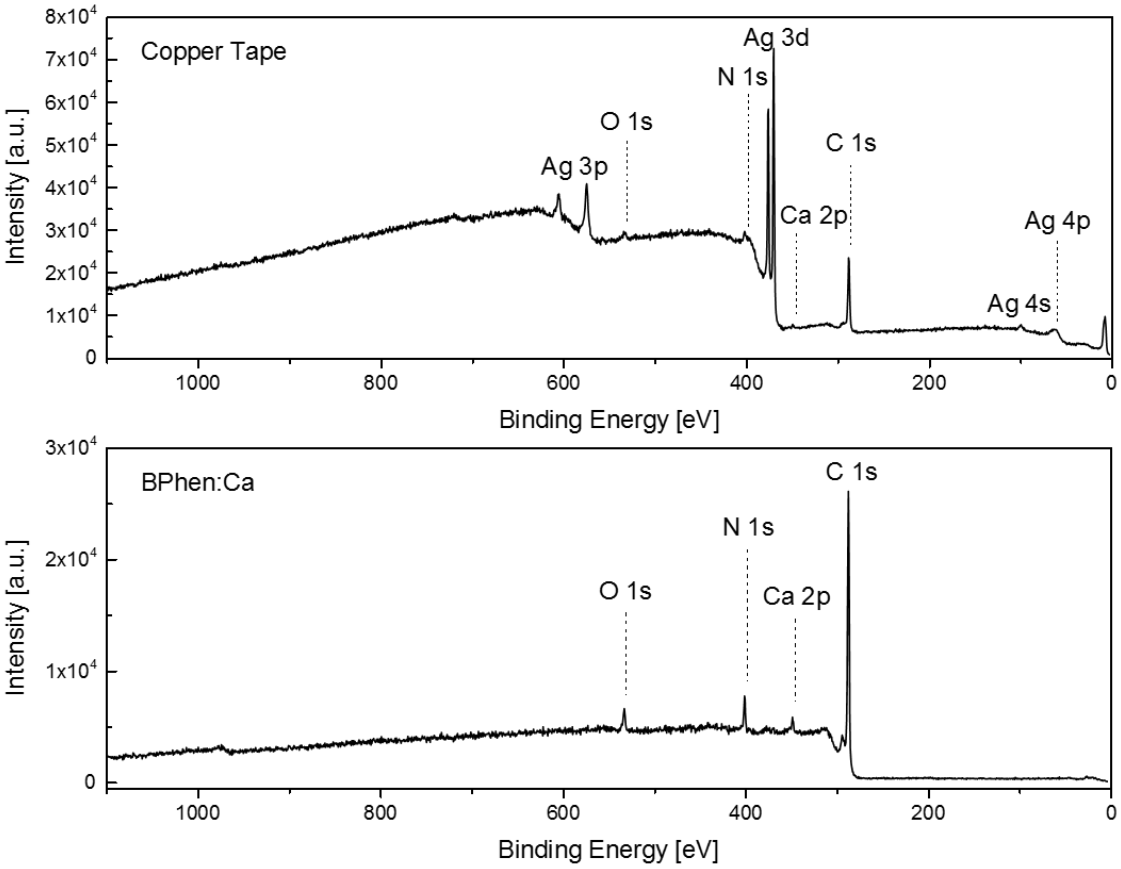

Figure 56 *XPS survey spectra of the adhesive copper tape that was used to remove the silver layer from the organic BPhen:Ca layer (top)and XPS survey from the remaining layer on the substrate after the scotch tape process (bottom).*

In both spectra, the O 1s peak is visible. This is because the scotch tape process was performed under ambient conditions instead of the glove box. This was done to facilitate the deposition of the tape onto the sample holder. Since this measurement was planned as demonstration for the scotch tape process, the oxidation of the surface was accepted. At the same time, this demonstrates the absolute necessity of handling the organic materials in a protected environment (e.g. nitrogen, argon or vacuum) in order to prevent surface modification by oxidation.

3.2.4.3. Summary

Overall, the two-step analytical approach presents the best alternative for the analysis of this kind of inorganic-organic interfaces. Especially with the consistency of the scotch tape removal process that might not be given for other samples.

4. Characterization of solution processed bilayers

4.1. Sample preparation

As mentioned in section 1.2, completely solution processed organic bilayers were studied as well. Here, the electron transport layers (ETL) in a fully solution processed OLED were analyzed. The work has been published in cooperation with Yolande Murat from the IMS in Bordeaux [163]. The sample preparation has been done by Yolande Murat. The OLED stack as well as the interface of interest are shown in Figure 57.

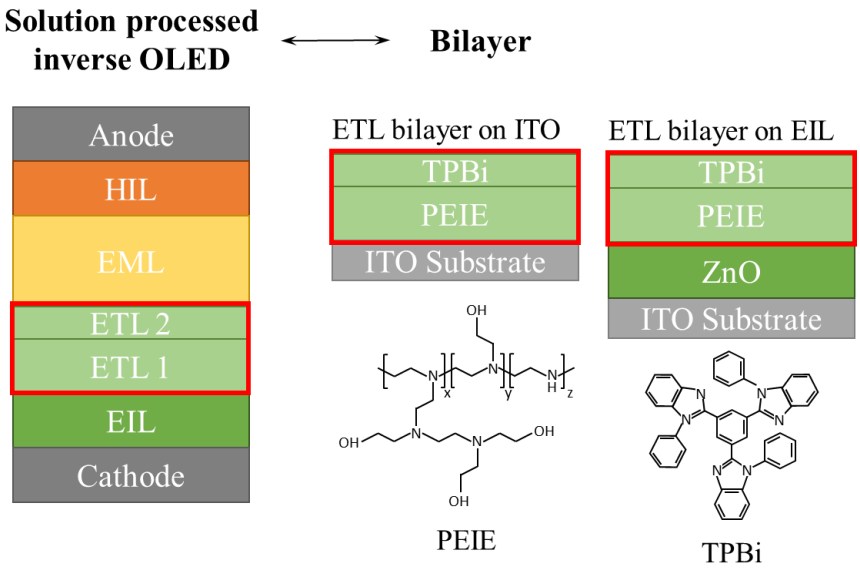

Figure 57 Schematic representation of the TPBi/PEIE bilayer and the location of the interface inside the solution processed OLED stack.

The ETL consists of a combination of a thick PEIE layer and a thinner TPBi layer on top of it. To simplify the studied system as much as possible, both materials were deposited directly on an ITO substrate. Later, a ZnO layer has been spin-coated onto the ITO substrate before the organic materials were deposited. This was done to simulate the final OLED stack, where the ZnO acts as the electron injection layer.

Figure 58 shows the two different deposition approaches that have been studied. The first approach is the classical deposition of both materials by two consecutive spin-coating steps. The PEIE was diluted in 2-methoxyethanol at a concentration of 4.82 mg/ml. The solution was filtered by a 0.45 µm polytetrafluoroethylene (PTFE) filter before deposition at 5000 rpm for 60 s. Afterwards, the sample was annealed at 100 °C for 10 min. Then, the TPBi layer has been deposited on top of the PEIE layer. The TPBi was diluted in ethanol at a concentration of 0.1 mg/ml. This solution was spin coated at 1000 rpm for 60 s. Finally, the sample was again annealed for 10 min at 100 °C.

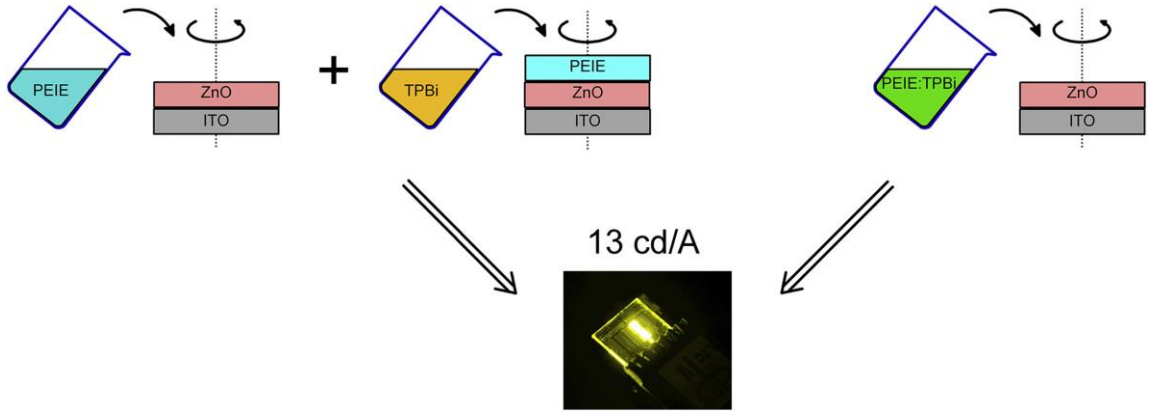

Figure 58 *Two deposition approaches for the fabrication of PEIE/TPBi bilayers for the use in completely solution processed OLEDs. On the left, each material is spin coated separately. On the right, a binary solution containing both materials is used to deposit both materials at the same time in a one-step-processing approach* [163].

The second approach that was investigated is a one-step process where both materials were deposited at the same time. This process might save time and material during manufacturing. Both of the above solutions were therefore mixed to form a binary solution. The resulting final concentration of PEIE in the solution was 1.1 mg/ml. The solution was spin-coated at 1000 rpm for 60 s and annealed at 100 °C for 10 min.

4.2. Chemical characterization of solution processed Bilayers

The produced bilayer samples were then analyzed by ToF-SIMS to gain information about the layer formation during the spin-coating of the binary solution. Therefore, samples with classical layer-by-layer deposited materials were compared to the one-step-processed samples where both materials were deposited at once from the binary solution.

4.2.1. Reference measurements of PEIE and TPBi single layers

First, two characteristic fragments for both materials need to be found to clearly identify both layers. With PEIE being a polymer, there are many fragments that are created during ToF-SIMS measurements. Some of them are identical to the fragments that are created by the TPBi molecule. Since the molecular signal for the TPBi layer is low, another characteristic fragment has been chosen to identify this layer. Figure 59 shows excerpts from the mass spectra of the single layer references for both materials at the masses of the chosen characteristic fragments.

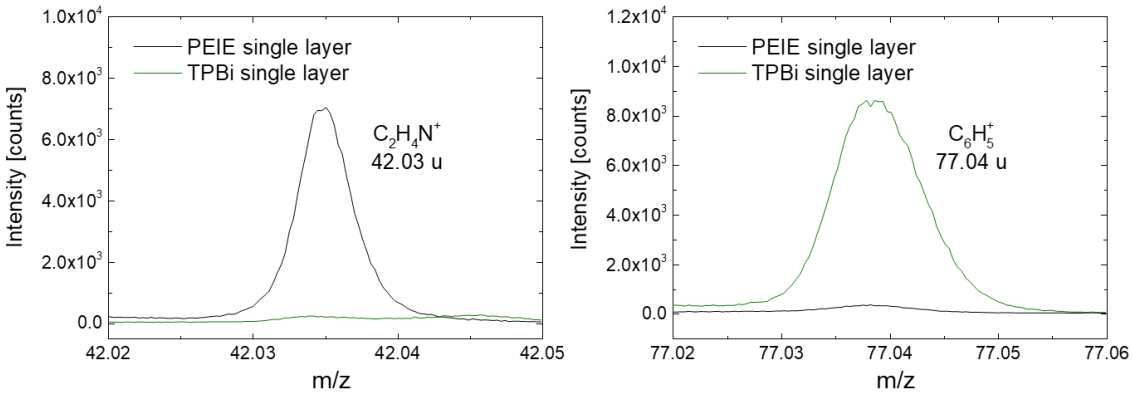

Figure 59 *ToF-SIMS mass spectra at the masses of the characteristic secondary ions $C_2H_4N^+$ for PEIE and $C_6H_5^+$ for TPBi. The black and green curves correspond to the PEIE and TPBi mass spectra, respectively.*

The black and the green curve represent the PEIE and the TPBi layer, respectively. For PEIE, the $C_2H_4N^+$ secondary ion is used and for the TPBi layer the $C_6H_5^+$ ion. Both graphs show that the chosen ions are characteristic for each of the materials. There is only a negligible signal from the opposite material at that mass range.

4.2.2. ToF-SIMS depth profiling of solution processed bilayers

Both deposition methods were used to deposit a bilayer on an ITO substrate. The results of a ToF-SIMS depth profile across those samples can be found in Figure 60. All profiles are normalized to the maximum of the respective secondary ion. The $In_2O_3^+$ ion was used to identify the substrate. All profiles have been acquired using 5 keV Ar_{4500}^+ sputtering at a current of about 0.75 nA. For the analysis beam, 30 keV Bi_3^{++} ions were used with a current of about 0.25 pA and a pulse width of 25 ns.

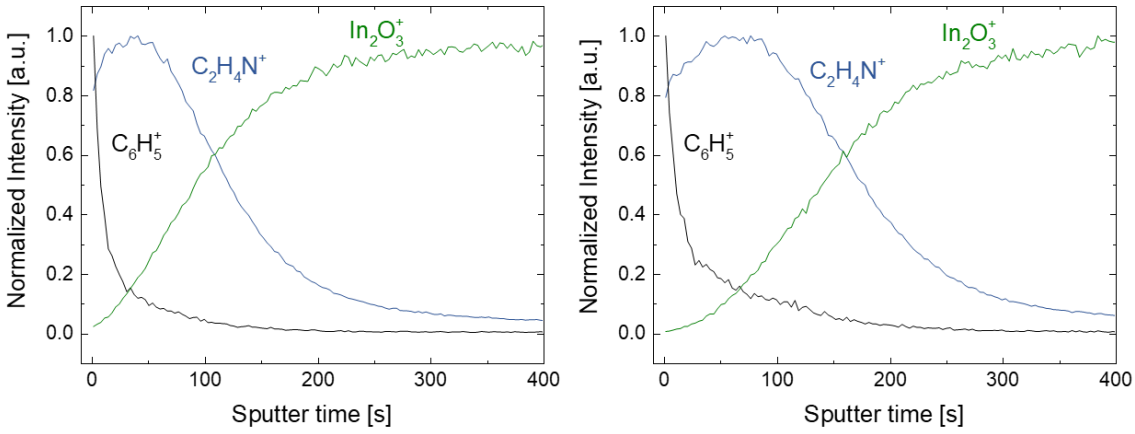

Figure 60 *ToF-SIMS depth profile across the TPBi/PEIE bilayer on an ITO substrate. On the left, the layers were deposited one by one and on the right, both materials were deposited by using only one solution.*

The left graph shows the depth profile of the sample where both layers have been deposited consecutively. The ultra-thin TPBi layer at the surface can be clearly distinguished from the thicker PEIE layer underneath it. For the one-step-processed sample on the right, a similar profile is observed. Both materials seem to separate well during the spin-coating, forming two different layers. Only the sputter time that is needed to reach the substrate is higher in the case of the one-step-processed sample. This could have two reasons. The PEIE layer could be thicker. However, the concentration of PEIE that is used in the binary solution is only a fourth of the concentration that is used in the regular PEIE solution. The other possible explanation could be a different arrangement of the polymer in the layer that hinders the sputtering by the argon clusters. The layer formation with another molecule present could be different from the layer formation when only PEIE is spin-coated.

In the final OLED, a zinc oxide layer will serve as the electron injection layer. That is why in the next step, the same TPBi/PEIE layers are deposited onto a solution processed ZnO layer to form the stack that will appear in the final device. The ZnO layer was deposited by spin-coating a solution of zinc acetate dehydrate diluted in absolute ethanol and ethanolamine. After spin-coating, the samples were annealed for 1 h at 180 °C to form a sol-gel layer of ZnO.

Figure 61 shows the depth profiles for the resulting TPBi/PEIE bilayer samples on ZnO. A similar profile as for the ITO samples can be observed when both layers are deposited one after the other (left graph).

However, for the one-step processed sample, an intermixing of both materials is observed. The signal for the characteristic secondary ions is superimposed. Moreover, the Zn^+ signal is elevated at the sample surface, even though no holes can be observed by optical microscopy.

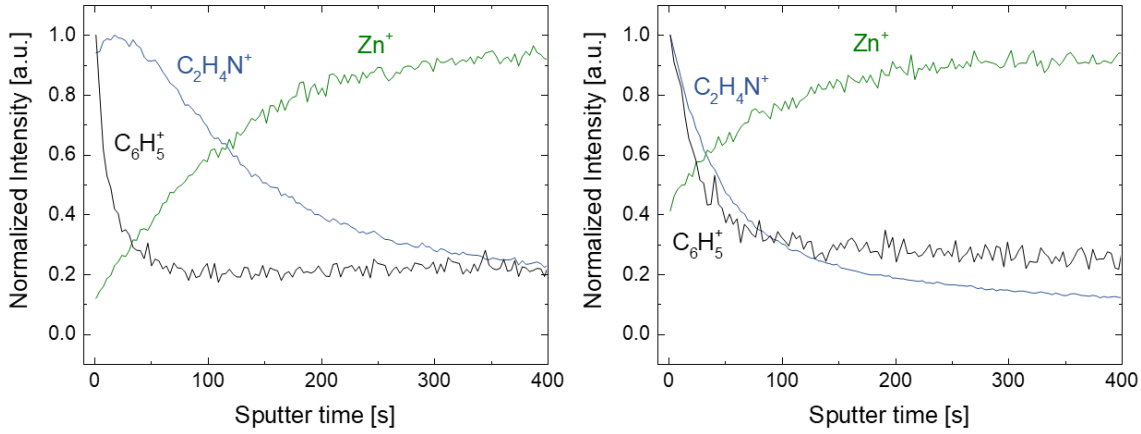

Figure 61 *ToF-SIMS depth profile across the TPBi/PEIE bilayer on a ZnO layer. On the left, the layers were deposited one by one and on the right, both materials were deposited by using only one solution.*

4.2.3. Comparison of treated one-step-processed Bilayers

The problem that causes the intermixing of both materials must be the ZnO substrate since the one-step-processing worked well on the ITO substrate. The increased intensity of Zn^+ led to the conclusion that the surface roughness of the ZnO layer might be higher than the one for ITO.

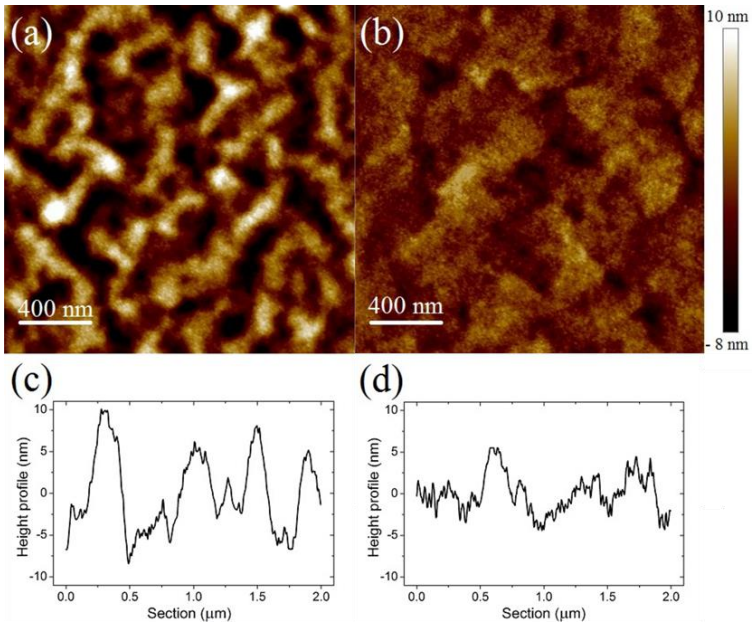

Figure 62 *a) AFM surface image of the as-deposited ZnO layer. b) AFM image of the rinsed ZnO layer. c) and d) Line spectra across the images for the as-deposited and the rinsed layer, respectively.*

AFM measurements of the ZnO surface confirm the expected high surface roughness. Figure 62 a) shows an AFM surface measurement that has been taken on the as-deposited ZnO layer. In Figure 62 c), a line scan across the image can be found. The roughness is very high with many ripples at the surface. To reduce that roughness, the ZnO layer can be rinsed with water before the deposition of the organic layers. The AFM image after rinsing of the ZnO can be found in Figure 62 b) and the respective line scan in Figure 62 d). Both images clearly show the reduction of ripples at the surface and the roughness overall.

Figure 63 shows the ToF-SIMS depth profile of the one-step-processed organic bilayer on a rinsed ZnO substrate. This time, a phase separation can be observed for both materials. The roughness of the ZnO layer seems indeed to have been the limiting factor for the efficient one-step-processing of the materials.

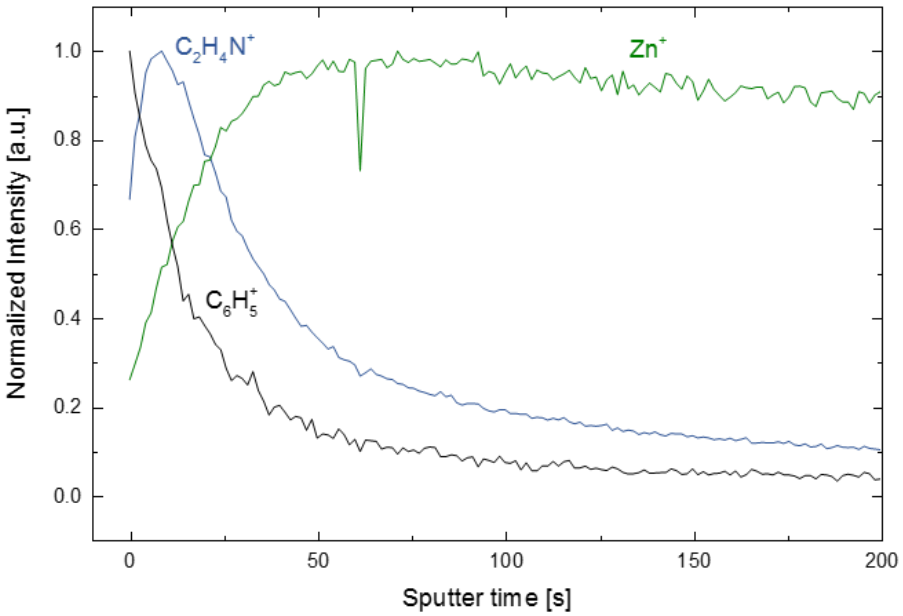

Figure 63 ToF-SIMS depth profile across the TPBi/PEIE bilayer on a rinsed ZnO layer.

4.2.4. Summary

With the help of the rinsing process, it was finally possible to produce completely solution processed OLEDs in which both electron transport materials are deposited during one spin-coating step.

Figure 64 shows the electrical properties of an OLED with conventionally deposited layers (red) and an OLED with the one-step-processed electron transport layers (black). The current density in the left graph is even lower for the one-step-processed OLED at low voltages. This is beneficial for the device operation since less current means lower degradation of the organic layers through charge carriers. The maximal luminance is identical for both devices. The current efficiency of the conventional device is only better at low luminance. At higher values at operating luminance, both devices show very efficient behavior with values around 14 cd/A.

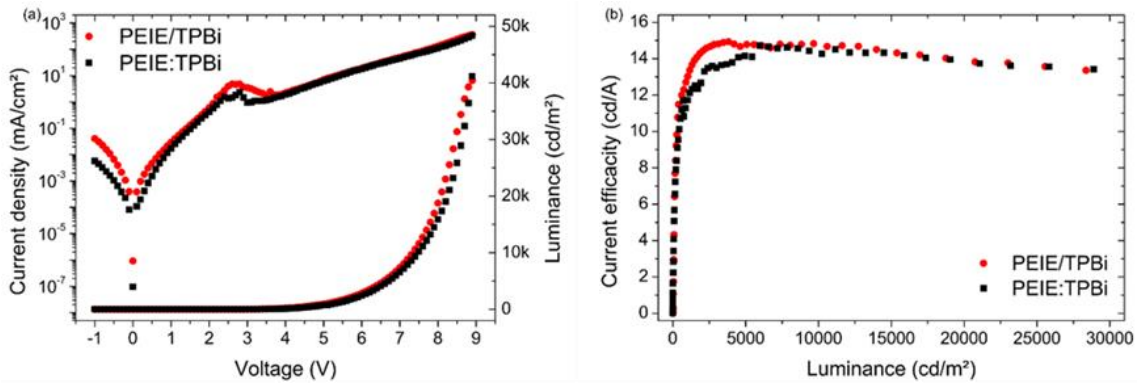

Figure 64 a) Current density and luminance over the applied voltage for a conventionally solution-processed OLED (red) and a device with one-step-processed electron transport layers (black). b) Current efficiency over luminance for the same devices.

Conclusion

In this chapter, the optimized analysis parameters from chapter 3 were used to characterize bilayer samples of critical interfaces in OLED devices.

The most challenging interface is the inorganic-organic hybrid interface at the top electrode. The high difference in sputter rates between inorganic materials and organic materials is challenging for optimal depth profiling. Several approaches for depth profiling of such interfaces have been evaluated. The best option is the combination of monoatomic sputtering and cluster sputtering in a two-step analysis approach. A first analysis of the complete sample is performed with monoatomic sputtering. During this analysis, information about the inorganic part is collected. The destruction of the organic molecules is accepted. Then, on another sample, the inorganic layer is removed by applying scotch tape to the surface and ripping it off. The inorganic part will stick to the tape, leaving the organic part exposed for a second analysis with cluster sputtering.

It has been shown that this approach provides precise information about both parts of the bilayer. The scotch tape removal process is consistent and XPS measurements showed that no inorganic residues can be found on the remaining organic layer and only a thin part of the organic layer is removed together with the inorganic material.

Next to the inorganic-organic bilayer, purely organic bilayers have been investigated as well. Reference profiles across those bilayers confirm the optimal depth profiling parameters that were optimized in chapter 3. The ToF-SIMS profiles showed steady and strong molecular signals across the depth profiles. XPS depth profiles with high-resolution spectra of the valence band regions confirmed the non-damaging character of the argon cluster sputtering. However, the depth profile of the Alq_3 layer showed a small changes in the valence band. The continuous X-ray exposure during the depth profiling seems to be the origin of this degradation. The analysis time during XPS depth profiling must be reduced to prevent damaging of the molecules.

Finally, these optimized parameters were used to characterize an organic bilayer in a completely solution processed OLED in which two materials were spin-coated from one solution. Thanks to the ToF-SIMS results, it was possible to identify problems in the device structure in the form of high roughness in the solution processed ZnO electron injection layer. By improving the fabrication process, it was possible to reduce the roughness of the ZnO layer. This led to a defined interface between the two materials that were deposited from one single solution. The resulting OLEDs exhibit excellent electrical properties that are comparable with devices where both materials are deposited separately. This way, the fabrication process has been reduced by one spin-coating step which results in the economy of time and material and therefore the overall costs of such devices.

Chapter V:

Analysis of complete state-of-the-art OLED devices

1.OLED structure

1.1. Direct and inverse OLED stacks

Different OLEDs have been studied during this thesis. Figure 65 gives an overview of the two OLED types that were analyzed.

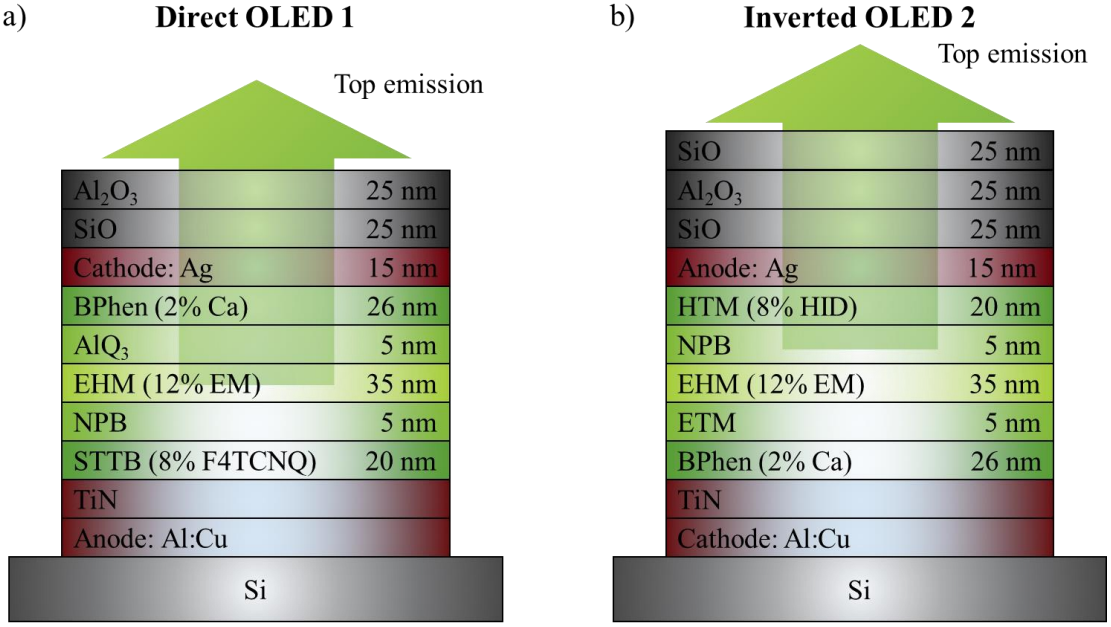

Figure 65 Schematic representation of the studied OLED structures. All OLEDs emit light through the top transparent electrode. OLED 1 and 2 have different ETL and HIL layers.

All OLEDs are top emitting structures. The light is emitted through the top electrode and the encapsulation layers. The encapsulation consists of either two 25 nm thick layers of Al_2O_3 and SiO or three 25 nm thick layers with an additional SiO layer at the top. The top electrode is a 15 nm thick silver layer. Silver is highly transparent for such thicknesses and results in higher luminance for the OLED than structures with other commonly used electrode materials such as aluminum or calcium. Silver is used as cathode or anode in the case of direct or inverse OLEDs, respectively.

The organic stack consists of 5 different organic layers. Doped hole injection and electron injection layers, hole and electron transport layers, and the emissive layer with a host and an emissive material. Only the hole injection material and the electron transport material are different between OLED 1 and OLED 2.

For the direct OLED, the silver electrode is the cathode. Electrons are extracted, or holes injected. In inverse OLEDs, the silver electrode acts as the anode where holes are injected to the device. The organic stack is inverted for direct and inverse OLEDs.

Figure 66 a) shows an image of two OLEDs as they were used in this thesis. The OLED pad has an area of 5 mm by 10 mm. Both electrodes are contacted from outside of the OLED stack via silver contact

pads. The OLED on the left side of the picture is encapsulated with an Al_2O_3/SiO combination. An organic resin was additionally deposited onto the OLED on the right side. Only the OLED without the organic resin (left side) was analyzed during this thesis.

Figure 66 b) shows an electroluminescence spectrum of the direct OLED 1 device which has been acquired at a current density of 11.2 mA/cm^2. The device emits light of a bright green color at a wavelength of 512 nm. The maximal luminance at a driving voltage of 7 V is about 16890 cd/m^2 which is in the range of commercially available state-of-the-art OLED devices.

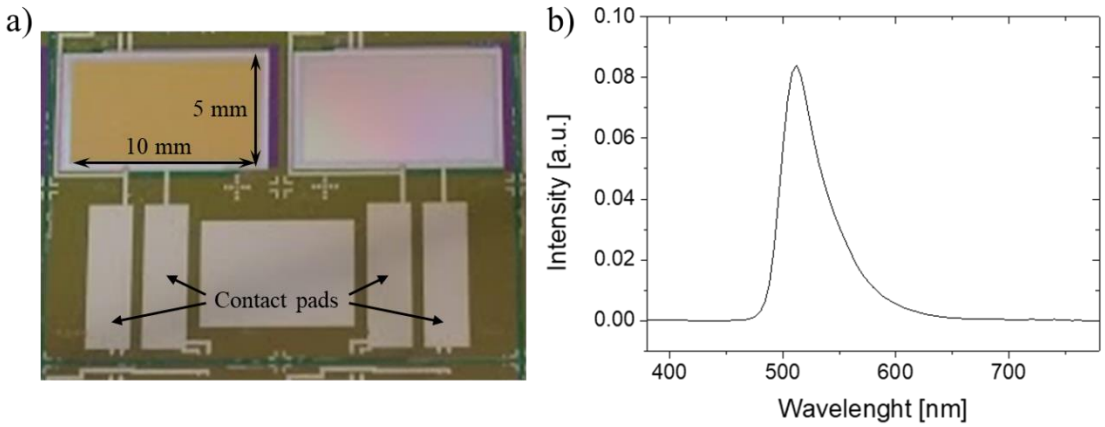

Figure 66 *a) Image of two OLEDs with an area of 5 mm by 10 mm. Both electrodes can be contacted from outside of the OLED by contact pads. The OLED on the left side is encapsulated with 15 nm Al_2O_3 and 15 nm SiO. The OLED on the right has additionally an organic resin on top of the encapsulation. b) Electroluminescence spectrum of the direct OLED 1 device at a current density of 11.2 mA/cm^2.*

2. Depth profiling methods of complete OLED stacks

2.1. Two-Step Analysis Protocol

As already mentioned in chapter 4, a two-step analysis protocol was developed to analyze the complete OLED stack. In the following, a proof of concept will be shown for this two-step protocol on state-of-the-art OLED devices.

2.1.1. Monoatomic sputtering with cesium or argon ions

First, information about the inorganic part of the OLED is gathered by sputtering through the device with a monoatomic sputter species. Cesium and argon ions were used for the ToF-SIMS measurements and the XPS depth profiles, respectively. Table 9 gives an overview of the analysis parameters that were used for the characterization of the inorganic part of the OLEDs.

Table 9 Summary of the XPS and ToF-SIMS analysis parameters that have been used for the characterization of the inorganic part of the OLEDs

ToF-SIMS	**Species**	**Energy**	**Current**	**Pulsing**	**Raster size**
Analysis	Bi_3^+	30 keV	0.45 pA	20 ns	150 x 150 µm²
	Species	**Energy**	**Current**	**Sputter time**	**Raster size**
Sputter	Cs^+	2 keV	60 nA	1 s	500 x 500 µm²
XPS	**Source**	**Energy**	**Power**	**Pass energy (energy step)**	**Diameter**
X-Rays	Al $K\alpha_1$	1486.6 eV	25 W	Core level: 23.5 eV (0.05 eV) Valence band: 46.95 eV (0.05 eV)	100 µm
	Species	**Energy**	**Current**	**Sputter time**	**Raster size**
Sputter	Ar^+	2 keV	40 nA	60 s	1 x 1 mm²

Figure 67 shows the negative secondary ion Cs^+-profile of the direct OLED 1 (Figure 65 a)). The encapsulation layers (Al_2O_3 and SiO) can clearly be identified by the Al^- and Si^- signals. The silver top

electrode as well as the bottom electrode consisting of a thin TiN injection layer and the actual Al:Cu electrode are also indicated by their respective characteristic secondary ions (TiN^- and Al^-). None of the molecular ions in the organic stack could be detected. However, characteristic non-organic ions can help to differentiate different layers in the organic stack. The Al^- ion shows a small peak in the organic stack. This indicates the position of the Alq_3 layer. The weak Ir^- signal stems from the emissive material EM and the F^- signal shows the position of the F4TCNQ dopant in the hole injection layer. No calcium signal can be identified in the negative secondary ion profile. Calcium has a low electronegativity and is likely to be ionized positively. Therefore, the calcium is only detected in the positive secondary ion mode which is not shown here.

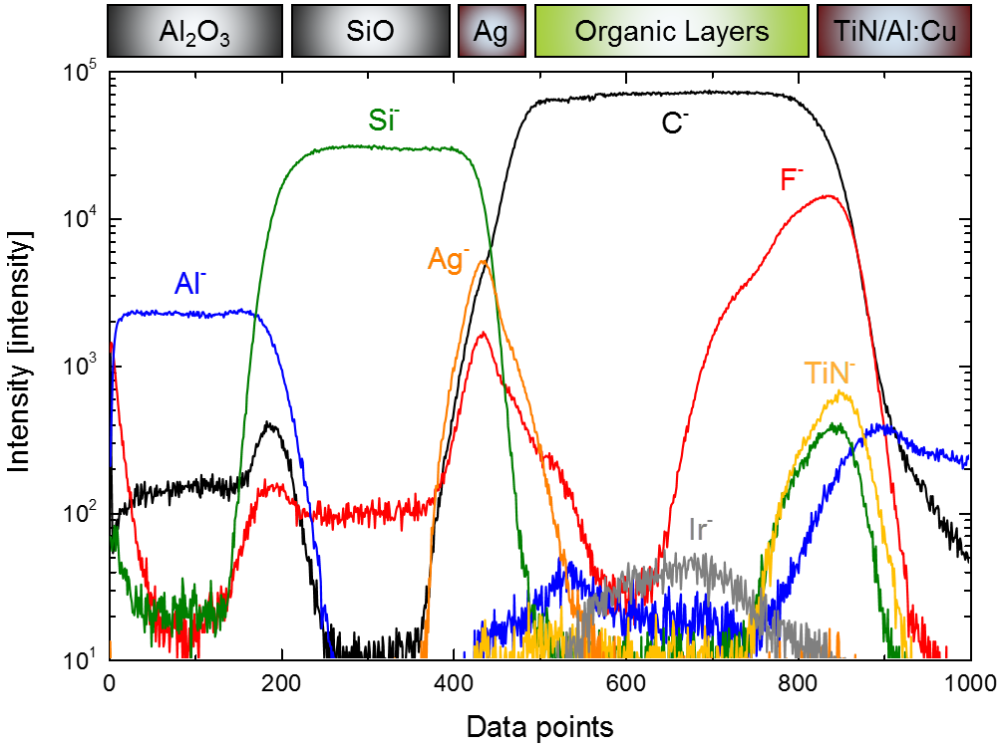

Figure 67 Negative ToF-SIMS depth profile of the direct OLED 1 sample. 2 keV Cs^+ sputtering was used for sputtering and 15 keV Bi_3^+ for analysis to gain information about the inorganic layers in the OLED.

A similar measurement of the inorganic part by monoatomic sputtering can be done in the XPS. The analysis parameters can be found in Table 9.

In this case, the depth profile was generated by using the information from survey spectra at each data point. Both low energy electron and ion bombardment have been used to counter charging effects on the sample. Photoelectrons were detected using an analyzer pass energy/resolution of 117.4/1.6 eV and an energy step of 1 eV. This ensures a fast profile acquisition. Core level spectra can also be acquired during this analysis to gain information about the exact oxidation states of silicon, aluminum or silver at the interfaces, but this takes considerably more time and was therefore not done for this proof of principle experiment. The result is shown in Figure 68.

The quantification of the data corresponds well to the expected elemental ratios for the encapsulation layers. The ratio of Si to O in the SiO layer is 50:50 and the ratio of Al to O in the Al_2O_3 layer 40:60. However, the maximum of the Ag concentration lies at only 80 %. A composition of 100 % is expected. This illustrates the main problem for the quantification of such samples in XPS. Due to the relatively fast sputter rate in the silver layer and its small thickness, it is not possible to acquire a spectrum of the pure silver layer without contributions from the layers around. Since XPS probes photoelectrons generated from up to 10 nm deep into the sample and surface roughening during inhomogeneous sputtering, there are contributions from three different layers at a sputter time of 2000 s in the profile. This is where the quantification fails.

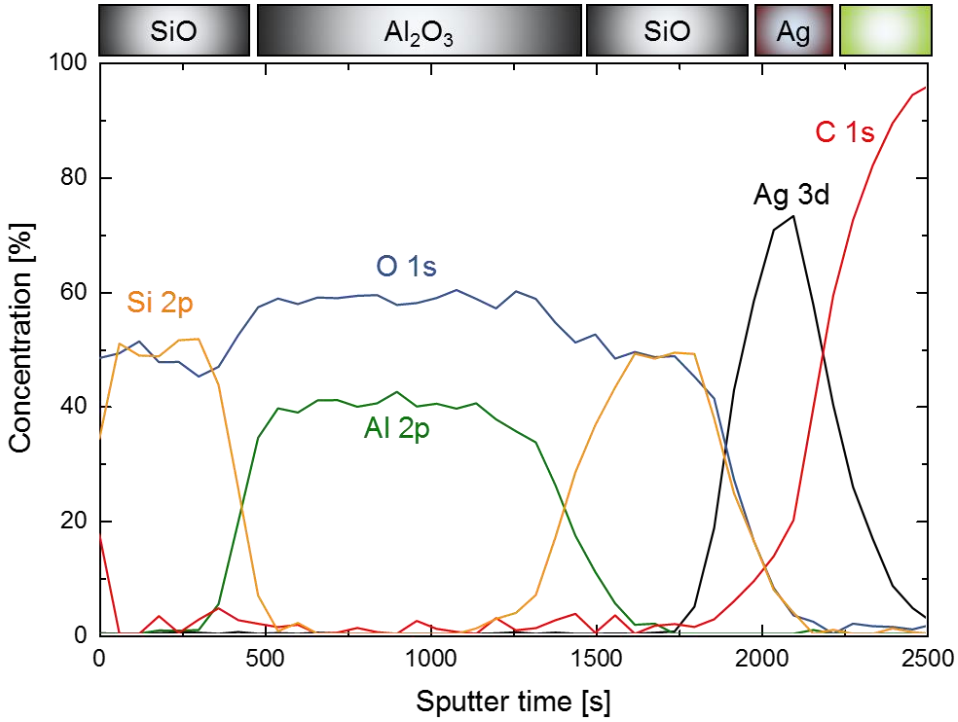

Figure 68 XPS depth profile of the direct OLED 1 sample with modified encapsulation layers. The encapsulation has an additional SiO layer on top of it. 2 keV Ar^+ sputtering was used for sputtering.

2.1.2. Argon cluster sputtering

After the analysis of the inorganic part, the topmost inorganic layers, namely the Al_2O_3/SiO encapsulation stack and the silver electrode, are stripped from the OLED. This is done by applying 3M adhesive tape to the sample and ripping it off. In the ideal case, only the inorganic layers stick to the tape, leaving the organic layers exposed. It has been found, that the success rate on inverse OLED stacks is 100 %. However, this process is not always reliable on direct OLEDs (success rate about 50 %). The reason for this effect is most likely a difference in the adhesion between the top electrode and the EIL or HIL for direct and inverted devices, respectively. This is why most of the OLEDs that were studied throughout this thesis were inverse samples. Since the removal process leaves the organic layers exposed

without encapsulation, it is indispensable to perform this operation under protected environment. Here, the samples are taken out of the ToF-SIMS analysis chamber. The removal process is then performed in the adjacent glovebox. After the removal process, the sample is put back into the ToF-SIMS instrument for the analysis of the exposed organic stack with argon cluster sputtering. The parameters from chapter 3 were used for the data acquisition.

Figure 69 shows the positive secondary ion depth profile of the organic stack in the direct OLED 1 sample. All five molecular ions can be detected except for F4TCNQ, the dopant in the HIL. This electron acceptor can only be detected in the negative mode. Again, positive and negative secondary ion profiles have been acquired but only the positive profile is shown.

The analysis of organic molecules is more complex than the analysis of the inorganic parts. It can be seen that for example the NPB^+ signal overlaps into the adjacent EHM:EM and STTB:F4TCNQ layers. The contribution of the NPB^+ signal in those layers seems important but considering the logarithmic scale for the intensity, the amount is negligible in comparison to the maximum signal in the NPB layer itself. Additionally, contributions from overlapping fragments from the adjacent molecules can be the source of such high signal intensities in other layers. Normalizing the profile to the maximum intensity of each ion can be a solution to better illustrate the different layers. Several characteristic fragments are detected as well and can be used as additional information for each molecule. For clarity, only the molecular ions are shown in Figure 69.

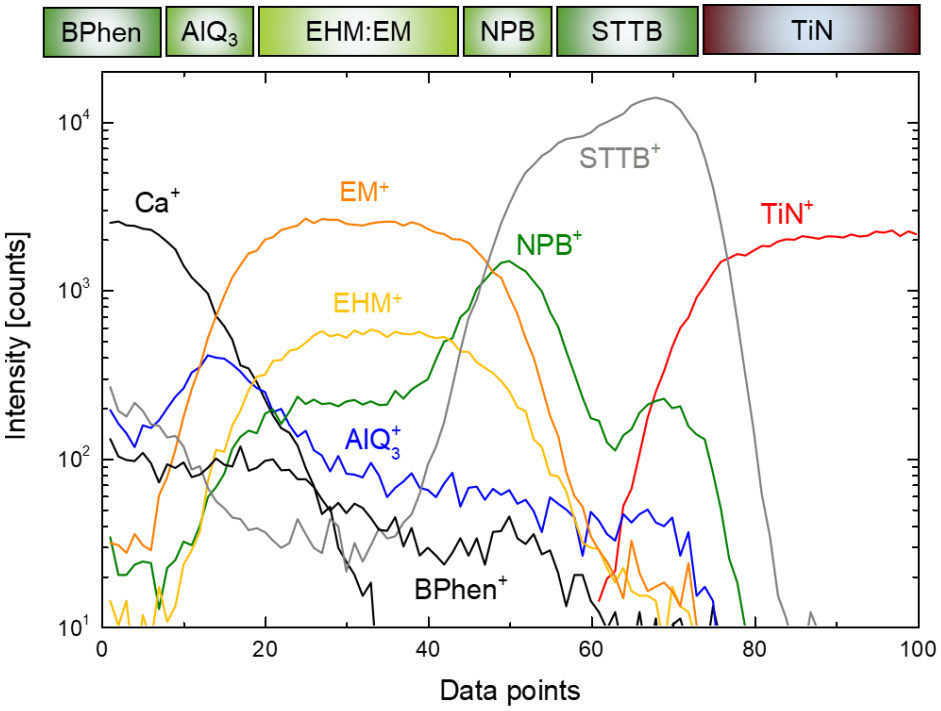

Figure 69 Positive ToF-SIMS depth profile of the direct OLED 1 sample. 5 keV Ar_{4500}^+ was used for sputtering and 30 keV Bi_3^{++} for analysis to gain information about the organic layers in the OLED after the topmost inorganic layers have been removed.

Even though the mass resolution is very high for these measurements (about 7000 m/Δm), some mass overlaps are not avoidable. BPhen is the molecule with the lowest mass in the stack. There are numerous possibilities for fragmentation of the higher mass molecules. The fragments can then cross-link with each other to form even more different fragments. The possibility of forming a fragment with a very similar mass as BPhen is high. That is why it is difficult to define the BPhen layer only by using the $BPhen^+$ signal. The calcium signal can be used to help complete the identification of the layer.

After the second ToF-SIMS analysis, the sample is taken out of the instrument again. In the glovebox, the sample is transferred into a transport vessel that is hermetically sealed. The sample can be taken out of the glovebox and be transferred to the XPS instrument where the transport vessel can be attached to the nitrogen flooded transfer chamber. This way, the exposed organic layers are protected from humidity during the transfer between both instruments.

The final step is the XPS depth profiling of the organic layers. At this point it is indispensable to acquire core level and valence band data. The differences between the different organic molecules is too small to be seen in survey spectra (see chapter 3). The utility of valence band spectra as fingerprints for the organic molecules has also been shown in chapter 3. For the core level spectra, the signal of 15 analysis cycles has been averaged to get the final spectrum. For the valence band region, 30 cycles were used. The remaining analysis parameters have been adapted from chapter 3.

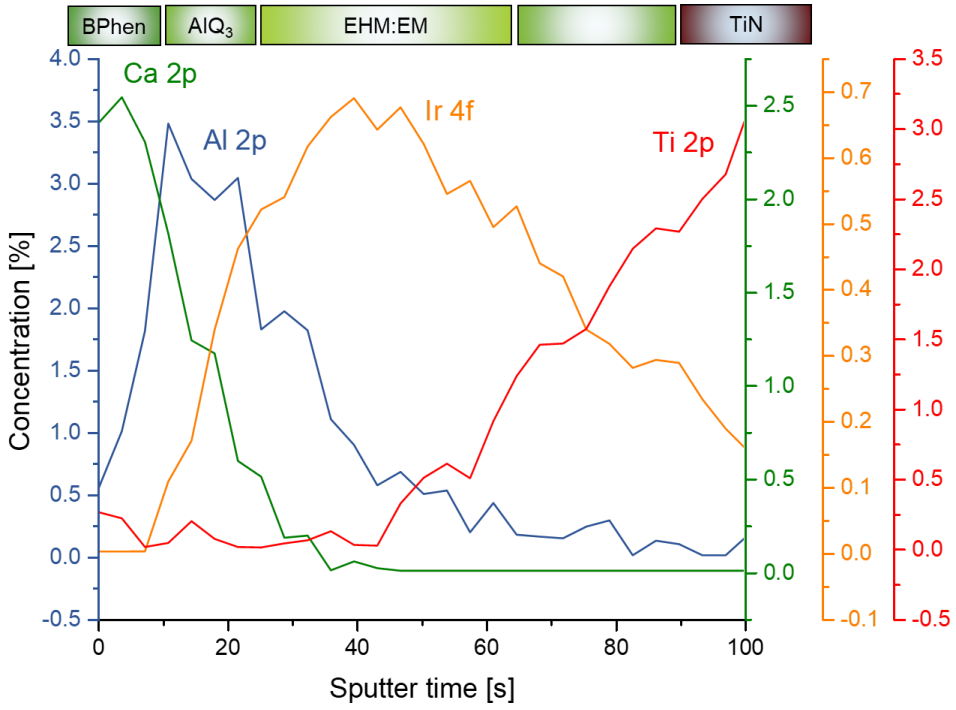

Figure 70 XPS depth profile of the organic part of the direct OLED 1 sample. 5 keV Ar_{4200}^+ was used for sputtering. The elemental percentages of characteristic elements are shown for each layer.

Figure 70 shows the depth profile of the organic part of the direct OLED 1 structure. The elemental concentrations of characteristic elements for each layer are displayed based on the elemental core level signals: Ca 2p for the calcium doped BPhen layer, Al 2p for the Alq_3 layer and Ir 4f for the emissive

material. The F 1s signal for identification of the F4TCNQ molecule was not recorded. The rise of the Ti 2p signal refers to the bottom TiN charge injection layer. The C 1s and N 1s signal are not shown but they were recorded, and their contributions have been accounted for to calculate the elemental concentrations. The relatively low abundance of titanium with a maximum of 3 % shows that the interface has not yet been reached. Further profiling would have been needed but was not possible due to time constraints.

As for the quantification, the concentration of calcium at the surface is 2.5 % which is a bit higher than the nominal doping value of 2 %. However, the signal to noise ratio is low for the Ca 2p peak so that the difference in concentration lies in the range of error. The value for aluminum is 3.5 %, slightly lower than in the reference measurements of the Alq_3 single layer sample (4.2 %). This difference could come from contributions of surrounding layers because of the extreme thinness of the Alq_3 layer (5 nm) in the stack. The actual concentration of iridium in the emissive layer cannot be estimated because the molecular structure of the host is unknown.

2.1.3. Conclusion

Overall, these results show the possibility of depth profiling the organic as well as the inorganic part of complete OLED stacks.

Depth profiles with monoatomic sputter sources provide sharp ToF-SIMS profiles and good quantification results in the XPS measurements. Once the top inorganic layers are stripped, the organic stack can be analyzed by argon cluster sputtering. The ideal analysis parameters that have been determined in the previous chapters ensure minimum induced damage. Even though quantification of these kind of samples is difficult because of the thin layers and the small elemental concentrations, the difference between different treated samples can be detected. This is of interest during the analysis of degradation in electrically aged devices, which will be investigated in section 3.

2.2. Beveled crater analysis

2.2.1. Sample preparation

Besides classical depth profiling, the preparation and characterization of beveled craters has been studied. A schematic representation of the analysis protocol can be found in Figure 71.

The beveled crater is fabricated in the ToF-SIMS instrument. After the inorganic layers are stripped from the OLED, a classical depth profile is acquired. With this depth profile the sputter time and the dose that is needed to reach the bottom electrode is determined. This time can then be used to perform a sputter profile with a dose gradient. A linear gradient is applied, and argon clusters are used for

sputtering. This ensures minimal damaging of the organic layers by the sputter beam. The surface will be untouched at the left side of the crater and the sputter dose will be linearly increased towards the right side where it reaches the maximum dose that was calculated with the depth profile. The beam starts to sputter along the left side of the crater from top to bottom before it moves on to the next line. The sputter time of the next line is increased which is equivalent to a higher dose. Sputtering of the last line on the right side will take the longest. The direction of the sputter beam is perpendicular to the direction of the dose gradient. It bombards the sample surface at a 45° angle from top to bottom. This is thought to minimize the redeposition of sputtered material. However, this has not been studied.

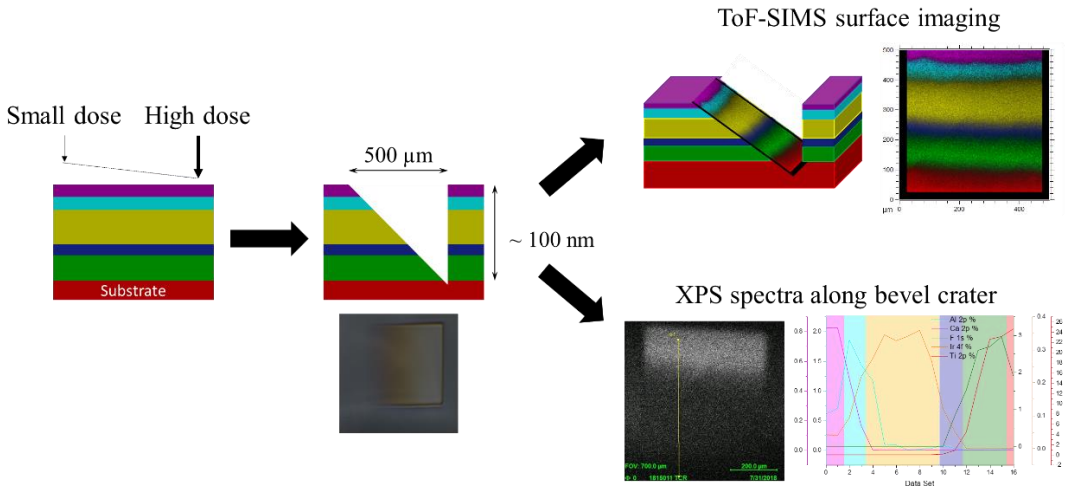

Figure 71 Schematic representation of the beveled crater analysis protocol. After sputtering with a dose gradient, the beveled crater is formed and can be analyzed by ToF-SIMS surface imaging or by XPS measurements along the crater.

The creation of beveled craters opens up new possibilities for characterization. It is possible to create surface images of multilayer samples with ToF-SIMS and to perform XPS depth profiling without additional sputtering in between each data point acquisition.

The beveled crater increases the surface of each layer. The size of the sputter crater is 500 by 500 µm^2 and the thickness of the whole organic stack is about 100 nm with the thinnest layers only being 5 nm thick. Through the shallow angle of the beveled crater, the exposed surface for these thin layers increases to several tens of micrometers. This makes surface imaging with ToF-SIMS possible. The bismuth beam can be focused to about 100 nm which results in high resolution chemical images of the beveled crater. For an image of 500 µm by 500 µm of the complete organic part of the OLED, which is about 100 nm thick, 1 µm in the image equals to about 0.2 nm in depth. Even argon clusters can be used as the analysis beam. This would decrease the lateral resolution to about 20 µm and the mass resolution to only a few hundred m/Δm. Moreover, the signal intensity decreases significantly. However, the fragmentation should decrease when using large argon clusters as they have shown to induce less damage to organic molecules than the small bismuth clusters (see chapter 3).

2.2.2. ToF-SIMS imaging in beveled craters

Figure 72 illustrates the difference between argon cluster imaging and bismuth imaging. The TCTA:Ir(mppy)$_3$/Alq$_3$ bilayer sample from chapter 4 was prepared with two beveled craters and has subsequently been analyzed by ToF-SIMS surface imaging. Figure 72 a) shows the secondary ion image that has been recorded over 5 scans with a resolution of 512 by 512 pixels on an area of 500 by 500 µm^2. 10 shots per pixel have been fired during the analysis. For the analysis beam, 10 keV Ar$_{1000}$ clusters were used at a current of about 0,05 pA. The respective mass spectrum can be found in Figure 72 c). For the secondary ion image in Figure 72 b), the exact same parameters have been used except for the analysis beam. Here, the 30 keV Bi_3^{++} beam was used at a current of about 0,09 pA. The respective mass spectrum is found in Figure 72 d).

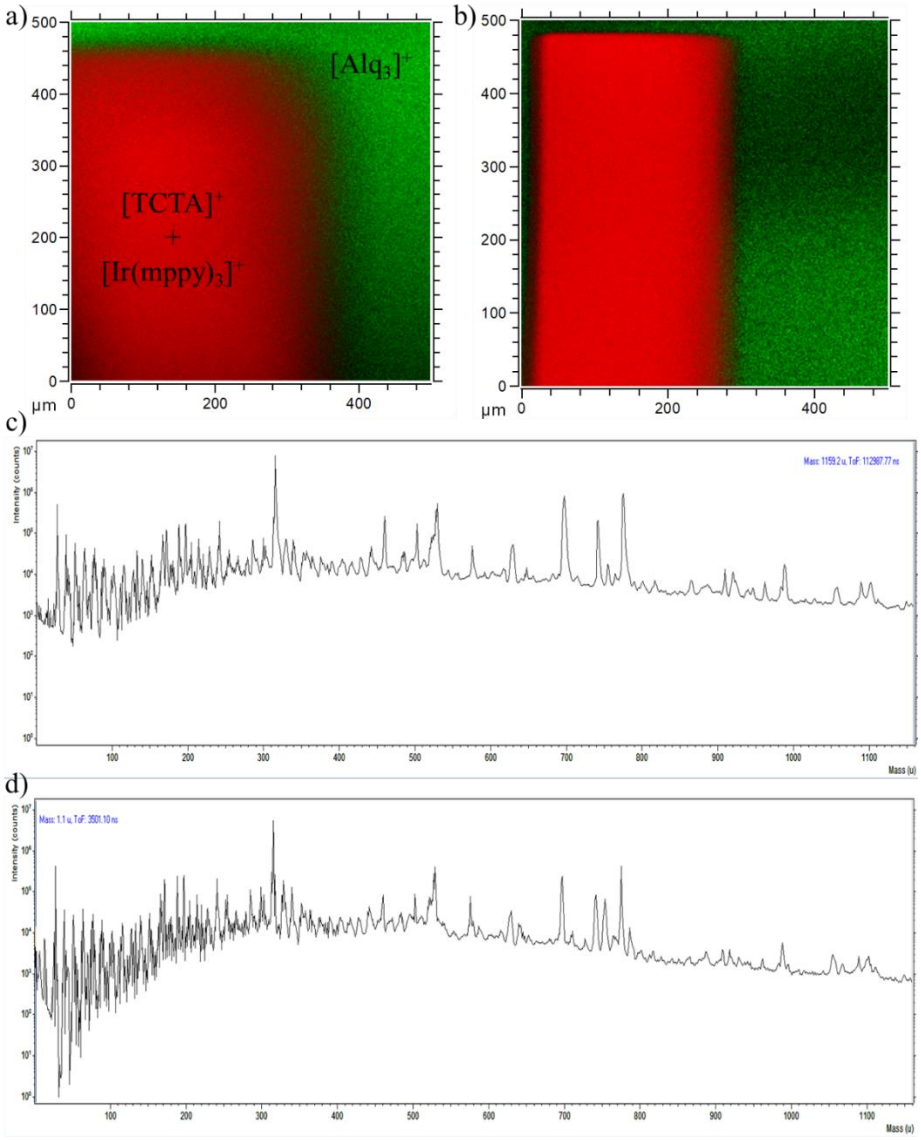

Figure 72 a) and b) Secondary ion images of the TCTA:Ir(mppy)$_3$/Alq$_3$ bilayer sample acquired with 10 keV Ar$_{1000}$ clusters and 30 keV Bi_3^{++} ions, respectively. The green signal is an addition of the molecular signals of TCTA and Ir(mppy)$_3$ while the red signal shows the molecular signal of Alq$_3$. The graphs in c) and d) show the mass spectra for the argon cluster analysis and the bismuth analysis, respectively.

The images show the addition of the molecular signals of TCTA and $Ir(mppy)_3$ in green and the molecular signal of Alq_3 in red. The direct comparison of both images shows a much better-defined interface for the bismuth image. The highly focused Bi_3^{++} beam provides better lateral resolution than the argon cluster beam. The interface width in the Bi_3^{++} image is about 12 µm while it is almost 22 µm for the argon cluster image. The broad interface in the argon cluster image can be a problem during the analysis of samples with thinner layers. Some of the layers in the OLED devices have a thickness of only a tenth of the layers that are analyzed here.

The mass spectra show some differences. At low masses, there are more peaks in the bismuth spectrum. This is expected due to the higher fragmentation by the bismuth bombardment compared to cluster bombardment. However, at higher masses, all important characteristic fragments can be found in both spectra. Moreover, the bismuth spectrum exhibits a higher mass resolution than the cluster spectrum thanks to the extremely short analysis pulses. With the higher primary ion current (0.09 pA compared to 0.05 pA for the argon clusters) and a good ionization yield, the intensity of the large secondary ions is comparable to that for the argon cluster analysis despite the higher fragmentation. Overall, the use of Bi_3^{++} ions for the imaging seems to have more advantages than the use of argon clusters. The argon clusters exhibit lower fragmentation but at the same time, the bismuth analysis yields acceptable intensities for the more interesting high mass fragments.

2.2.3. XPS analysis of beveled craters

Another possibility that arises with beveled craters is the acquisition of XPS spectra along the crater. The beam diameter can be reduced to 7 µm. This way, several spectra can be taken along a line that crosses the beveled crater and the resulting information can be transformed in a depth profile. The advantage of using the beveled crater for the creation of depth profiles is that each point of the spectrum is only analyzed once. During traditional depth profiling, the X-ray beam is focused on the same sample spot during the whole analysis. During the creation of depth profiles with the help of beveled craters, the beam will be focused on a new sample spot for each data point. The overall X-ray exposure is therefore substantially reduced which results in a decreased degradation due to irradiation.

The different possibilities for XPS depth profiling with beveled craters will be explained in section 3.3.2.

3. Comparison of aged and non-aged devices

For the final part of this thesis, aged OLEDs have been studied. Chemical depth profiles of aged devices are compared to fresh devices to gain information about degradation mechanisms in OLEDs. Some studies on environmentally aged devices have been performed in the past by different groups [137], [146]. Also different fabrication methods have been examined by depth profiling techniques [134], [144]. Only one study of electrically aged devices is known [164]. However, the sputtering in this publication was done by using an oxygen beam. The molecules in the organic part were destroyed. Here, the chemical depth profiling of electrically aged state-of the-art OLED devices by argon cluster sputtering is shown.

3.1. Electrical ageing

To age the devices, they have been turned on under controlled conditions for a specific amount of time.

Before the ageing process, reference spectra for all analyzed devices are recorded. Figure 73 a) shows an example for the calibration measurement before the ageing on the direct OLED 1 device.

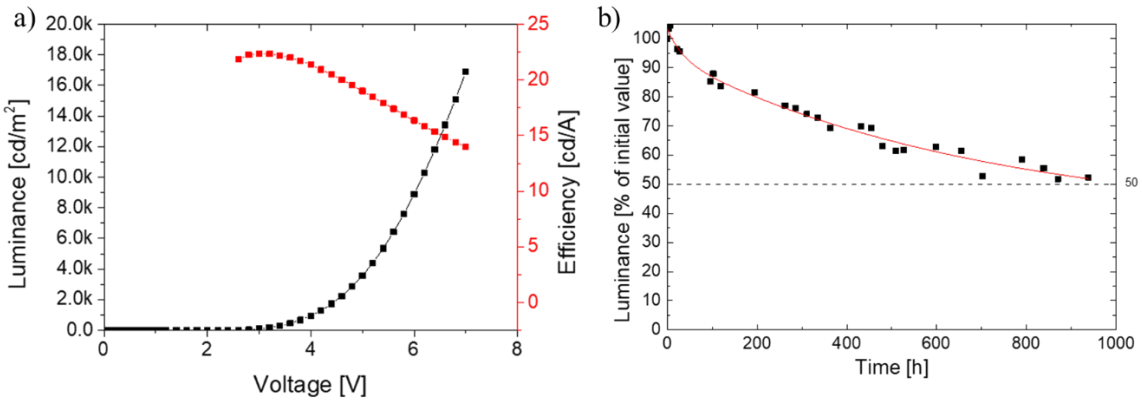

Figure 73 *a) Electrical calibration measurements for the direct OLED 1 device. The luminance as well as the electrical current is measured as a function of the applied voltage. With the current it is then possible to calculate the efficiency of the device. b) Degradation curve of the device where the luminance is recorded over time while a constant current is applied to the device.*

The device is connected to a DC voltage/current source. As the voltage is slowly increased, the current that flows through the device is measured. The sample is mounted in an integrating sphere that focusses all the emitted light onto a photodiode which is used to measure the luminance of the device. With the luminance and the current, it is possible to calculate the efficiency at each datapoint. At the same time, electroluminescence spectra can be acquired by focusing the emitted light into a spectrograph where it is split into the different wavelengths and a spectrum is recorded by a CCD camera (Figure 66 b)).

After these reference measurements, some of the samples are analyzed by ToF-SIMS and XPS depth profiling as “fresh” OLEDs, while others are aged electrically. For the ageing, the samples are mounted in a box, where they are contacted and placed under a photodiode. A constant current is applied to the sample and the luminance is measured periodically. Here, a current of 10 mA was used. This corresponds to a voltage of about 3.85 V. The first measurement of the luminance acts as the reference for the aging experiment and is defined as the initial luminance. Over time, the luminance will decrease due to degradation of the device as can be seen in Figure 73 b). Once the luminance reaches a value of only 50 % of the initial value, the experiment is stopped, and the OLEDs are analyzed as “aged” devices.

3.2. ToF-SIMS measurements on whole OLED stacks

3.2.1. ToF-SIMS depth profiling

3.2.1.1. Results and interpretation

3.2.1.1.1. Monoatomic sputtering

First, the ageing of the inverted OLED 2 structure has been analyzed by traditional ToF-SIMS depth profiling. In Figure 74, the ToF-SIMS depth profile of that sample in positive mode and with monoatomic 1 keV Cs^+ sputtering can be seen for a fresh device (plain lines) and an aged device (dashed lines). As a reminder for the stack that was analyzed, the position of the different layers is indicated roughly over the graph.

Both profiles superimpose almost perfectly. The measurements were performed directly one after the other with a stable sputter current. However, some small deviations between the fresh and the aged sample are visible. In both samples, there is a fluorine contamination of the bottom electrode as can be seen from the purple Cs_2F^+ peak near the TiN layer. However, in the aged device, the signal extends further into the organic part. A stronger shoulder peak is observed in the BPhen:Ca layer that is marked by the yellow Ca^+ signal.

Fluorine contamination is also found between the upper encapsulation interface of SiO and Al_2O_3. The aged device exhibits a stronger Cs_2F^+ signal at this interface.

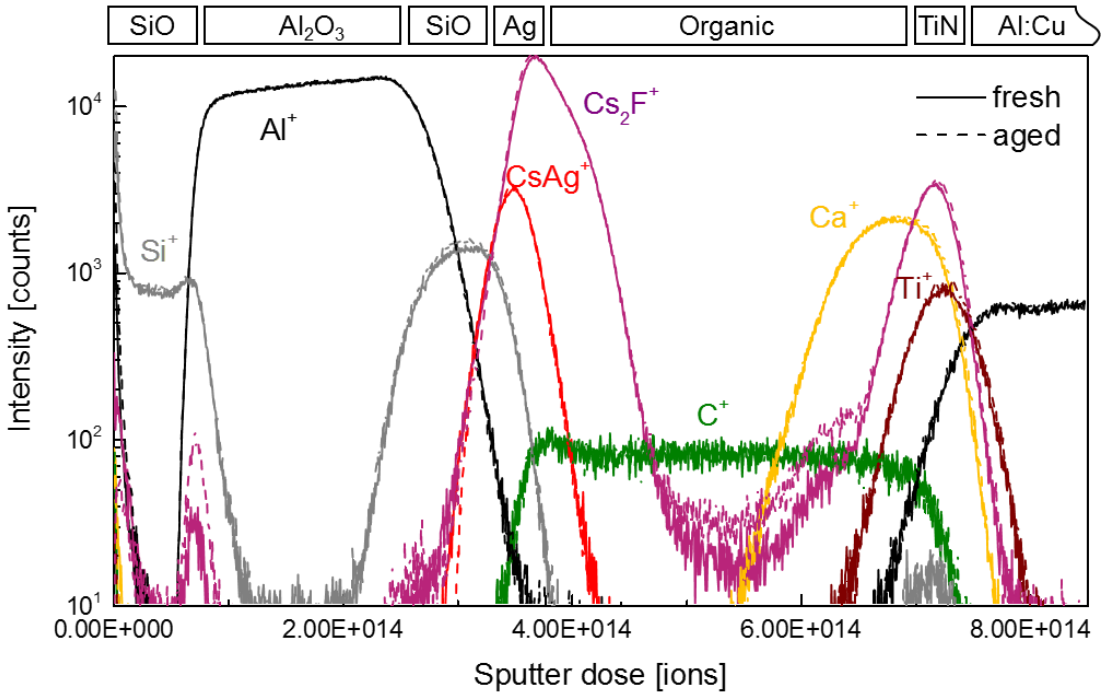

Figure 74 ToF-SIMS depth profile of the complete inverted OLED 2 device in positive mode. 1 keV Cs^+ was used as the sputter beam. The spectra of a fresh device (plain lines) and an aged device (dashed lines) are overlaid.

A similar trend for the fluorine signal is observed in the negative secondary ion mode that is shown in Figure 75.

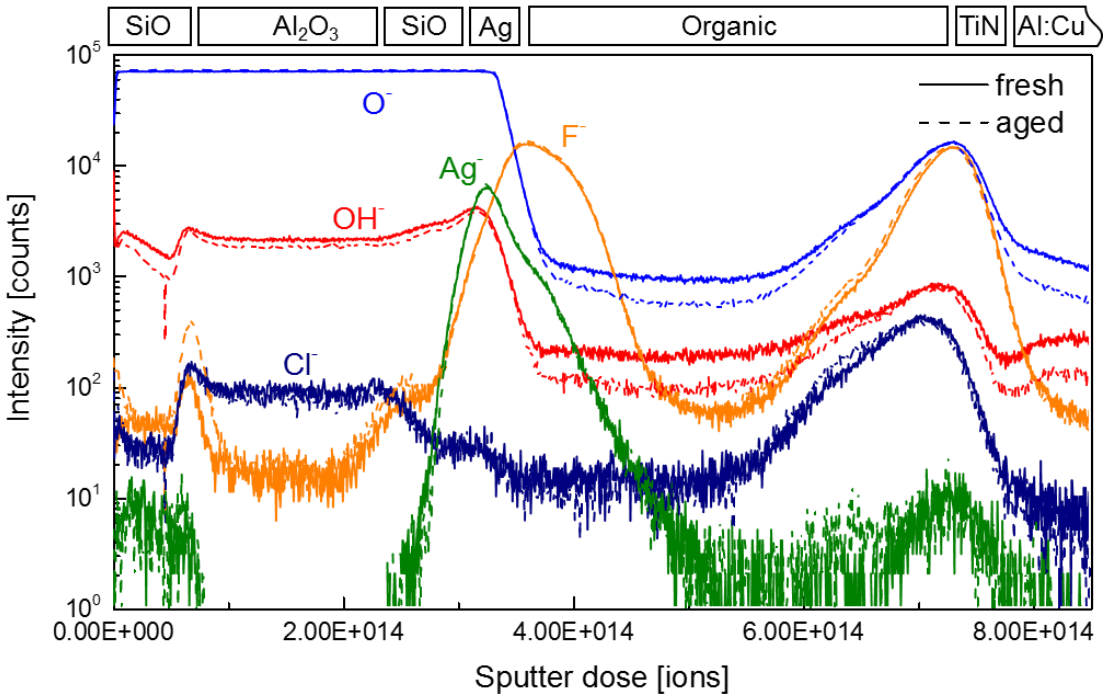

Figure 75 ToF-SIMS depth profile of the complete inverted OLED 2 device in negative mode. 1 keV Cs^+ was used as the sputter beam. The spectra of a fresh device (plain lines) and an aged device (dashed lines) are overlaid.

The same contaminations as in the positive mode are visible. The shoulder peak in the BPhen:Ca layer is again differently pronounced although the difference appears not as big as in the positive mode.

However, not only the fluorine appears to be a contaminant at the TiN interface, the blue chlorine signal shows a strong peak at the same interface. Moreover, it exhibits the same diffusion behavior into the BPhen:Ca layer, where the shoulder peak is more pronounced after the device ageing.

Other interesting ions in the negative mode are O^- and OH^- as they are considered to be responsible for a number of degradation mechanisms in organic electronics [165]. The oxygen signal is saturated in the oxides that build up the encapsulation part of the device. In the organic part, the signal is lower and a substantial difference between the fresh and the aged device can be seen. The signal is lower in the aged OLED. This might indicate the reaction of oxygen with some of the molecules. The formation of new molecules or fragments in which the oxygen is bound might explain the reduced intensity of O^-. The OH^- ion shows a similar curve. However, the signal is not saturated in the encapsulation part. Throughout all three oxide layers, the signal is slightly lower in the aged device, but the difference is not as important as in the organic part.

The peak of the O^- signal at the TiN electrode shows that a thin oxide layer is formed at this interface. This is confirmed by the detection of the TiO^- ion which is not shown. The TiO^- signal does not change after ageing, however.

The last secondary ion signal in Figure 75 is Ag^-. The electrode does not change. However, there is a small additional signal at the bottom electrode near the TiN layer. In the aged device, the Ag seems to have diffused into the BPhen:Ca layer. Beneath the shoulder peaks of fluorine and chloride, a small silver peak can be observed for the aged device that is not present in the fresh OLED.

The presence of contaminants like chlorine, fluorine and silver in the organic layers can alter the electronic band stucture of the layers. Since every layer in the organic stack is designed to ensure an efficient charge carrier recombination in the emissive layer, it is important that all layers are stable and that they fulfill their purpose. Small changes in the band structure may change the energy alignment of the layers and make it more difficult for charge carriers to pass. This can result in an unbalanced charge carrier distribution and therefore in decreased efficiency of the device.

A temporary fluctuation of the analysis current might be suspected in the depth profile of the aged device near the BPhen layer since most of the shown signals exhibit the same trend at this point. However, a higher bismuth current would cause a rise of intensity for all secondary ions, but since the oxygen signal shows the inverse tendency, and the carbon signal, that is not shown, has the same intensity in the fresh and in the aged device, this is not the case.

3.2.1.1.2. Argon cluster sputtering

As explained in section 2.1, this was the first part of the ToF-SIMS analysis to gain information about the inorganic layers in the device. For the second part, the encapsulation and the top electrode were stripped from the device by scotch tape. Afterwards, new depth profiles with argon cluster beams were

acquired. Because of the huge amount of different secondary ions, only certain signals will be shown in each graph to keep the illustrations clear.

- Comparability of spectra

Before any conclusions can be made from comparing two depth profiles, it must be made sure that the primary ion current did not change during the analysis of both samples. Figure 76 shows therefore selected secondary ions in the positive (top) and negative mode (bottom) that were detected during the depth profiling of the organic part with 5 keV Ar_{4500} sputtering. Again, the sputter current was very stable. The profiles of the fresh and the aged device show almost a perfect overlay. Moreover, the maximum intensity for the selected ions is the same. Especially the intensity of the bottom electrode (TiN^+ in the positive mode, TiO_2^- in the negative mode) shows the same values in both profiles. Since this signal is not expected to change, and the other signals show similar maximum intensities, the profiles are comparable.

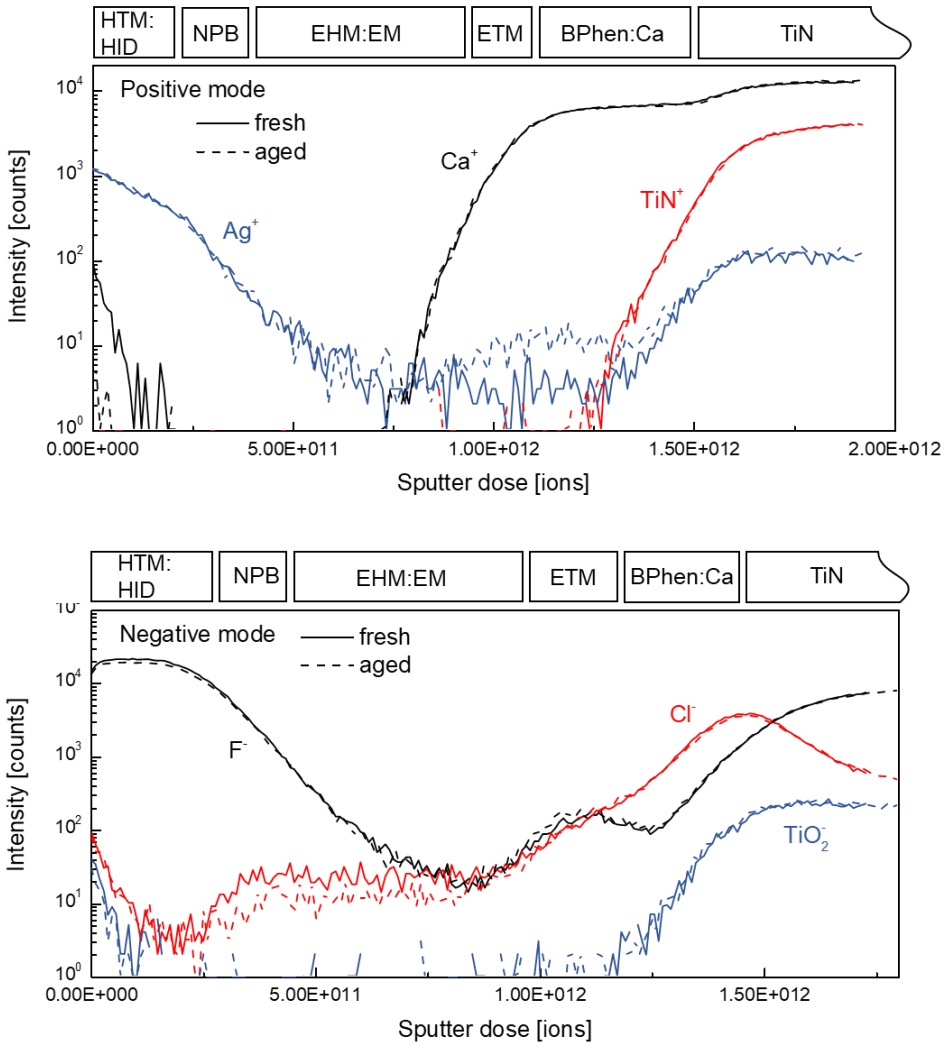

Figure 76 ToF-SIMS depth profiles of the organic part of the inverted OLED 2 device in positive (top) and negative mode (bottom). 5 keV Ar_{4500}^+ was used as the sputter beam. The spectra of a fresh device (plain lines) and an aged device (dashed lines) are overlaid.

- Contaminant diffusion

There are already some interesting findings in these two plots. The Ag^+ signal in the upper graph confirms the presence of silver at the bottom TiN electrode. Moreover, there are also signs of diffusion of silver into the BPhen:Ca layer that was already seen in Figure 75. It should be noted that the Ag^- signal at the surface of the sample seems high, but the XPS measurement of the scotch tape in Figure 56 showed that the silver content of the exposed organic layer lay below the XPS detection limit and must therefore be less than about 1 %. This small silver contamination at the sample surface could be expected to be a residue from the top electrode, but the XPS spectrum from the copper tape in Figure 18 of chapter 4 as well as the shape of the Ag^+ signal in the positive ion depth profile in Figure 76 indicate rather a diffusion of silver into the HTL of the organic stack. The XPS analysis showed, that the breaking point during the scotch tape process lies somewhere inside the uppermost organic layer, which suggests a complete removal of the top electrode. The depth profile in Figure 76 shows the exact same intensity of silver at the sample surface which would be surprising if it was due to random top electrode residues. A diffusion of silver into adjacent organic layers seems more likely and has already been observed in the literature [166].

In the negative profile, the fluorine signal shows the shoulder peak that was seen in the inorganic profiles. However, the difference between the fresh and the aged sample is only marginal. However, with the detection of molecular signals, the exact location of the shoulder peak can now be determined. The bars over the graph, that indicate the layer names, were created by using the molecular signal of each layer. It can be seen, that the F^- shoulder peak does not lie in the BPhen:Ca layer, but rather in the ETM layer. For the chloride peak, a very small difference can only be suspected. However, in the emissive EHM:EM layer and in the NPB layer, the Cl^- signal decreases with the ageing of the device. This tendency might not have been visible in Figure 75 because of the high noise in the Cl^- signal in that region.

The profiles in Figure 76 confirm the stable analysis parameters throughout all of the measurements so that the profiles can be overlaid, and the intensities of fresh and aged devices can be compared directly.

- Comparison of molecular secondary ions before and after ageing

Figure 77 shows the same depth profiles of the organic part of the inverted OLED 2 device as in Figure 76, except that this time, the molecular secondary ions of each layer are shown.

All five layers can be differentiated by using these molecular signals except for the NPB- signal which has a heavy overlap with characteristic fragments of the molecules from the emissive layer.

Overall, no big differences between the fresh and the aged devices can be observed. However, the characteristic fragments of some of the materials show changes. In the following, certain interesting secondary ions have been extracted into individual graphs. The layer interfaces that can roughly be derived from Figure 77 are always indicated by vertical dashed lines.

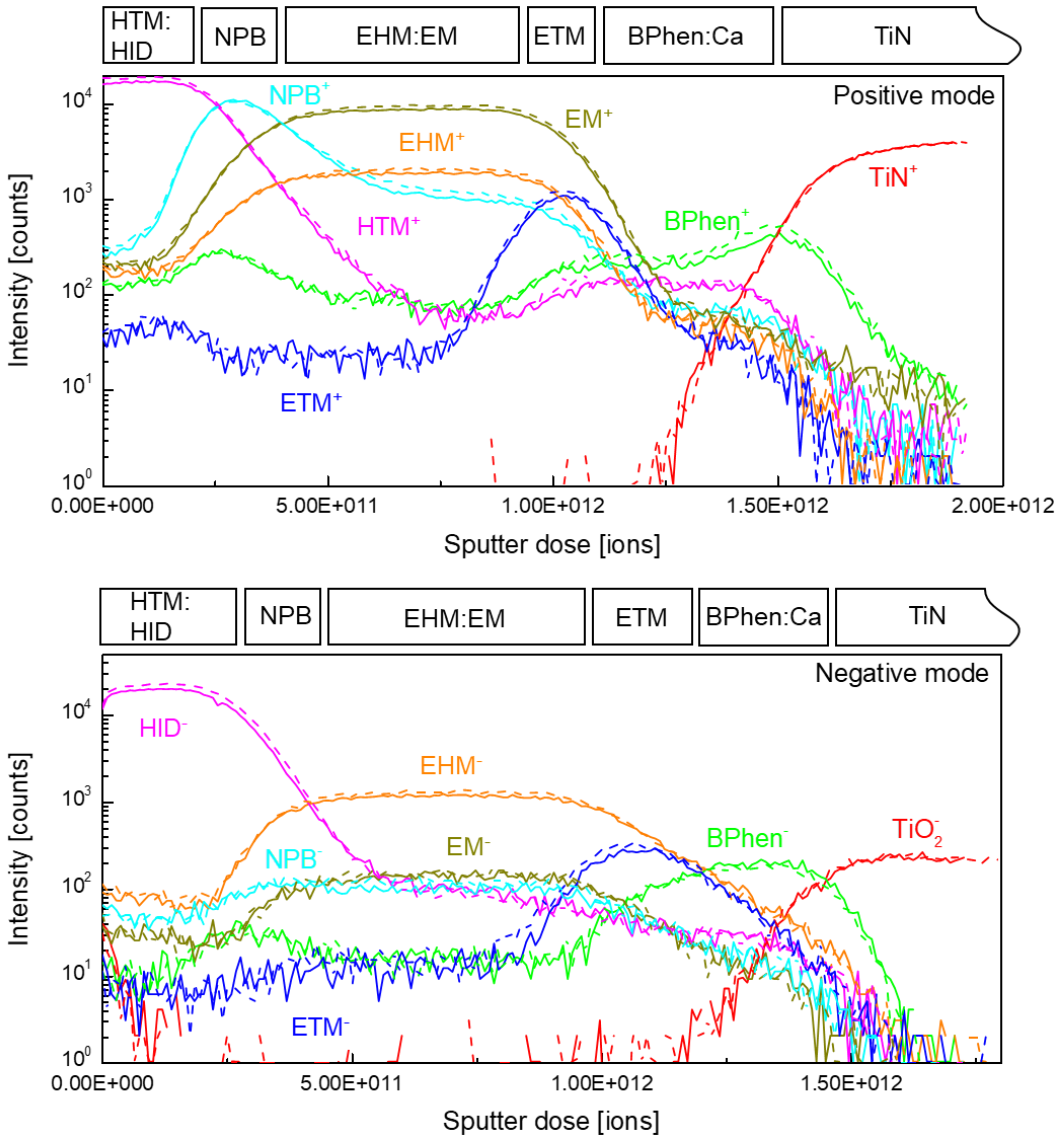

Figure 77 *ToF-SIMS depth profiles of the organic part of the inverted OLED 2 device in positive (top) and negative mode (bottom) with the molecular secondary ions of each molecule. 5 keV Ar_{4500}^+ was used as the sputter beam. The spectra of a fresh device (plain lines) and an aged device (dashed lines) are overlaid.*

- Layer-by-layer comparison of characteristic ions in negative secondary ion mode

Figure 78 a) shows the comparison of the O^- signal in the fresh and in the aged device. Differently than expected from the results in Figure 75, no change between both profiles can be observed. The signal shows in both profiles the same peak at the interface of the organic stack with the TiN electrode, indicating an oxidized electrode. The signal extends to the BPhen:Ca and ETM layers. However, the intensity of the signal does not change. This oxygen contamination is most likely induced during the device fabrication. Other than observed in the depth profiling with monoatomic cesium sputtering, the signal does not extend all the way through the organic stack.

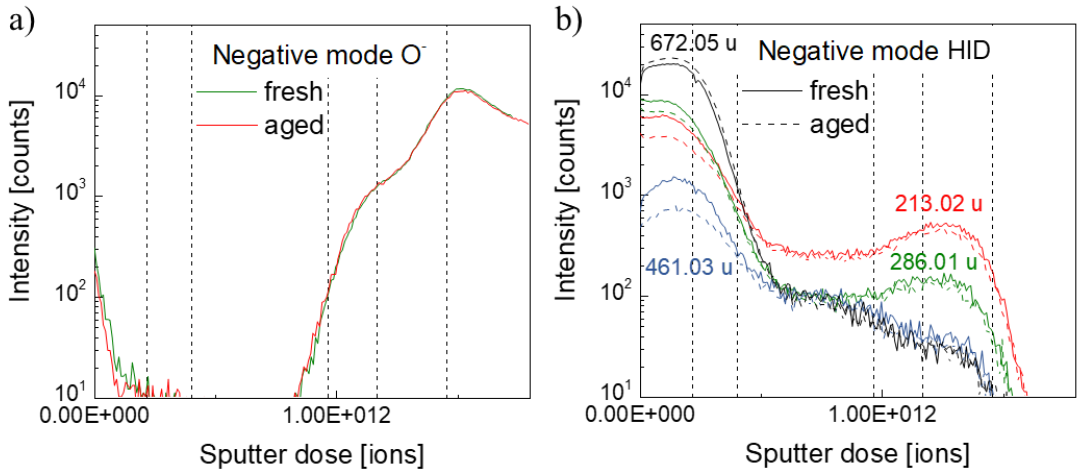

Figure 78 Comparison of the ToF-SIMS depth profiles of the fresh and the aged inverted OLED 2 sample for the O^- signal in a) and some characteristic secondary ions of HID in b).

Figure 78 b) shows the same comparison for some characteristic fragments of the HID molecule which is the electron acceptor that is used as a dopant in the hole injection layer. This is the only molecule in the whole stack that is more likely to be detected in negative mode during depth profiling. The material's chemical structure is not known. Therefore, the molecular secondary ion cannot be determined with certainty. The only certain information about the molecule from reference measurements is that it contains fluorine. The heaviest secondary ion is not necessarily the molecular ion. Some molecules, like BPhen for example, show higher intensities for dimer secondary ions than for the actual mother molecule. The highest mass ion (672.05 u) shows a different behavior than all other ions. The intensity of this fragment increases after ageing which is counter intuitive to the degradation of organic materials through chain scission. All other ions decrease with ageing. This might indicate that the highest mass ion is not the mother molecule. This hypothesis can be reinforced by the assumption that this fluorine containing molecule is from the same family as F4TCNQ that is used in the OLED 1 device as the dopant in the HIL. F4TCNQ has a molecular weight of 276.15 u. The secondary ions of masses 213.02 u or 286.01 u could therefore be the molecular signal of HID. A decrease of the signals after ageing would be a clear indicator for degradation of the molecule and could lead to a dysfunction of the hole injection layer. This could again have an impact on the charge carrier balance inside the emissive layer which can be a reason for reduced device luminance.

- Layer-by-layer comparison of characteristic ions in positive secondary ion mode

Figure 79 shows different parts of the positive depth profiles of the inverted OLED 2 device. In part a), certain characteristic secondary ions of the BPhen molecule are shown. Some changes in the BPhen:Ca layers have been shown already with the diffusion of contamination elements like Cl, F and Ag into the layer after ageing. The intensity of the molecule itself changes also. The detected amount increases in the positive mode. This might be another indicator for an increased amount of those contaminations in the layer. Chlorine and fluorine are strongly electronegative. The presence of such elements could

facilitate the ionization of the organic molecule as it has already been demonstrated for inorganic materials [167]. The result would be an increased intensity for the molecular signal as it is observed. An increased intensity of the BPhen dimer cannot be observed. In previous studies, the formation of dimers during device operation has been suspected to one of the reasons for the device degradation [62].

In parts b) and c) of Figure 79, some characteristic secondary ions of ETM and NPB are shown, respectively. Both ions in the ETM layer show a slightly increased intensity after ageing. As in the case of HID, the chemical formula of ETM is not known. The ion labeled with ETM^+ is the highest mass fragment that was detected in the reference spectrum for this material at 852.34 u. This increased intensity might have the same cause as the increase of the BPhen signal. Moreover, the characteristic fragment with the mass 256.12 u has an overlap with the $C_{18}H_{11}N_2^+$ fragment of BPhen. The intensity of this fragment is also heavily increased at the BPhen:Ca/TiN interface.

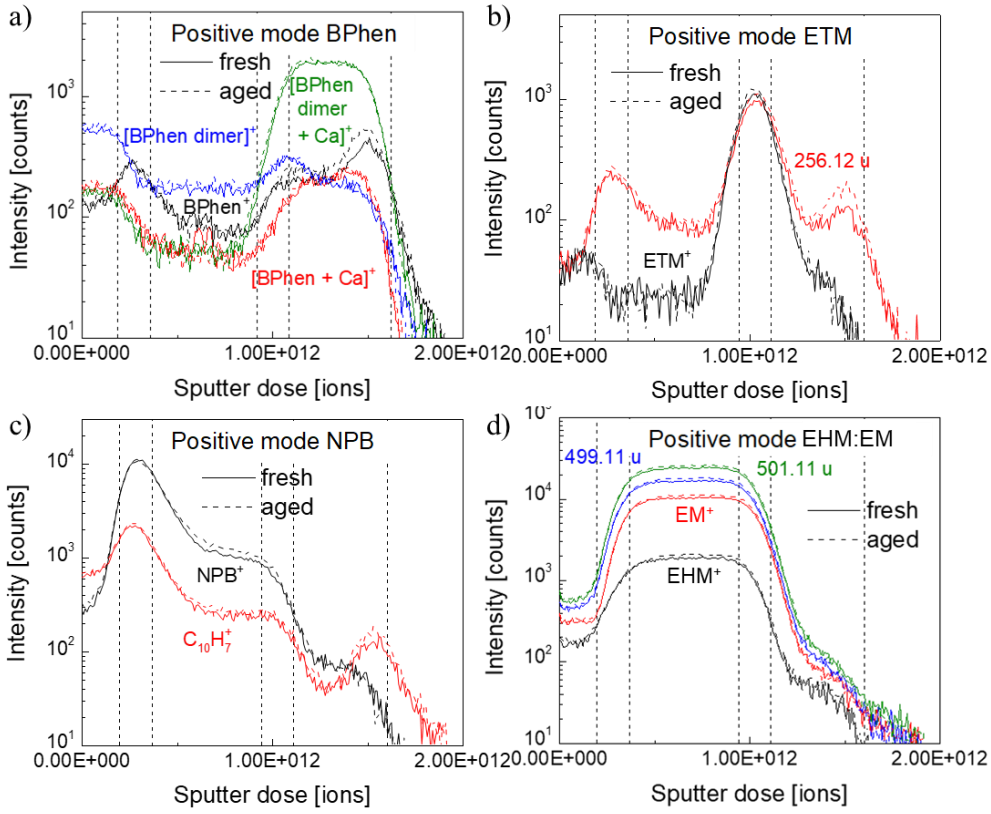

Figure 79 *Comparison of the ToF-SIMS depth profiles of the fresh and the aged inverted OLED 2 sample for some characteristic secondary ions of BPhen (a)), ETM (b)), NPB (c)) and EHM:EM (d)).*

As for the NPB layer, the intensity of all characteristic fragments is unchanged. In Figure 79 c), two of them are shown. However, the mass overlaps with fragments from other layers in the device show some change. The NPB^+ signal extends all the way through the emissive layer. It is unlikely that this is a diffusion of the NPB molecule into the emissive materials. Some characteristic secondary ions of the EHM molecule lie in the same range as the NPB^+ ion. However, a diffusion of NPB cannot completely be excluded. But the increased intensity of the NPB^+ signal in the emissive layer after ageing is most probably due to an increase of the characteristic ion from the emissive layer itself. The increase of

intensity of the $C_{10}H_7^+$ ion at the BPhen:Ca/TiN interface is very similar to the change of the 256.12 u ion in Figure 79 b). It is another indication for the changed chemistry in the BPhen layer after ageing of the device.

Finally, Figure 79 d) shows characteristic secondary ions for the emissive EHM:EM layer. The ions labeled EHM^+ and EM^+ have a mass of 603.27 u and 655.17 u, respectively. The chemical formulas of the molecules are not known, however, with the help of the single layer database, two additional characteristic fragments of the emissive material EM can be identified and are shown with the masses 499.11 u and 501.11 u.

All four secondary ions have a slightly increased signal after the ageing. This could be expected for the fragments, but not for the mother molecule. The concentration of the mother molecule will not increase over time. The only explanation for a higher signal is therefore a higher ionization probability due to a change of the chemical environment in this part of the device.

In Figure 80, two other characteristic ions are shown. The ion with mass 345 u is a characteristic fragment of EM while the ion with mass 340 u cannot clearly be assigned to one molecule or layer.

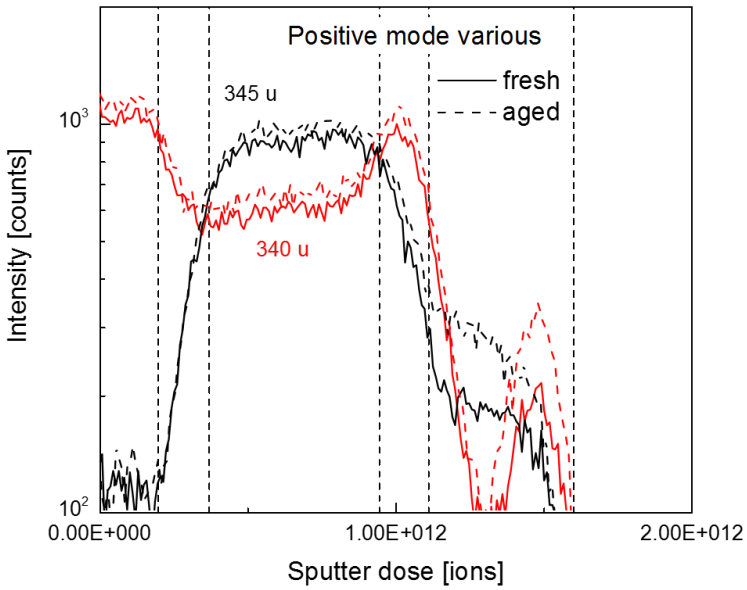

Figure 80 Comparison of the ToF-SIMS depth profiles of the fresh and the aged inverted OLED 2 sample for some unknown characteristic secondary ions in positive mode.

The 345 u ion shows a clear diffusion into the ETM layer. In the BPhen layer, the signal is heavily increased after ageing. This might be because of diffusion processes. The 340 u ion shows also a heavy change in the BPhen:Ca layer. It has been chosen exemplarily for many other secondary ions that show similar change in the BPhen layer after ageing of the device.

3.2.1.2. Summary

Overall, no additional peaks can be found in the mass spectra of the aged device when it is compared to the mass spectrum of the fresh device. All degradation products must therefore already be formed by

the primary ion bombardment during the analysis. This makes the detection of hints for degradation mechanisms quite tricky.

However, many of the changes that are observed in the device are located in the BPhen:Ca layer. The diffusion of ions like F^-, Cl^- or even Ag^- can cause changes in the energy levels of the device during ageing. Gap states can be created that hinder the injection of electrons into the device and the degraded material can cause quenching of excitons. The intensity of several characteristic fragments of the BPhen:Ca layer and the ETM layer is increased after ageing. This could be a direct consequence of the increased contaminant concentration in those layers after ageing. These results indicate a strong degradation at the side of the electron injection.

Furthermore, there is a possible diffusion of the characteristic fragment with a mass of 345 u that can clearly be attributed to the EM layer. It seems to diffuse through the ETM to BPhen. This would mean that there is a direct degradation of the emissive molecule which could be an explanation for the decreasing luminance of the device during operation.

Finally, the HID layer shows possible degradation. The intensity of the suspected mother molecule as well as some other characteristic ions decreases after ageing.

3.2.2. ToF-SIMS surface imaging inside beveled craters

3.2.2.1. Results and comments

In addition to the classical ToF-SIMS depth profiles, surface images of both samples were acquired after beveled craters had been created at the sample surface. Figure 81 shows a chemical overlay that has been generated after the ToF-SIMS imaging. The imaging was done by using 30 keV Bi_3^{++} as analysis beam to provide a high lateral resolution. The molecular signals or the highest intensity signal of each layer were used to create the overlay. 1096 u and 286 u for HTM and HID in purple, NPB^+ in turquoise, 603 u and 655 u for EHM and EM in yellow, 852 u for ETM in blue, Ca^+ and $BPhen^+$ in green and TiN^+ in red.

No difference between the images can be detected. Other characteristic secondary ions don’t show a difference either. This analysis can therefore not provide any additional information for the degradation of OLEDs during ageing.

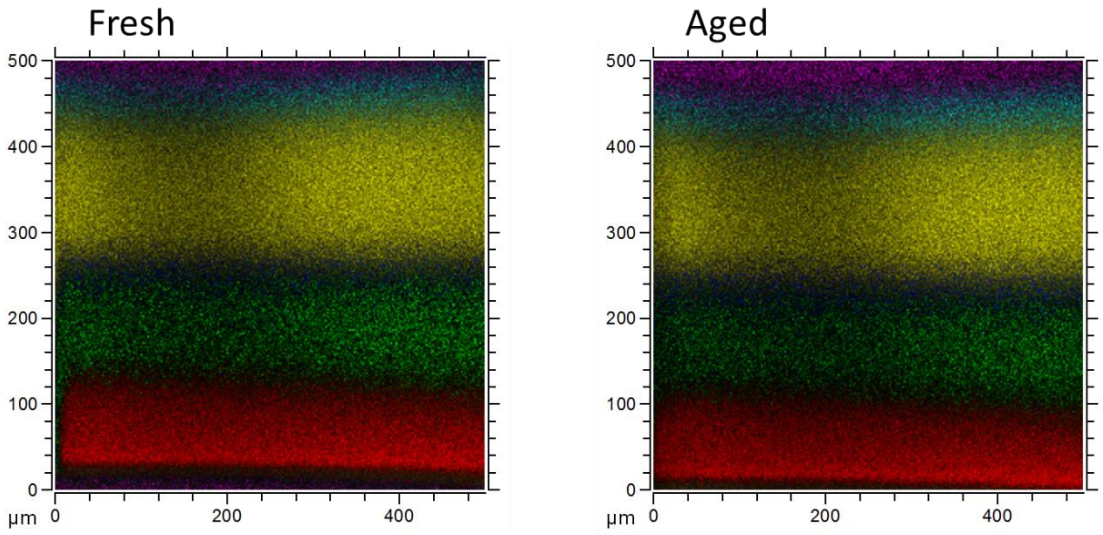

Figure 81 Chemical overlays from the ToF-SIMS imaging in a beveled crater of the fresh and aged OLED. The molecular signals or the highest intensity signal of each layer were used to create the overlay. 1096 u and 286 u for HTM and HID in purple, NPB^+ in turquoise, 603 u and 655 u for EHM and EM in yellow, 852 u for ETM, Ca^+ and $BPhen^+$ in green and TiN^+ in red.

3.2.2.2. Summary

With optimized analysis parameters and a possible analysis with argon clusters instead of bismuth, this analysis approach might provide useful information in the future. The high lateral resolution of this technique seems very promising for the localization of certain degradation products.

For this analysis, the analysis beam has been scanned over a large area of 500 µm by 500 µm with a resolution of 512 by 512 pixel. This analysis window can be reduced to a hundred µm or less while keeping the resolution the same. This can potentially provide even higher resolution images of certain interfaces. The surface of the thinnest layers, NPB and ETM with a thickness of only 5 nm, is increased by the beveled crater approach to an exposed surface of about 40 µm which corresponds to a magnification factor of around 8000. This value can be even further increased when specific interfaces are targeted. The use of the argon cluster sputter beam for the creation of the beveled crater keeps the molecular structure intact.

3.3. XPS analysis on complete organic OLED stacks

Three different techniques have been tested for the depth profiling of the organic part of complete OLED stacks. First, the classical depth profiling with argon clusters and high-resolution spectra that are taken between each sputter cycle. Secondly, the acquisition of several high-resolution spectra along a line in the beveled crater. By calculating the elemental composition at each point, a depth profile can be created. The third technique that has been tested is a similar method where an XPS line scan is performed across

the beveled crater to gain a rough overview of the sample. Then, high-resolution spectra are recorded at specific sample spots.

3.3.1. Classical XPS depth profiling

3.3.1.1. Results and interpretation

Figure 82 shows the traditional XPS depth profile that has been acquired on the direct OLED 1 device.

To create the profile, high-resolution spectra of the C 1s, N 1s, Ca 2p, Al 2p, O 1s, Ir 4f and Ti 2p core level spectra have been recorded at each datapoint. Additionally, a spectrum in the valence band region has been acquired for each datapoint.

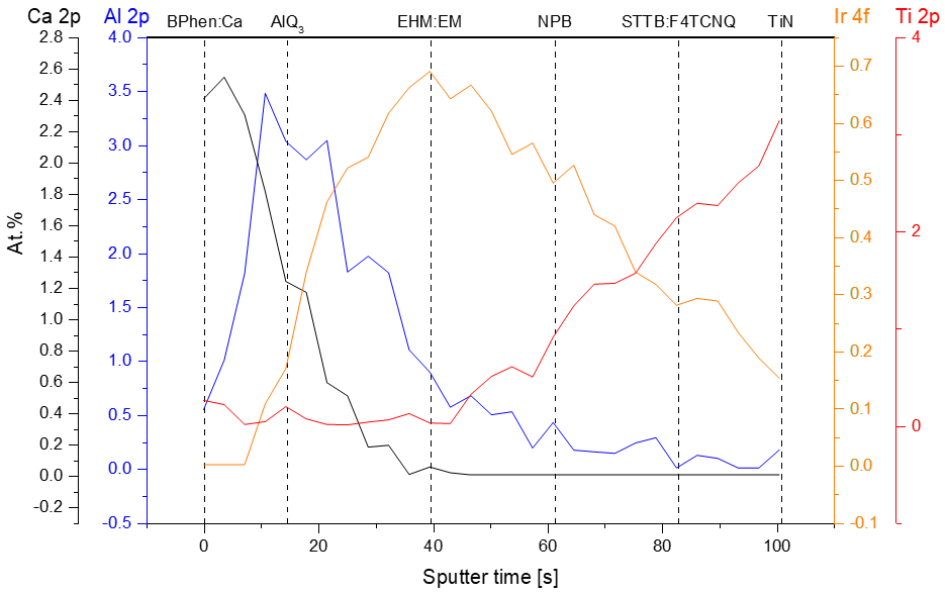

Figure 82 XPS depth profile of the direct OLED 1 sample. The depth profile has been acquired by using 3.6 s of 5 keV Ar4200 sputtering in between each data point acquisition. High-resolution spectra of the C 1s, N 1s, O 1s, Ca 2p, Al 2p, Ir 4f and Ti 2p core levels are used to create the profile.

Figure 82 shows only the elemental concentrations of calcium, aluminum, iridium and titanium to keep the graph clear. To obtain a high depth resolution, only 3.6 s of sputtering was done between each datapoint. This is a bit longer than the time that is needed for two sputter frames in the ToF-SIMS instrument which corresponds to 2.92 s. This high resolution is needed to obtain information about the thin Alq_3 and NPB layers in the device. With the aid of the elemental concentrations that are shown in Figure 82 and the contribution of the C 1 s, N 1s and O 1s peaks, that are not shown, it was possible to roughly define the positions of the five different organic layers. The layers are marked with vertical dashed lines.

The relatively low concentration of titanium at the end of the profile suggests that the TiN substrate has not yet been reached. A concentration around 50 % would be expected at this point. The profile should have been run longer.

The dopant concentration of calcium in the BPhen layer is expected to be 2 %. The measured value lies a bit higher at around 2.5 %. The aluminum concentration in the Alq_3 layer lies around the estimated value of 2.9 % and the value for the iridium with a maximum value of 0.7 % cannot be evaluated since the chemical formulas for EHM and EM are not known.

To assess the quality of the depth profile, valence band spectra at the estimated layer marks from Figure 82 are compared to the single layer reference spectra from chapter 3. The result is shown in Figure 83.

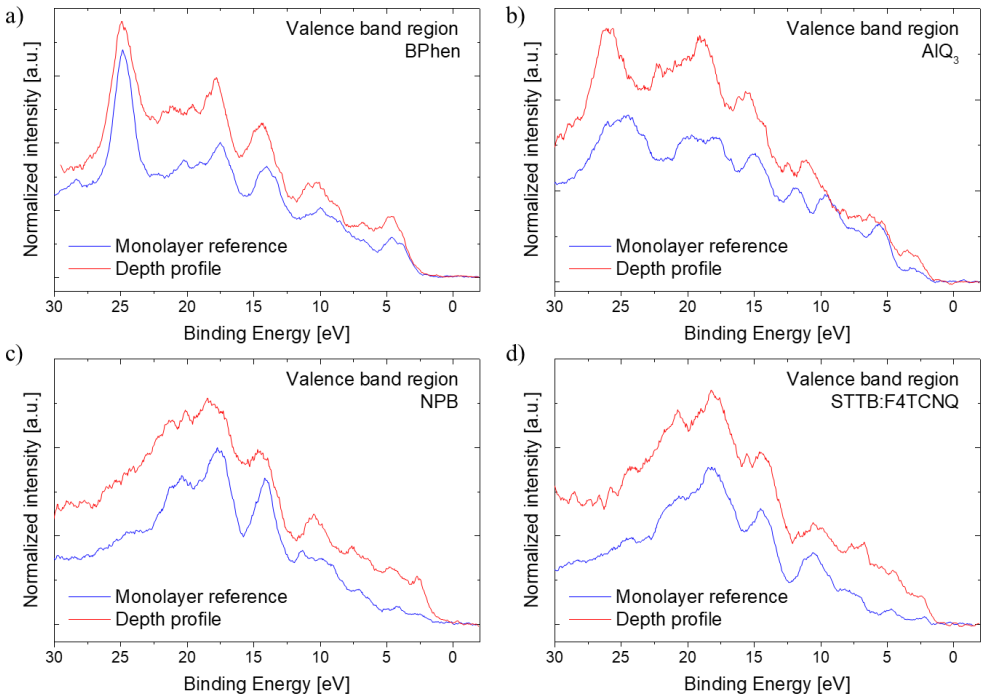

Figure 83 Comparison of the XPS valence band regions of reference samples for BPhen:Ca, Alq_3, NPB and STTB:F4TCNQ with the valence band spectra from the corresponding layers in the XPS depth profile from Figure 82.

For the BPhen:Ca layer, all of the features are present in the valence band region that is taken from the depth profile. Only an additional peak around 12 eV seems to appear which might be a contribution from the underlying Alq_3 layer.

The Alq_3 layer itself shows generally the same shape as the reference measurement, with some additional peaks at binding energies above 17 eV. The dashed line with the label Alq_3 in Figure 82 indicates the data point from which the valence band region has been taken. The Ca 2p signal is still at about half of its maximum value and the Ir 4f signal has started to appear. There will be contributions of the surrounding layers in the Alq_3 valence band region. This cannot be avoided due to the small thickness of the layer and the probing depth of the XPS technique.

For the NPB layer, the same reasoning can be applied. The main features can be recognized in the valence band region, but also other contributions are seen.

In the STTB:F4TCNQ layer, the fit seems almost perfect. All features of the reference measurement are found in the depth profile except for a small peak around 16 eV that only appears in the spectrum of the depth profile.

A more profound interpretation is hard to give for the different changes in the valence band region compared to the reference spectrum due to the lack of literature on most molecules and due to the fact that several molecules contribute to the valence band signal because of the small thickness of the layer. Only a direct comparison between aged and non-aged devices at the exact same depth could provide some information about chemical or electrical changes of the device during ageing.

3.3.1.2. Summary

Overall, this technique of depth profiling could be used for the characterization of complete OLED stacks. However, the analysis is quite long. For a depth profile with this depth resolution and high-resolution spectra of all relevant elemental core levels and the valence band region, the analysis took about 8 hours. The depth resolution is necessary to get the minimum amount of information of the thin Alq_3 and NPB layers. Another drawback of this technique is that the X-ray beam hits the sample on the same spot each time a data point is taken. Considering the long data acquisition, the sample is exposed to an excessive amount of X-ray irradiation which can damage the organic molecules as it was shown in chapter 3. For this reason, an alternative approach is described in the following.

3.3.2. XPS analysis on beveled craters

3.3.2.1. Generation of depth profiles from several high-resolution data points along a beveled crater

3.3.2.1.1. Experimental setup

Another possibility to obtain XPS depth profiles is to acquire a series of high-resolution spectra along a line across a beveled crater. A schematic representation of the analysis protocol is shown in Figure 84. The resulting depth profile from a beveled crater on the direct OLED 1 sample is shown in Figure 85 b).

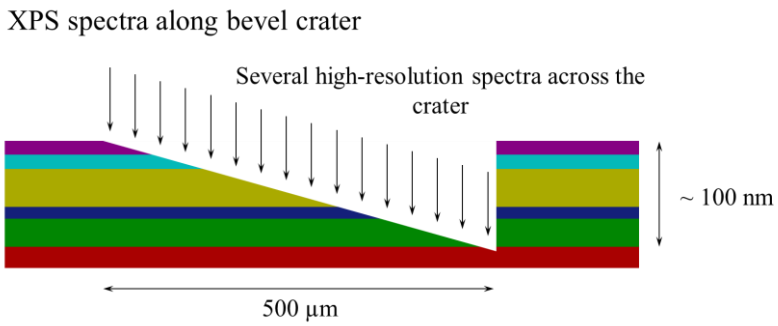

Figure 84 Schematic representation of the beveled crater analysis protocol for generation of a depth profile from several high-resolution XPS spectra across a beveled crater.

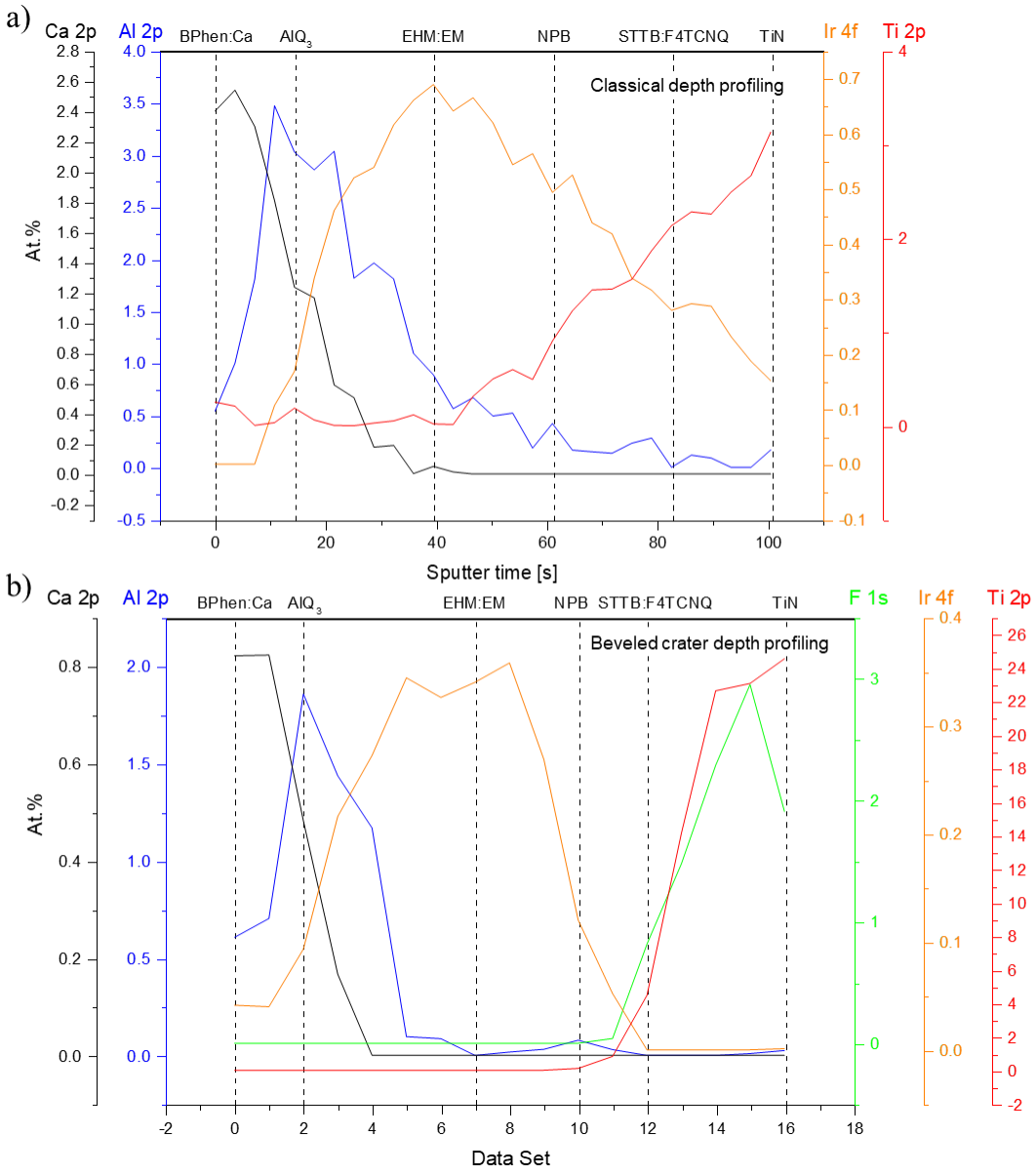

Figure 85 a) classical XPS depth profile and b) XPS profile from multiple acquisitions along a line in a beveled crater of the direct OLED 1 sample. High-resolution spectra of the C 1s, N 1s, Ca 2p, Al 2p, F 1s, Ir 4f and Ti 2p core levels are used to create the profile.

To create the depth profile, 16 datapoints have been acquired along a line with a length of about 500 µm. The X-ray beam diameter is reduced from the standard 100 µm diameter to 20 µm so that none of the datapoints overlap. Each sample point will only be exposed to the X-rays for the time of one analysis. This is an advantage to the traditional depth profiling technique. However, by reducing the beam diameter, the intensity of the spectra will also be reduced.

3.3.2.1.2. Results and interpretation

The resulting depth profile seems to be better defined than the traditional profile which can be found again in Figure 85 a). However, the fluorine signal from the F4TCNQ layer rises very late. It appears to overlay with the TiN layer and the calculated elemental concentrations differ more from the expected values. Both, the calcium and the aluminum content have reached only about half of the expected

concentration in this profile. Also, the iridium concentration is only about half of the value that was found in the traditional depth profile. The steady signal of the Ti 2p core level suggests that the substrate is reached. A strong oxygen concentration at this point confirms also the presence of TiO_2 that was detected during the ToF-SIMS measurements in the previous section.

Again, the five different organic layers are determined and labeled by vertical dashed lines. The valence band spectra at these points are compared to the single layer reference spectra for the corresponding materials in Figure 86.

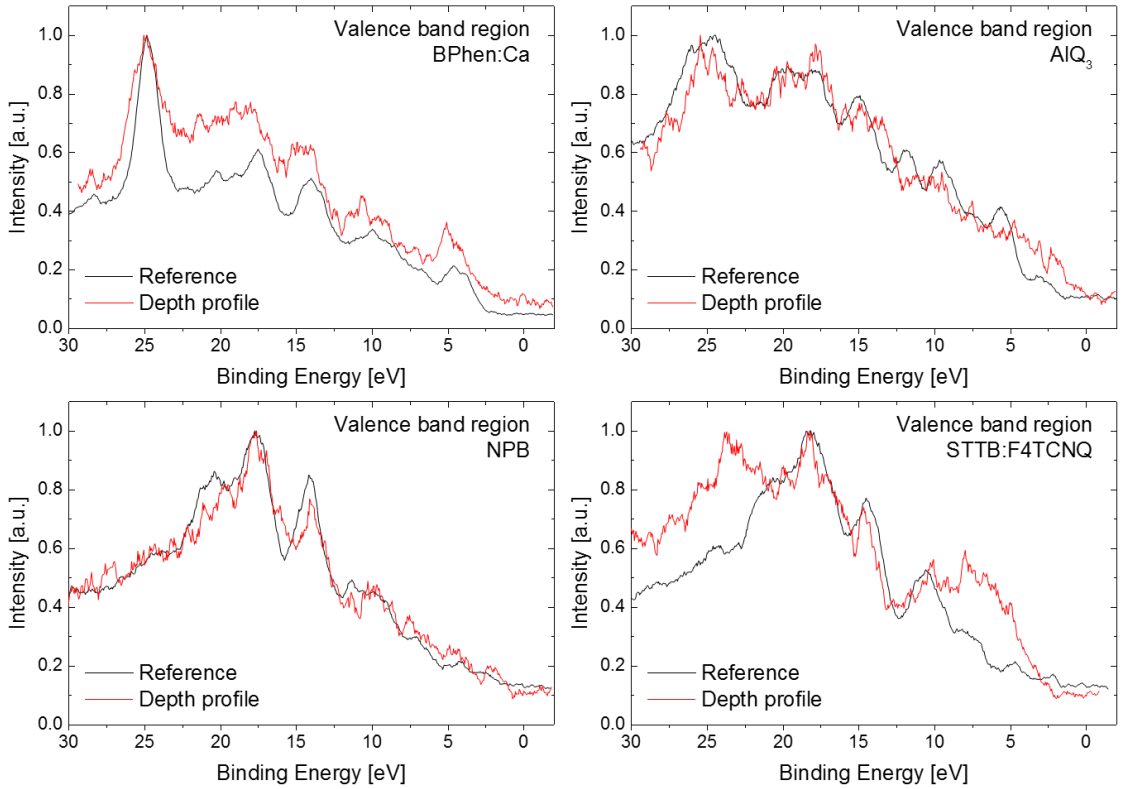

Figure 86 Comparison of the XPS valence band regions of the single layer reference samples for BPhen:Ca, Alq_3, NPB and STTB:F4TCNQ with the valence band spectra from the corresponding layers in the XPS depth profile from Figure 85. The spectra are normalized to their maximum intensity.

Because the intensity of the spectra along the beveled crater is considerably lower, all spectra are normalized to their maximum intensity for better comparability.

For the BPhen:Ca and the NPB layer, the agreement is quite good. For the Alq_3 layer however, the same problem as before is observed. Since the layer has only a thickness of 5 nm, there are contributions from the surrounding layers. This is also the case for the STTB:F4TCNQ layer, which shows heavy contributions from the underlying TiN layer.

These results present only a proof of concept. A comparison of fresh and aged OLEDs to study degradation was not possible due to time restraints. The beveled crater sample preparation became only possible during the last month of the thesis.

3.3.2.1.3. Summary

Overall, this depth profiling technique shows promising results. By dividing the number of datapoints by two, the acquisition time is also halved. The resulting depth profiles show clearly defined interfaces even though the depth resolution is halved because of the reduced number of datapoints. Also, the quantification results exhibit overall lower elemental concentrations than expected. Moreover, the X-ray dose for each point on the sample is considerably reduced. For each datapoint, a new sample spot is analyzed. The analysis of one datapoint takes about 15 min. This reduces the X-ray induced degradation of the molecules, compared to almost 8 h of accumulated X-ray exposure for the last datapoint in the classical depth profile. However, the small spot size of the X-ray beam results in a lower photoelectron intensity. The resulting spectra show more noise. More iterations during the measurement can be considered to increase the statistical relevance of the data and reduce the noise.

3.3.2.2. Depth profiling with XPS line scans across beveled craters

3.3.2.2.1. Experimental setup

XPS line scans are a feature that the Phi Versaprobe II instrument proposes which was used to perform the XPS measurements for this thesis. In this mode, the X-ray beam will scan on a defined line over the sample surface. An energy in the center of each core level, that needs to be detected, is chosen. The instrument calculates an energy range around this center energy by using instrument parameters and the given analyzer pass energy. At each point of the scan, all electrons that hit the analyzer and detector array will lie in that energy range. The signal will be integrated over the whole analyzer array and the result will be saved as a datapoint in the line scan profile. The beam moves then on to the next position of the scan. Once the last point of the scan is reached, the next energy range for the next element is set and another scan is run.

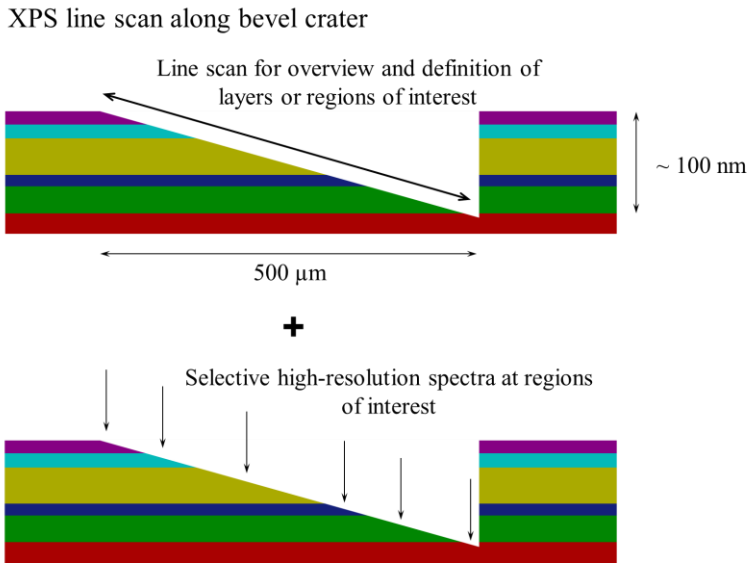

Figure 87 Schematic representation of the beveled crater analysis protocol for the acquisition of high-resolution spectra at specific sample areas that have been defined with the help of a line scan.

The number of pixels that are analyzed is automatically calculated by the length of the defined line and the diameter of the X-ray beam. For the line scans in this thesis, a beam diameter of 10 µm and a line of about 680 µm were used. This results in 274 pixels along the line which means that each pixel has a size of about 2.5 µm.

The analysis time for each line scan depends on the selected pass energy, which was 93.9 eV, the number of iterations for each element, which was 20, and the time that the beam stays at each pixel, which was 50 ms. The line scan across a beveled crater took with these measurements about 45 min. From these line scans, certain layers or regions of interest can be specified and analyzed with high-resolution measurements. The analysis protocol is schematically presented in Figure 87.

3.3.2.2.2. Results and interpretation

The result of such a line scan across a beveled crater on the inverted OLED 2 sample for a fresh and an aged device are shown in Figure 88.

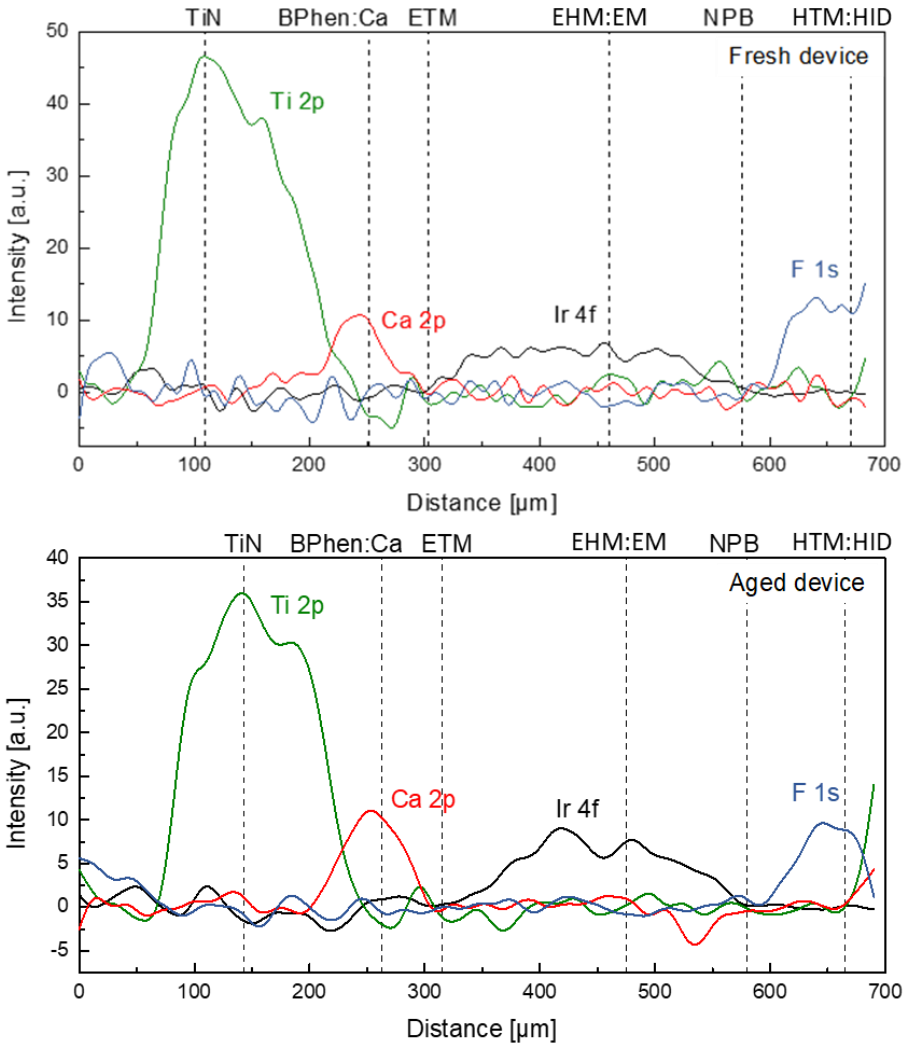

Figure 88 XPS line scan across a beveled crater of a fresh and an aged inverted OLED 2 sample. The C 1s, N 1s, Ca 2p, Al 2p, F 1s, Ir 4f and Ti 2p core levels were measured to create the profile. The data has been treated and only the Ti 2p, Ca 2p, Ir 4f and F 1s contributions are shown.

The data has been deconvoluted using the linear least-squares fitting tool from PHI Multipak software. With the help of this tool, regions of interest can manually be defined and the elemental contributions to each region can be displayed separately. This way, the contribution of an element that exhibits only noise in a certain region can be hidden in that part of the scan. This makes the very noisy line scans much clearer. Afterwards, the scan can be smoothened to obtain profiles as they can be seen in Figure 88.

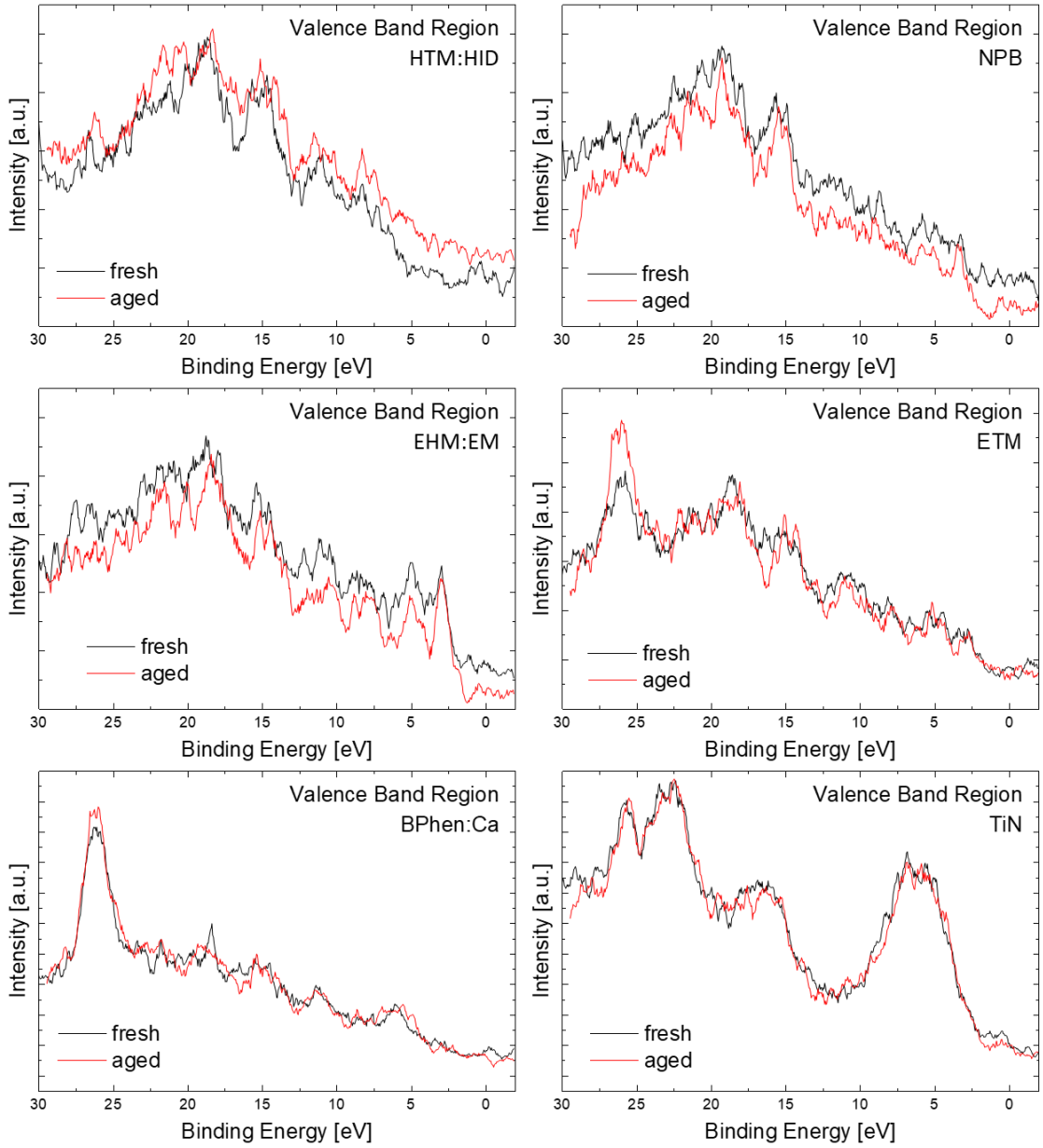

Figure 89 *XPS line scan across a beveled crater of a fresh and an aged inverted OLED 2 sample. The C 1s, N 1s, Ca 2p, Al 2p, F 1s, Ir 4f and Ti 2p core levels were measured to create the profile. The data has been deconvoluted and only the Ti 2p, Ca 2p, Ir 4f and F 1s contributions are shown.*

From the line scans themselves, no direct conclusions to degradation mechanisms can be made because the scans have been modified heavily by the data treatment. However, this technique provides a quick way to gain an overview of the sample surface. Profiles with a similar quality can be acquired with a

time per pixel of only 25 ms. This reduces the analysis time to only 22 min. With this overview, a number of regions of interest can be chosen for high-resolution analysis.

Figure 89 shows the comparison of the valence band spectra for the fresh and the aged inverted OLED 2 sample of the five different organic layers and the TiN electrode at the sample spots that have been defined with the help of the line scans in Figure 88.

The spectra are overall very noisy since they have been acquired with a beam diameter of only 10 µm. From the line spectra in Figure 88 it is hard to hit the same spot in the stack for both devices. Especially for the thin layers, a deviation of a few microns between the analysis on the fresh device and the aged device could mean a stronger contribution from the underlying layer to the recorded valence band spectrum. This is no problem for the TiN region. The valence band is overlaid perfectly. However, fewer electronic states around the fermi edge might be an indication for lower conductance of the electrode in the aged device. This would be a confirmation of the changed chemistry that has been observed at the BPhen:Ca/TiN interface in the ToF-SIMS measurements.

The valence band spectra of the BPhen:Ca regions are quite similar. Only the peak around 27 eV shows a relatively higher intensity after ageing. Moreover, two peaks at 6 and 18 eV, that show sharp maxima in the fresh device, are broadened after ageing. Again, this might be an indication for the changed chemistry that has been observed in earlier ToF-SIMS measurements.

For the HTM:HID, NPB and ETM layers, changes are detected, but the contribution of these changes to degradation of the materials is uncertain because the layers are extremely thin and as mentioned before, the measurements are probably from different depths in the stack which alters the shape of the spectra by default.

For the EHM:EM region, the analysis spots have been chosen at the beginning of the layer. With a layer thickness of 35 nm, there should be no influence from the surrounding layers on the valence band spectrum. The comparison of the fresh and the aged device reveals changes in the valence band region. Mainly the relative increase of intensity for the peak at 3 eV, the disappearance of several features above 20 eV. Unfortunately, no reference data for these materials is available and the molecular structure is unknown. The contribution of different elements to these peaks can therefore not be explained. The contribution of the emitting material EM to the overall valence band is also unknown. It is not clear if these changes indicate a degradation of the emitter or the host. But the data suggests a change in chemistry as it was observed by the ToF-SIMS measurements.

However, as mentioned before, it is difficult to compare the spectra of the fresh and aged device directly as they have their origin probably in different depths of the stack. Especially for the thin ETM and NPB layers, an interpretation of the results is very difficult because of the strong contributions from adjacent layers. This applies also to the core level spectra. For the thinner layers, no conclusions can be deducted from the data because of slightly different probing depths between the fresh and the aged device. For

the thicker layer, no differences are found between both devices, also due to the small X-ray spot (7 µm) that provides very low intensities.

3.3.2.2.3. Summary

Overall, this technique provides the fastest analysis of all three XPS approaches that were examined. With line spectra that take only 22 min to get an overview of the beveled crater it is possible to locate the different organic layers on the surface. With only 6 high-resolution measurements at precise sample spots afterwards, the analysis time is reduced to about a fourth of the traditional depth profiling. However, the main problem is the relatively low intensity of the spectra. It might be increased by longer acquisitions. Moreover, it is difficult to find the exact same point in depth on different samples. Especially for thin layers. This technique would be easier to use on samples with thicker layers. Valence band spectra without contributions of different layers could be acquired and a broader X-ray beam could be used for higher intensities.

Conclusion

In this chapter, the knowledge for depth profiling from chapters 3 and 4 has been applied to complete OLED stacks.

With the ToF-SIMS instrument, two approaches for the chemical analysis of OLED devices have been explored. First, the analysis by classical depth profiling. The characterization of complete devices was done in two consecutive measurements. Monoatomic cesium sputtering was used for the first measurement to gain information about the inorganic layers in the device. For the second measurement, the uppermost inorganic layers have been stripped from the device by using scotch tape. This leaves the organic materials exposed for an analysis with argon clusters as the sputter source.

The monoatomic as well as the cluster analysis suggest the presence of low amounts of contamination of fluorine, chloride and silver near the TiN bottom electrode of the studied OLEDs. The comparison of fresh devices with aged devices shows that these contaminants diffuse further into the organic layers. This could cause a malfunctioning of the BPhen:Ca electron injection layer and the ETM electron transport layer. Several characteristic secondary ions in these layers show a change of intensity after ageing.

The emitter material itself shows an increased intensity for characteristic fragments after ageing. Most notably, there is a diffusion of the characteristic fragment with mass 345 u towards the BPhen:Ca layer.

Finally, the p-type dopant HID in the hole injection layer shows a decreased intensity after ageing for some fragments that are believed to be the mother molecule. This would be a direct indication of molecular fragmentation and degradation.

The second characterization method that was explored with the ToF-SIMS instrument was the creation of beveled craters in the organic stack with subsequent surface imaging. However, no additional information about degradation in the organic materials could be gained by these measurements. However, with optimized parameters and higher lateral resolution, this technique looks promising for the characterization of organic electronics.

Concerning the XPS analyses, three different approaches have been studied for depth profiling. First, classical depth profiling was carried out. The analysis is quite long because high-resolution spectra need to be combined with high depth resolution. The long analysis time causes high X-ray exposure of the organic materials which can cause degradation of the molecules as it was shown in chapter 3. However, the calculated elemental concentrations in each layer correspond quite well to the expected values. Moreover, the valence band spectra are comparable to those of reference measurements.

A second depth profiling technique that was explored with the XPS instrument is the creation of depth profiles from a series of high-resolution spectra along a line in a beveled crater. The analysis time can be divided by two compared to classical depth profiling when this technique is used. The resulting depth profile exhibits clearly defined interfaces. However, the quantification with this approach seems to be worse for an unknown reason. A possible explanation might be the low intensity of the recorded spectra. In order to get a sufficient depth resolution with this technique, the X-ray beam diameter and therefore the X-ray power needs to be reduced. This causes a reduction of the photoelectron intensity as well.

Finally, XPS line scans have been used to gain depth profiles from beveled craters. These measurements can provide an overview of the sample within 22 min. This overview can then be used to define a few regions of interest where high-resolution spectra can be taken. The comparison of fresh and aged devices by this technique could confirm the change in chemistry in the emissive layer of the OLED that was seen in the ToF-SIMS measurements. Moreover, changes in the BPhen:Ca layer and at the TiN interface were observed. However, the interpretation of the results is tricky. Comparing valence band regions is easier with traditional profiles because they are comparable after the same time of sputtering. The points that are created using line scans might deviate on different samples. This changes the contribution of surrounding layers to the valence band region.

Overall, it is hard to gain reliable data from XPS depth profiling. Quantification is possible with classical depth profiling, but small concentrations of contaminants that are seen in ToF-SIMS spectra cannot be detected by XPS. Moreover, the continuous X-ray irradiation may cause degradation itself during the long depth profile acquisitions.

Final conclusion and perspectives

During this thesis, a reliable protocol for high resolution depth profiling of complete organic electronic devices has been developed. By optimizing the analysis parameters of ToF-SIMS and XPS measurements, it was possible to show small differences between fresh and electrically aged, state-of-the-art OLED devices.

The single layer samples that were studied first, served as references in order to help to identify the different molecules in depth profiles of complete stacks. At the same time, important analysis parameters were optimized by studying their impact on the measurement of these single layer samples. This knowledge is necessary to distinguish between material degradation and analysis induced damage in aged devices later on. The combination of ToF-SIMS and XPS measurements was a key element in this regard. ToF-SIMS provides information about the concentration of certain secondary ions which can directly be related to the fragmentation behavior of the organic molecules under the analysis beam. The XPS measurements can add information about changes in the electronic structure at the sample surface which are not visible in ToF-SIMS depth profiles.

The optimized parameters were then used to acquire depth profiles of bilayers. The ToF-SIMS results showed high intensities for the molecular secondary ions together with steady signals. The XPS measurements showed only minimal changes in chemistry and the electronic structure during depth profiling. The changes stem mainly from the continuous X-Ray exposure during classical XPS depth profiling. Overall, the depth profiling of bilayers confirmed the optimal parameters that were found during the characterization of the single layer samples, and they were successfully applied to depth profiling of organic interfaces.

The characterization of bilayers was also applied to solution processed OLEDs. ToF-SIMS analysis helped to identify problems during the device fabrication where two materials were spin-coated from one solution. Thanks to the insight provided by the high depth resolution ToF-SIMS measurements, the deposition process could be adapted, and the performance of the OLED could be improved.

Lastly, the depth profiling of hybrid inorganic-organic bilayers was studied by different approaches. The analysis of such interfaces is one of the biggest challenges in ToF-SIMS and XPS depth profiling. It has been found that a two-step analysis approach provides the best results on these hybrid interfaces. A first depth profile is done by monoatomic sputtering. It provides information about the inorganic part. Then, the inorganic layer is stripped from the organic part by applying scotch tape to the sample and peeling it off again. This leaves the organic part exposed and depth profiling can be done with argon clusters.

This two-step approach was then successfully applied to complete OLED stacks. Depth profiles in the ToF-SIMS and the XPS instrument were acquired for the inorganic part by monoatomic sputtering and for the organic part by cluster sputtering.

As a last step, electrically aged OLEDs have been compared to non-aged devices. The comparison of the inorganic ToF-SIMS profiles showed contamination of the bottom electrode and of the electron injection layers by fluorine and chloride. Moreover, it revealed a diffusion of silver from the top electrode towards this area. These findings could be confirmed by the depth profiling of the organic part with argon clusters. Overall, many changes on the electron injection side of the device were observed. But also the hole injection dopant showed possible molecular scission during ageing. The emitter material itself showed direct signs of degradation. A fragment of the molecule diffused through the electron transport material into the electron injection layer. All of those changes contribute to the loss of luminance during device ageing. The misfunctioning of the supporting layers due to chemical and electronical changes can lead to unbalanced charge carrier concentration in the device which diminishes the efficiency of the device. To my best knowledge, this was the first time, that the extremely small changes in the chemistry of OLEDs after electrically ageing could be demonstrated.

However, the depth profiling of complete devices by XPS has turned out to be very difficult due to the excessive X-ray exposure of the organic materials throughout the analysis. No direct evidence for electronic changes in the electron injection side of the devices could be found.

To reduce the X-ray exposure time, a beveled crater has been prepared in the ToF-SIMS instrument on the organic stack. This opens up the possibility to create XPS depth profiles by acquiring XPS scans along the beveled crater. This way, each data point in the depth profile is taken on a fresh sample spot that hasn't been exposed to X-rays before. The beveled crater also allows for ToF-SIMS imaging of the whole organic stack. This can potentially be done using argon clusters to minimize damage to the organic molecules.

For the future, as far as the characterization protocol is concerned, mainly the beveled crater approach should be further studied. The analysis of beveled craters by ToF-SIMS imaging and XPS depth profiling showed promising results. However, essential parameters have not been optimized during this thesis.

First, the parameters during the crater formation must be checked. Different angles or sputter directions could potentially improve the quality of the crater. Especially with regard to material redeposition, the process can be enhanced. The measurement of the slope would also allow difference in sputter rates to be taken into account in the reconstructed profile.

Next, the lateral resolution during ToF-SIMS imaging should be increased. A possibility could be to only focus on one certain interface per crater. The exposed area of each layer could be increased to a maximum and the imaging could be done by argon clusters to ensure minimal damaging.

Focusing on one specific interface can also be beneficial for XPS depth profiles. It has been shown that the created depth profiles in the beveled crater suffer from low intensities because of the small beam

diameter that is used. By increasing the exposed area of each layer, a larger beam can be used. This could significantly improve the signal intensity and therefore the quality of the recorded spectra. This could make the visualization of electronic changes in the organic materials during ageing of the OLED devices easier.

As far as the studied devices are concerned, it could be interesting to compare direct and inverted OLEDs that contain the same materials but with an inverted layer structure. The inverted flow of charge carriers can have different impacts on the organic molecules and on the diffusion of contaminants like fluorin, chlorine or silver.

Also, other ageing mechanisms could be investigated like UV-irradiation or environmental degradation by moisture and oxygen due to insufficient encapsulation of the devices.

The characterization protocol is not restricted to OLED samples. It can be applied to other organic electronic devices such as OPVs or sensor applications.

Finally, one of the advantages of ToF-SIMS besides the excellent mass resolution and depth resolution is a high lateral resolution. The analysis protocol could be applied to nanostructured samples. In modern display applications, the pixel size of an OLED is in the range of 20 to 40 µm. With a lateral resolution of up to 100 nm, ToF-SIMS is able to create precise 3D chemical reconstructions of such structures.

Appendix

A. ToF-SIMS instrumentation

The instrument that was used to carry out all the measurements in this thesis was a ToF.SIMS 5 from IONTOF. The instrument can be seen in Figure 90 a).

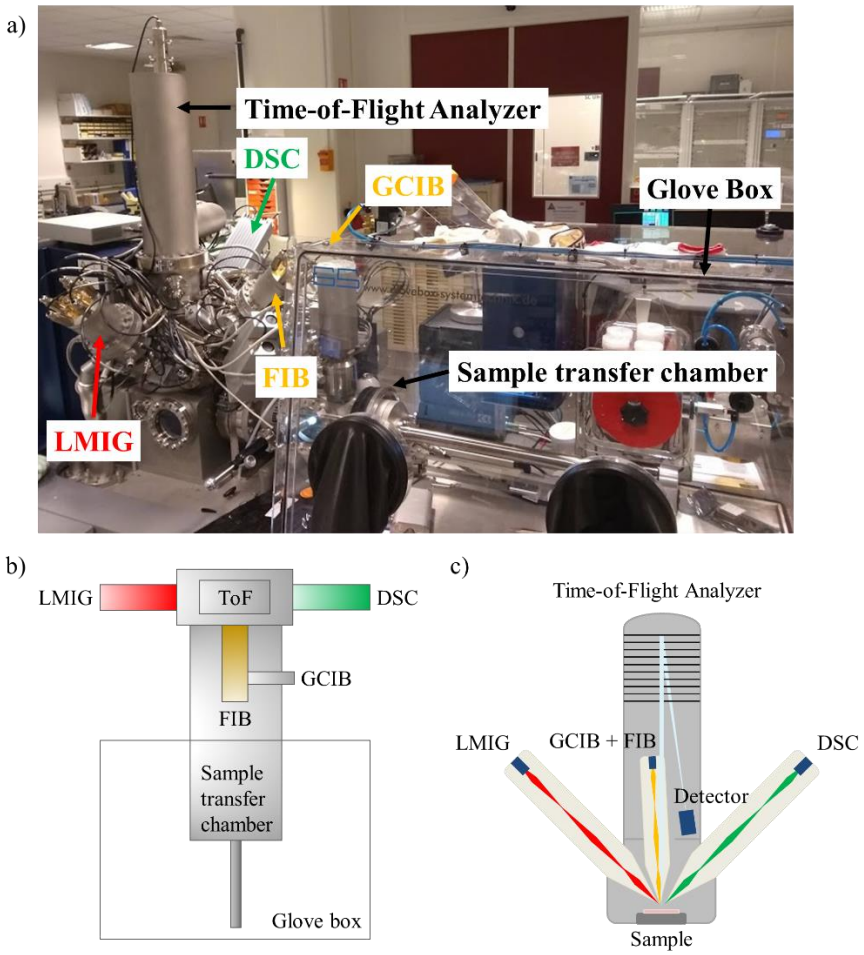

Figure 90 *a) Photo of the instrument that was used throughout this thesis to perform the ToF-SIMS measurements. b) Schematic view from the top and c) from the side of the instrument.*

In the top (Figure 90 b) and side view (Figure 90 c), it can be seen that the instrument is equipped with a bismuth LMIG as analysis gun. Five different species can be used: Bi_1^+, Bi_3^+, Bi_3^{++}, Bi_5^+ and Bi_5^{++}.

The instrument offers different possibilities for sputtering. Monoatomic sources can be used via the dual source column (DSC). The two sputter species in this source are cesium and xenon, which is different from most instruments that are equipped with cesium and oxygen. Additional to the monoatomic sources, argon clusters can be produced in the gas cluster ion beam source (GCIB). The clusters can also be used as analysis beam.

An electron flood gun is equipped to the instrument to provide charge neutralization for insulating samples that charge up during analysis.

It is moreover possible to open an oxygen leak in the chamber which can be used to oxidize the sample surface to increase the secondary ion yield for some samples.

Finally, the sample transfer chamber is located inside of a glove box with a nitrogen atmosphere (154 ppm O_2). Samples that are sensitive to oxygen or humidity can be handled inside of the glovebox in a protected environment. There is the possibility to transfer samples into hermetically sealed transfer vessels which allows for samples to be transported to other characterization or deposition instruments without being exposed to air.

The glove box is also equipped with an annealing plate to heat up samples. The sample temperature can be measured with a special sample holder. There is also a liquid nitrogen inlet for the main chamber that can be used to cool down samples.

B. XPS instrumentation

The instrument that was used to carry out all the measurements in this thesis was a Versaprobe II from PHI. The instrument can be seen in Figure 91 a).

The instrument is equipped with a scannable monochromatic Al Kα source. The spot size can be varied between 7 and 200 µm.

For charge neutralization, a low energy electron gun and an argon ion gun can be used.

The argon ion gun can also be used to create depth profiles. A GCIB source can provide argon clusters that can be used for surface cleaning or sputtering as well. There is even the possibility to combine monoatomic and cluster sputtering in a co-sputtering mode.

The sample stage can be rotated and tilted which opens up the possibility of angle resolved XPS measurements.

A hermetically sealed transfer vessel can be attached to the sample transfer chamber. This allows for a protected sample transfer between different instruments without the sample being exposed to air.

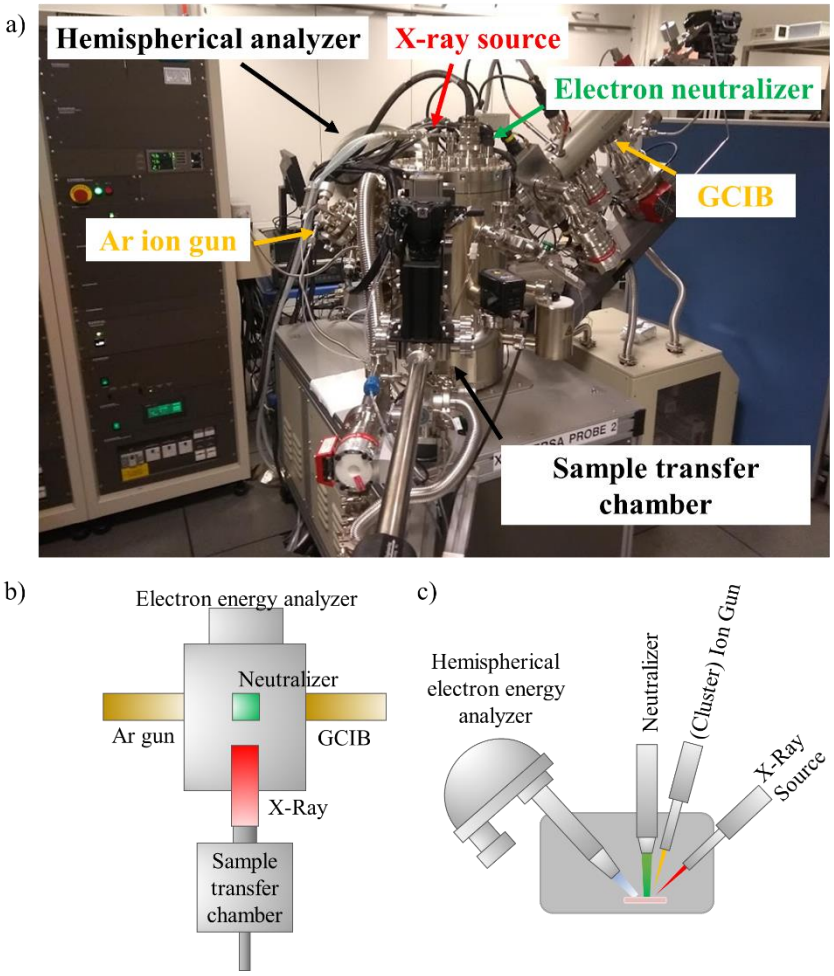

Figure 91 *a) Photo of the instrument that was used throughout this thesis to perform the XPS measurements. b) Schematic view from the top and c) from the side of the instrument.*

C. ToF-SIMS reference spectra

In the following, the ToF-SIMS reference spectra for all of the analyzed organic molecules are shown. The analysis was carried out using standard parameters for organic depth profiling. The analysis beam was a Bi_3^{++} beam that was operated at 30 keV and 0.40 to 0.45 pA. The raster size was 300 by 300 µm. Ar_{5000} at 5 keV and 1 nA was used as the sputter beam.

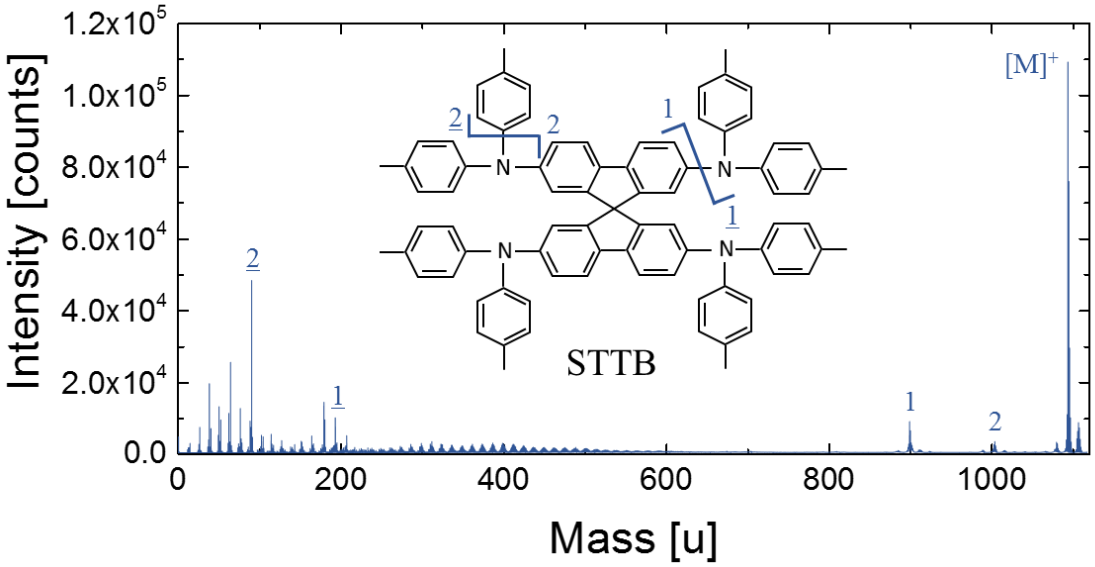

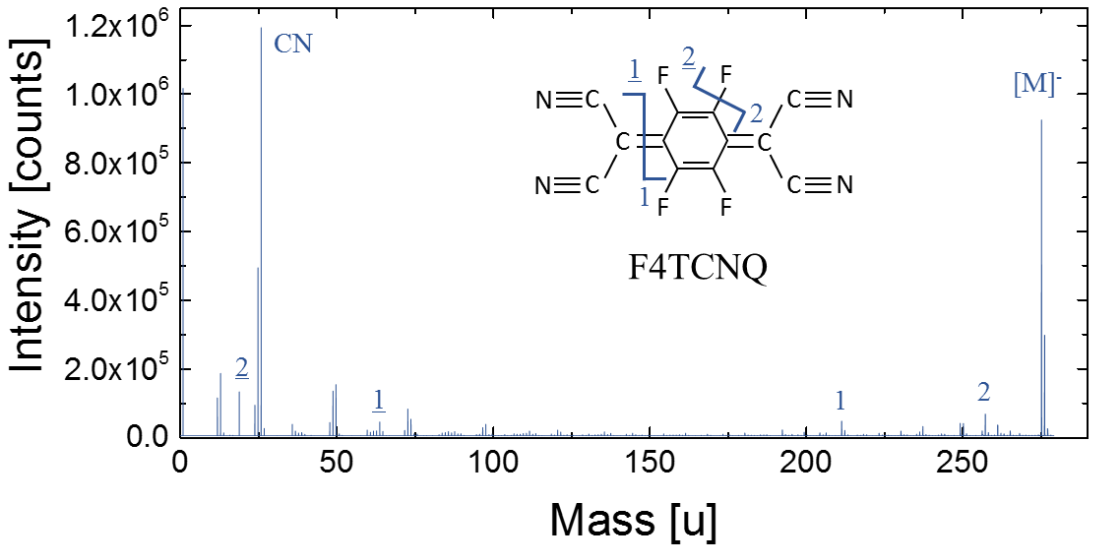

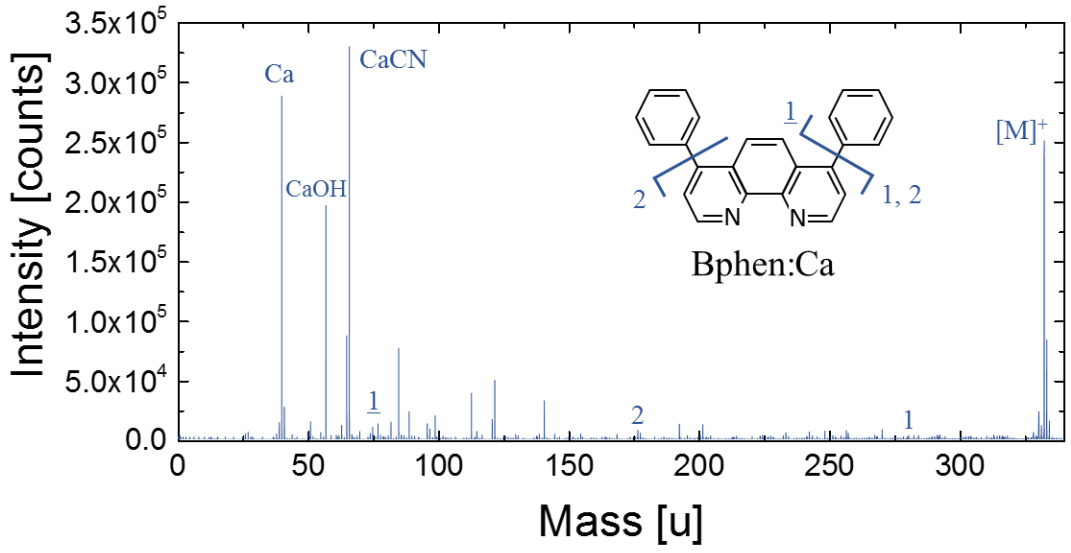
Intensity [counts]
Mass [u]
Ca
CaCN
CaOH
[M]+
Bphen:Ca

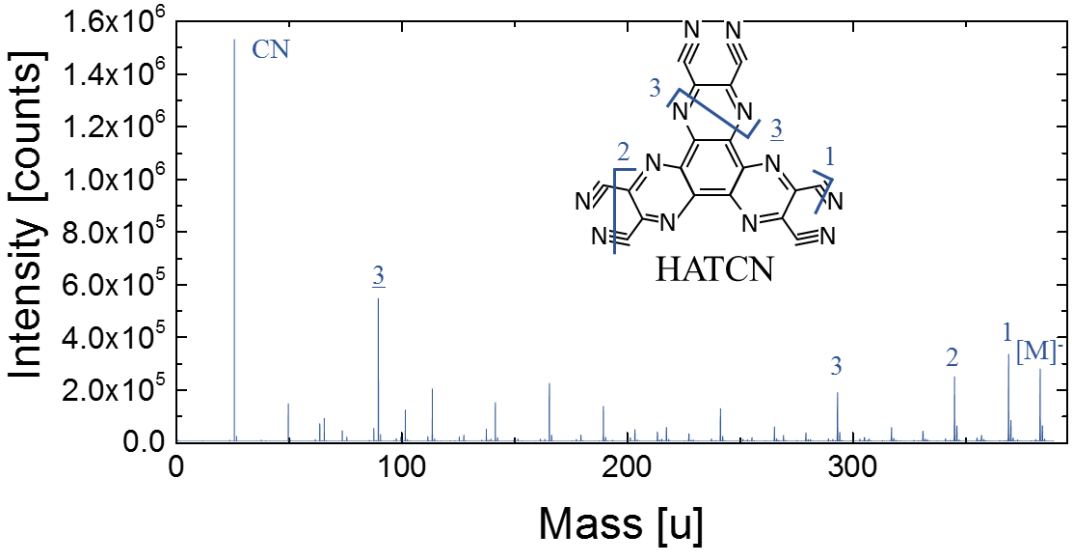
Intensity [counts]
Mass [u]
CN
[M]-
HATCN

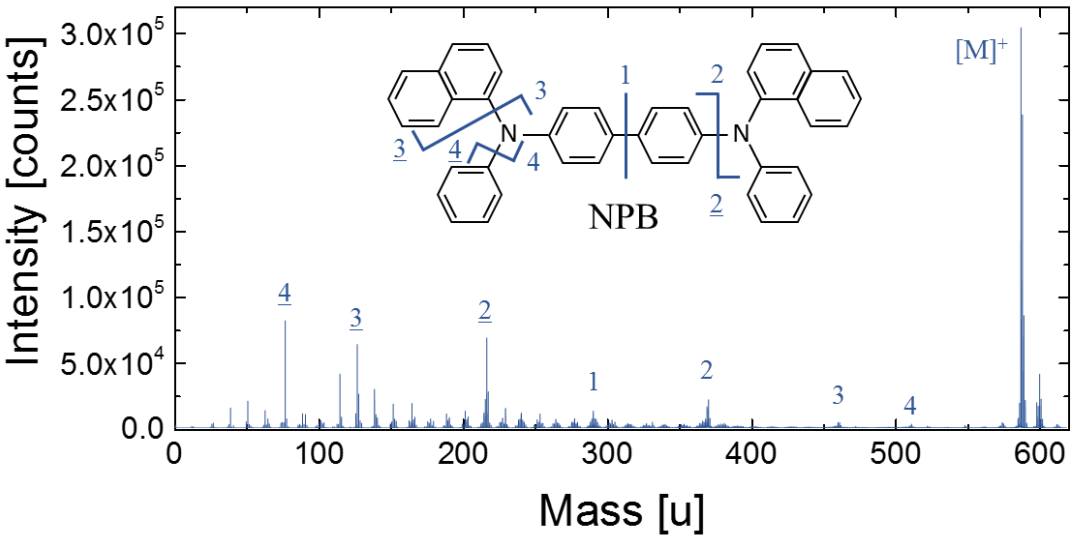
Intensity [counts]
Mass [u]
[M]+
NPB

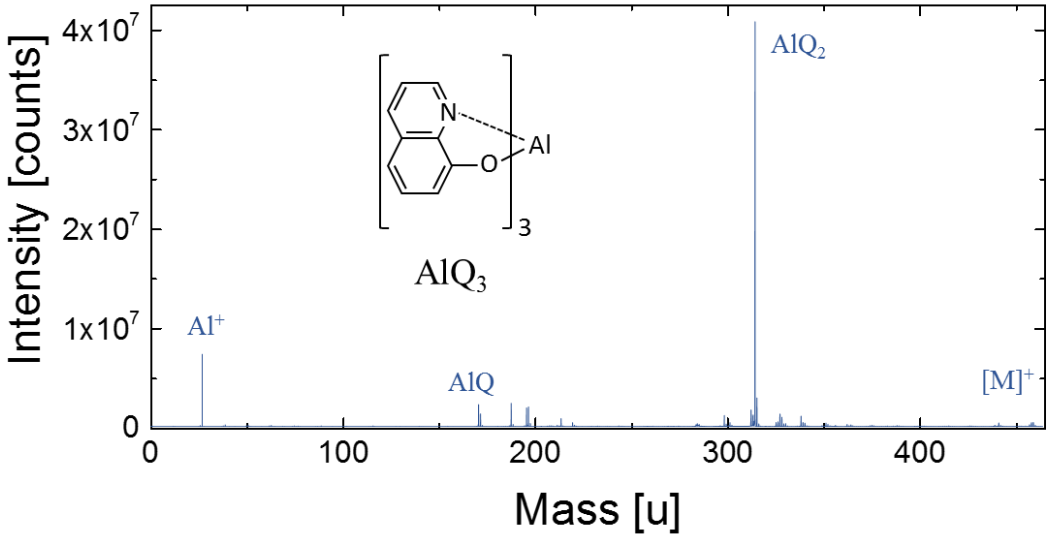
Intensity [counts]
4x10^7
3x10^7
2x10^7
1x10^7
0
0
100
200
300
400
Mass [u]
AlQ2
AlQ3
Al+
AlQ
[M]+
N
Al
O
3

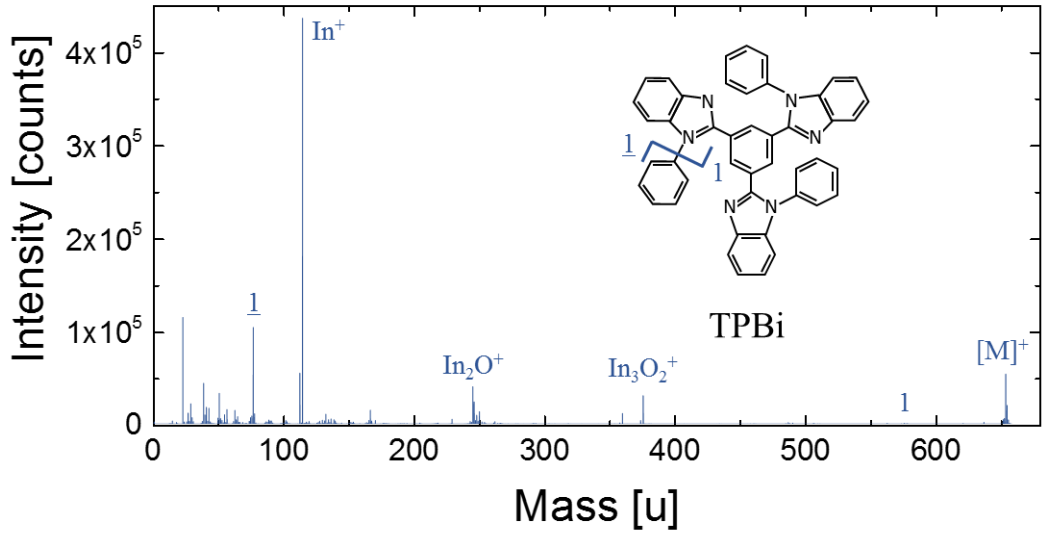
Intensity [counts]
4x10^5
3x10^5
2x10^5
1x10^5
0
0
100
200
300
400
500
600
Mass [u]
In+
In2O+
In3O2+
[M]+
TPBi
1

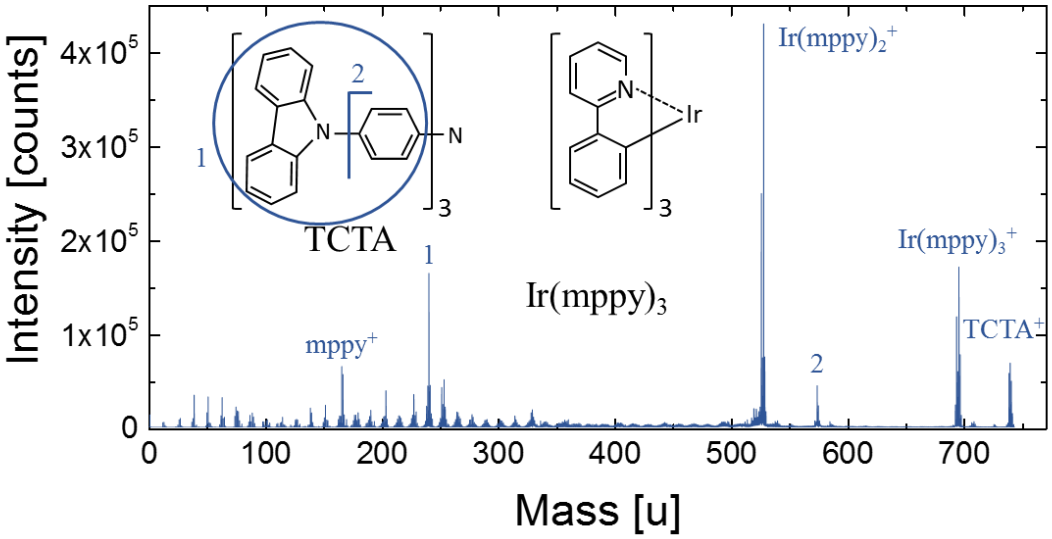
Intensity [counts]
4x10^5
3x10^5
2x10^5
1x10^5
0
0
100
200
300
400
500
600
700
Mass [u]
Ir(mppy)2+
Ir(mppy)3+
TCTA+
mppy+
TCTA
Ir(mppy)3
N
Ir
3

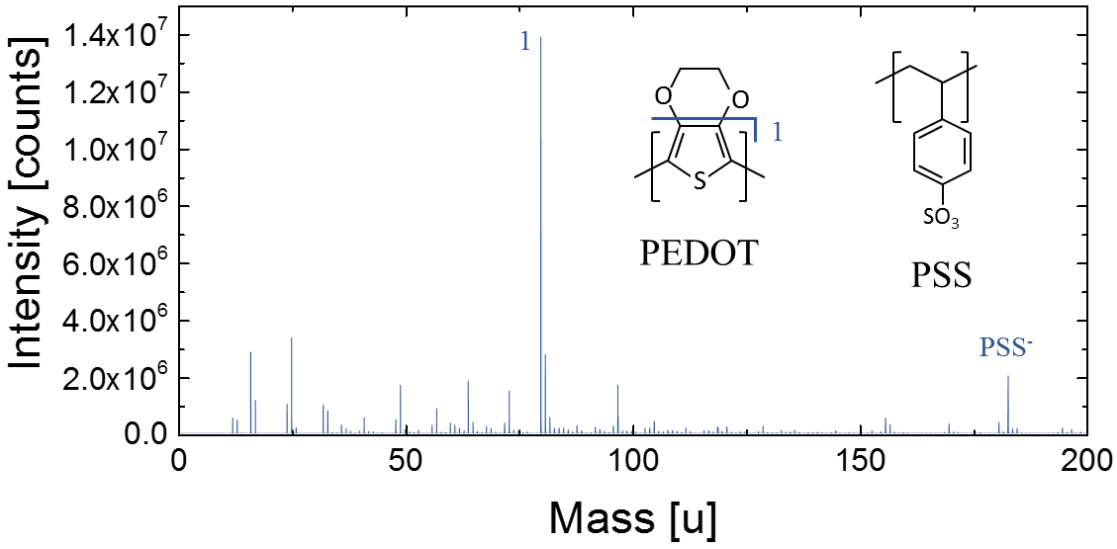
Intensity [counts]
1.4x10^7
1.2x10^7
1.0x10^7
8.0x10^6
6.0x10^6
4.0x10^6
2.0x10^6
0.0
0
50
100
150
200
Mass [u]
1
PEDOT
PSS
PSS-

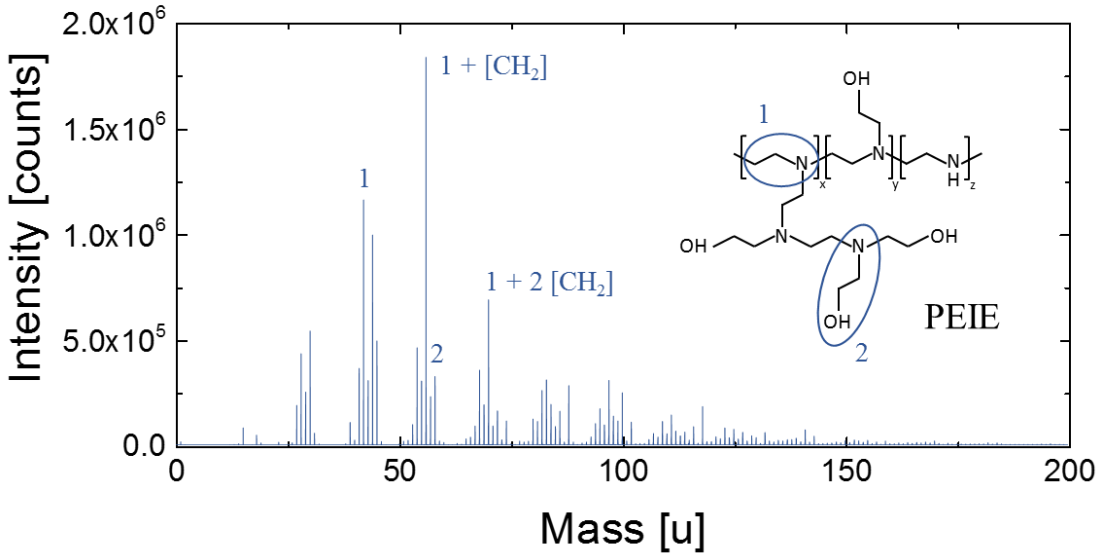
Intensity [counts]
2.0x10^6
1.5x10^6
1.0x10^6
5.0x10^5
0.0
0
50
100
150
200
Mass [u]
1 + [CH2]
1
1 + 2 [CH2]
2
PEIE

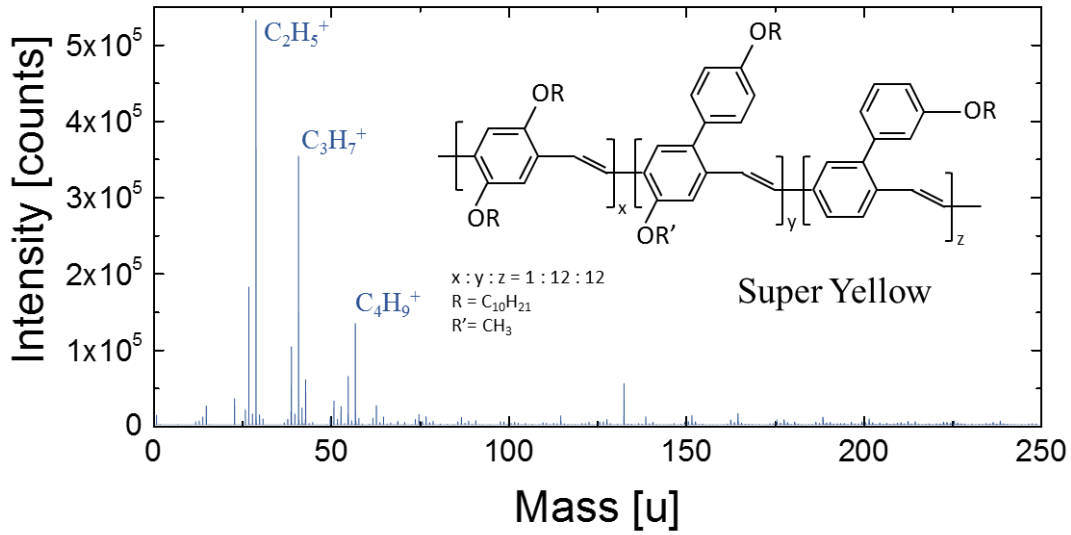
Intensity [counts]
5x10^5
4x10^5
3x10^5
2x10^5
1x10^5
0
0
50
100
150
200
250
Mass [u]
C2H5+
C3H7+
C4H9+
x : y : z = 1 : 12 : 12
R = C10H21
R'= CH3
Super Yellow

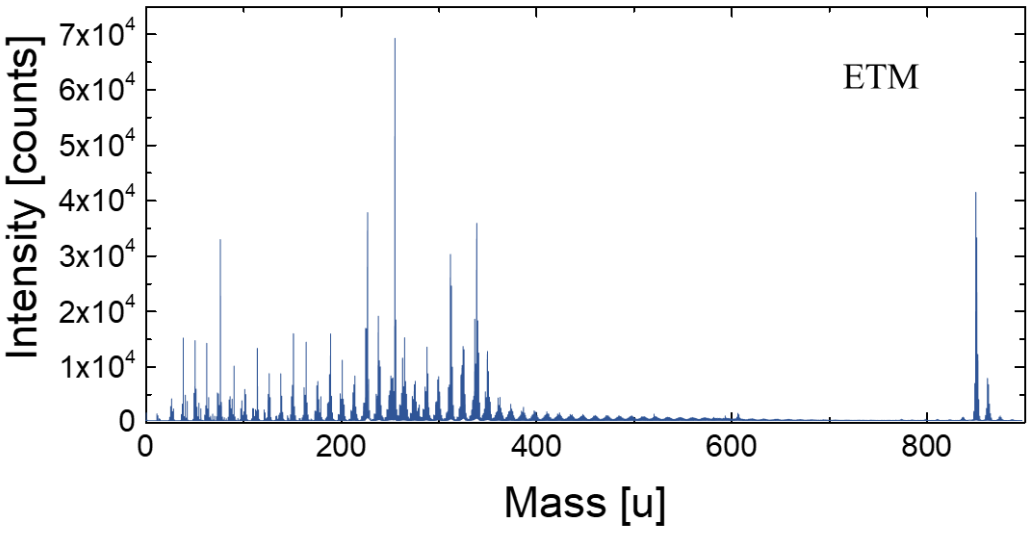
ETM
Intensity [counts]
7x10^4
6x10^4
5x10^4
4x10^4
3x10^4
2x10^4
1x10^4
0
0
200
400
600
800
Mass [u]

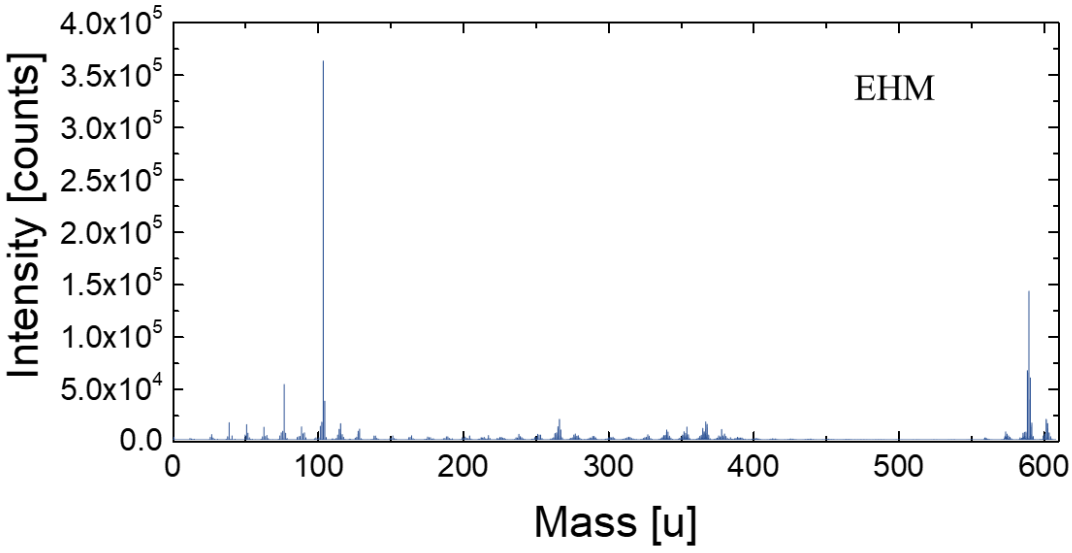
EHM
Intensity [counts]
4.0x10^5
3.5x10^5
3.0x10^5
2.5x10^5
2.0x10^5
1.5x10^5
1.0x10^5
5.0x10^4
0.0
0
100
200
300
400
500
600
Mass [u]

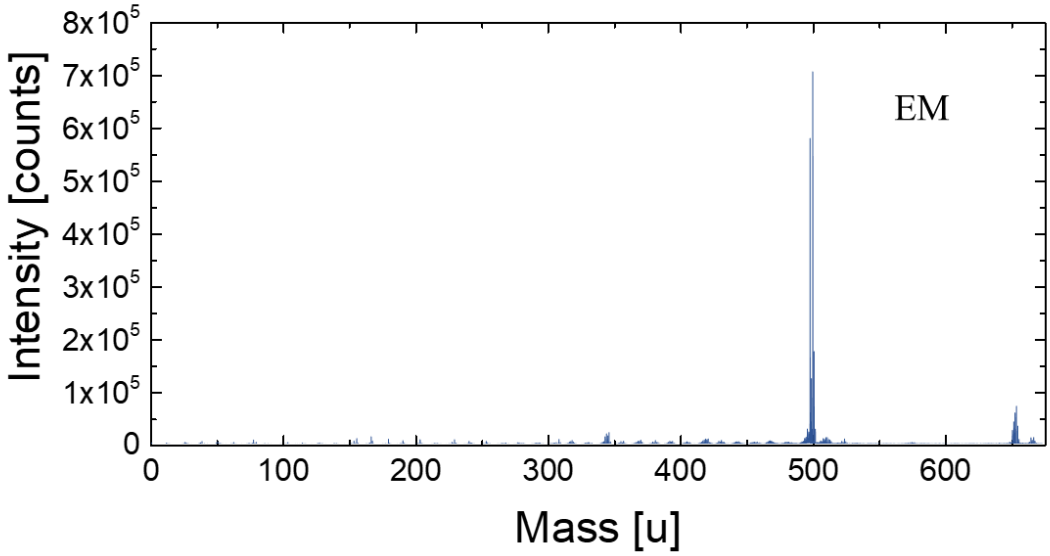
EM
Intensity [counts]
8x10^5
7x10^5
6x10^5
5x10^5
4x10^5
3x10^5
2x10^5
1x10^5
0
0
100
200
300
400
500
600
Mass [u]

D. XPS reference spectra

In the following, the XPS reference spectra for most of the analyzed organic molecules are shown. The analysis was carried out using an aluminum Kα X-ray source at 1486 eV and 25 W with a beam diameter of 100 µm. The pass energy for elemental core levels was 23.5 eV and 46.95 eV for the valence band region. The core level spectra were acquired over 25 cycles and the valence band spectra over 50 cycles. For the valence band spectra, the raw acquired data as well as the smoothened line that was used throughout this thesis are shown.

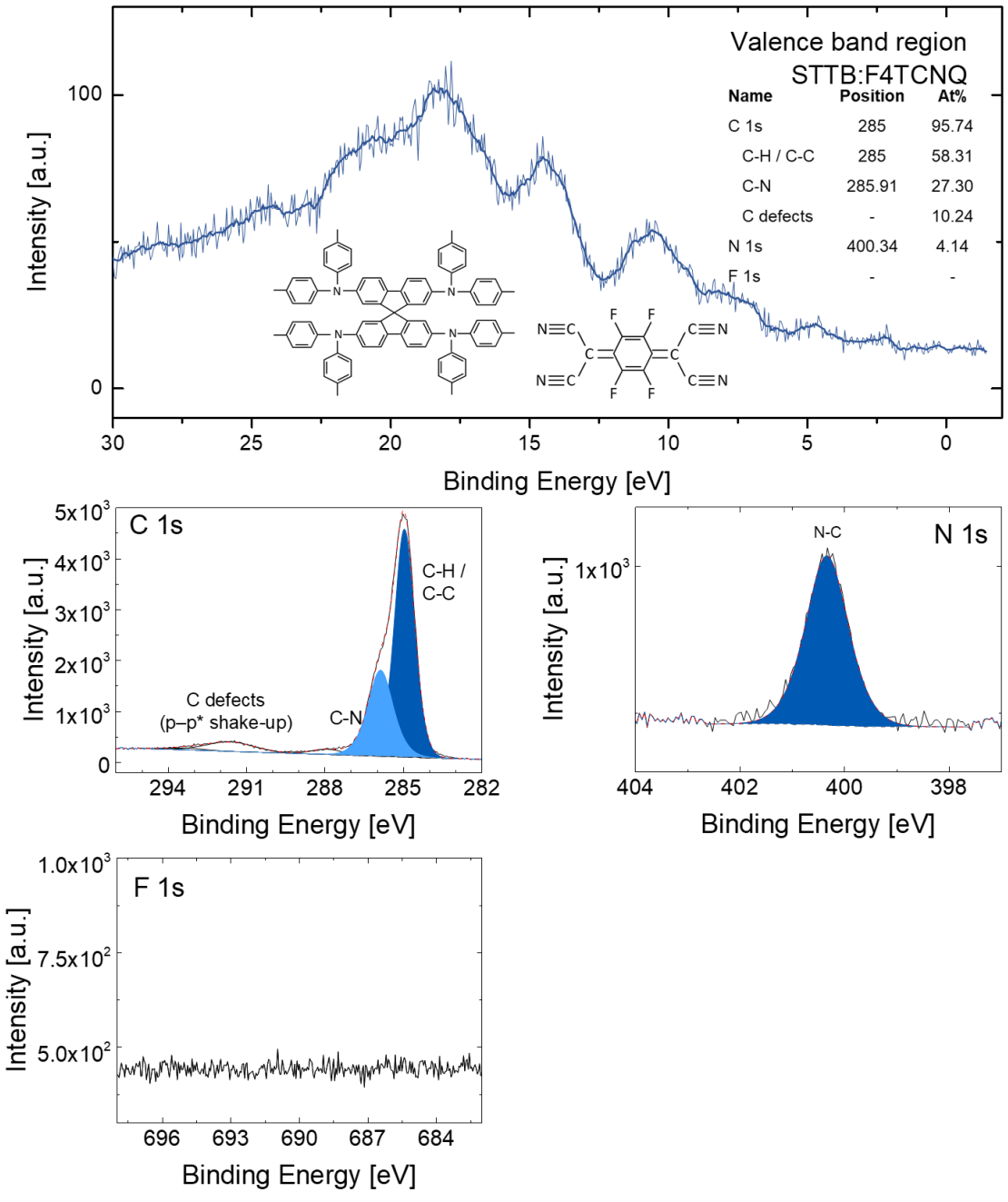

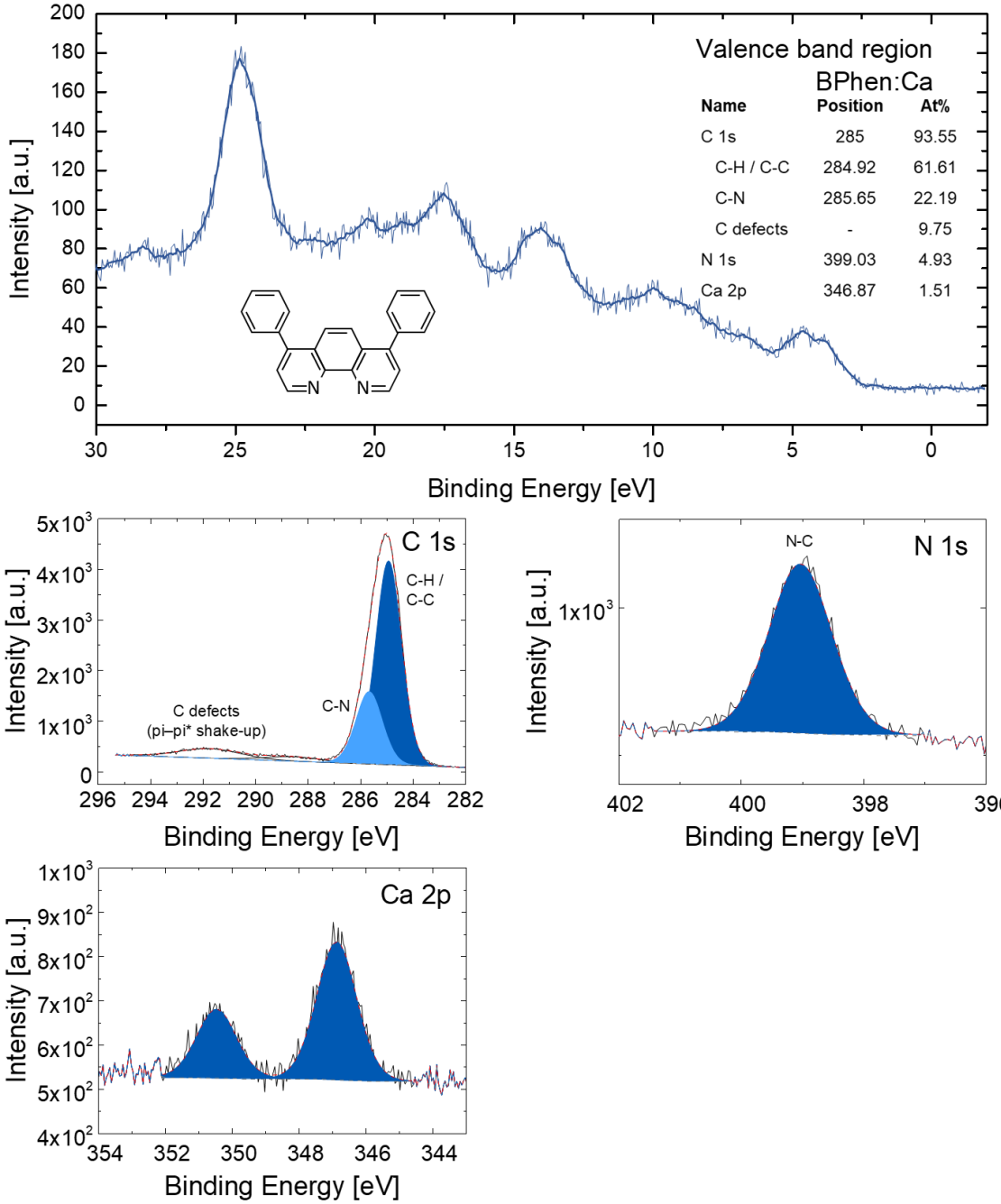
Valence band region
BPhen:Ca
Name Position At%
C 1s 285 93.55
C-H / C-C 284.92 61.61
C-N 285.65 22.19
C defects - 9.75
N 1s 399.03 4.93
Ca 2p 346.87 1.51
Intensity [a.u.]
Binding Energy [eV]
C 1s
C-H / C-C
C-N
C defects
(pi–pi* shake-up)
N 1s
N-C
Ca 2p

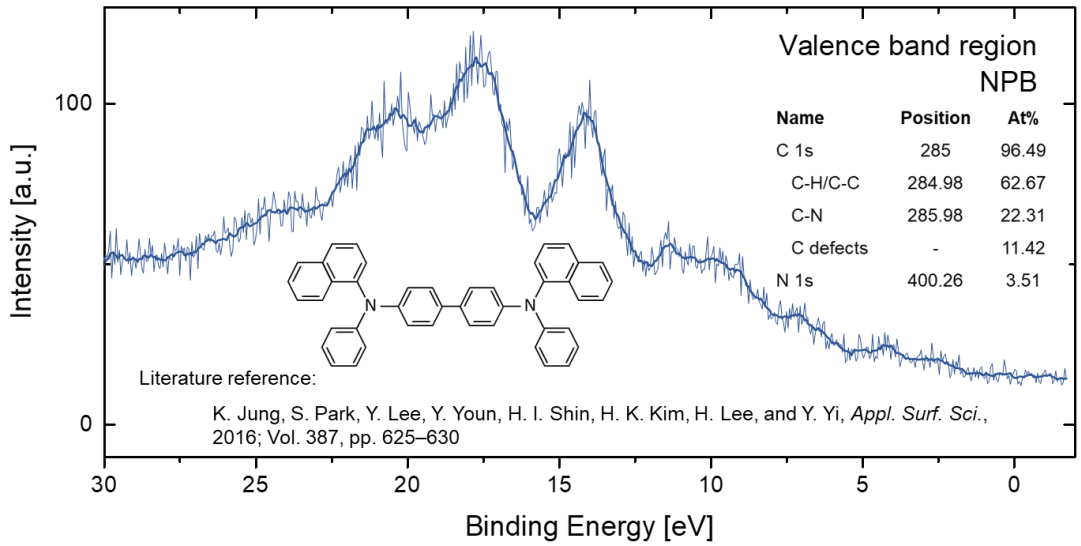
Valence band region
NPB
Name Position At%
C 1s 285 96.49
C-H/C-C 284.98 62.67
C-N 285.98 22.31
C defects - 11.42
N 1s 400.26 3.51
Literature reference:
K. Jung, S. Park, Y. Lee, Y. Youn, H. I. Shin, H. K. Kim, H. Lee, and Y. Yi, Appl. Surf. Sci., 2016; Vol. 387, pp. 625–630
Intensity [a.u.]
Binding Energy [eV]

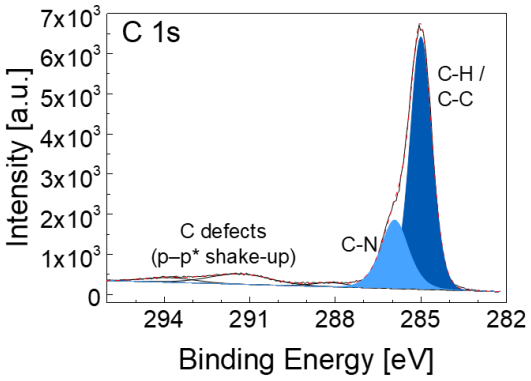
C 1s
C-H / C-C
C-N
C defects (p–p* shake-up)
Intensity [a.u.]
Binding Energy [eV]

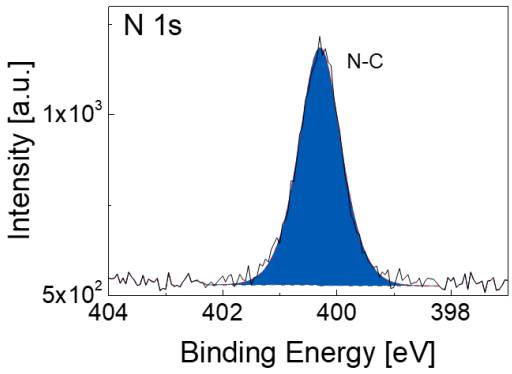
N 1s
N-C
Intensity [a.u.]
Binding Energy [eV]

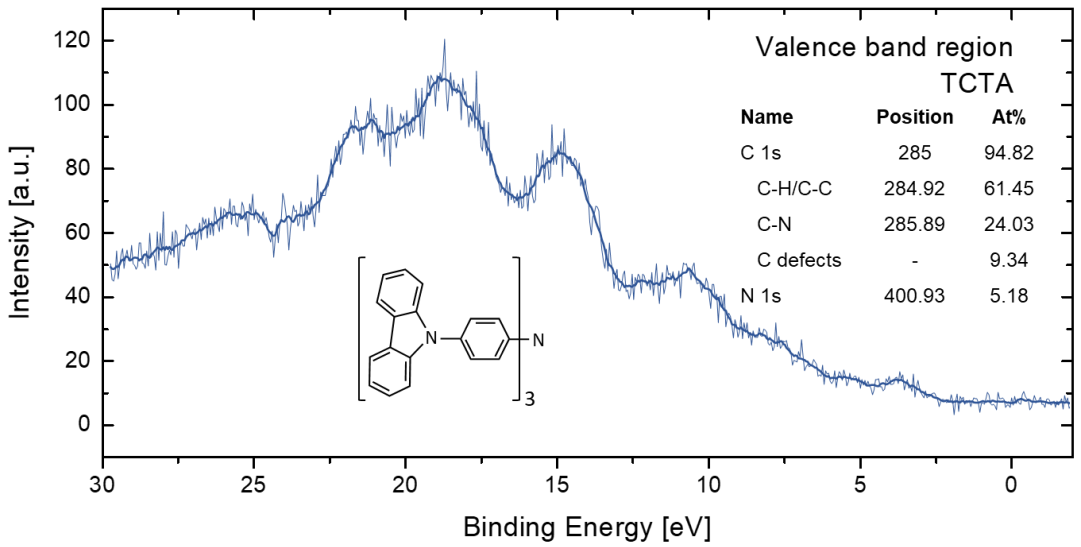
Valence band region
TCTA
Name Position At%
C 1s 285 94.82
C-H/C-C 284.92 61.45
C-N 285.89 24.03
C defects - 9.34
N 1s 400.93 5.18
Intensity [a.u.]
Binding Energy [eV]

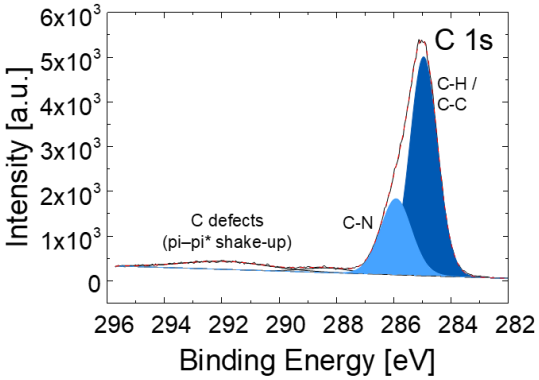
C 1s
C-H / C-C
C-N
C defects (pi–pi* shake-up)
Intensity [a.u.]
Binding Energy [eV]

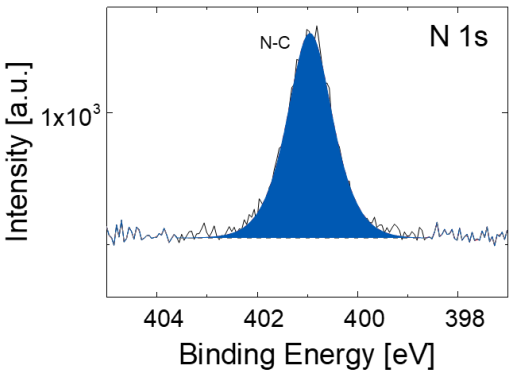
N 1s
N-C
Intensity [a.u.]
Binding Energy [eV]

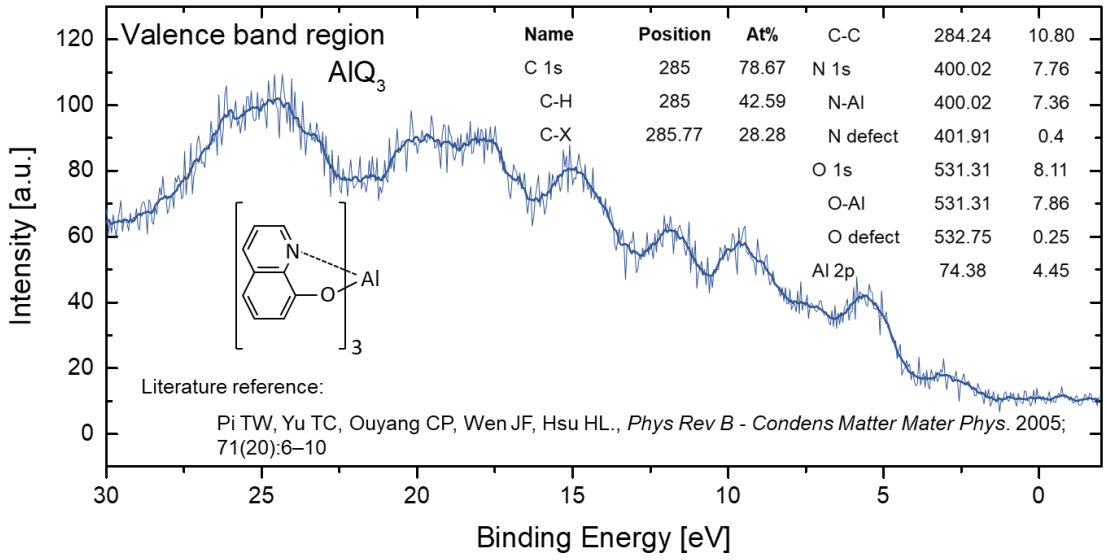

Name	Position	At%
C 1s	285	78.67
C-H	285	42.59
C-X	285.77	28.28
C-C	284.24	10.80
N 1s	400.02	7.76
N-Al	400.02	7.36
N defect	401.91	0.4
O 1s	531.31	8.11
O-Al	531.31	7.86
O defect	532.75	0.25
Al 2p	74.38	4.45

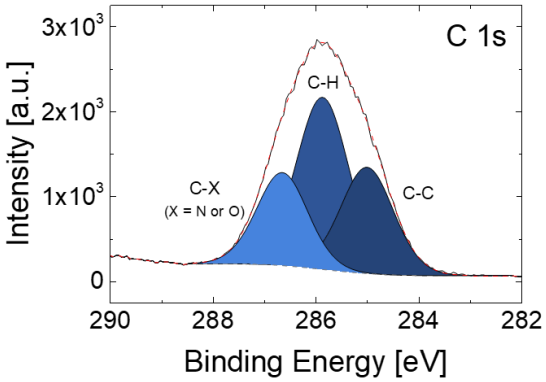

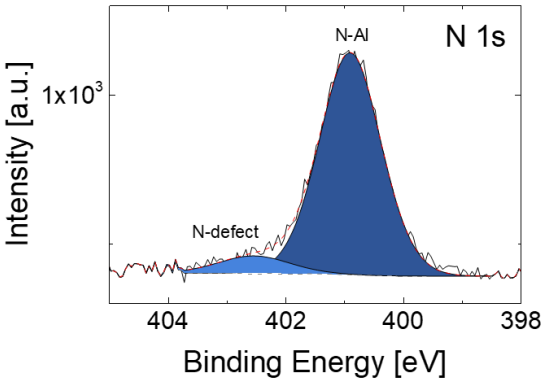

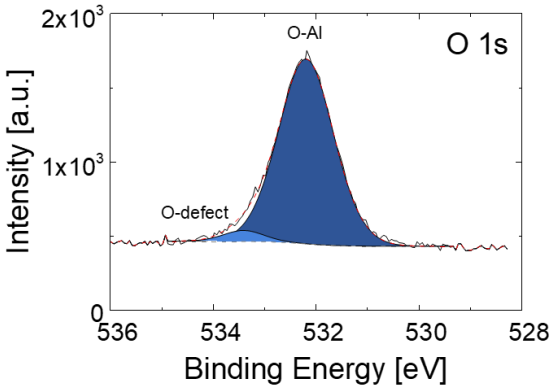

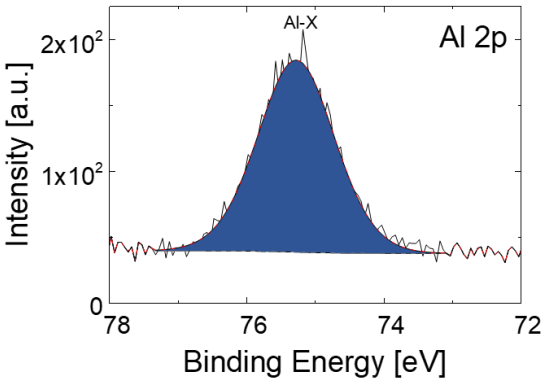

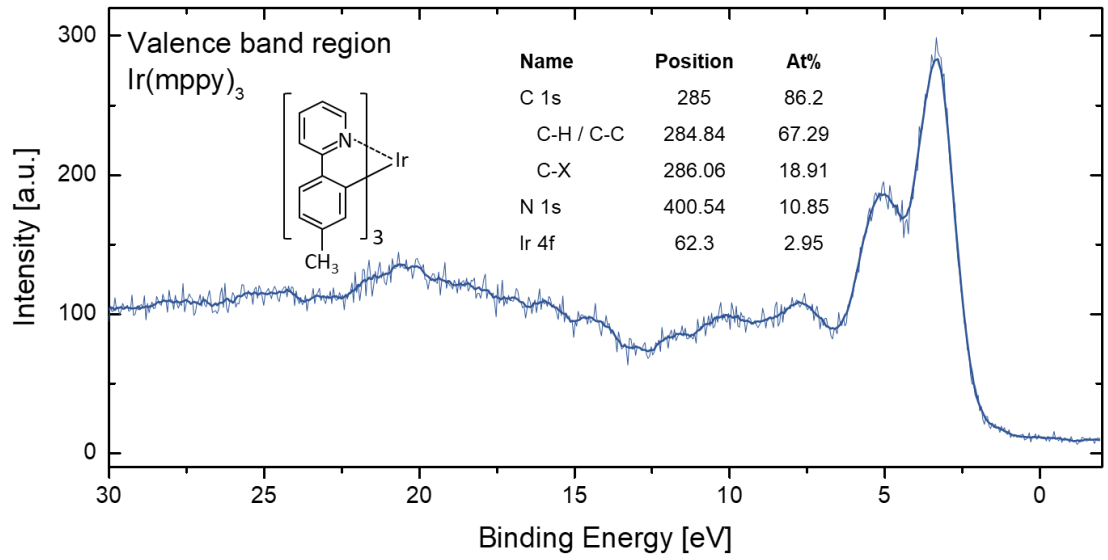
Valence band region
Ir(mppy)3
Name Position At%
C 1s 285 86.2
C-H / C-C 284.84 67.29
C-X 286.06 18.91
N 1s 400.54 10.85
Ir 4f 62.3 2.95
Intensity [a.u.]
Binding Energy [eV]

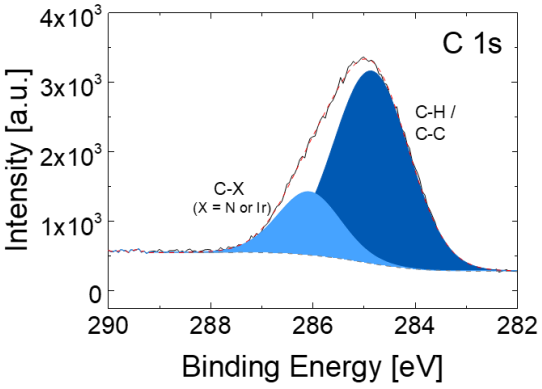
C 1s
C-H / C-C
C-X
(X = N or Ir)
Intensity [a.u.]
Binding Energy [eV]

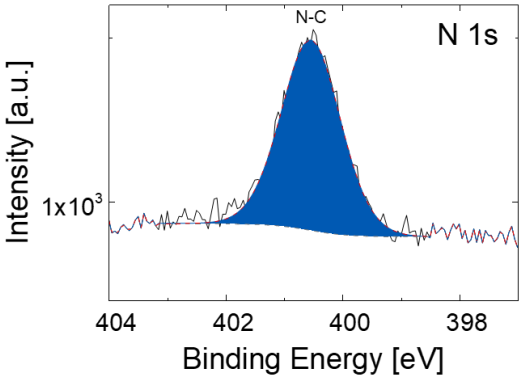
N 1s
N-C
Intensity [a.u.]
Binding Energy [eV]

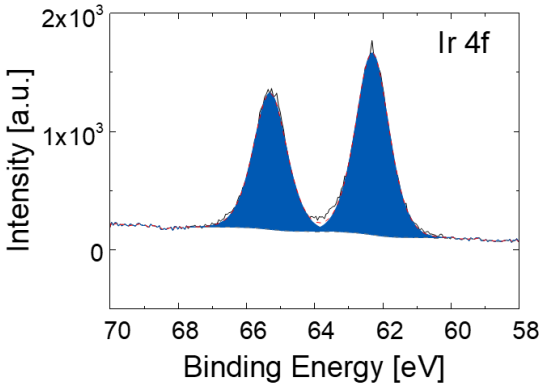
Ir 4f
Intensity [a.u.]
Binding Energy [eV]

Bibliography

[1] H. J. Round, “A note on carborundum,” *Electrical World*, vol. 49. p. 309, 1907.

[2] O. V. Losev, “Luminous carborundum detector and detection with crystals,” *Telegr. i Telef. bez Provodov*, vol. 44, pp. 485–494, 1927.

[3] R. Braunstein, “Radiative Transitions in Semiconductors,” *Phys. Rev.*, vol. 99, no. 6, pp. 1892–1893, Sep. 1955.

[4] N. Holonyak and S. F. Bevacqua, “Coherent (visible) light emission from Ga(As1-xPx) junctions,” *Appl. Phys. Lett.*, vol. 1, no. 4, pp. 82–83, 1962.

[5] A. Bernanose, M. Comte, and P. Vouaux, “Sur Un Nouveau Mode D’Emission Lumineuse Chez Certains Composés Organiques,” *J. Chim. Phys.*, vol. 50, pp. 64–68, 1953.

[6] H. Kallmann and M. Pope, “Positive hole injection into organic crystals,” *J. Chem. Phys.*, vol. 32, no. 1, pp. 300–301, 1960.

[7] C. W. Tang and S. A. VanSlyke, “Organic electroluminescent diodes,” *Appl. Phys. Lett.*, vol. 51, no. 12, pp. 913–915, 1987.

[8] C. K. Chiang, C. R. Fincher, Y. W. Park, A. J. Heeger, H. Shirakawa, E. J. Louis, S. C. Gau, and A. G. MacDiarmid, “Electrical conductivity in doped polyacetylene,” *Phys. Rev. Lett.*, vol. 39, no. 17, pp. 1098–1101, 1977.

[9] J. H. Burroughes, D. D. C. Bradley, A. R. Brown, R. N. Marks, K. Mackay, R. H. Friend, P. L. Burns, and A. B. Holmes, “Light-emitting diodes based on conjugated polymers,” *Nature*, vol. 347, no. 6293, pp. 539–541, 1990.

[10] N. Thejo Kalyani and S. J. Dhoble, “Novel materials for fabrication and encapsulation of OLEDs,” *Renew. Sustain. Energy Rev.*, vol. 44, pp. 319–347, 2015.

[11] M. Pfeiffer, S. R. Forrest, K. Leo, and M. E. Thompson, “Electrophosphorescent p-i-n Organic Light-Emitting Devices for Very-High-Efficiency Flat-Panel Displays,” *Adv. Mater.*, vol. 14, no. 22, pp. 1633–1636, 2002.

[12] S. Olthof, R. Meerheim, M. Schober, and K. Leo, “Energy level alignment at the interfaces in a multilayer organic light-emitting diode structure,” *Phys. Rev. B - Condens. Matter Mater. Phys.*, vol. 79, no. 24, pp. 1–7, 2009.

[13] C. N. Li, C. Y. Kwong, A. B. Djurišić, P. T. Lai, P. C. Chui, W. K. Chan, and S. Y. Liu, “Improved performance of OLEDs with ITO surface treatments,” *Thin Solid Films*, vol. 477, no. 1–2, pp. 57–62, 2005.

[14] R. Bathelt, D. Buchhauser, C. Gärditz, R. Paetzold, and P. Wellmann, “Light extraction from OLEDs for lighting applications through light scattering,” *Org. Electron. Physics, Mater. Appl.*, vol. 8, no. 4, pp. 293–299, 2007.

[15] W. H. Lee, D. H. Kim, P. Justin Jesuraj, H. Hafeez, J. C. Lee, D. K. Choi, T.-S. Bae, S. M. Yu, M. Song, C. S. Kim, and S. Y. Ryu, “Improvement of charge balance, recombination zone confinement, and low efficiency roll-off in green phosphorescent OLEDs by altering electron transport layer thickness,” *Mater. Res. Express*, vol. 5, no. 7, pp. 1–8, 2018.

[16] Y. L. Chang, Z. B. Wang, M. G. Helander, J. Qiu, D. P. Puzzo, and Z. H. Lu, “Enhancing the efficiency of simplified red phosphorescent organic light emitting diodes by exciton harvesting,” *Org. Electron. physics, Mater. Appl.*, vol. 13, no. 5, pp. 925–931, 2012.

[17] M. G. Helander, Z. B. Wang, J. Qiu, and M. T. Greiner, “Chlorinated indium tin oxide electrodes with high work function for organic device compatibility,” *Science (80-.).*, no. April, pp. 944–948, 2011.

[18] C. W. Lee and J. Y. Lee, “Above 30% external quantum efficiency in blue phosphorescent organic light-emitting diodes using pyrido[2,3-b]indole derivatives as host materials,” *Adv. Mater.*, vol. 25, no. 38, pp. 5450–5454, 2013.

[19] W. Song, L. Shi, L. Gao, P. Hu, H. Mu, Z. Xia, J. Huang, and J. Su, “[1,2,4]Triazolo[1,5- *a*]pyridine as Building Blocks for Universal Host Materials for High-Performance Red, Green, Blue and White Phosphorescent Organic Light-Emitting Devices,” *ACS Appl. Mater. Interfaces*, vol. 10, no. 6, pp. 5714–5722, 2018.

[20] P. Cossari, M. Pugliese, S. Gambino, A. Cannavale, V. Maiorano, G. Gigli, and M. Mazzeo, “Fully integrated electrochromic-OLED devices for highly transparent smart glasses,” *J. Mater. Chem. C*, vol. 6, no. 27, pp. 7274–7284, 2018.

[21] M. Mizukami, S.-I. Cho, K. Watanabe, M. Abiko, Y. Suzuri, S. Tokito, and J. Kido, “Flexible Organic Light-Emitting Diode Displays Driven by Inkjet Printed High Mobility Organic Thin Film Transistors,” *IEEE Electron Device Lett.*, vol. 39, no. 1, pp. 1–1, 2017.

[22] T. Tsujimura, J. Fukawa, K. Endoh, Y. Suzuki, K. Hirabayashi, and T. Mori, “10.1: Invited Paper : Flexible OLED using Plastic Barrier Film and its Roll-to-Roll Manufacturing,” *SID Symp. Dig. Tech. Pap.*, vol. 45, no. 1, pp. 104–107, Jun. 2014.

[23] S. Sato, S. Ohisa, Y. Hayashi, R. Sato, D. Yokoyama, T. Kato, M. Suzuki, T. Chiba, Y. J. Pu, and J. Kido, “Air-Stable and High-Performance Solution-Processed Organic Light-Emitting Devices Based on Hydrophobic Polymeric Ionic Liquid Carrier-Injection Layers,” *Adv. Mater.*, vol. 30, no. 18, pp. 1–8, 2018.

[24] H. Zheng, Y. Zheng, N. Liu, N. Ai, Q. Wang, S. Wu, J. Zhou, D. Hu, S. Yu, S. Han, W. Xu, C. Luo, Y. Meng, Z. Jiang, Y. Chen, D. Li, F. Huang, J. Wang, J. Peng, and Y. Cao, “All-solution processed polymer light-emitting diode displays,” *Nat. Commun.*, vol. 4, no. May, pp. 1–7, 2013.

[25] X. Zhang, Q. Zheng, Z. Tang, W. Li, Y. Zhang, K. Xu, X. Xue, J. Xu, H. Wang, and B. Wei, “Tunable hole injection of solution-processed polymeric carbon nitride towards efficient organic light-emitting diode,” *Appl. Phys. Lett.*, vol. 112, no. 8, pp. 0–4, 2018.

[26] R. Bail, J. Y. Hong, and B. D. Chin, “Inkjet printing of blue phosphorescent light-emitting layer based on bis(3,5-di(9: H -carbazol-9-yl))diphenylsilane,” *RSC Adv.*, vol. 8, no. 20, pp. 11191–11197, 2018.

[27] B. Sun, X. Fan, H. Ye, J. Fan, C. Qian, W. van Driel, and G. Zhang, “A novel lifetime prediction for integrated LED lamps by electronic-thermal simulation,” *Reliab. Eng. Syst. Saf.*, vol. 163, no. January 2016, pp. 14–21, 2017.

[28] S. Scholz, D. Kondakov, B. Lüssem, and K. Leo, “Degradation mechanisms and reactions in organic light-emitting devices,” *Chem. Rev.*, vol. 115, no. 16, pp. 8449–8503, 2015.

[29] P. Kathirgamanathan, L. M. Bushby, M. Kumaraverl, S. Ravichandran, and S. Surendrakumar, “Electroluminescent organic and quantum Dot LEDs: The state of the art,” *IEEE/OSA J. Disp. Technol.*, vol. 11, no. 5, pp. 480–493, 2015.

[30] D. D. ELEY, “Phthalocyanines as Semiconductors,” *Nature*, vol. 162, no. 4125, pp. 819–819, Nov. 1948.

[31] H. Shirakawa, E. J. Louis, A. G. MacDiarmid, C. K. Chiang, and A. J. Heeger, “Synthesis of electrically conducting organic polymers: halogen derivatives of polyacetylene, (CH) x,” *J. Chem. Soc. Chem. Commun.*, no. 16, p. 578, 1977.

[32] C. Wang, H. Dong, W. Hu, Y. Liu, and D. Zhu, “Semiconducting π-conjugated systems in field-effect transistors: A material odyssey of organic electronics,” *Chem. Rev.*, vol. 112, no. 4, pp.

2208–2267, 2012.

[33] C. Liu, K. Huang, W. T. Park, M. Li, T. Yang, X. Liu, L. Liang, T. Minari, and Y. Y. Noh, "A unified understanding of charge transport in organic semiconductors: The importance of attenuated delocalization for the carriers," *Mater. Horizons*, vol. 4, no. 4, pp. 608–618, 2017.

[34] C. Wang, H. Dong, L. Jiang, and W. Hu, "Organic semiconductor crystals," *Chem. Soc. Rev.*, vol. 47, no. 2, pp. 422–500, 2018.

[35] J. L. Brédas, D. Beljonne, V. Coropceanu, and J. Cornil, "Charge-transfer and energy-transfer processes in π-conjugated oligomers and polymers: A molecular picture," *Chem. Rev.*, vol. 104, no. 11, pp. 4971–5003, 2004.

[36] V. Coropceanu, J. Cornil, D. A. da Silva Filho, Y. Olivier, R. Silbey, and J. L. Brédas, "Charge transport in organic semiconductors," *Chem. Rev.*, vol. 107, no. 4, pp. 926–952, 2007.

[37] T. T. Bui, F. Goubard, M. Ibrahim-Ouali, D. Gigmes, and F. Dumur, "Recent advances on organic blue thermally activated delayed fluorescence (TADF) emitters for organic light-emitting diodes (OLEDs)," *Beilstein J. Org. Chem.*, vol. 14, pp. 282–308, 2018.

[38] N. Tessler, "Excitons," in *Organic Semiconductors and devices*, Technion, Ed. Electrical Engineering Department, 1999.

[39] H. Yersin, Ed., *Highly Efficient OLEDs with Phosphorescent Materials*. Weinheim, Germany: Wiley-VCH Verlag GmbH & Co. KGaA, 2007.

[40] W. Song and J. Y. Lee, "Degradation Mechanism and Lifetime Improvement Strategy for Blue Phosphorescent Organic Light-Emitting Diodes," *Adv. Opt. Mater.*, vol. 5, no. 9, 2017.

[41] S. Schmidbauer, A. Hohenleutner, and B. König, "Chemical degradation in organic light-emitting devices: Mechanisms and implications for the design of new materials," *Adv. Mater.*, vol. 25, no. 15, pp. 2114–2129, 2013.

[42] A. Turak, "Interfacial degradation in organic optoelectronics," *RCS Adv.*, vol. 3, no. 18, pp. 6188–6225, 2013.

[43] Y.-F. Liew, F. Zhu, and S.-J. Chua, "Effect of organic layer combination on dark spot formation in organic light emitting devices," *Chem. Phys. Lett.*, vol. 394, no. 4–6, pp. 275–279, 2004.

[44] K. K. Lin, S. J. Chua, and S. F. Lim, "Influence of electrical stress voltage on cathode degradation of organic light-emitting devices," *J. Appl. Phys.*, vol. 90, no. 2, pp. 976–979, 2001.

[45] P. Melpignano, A. Baron-Toaldo, V. Biondo, S. Priante, R. Zamboni, M. Murgia, S. Caria, L. Gregoratti, A. Barinov, and M. Kiskinova, "Mechanism of dark-spot degradation of organic light-emitting devices," *Appl. Phys. Lett.*, vol. 86, no. 4, p. 041105, 2005.

[46] W. Wang, S. F. Lim, and S. J. Chua, "Bubble formation and growth in organic light-emitting diodes composed of a polymeric emitter and a calcium cathode," *J. Appl. Phys.*, vol. 91, no. 9, pp. 5712–5715, 2002.

[47] H. Aziz and Z. D. Popovic, "Degradation Phenomena in Small-Molecule Organic Light-Emitting Devices," *Chem. Mater.*, vol. 16, no. 23, pp. 4522–4532, 2004.

[48] Y. Kim, D. Choi, H. Lim, and C. S. Ha, "Accelerated pre-oxidation method for healing progressive electrical short in organic light-emitting devices," *Appl. Phys. Lett.*, vol. 82, no. 14, pp. 2200–2202, 2003.

[49] D. Yu, Y. Q. Yang, Z. Chen, Y. Tao, and Y. F. Liu, "Recent progress on thin-film encapsulation technologies for organic electronic devices," *Opt. Commun.*, vol. 362, pp. 43–49, 2016.

[50] H. Kaji, H. Suzuki, T. Fukushima, K. Shizu, K. Suzuki, S. Kubo, T. Komino, H. Oiwa, F. Suzuki, A. Wakamiya, Y. Murata, and C. Adachi, "Purely organic electroluminescent material realizing 100% conversion from electricity to light," *Nat. Commun.*, vol. 6, no. May, pp. 1–8, 2015.

[51] T. Yamada, D. Zou, H. Jeong, Y. Akaki, and T. Tsutsui, “Recoverable degradation and internal field forming process accompanied by the orientation of dipoles in organic light emitting diodes,” *Synth. Met.*, vol. 111, pp. 237–240, 2000.

[52] S. T. Lee, Z. Q. Gao, and L. S. Hung, “Metal diffusion from electrodes in organic light-emitting diodes,” *Appl. Phys. Lett.*, vol. 75, no. 10, pp. 1404–1406, 1999.

[53] N. C. Giebink, B. W. D’Andrade, M. S. Weaver, P. B. MacKenzie, J. J. Brown, M. E. Thompson, and S. R. Forrest, “Intrinsic luminance loss in phosphorescent small-molecule organic light emitting devices due to bimolecular annihilation reactions,” *J. Appl. Phys.*, vol. 103, no. 4, 2008.

[54] P. E. Burrows, V. Bulovic, S. R. Forrest, L. S. Sapochak, D. M. McCarty, and M. E. Thompson, “Reliability and degradation of organic light emitting devices,” *Appl. Phys. Lett.*, vol. 65, no. 23, pp. 2922–2924, 1994.

[55] M. Murgia, R. H. Michel, G. Ruani, W. Gebauer, O. Kapousta, R. Zamboni, and C. Taliani, “In-situ characterisation of the oxygen induced changes in a UHV grown organic light-emitting diode,” *Synth. Met.*, vol. 102, no. 1–3, pp. 1095–1096, 1999.

[56] J. E. Knox, M. D. Halls, H. P. Hratchian, and H. B. Schlegel, “Chemical failure modes of AlQ3-based OLEDs: AlQ3 hydrolysis,” *Phys. Chem. Chem. Phys.*, vol. 8, no. 12, pp. 1371–1377, 2006.

[57] C.-C. Lee, S.-W. Liu, and Y.-T. Chung, “Effect of deposition rate on device performance and lifetime of planar molecule-based organic light-emitting diodes,” *J. Phys. D. Appl. Phys.*, vol. 43, no. 7, p. 075102, 2010.

[58] L. M. Do, E. M. Han, Y. Niidome, M. Fujihira, T. Kanno, S. Yoshida, A. Maeda, and A. J. Ikushima, “Observation of degradation processes of Al electrodes in organic electroluminescence devices by electroluminescence microscopy, atomic force microscopy, scanning electron microscopy, and Auger electron spectroscopy,” *J. Appl. Phys.*, vol. 76, no. 9, pp. 5118–5121, Nov. 1994.

[59] M. Fujihira, L. Do, A. Koike, and E. Han, “Growth of dark spots by interdiffusion across organic layers in organic electroluminescent devices,” *Appl. Phys. Lett.*, vol. 68, no. 13, pp. 1787–1789, Mar. 1996.

[60] D. Y. Kondakov, W. C. Lenhart, and W. F. Nichols, “Operational degradation of organic light-emitting diodes: Mechanism and identification of chemical products,” *J. Appl. Phys.*, vol. 101, no. 2, 2007.

[61] S. Auschill, I. Rabelo De Moraes, B. Lüssem, M. C. Gather, and K. Leo, “A high performance liquid chromatography method to determine phenanthroline derivatives used in OLEDs and OSCs,” *Synth. Met.*, vol. 162, no. 21–22, pp. 1834–1838, 2012.

[62] S. Scholz, K. Walzer, and K. Leo, “Analysis of complete organic semiconductor devices by laser desorption/ionization time-of-flight mass spectrometry,” *Adv. Funct. Mater.*, vol. 18, no. 17, pp. 2541–2547, 2008.

[63] Y. Tachibana, Y. Nakajima, T. Isemura, K. Yamamoto, T. Satoh, J. Aoki, and M. Toyoda, “High Spatial Resolution Laser Desorption/Ionization Mass Spectrometry Imaging of Organic Layers in an Organic Light-Emitting Diode,” *Mass Spectrom.*, vol. 5, no. 1, pp. A0052–A0052, 2017.

[64] W. J. Mitchell, P. L. Burn, R. K. Thomas, G. Fragneto, J. P. J. Markham, and I. D. W. Samuel, “Relating the physical structure and optical properties of conjugated polymers using neutron reflectivity in combination with photoluminescence spectroscopy,” *J. Appl. Phys.*, vol. 95, no. 5, pp. 2391–2396, 2004.

[65] J. A. McEwan, A. J. Clulow, P. E. Shaw, A. Nelson, T. A. Darwish, P. L. Burn, and I. R. Gentle, “Diffusion at Interfaces in OLEDs Containing a Doped Phosphorescent Emissive Layer,” *Adv. Mater. Interfaces*, vol. 3, no. 17, pp. 1–9, 2016.

[66] J. A. McEwan, A. J. Clulow, A. Nelson, R. D. Jansen-Van Vuuren, P. L. Burn, and I. R. Gentle,

"Morphology of OLED Film Stacks Containing Solution-Processed Phosphorescent Dendrimers," *ACS Appl. Mater. Interfaces*, vol. 10, no. 4, pp. 3848–3855, 2018.

[67] J. J. Thomson, "Bakerian Lecture: Rays of Positive Electricity," *Proc. R. Soc. A Math. Phys. Eng. Sci.*, vol. 89, no. 607, pp. 1–20, Aug. 1913.

[68] A. J. Dempster, "The properties of slow canal rays," *Phys. Rev.*, vol. 8, no. 6, pp. 651–662, 1916.

[69] H. D. Smyth, "A New Method for Studying Ionising Potentials," *Proc. R. Soc. A Math. Phys. Eng. Sci.*, vol. 102, no. 716, pp. 283–293, Dec. 1922.

[70] F. L. Arnot and J. C. Milligan, "A New Process of Negative Ion Formation," *Proc. R. Soc. A Math. Phys. Eng. Sci.*, vol. 156, no. 889, pp. 538–560, Sep. 1936.

[71] R. F. K. Herzog and F. P. Viehböck, "Ion Source for Mass Spectrography," *Phys. Rev.*, vol. 76, pp. 855–856, 1949.

[72] H. Liebl, "Ion microprobe mass analyzer," *J. Appl. Phys.*, vol. 38, no. 13, pp. 5277–5283, 1967.

[73] H. W. Werner, "Investigation of Solids by Means of an Ion-Bombardment Mass Spectrometer," in *Developments in Applied Spectroscopy*, vol. 7a, Boston, MA: Springer US, 1969, pp. 239–266.

[74] A. Benninghoven, "Analysis of sub-monolayers on silver by secondary ion emission," *Phys. Status Solidi*, vol. 34, p. K169, 1969.

[75] R. D. Macfarlane and D. F. Torgerson, "252Cf-plasma desorption time-of-flight mass spectrometry," *Int. J. Mass Spectrom. Ion Phys.*, vol. 21, no. 1–2, pp. 81–92, 1976.

[76] B. T. Chait and K. G. Standing, "A time-of-flight mass spectrometer for measurement of secondary ion mass spectra," *Int. J. Mass Spectrom. Ion Phys.*, vol. 40, no. 2, pp. 185–193, 1981.

[77] A. Pirkl, R. Moellers, H. Arlinghaus, F. Kollmer, E. Niehuis, A. Makarov, S. Horning, M. Passarelli, R. Havelund, P. Rakowska, A. Race, A. G. Shard, A. West, P. Marshall, C. F. Newman, M. Alexander, C. Dollery, and I. S. Gilmore, "A Novel Hybrid Dual Analyzer SIMS Instrument for Improved Surface and 3D-Analysis," *Microsc. Microanal.*, vol. 22, no. S3, pp. 340–341, 2016.

[78] G. L. Fisher, A. L. Bruinen, N. Ogrinc Potočnik, J. S. Hammond, S. R. Bryan, P. E. Larson, and R. M. A. Heeren, "A New Method and Mass Spectrometer Design for TOF-SIMS Parallel Imaging MS/MS," *Anal. Chem.*, vol. 88, no. 12, pp. 6433–6440, 2016.

[79] M. K. Passarelli, A. Pirkl, R. Moellers, D. Grinfeld, F. Kollmer, R. Havelund, C. F. Newman, P. S. Marshall, H. Arlinghaus, M. R. Alexander, A. West, S. Horning, E. Niehuis, A. Makarov, C. T. Dollery, and I. S. Gilmore, "The 3D OrbiSIMS—label-free metabolic imaging with subcellular lateral resolution and high mass-resolving power," *Nat. Methods*, vol. 14, no. 12, pp. 1175–1183, Nov. 2017.

[80] P. Gratia, G. Grancini, J. N. Audinot, X. Jeanbourquin, E. Mosconi, I. Zimmermann, D. Dowsett, Y. Lee, M. Grätzel, F. De Angelis, K. Sivula, T. Wirtz, and M. K. Nazeeruddin, "Intrinsic Halide Segregation at Nanometer Scale Determines the High Efficiency of Mixed Cation/Mixed Halide Perovskite Solar Cells," *J. Am. Chem. Soc.*, vol. 138, no. 49, pp. 15821–15824, 2016.

[81] "IONTOF." [Online]. Available: https://www.iontof.com/. [Accessed: 20-Oct-2017].

[82] M. A. Robinson, D. J. Graham, and D. G. Castner, "ToF-SIMS depth profiling of cells: Z-correction, 3D imaging, and sputter rate of individual NIH/3T3 fibroblasts," *Anal. Chem.*, vol. 84, no. 11, pp. 4880–4885, 2012.

[83] T. Wirtz, Y. Fleming, U. Gysin, T. Glatzel, E. Meyer, U. Maier, and U. Wegmann, "Combined SIMS-SPM Instrument For High Sensitivity And High Resolution Elemental 3D Analysis," *Microsc. Microanal.*, vol. 18, no. S2, pp. 888–889, 2012.

[84] M. A. Moreno, I. Mouton, N. Chevalier, J.-P. Barnes, F. Bassani, and B. Gautier, "Combined ToF-SIMS and AFM protocol for accurate 3D chemical analysis and data visualization," *J. Vac. Sci. Technol. B, Nanotechnol. Microelectron. Mater. Process. Meas. Phenom.*, vol. 36, no. 3, p. 03F122, 2018.

[85] A. Benninghoven, "The History of Static SIMS - A personal perspective," in *ToF-SIMS: Material Analysis by Mass Spectrometry*, 2nd ed., J. C. Vickerman and D. Briggs, Eds. Manchester, UK: IM Publications and SurfaceSpectra Ltd, 2013, pp. 39–67.

[86] P. Sigmund, "Sputtering by ion bombardment theoretical concepts," in *Sputtering by Particle Bombardment*, Berlin, Heidelberg: Springer, 1981, pp. 9–71.

[87] H. M. Urbassek, "Status of cascade theory," in *ToF-SIMS: Material Analysis by Mass Spectrometry*, 2nd ed., J. C. Vickerman and D. Briggs, Eds. Manchester, UK: IM Publications and SurfaceSpectra Ltd, 2013, pp. 67–87.

[88] T. Terlier, "Analyse par ToF-SIMS de matériaux organiques pour les applications en électronique organique," Université Claude Bernard de Lyon, 2015.

[89] P. Sigmund, "Theory of Sputtering. I. Sputtering Yield of Amorphous and Polycrystalline Targets," *Phys. Rev.*, vol. 184, no. 2, pp. 383–416, Aug. 1969.

[90] J. P. Biersack and W. Eckstein, "Sputtering studies with the Monte Carlo Program TRIM.SP," *Appl. Phys. A Solids Surfaces*, vol. 34, no. 2, pp. 73–94, 1984.

[91] G. Betz, R. Kirchner, W. Husinsky, F. Rüdenauer, and H. M. Urbassek, "Molecular dynamics study of sputtering of Cu (111) under Ar ion bombardment," *Radiat. Eff. Defects Solids*, vol. null, no. 1, pp. 251–266, Jul. 1994.

[92] N. P. Lockyer, "Laser post-ionization for elemental and molecular surface analysis," in *ToF-SIMS: Material Analysis by Mass Spectrometry*, 2nd ed., J. C. Vickerman and D. Briggs, Eds. Manchester, UK: IM Publications and SurfaceSpectra Ltd, 2013, pp. 361–396.

[93] N. J. Popczun, L. Breuer, A. Wucher, and N. Winograd, "Ionization Probability in Molecular Secondary Ion Mass Spectrometry: Protonation Efficiency of Sputtered Guanine Molecules Studied by Laser Postionization," *J. Phys. Chem. C*, vol. 121, no. 16, pp. 8931–8937, 2017.

[94] R. Hill, "Analysis beams used in ToF-SIMS," in *ToF-SIMS: Material Analysis by Mass Spectrometry*, 2nd ed., J. C. Vickerman and D. Briggs, Eds. Manchester, UK: IM Publications and SurfaceSpectra Ltd, 2013, pp. 271–290.

[95] Q. P. Vanbellingen, N. Elie, M. J. Eller, S. Della-Negra, D. Touboul, and A. Brunelle, "Time-of-flight secondary ion mass spectrometry imaging of biological samples with delayed extraction for high mass and high spatial resolutions," *Rapid Commun. Mass Spectrom.*, vol. 29, no. 13, pp. 1187–1195, 2015.

[96] M. P. Seah and A. G. Shard, "The matrix effect in secondary ion mass spectrometry," *Appl. Surf. Sci.*, vol. 439, pp. 605–611, 2018.

[97] V. R. Deline, W. Katz, C. A. Evans, and P. Williams, "Mechanism of the SIMS matrix effect," *Appl. Phys. Lett.*, vol. 33, no. 9, pp. 832–835, 1978.

[98] D. Sykes, A. Chew, M. Crapper, and R. Valizadeh, "The effect of oxygen flooding on the secondary ion yield of Cs in the Cameca IMS 3f," *Vacuum*, vol. 43, no. 1–2, pp. 159–162, 1992.

[99] B. Berghmans, B. Van Daele, L. Geenen, T. Conard, A. Franquet, and W. Vandervorst, "Cesium near-surface concentration in low energy, negative mode dynamic SIMS," *Appl. Surf. Sci.*, vol. 255, no. 4, pp. 1316–1319, 2008.

[100] S. Sheraz, A. Barber, I. Berrueta Razo, J. S. Fletcher, N. P. Lockyer, and J. C. Vickerman, "Prospect of increasing secondary ion yields in ToF-SIMS using water cluster primary ion beams," *Surf. Interface Anal.*, vol. 46, no. S1, pp. 51–53, Nov. 2014.

[101] H. Tian, A. Wucher, and N. Winograd, “Dynamic Reactive Ionization with Cluster Secondary Ion Mass Spectrometry,” *J. Am. Soc. Mass Spectrom.*, vol. 27, no. 2, pp. 285–292, 2016.

[102] H. Tian, A. Wucher, and N. Winograd, “Reducing the Matrix Effect in Organic Cluster SIMS Using Dynamic Reactive Ionization,” *J. Am. Soc. Mass Spectrom.*, vol. 27, no. 12, pp. 2014–2024, 2016.

[103] W. C. Wiley and I. H. McLaren, “Time-of-flight mass spectrometer with improved resolution,” *Rev. Sci. Instrum.*, vol. 26, no. 12, pp. 1150–1157, 1955.

[104] A. Henss, S.-K. Otto, K. Schaepe, L. Pauksch, K. S. Lips, and M. Rohnke, “High resolution imaging and 3D analysis of Ag nanoparticles in cells with ToF-SIMS and delayed extraction,” *Biointerphases*, vol. 13, no. 3, p. 03B410, 2018.

[105] B. W. Schueler, “Time-of-flight mass analysers,” in *ToF-SIMS: Material Analysis by Mass Spectrometry*, 2nd ed., J. C. Vickerman and D. Briggs, Eds. Manchester, UK: IM Publications and SurfaceSpectra Ltd, 2013, pp. 247–270.

[106] H. Hertz, “Ueber einen Einfluss des ultravioletten Lichtes auf die electrische Entladung,” *Ann. Phys.*, vol. 267, no. 8, pp. 983–1000, 1887.

[107] A. Einstein, “Über einen die Erzeugung und Verwandlung des Lichtes betreffenden heuristischen Gesichtspunkt,” *Ann. Phys.*, vol. 322, no. 6, pp. 132–148, 1905.

[108] K. Siegbahn, “Electron Spectroscopy for Atoms , Molecules and Condensed Matter,” *Rev. Mod. Phys.*, vol. 54, no. 709, 1982.

[109] P. van der Heide, *X-Ray Photoelectron Spectroscopy*. Hoboken, NJ, USA: John Wiley & Sons, Inc., 2011.

[110] C. N. Berglund and W. E. Spicer, “Photoemission Studies of Copper and Silver: Theory,” *Phys. Rev.*, vol. 136, no. 4A, pp. A1030–A1044, Nov. 1964.

[111] D. Briggs and J. C. Rivière, “Spectral Interpretation,” in *Practical Surface Analysis by Auger and X-ray Photoelectron Spectroscopy*, D. Briggs and M. P. Seah, Eds. John Wiley & Sons, Ltd, 1983, p. 87.

[112] M. P. Seah and W. A. Dench, “Quantitative electron spectroscopy of surfaces: A standard data base for electron inelastic mean free paths in solids,” *Surf. Interface Anal.*, vol. 1, no. 1, pp. 2–11, Feb. 1979.

[113] D. Briggs, “Applications of XPS in Polymer Technology,” in *Practical Surface Analysis by Auger and X-ray Photoelectron Spectroscopy*, D. Briggs and M. P. Seah, Eds. John Wiley & Sons, Ltd, 1983, p. 359.

[114] M. P. Seah, “Quantification of AES and XPS,” in *Practical Surface Analysis by Auger and X-ray Photoelectron Spectroscopy*, D. Briggs and M. P. Seah, Eds. John Wiley & Sons, Ltd, 1983, p. 181.

[115] J. J. Pireaux, J. Riga, R. Caudano, and J. Verbist, “Electronic Structure of Polymers,” in *Photon, Electron, and Ion Probes of Polymer Structure and Properties*, ACS Sympos., 1981, pp. 169–201.

[116] D. Briggs and M. J. Hearn, “Analysis of polymer surfaces by SIMS. Part 5. The effects of primary ion mass and energy on secondary ion relative intensities,” *Int. J. Mass Spectrom. Ion Process.*, vol. 67, no. 1, pp. 47–56, 1985.

[117] A. D. Appelhans and J. E. Delmore, “Comparison of polyatomic and atomic primary beams for secondary ion mass spectrometry of organics,” *Anal. Chem.*, vol. 61, no. 10, pp. 1087–1093, 1989.

[118] J. E. Delmore, A. D. Appelhans, and D. A. Dahl, “Focused, Rasterable, High-Energy Neutral Molecular Beam Probe for Secondary Ion Mass Spectrometry,” *Anal. Chem.*, vol. 59, no. 13, pp.

1685–1691, 1987.

[119] C. M. Mahoney and G. Gillen, “An Introduction to Cluster Secondary Ion Mass Spectrometry (Cluster SIMS),” in *Cluster Secondary Ion Mass Spectrometry*, Hoboken, NJ, USA: John Wiley & Sons, Inc., 2013, pp. 1–11.

[120] G. Gillen and S. Roberson, “Preliminary evaluation of an SF5+ polyatomic primary ion beam for analysis of organic thin films by secondary ion mass spectrometry.,” *Rapid Commun. Mass Spectrom.*, vol. 12, no. 19, pp. 1303–12, 1998.

[121] A. Delcorte, O. A. Restrepo, and B. Czerwinski, “Cluster SIMS of Organic Materials: Theoretical Insights,” in *Cluster Secondary Ion Mass Spectrometry*, Hoboken, NJ, USA: John Wiley & Sons, Inc., 2013, pp. 13–55.

[122] A. Delcorte and B. J. Garrison, “keV fullerene interaction with hydrocarbon targets: Projectile penetration, damage creation and removal,” *Nucl. Instruments Methods Phys. Res. Sect. B Beam Interact. with Mater. Atoms*, vol. 255, no. 1 SPEC. ISS., pp. 223–228, 2007.

[123] S. Ninomiya, K. Ichiki, H. Yamada, Y. Nakata, T. Seki, T. Aoki, and J. Matsuo, “Precise and fast secondary ion mass spectrometry depth profiling of polymer materials with large Ar cluster ion beams,” *Rapid Commun. Mass Spectrom.*, vol. 23, no. 11, pp. 1601–1606, Jun. 2009.

[124] M. Hada, S. Ninomiya, T. Seki, T. Aoki, and J. Matsuo, “Using ellipsometry for the evaluation of surface damage and sputtering yield in organic films with irradiation of argon cluster ion beams,” *Surf. Interface Anal.*, vol. 43, no. 1–2, pp. 84–87, 2011.

[125] M. Hada, S. Ibuki, Y. Hontani, Y. Yamamoto, K. Ichiki, S. Ninomiya, T. Seki, T. Aoki, and J. Matsuo, “Low-damage milling of an amino acid thin film with cluster ion beam,” *J. Appl. Phys.*, vol. 110, no. 9, pp. 1–6, 2011.

[126] M. P. Seah, R. Havelund, and I. S. Gilmore, “Universal equation for argon cluster size-dependence of secondary ion spectra in sims of organic materials,” *J. Phys. Chem. C*, vol. 118, no. 24, pp. 12862–12872, 2014.

[127] A. Delcorte, B. J. Garrison, and K. Hamraoui, “Dynamics of molecular impacts on soft materials: From fullerenes to organic nanodrops,” *Anal. Chem.*, vol. 81, no. 16, pp. 6676–6686, 2009.

[128] C. Fleischmann, T. Conard, R. Havelund, A. Franquet, C. Poleunis, E. Voroshazi, A. Delcorte, and W. Vandervorst, “Fundamental aspects of Ar n + SIMS profiling of common organic semiconductors,” *Surf. Interface Anal.*, vol. 46, no. S1, pp. 54–57, Nov. 2014.

[129] J. S. Fletcher, “Latest applications of 3D ToF-SIMS bio-imaging,” *Biointerphases*, vol. 10, no. 1, p. 018902, 2015.

[130] S. Muramoto, J. Brison, and D. G. Castner, “Exploring the Surface Sensitivity of TOF-Secondary Ion Mass Spectrometry by Measuring the Implantation and Sampling Depths of Bi_n and C_60 Ions in Organic Films,” *Anal. Chem.*, vol. 84, no. 1, pp. 365–372, Jan. 2012.

[131] R. Havelund, M. P. Seah, and I. S. Gilmore, “Sampling Depths, Depth Shifts, and Depth Resolutions for Bi_n^+ Ion Analysis in Argon Gas Cluster Depth Profiles,” *J. Phys. Chem. B*, vol. 120, no. 9, pp. 2604–2611, 2016.

[132] L. D. Detter, O. W. Hand, R. G. Cooks, and R. A. Walton, “Interfacial chemical reactions accompanying desorption ionization mass spectrometry,” *Mass Spectrom. Rev.*, vol. 7, no. 5, pp. 465–502, 1988.

[133] S. Höfle, C. Bernhard, M. Bruns, C. Kübel, T. Scherer, U. Lemmer, and A. Colsmann, “Charge generation layers for solution processed tandem organic light emitting diodes with regular device architecture,” *ACS Appl. Mater. Interfaces*, vol. 7, no. 15, pp. 8132–8137, 2015.

[134] S. Scholz, Q. Huang, M. Thomschke, S. Olthof, P. Sebastian, K. Walzer, K. Leo, S. Oswald, C. Corten, and D. Kuckling, “Self-doping and partial oxidation of metal-on-organic interfaces for organic semiconductor devices studied by chemical analysis techniques,” *J. Appl. Phys.*, vol.

104, no. 10, 2008.

[135] N. C. Erickson, S. N. Raman, J. S. Hammond, and R. J. Holmes, “Depth profiling organic light-emitting devices by gas-cluster ion beam sputtering and X-ray photoelectron spectroscopy,” *Org. Electron.*, vol. 15, no. 11, pp. 2988–2992, 2014.

[136] T. Mouhib, C. Poleunis, N. Wehbe, J. J. Michels, Y. Galagan, L. Houssiau, P. Bertrand, and A. Delcorte, “Molecular depth profiling of organic photovoltaic heterojunction layers by ToF-SIMS: comparative evaluation of three sputtering beams.,” *Analyst*, vol. 138, no. 22, pp. 6801–10, 2013.

[137] K. F. Jeltsch, G. Lupa, and R. T. Weitz, “Materials depth distribution and degradation of a FIrpic based solution-processed blue OLED,” *Org. Electron.*, vol. 26, pp. 365–370, 2015.

[138] S. Ninomiya, K. Ichiki, H. Yamada, Y. Nakata, T. Seki, T. Aoki, and J. Matsuo, “Analysis of organic semiconductor multilayers with Ar cluster secondary ion mass spectrometry,” *Surf. Interface Anal.*, vol. 43, no. 1–2, pp. 95–98, Jan. 2011.

[139] B. Andreasen, D. M. Tanenbaum, M. Hermenau, E. Voroshazi, M. T. Lloyd, Y. Galagan, B. Zimmernann, S. Kudret, W. Maes, L. Lutsen, D. Vanderzande, U. Würfel, R. Andriessen, R. Rösch, H. Hoppe, G. Teran-Escobar, M. Lira-Cantu, A. Rivaton, G. Y. Uzunoğlu, D. S. Germack, M. Hösel, H. F. Dam, M. Jørgensen, S. A. Gevorgyan, M. V. Madsen, E. Bundgaard, F. C. Krebs, and K. Norrman, “TOF-SIMS investigation of degradation pathways occurring in a variety of organic photovoltaic devices – the ISOS-3 inter-laboratory collaboration,” *Phys. Chem. Chem. Phys.*, vol. 14, no. 33, p. 11780, 2012.

[140] T. Terlier, T. Maindron, J. P. Barnes, and D. Léonard, “Characterization of advanced ALD-based thin film barriers for organic electronics using ToF-SIMS analysis,” *Org. Electron. physics, Mater. Appl.*, vol. 59, no. April, pp. 21–26, 2018.

[141] M. Hermenau, M. Riede, K. Leo, S. A. Gevorgyan, F. C. Krebs, and K. Norrman, “Water and oxygen induced degradation of small molecule organic solar cells,” *Sol. Energy Mater. Sol. Cells*, vol. 95, no. 5, pp. 1268–1277, 2011.

[142] C.-P. Liu, W.-B. Wang, C.-W. Lin, W.-C. Lin, C.-Y. Liu, C.-H. Kuo, S.-H. Lee, W.-L. Kao, G.-J. Yen, Y.-W. You, H.-Y. Chang, J.-H. Jou, and J.-J. Shyue, “Molecular migration behaviors in organic light-emitting diodes with different host structures,” *Org. Electron. physics, Mater. Appl.*, vol. 12, no. 2, pp. 376–382, 2011.

[143] B.-Y. Yu, Y.-Y. Chen, W.-B. Wang, M.-F. Hsu, S.-P. Tsai, W.-C. Lin, Y.-C. Lin, J.-H. Jou, C.-W. Chu, and J.-J. Shyue, “Depth profiling of organic films with X-ray photoelectron spectroscopy using C60+ and Ar+ co-sputtering.,” *Anal. Chem.*, vol. 80, no. 9, pp. 3412–5, 2008.

[144] L. Zhang, K. Lloyd, and A. Fennimore, “Characterization of organic light emitting diodes (OLED) using depth-profiling XPS technique,” *J. Electron Spectros. Relat. Phenomena*, vol. 231, pp. 88–93, Feb. 2019.

[145] A. G. Shard, R. Havelund, S. J. Spencer, I. S. Gilmore, M. R. Alexander, T. B. Angerer, S. Aoyagi, J. P. Barnes, A. Benayad, A. Bernasik, G. Ceccone, J. D. P. Counsell, C. Deeks, J. S. Fletcher, D. J. Graham, C. Heuser, T. G. Lee, C. Marie, M. M. Marzec, G. Mishra, D. Rading, O. Renault, D. J. Scurr, H. K. Shon, V. Spampinato, H. Tian, F. Wang, N. Winograd, K. Wu, A. Wucher, Y. Zhou, and Z. Zhu, “Measuring Compositions in Organic Depth Profiling: Results from a VAMAS Interlaboratory Study,” *J. Phys. Chem. B*, vol. 119, no. 33, pp. 10784–10797, 2015.

[146] H. Nakamura, S.-H. Noh, M. Kuribayashi, and C. Adachi, “Influence of the atmosphere on organic-organic interfacial layers and deterioration in organic light-emitting diodes,” *J. Soc. Inf. Disp.*, vol. 23, no. 3, pp. 129–137, Mar. 2015.

[147] A. Chapiro, “Radiation Chemistry of Polymers,” *Radiat. Res. Suppl.*, vol. 4, p. 179, 1964.

[148] C. M. Mahoney, “Cluster secondary ion mass spectrometry of polymers and related materials,”

Mass Spectrom. Rev., vol. 29, pp. 247–293, 2010.

[149] T. W. Pi, T. C. Yu, C. P. Ouyang, J. F. Wen, and H. L. Hsu, "Electronic structure of tris(8-hydroxyquinolato) aluminum at room temperature and during annealing," *Phys. Rev. B - Condens. Matter Mater. Phys.*, vol. 71, no. 20, pp. 6–10, 2005.

[150] K. Jung, S. Park, Y. Lee, Y. Youn, H. I. Shin, H. K. Kim, H. Lee, and Y. Yi, "Energy level alignments at the interface of N,N'-bis-(1-naphthyl)-N,N'-diphenyl-1,1′-biphenyl-4,4′-diamine (NPB)/Ag-doped In2O3and NPB/Sn-doped In2O3," *Appl. Surf. Sci.*, vol. 387, pp. 625–630, 2016.

[151] A. Curioni, W. Andreoni, R. Treusch, F. J. Himpsel, E. Haskal, P. Seidler, C. Heske, S. Kakar, T. van Buuren, and L. J. Terminello, "Atom-resolved electronic spectra for Alq3 from theory and experiment," *Appl. Phys. Lett.*, vol. 72, no. 13, pp. 1575–1577, Mar. 1998.

[152] K. Ichiki, S. Ninomiya, Y. Nakata, Y. Honda, T. Seki, T. Aoki, and J. Matsuo, "High sputtering yields of organic compounds by large gas cluster ions," *Appl. Surf. Sci.*, vol. 255, no. 4, pp. 1148–1150, 2008.

[153] R. J. Paruch, Z. Postawa, and B. J. Garrison, "Physical basis of energy per cluster atom in the universal concept of sputtering," *J. Vac. Sci. Technol. B*, vol. 105, pp. 1–6, 2016.

[154] J. Van de Walle and P. Joyes, "Study of Bi n p + ions formed in liquid-metal ion sources," *Phys. Rev. B*, vol. 35, no. 11, pp. 5509–5513, Apr. 1987.

[155] H. Tohma and K. Miura, "Surface Damage of Organic Materials during XPS Analysis (1)," *Journal of Surface Analysis*, vol. 5, no. 2. pp. 220–223, 1999.

[156] N. Toyoda and I. Yamada, "Cluster size dependence of surface morphology after gas cluster ion bombardments," *Nucl. Instruments Methods Phys. Res. Sect. B Beam Interact. with Mater. Atoms*, vol. 266, no. 10, pp. 2529–2532, 2008.

[157] P. Philipp, Q. K. Ngo, M. Shtein, J. Kieffer, and T. Wirtz, "Ag-organic layered samples for optoelectronic applications: Interface width and roughening using a 500 eV Cs+ probe in dynamic secondary ion mass spectrometry," *Anal. Chem.*, vol. 85, no. 1, pp. 381–388, 2013.

[158] A. G. Shard, R. Havelund, M. P. Seah, S. J. Spencer, I. S. Gilmore, N. Winograd, D. Mao, T. Miyayama, E. Niehuis, D. Rading, and R. Moellers, "Argon Cluster Ion Beams for Organic Depth Profiling: Results from a VAMAS Interlaboratory Study," *Anal. Chem.*, vol. 84, no. 18, pp. 7865–7873, Sep. 2012.

[159] C. Noël and L. Houssiau, "Hybrid Organic/Inorganic Materials Depth Profiling Using Low Energy Cesium Ions," *J. Am. Soc. Mass Spectrom.*, vol. 27, no. 5, pp. 908–916, 2016.

[160] J. Brison, N. Mine, N. Wehbe, X. Gillon, T. Tabarrant, R. Sporken, and L. Houssiau, "Molecular depth profiling of model biological films using low energy monoatomic ions," *Int. J. Mass Spectrom.*, vol. 321–322, pp. 1–7, 2012.

[161] T. Conard, C. Fleischmann, R. Havelund, A. Franquet, C. Poleunis, A. Delcorte, and W. Vandervorst, "Inorganic material profiling using Arn+cluster: Can we achieve high quality profiles?," *Appl. Surf. Sci.*, vol. 444, pp. 633–641, 2018.

[162] H.-Y. Liao, K.-Y. Lin, W.-L. Kao, H.-Y. Chang, C.-C. Huang, and J.-J. Shyue, "Enhancing the sensitivity of molecular secondary ion mass spectrometry with C60+-O2+ cosputtering," *Anal. Chem.*, vol. 85, no. 7, pp. 3781–3788, 2013.

[163] Y. Murat, E. Langer, J.-P. Barnes, J.-Y. Laurent, G. Wantz, L. Hirsch, and T. Maindron, "Bright and efficient inverted organic light-emitting diodes with improved solution-processed electron-transport interlayers," *Org. Electron.*, vol. 48, pp. 377–381, Sep. 2017.

[164] P. Tyagi, M. K. Dalai, C. K. Suman, S. Tuli, and R. Srivastava, "Study of 2,3,5,6-tetrafluoro-7,7′,8,8′- tetracyano quinodimethane diffusion in organic light emitting diodes using secondary ion mass spectroscopy," *RSC Adv.*, vol. 3, no. 46, p. 24553, 2013.

[165] F. So and D. Kondakov, “Degradation mechanisms in small-molecule and polymer organic light-emitting diodes,” *Adv. Mater.*, vol. 22, pp. 3762–3777, 2010.

[166] P. Philipp, Q. K. Ngo, J. Kieffer, and T. Wirtz, “Silver Diffusion in Organic Optoelectronic Devices: Deposition-Related Processes versus Secondary Ion Mass Spectrometry Analysis Artifacts,” *J. Phys. Chem. C*, vol. 119, no. 41, pp. 23334–23341, 2015.

[167] T. Mouhib, A. Delcorte, C. Poleunis, and P. Bertrand, “Organic secondary ion mass spectrometry: Signal enhancement by water vapor injection,” *J. Am. Soc. Mass Spectrom.*, vol. 21, no. 12, pp. 2005–2010, 2010.